NBS SPECIAL PUBLICATION 400-23

U.S. DEPARTMENT OF COMMERCE / National Bureau of Standards

Semiconductor Measurement Technology:

ARPA/NBS Workshop IV. Surface Analysis for Silicon Devices

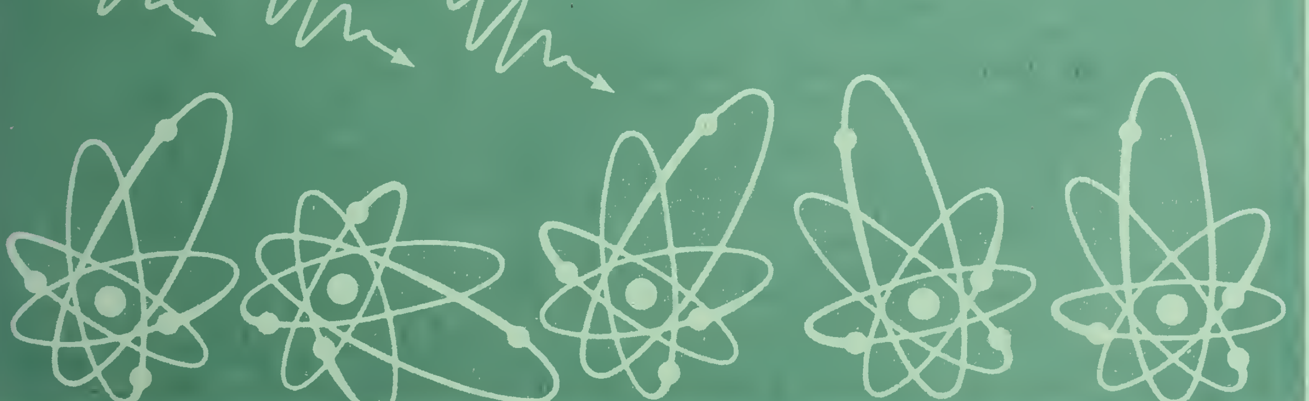

NATIONAL BUREAU OF STANDARDS

The National Bureau of Standards[1] was established by an act of Congress March 3, 1901. The Bureau's overall goal is to strengthen and advance the Nation's science and technology and facilitate their effective application for public benefit. To this end, the Bureau conducts research and provides: (1) a basis for the Nation's physical measurement system, (2) scientific and technological services for industry and government, (3) a technical basis for equity in trade, and (4) technical services to promote public safety. The Bureau consists of the Institute for Basic Standards, the Institute for Materials Research, the Institute for Applied Technology, the Institute for Computer Sciences and Technology, and the Office for Information Programs.

THE INSTITUTE FOR BASIC STANDARDS provides the central basis within the United States of a complete and consistent system of physical measurement; coordinates that system with measurement systems of other nations; and furnishes essential services leading to accurate and uniform physical measurements throughout the Nation's scientific community, industry, and commerce. The Institute consists of the Office of Measurement Services, the Office of Radiation Measurement and the following Center and divisions:

Applied Mathematics — Electricity — Mechanics — Heat — Optical Physics — Center for Radiation Research: Nuclear Sciences; Applied Radiation — Laboratory Astrophysics[2] — Cryogenics[2] — Electromagnetics[2] — Time and Frequency[2].

THE INSTITUTE FOR MATERIALS RESEARCH conducts materials research leading to improved methods of measurement, standards, and data on the properties of well-characterized materials needed by industry, commerce, educational institutions, and Government; provides advisory and research services to other Government agencies; and develops, produces, and distributes standard reference materials. The Institute consists of the Office of Standard Reference Materials, the Office of Air and Water Measurement, and the following divisions:

Analytical Chemistry — Polymers — Metallurgy — Inorganic Materials — Reactor Radiation — Physical Chemistry.

THE INSTITUTE FOR APPLIED TECHNOLOGY provides technical services to promote the use of available technology and to facilitate technological innovation in industry and Government; cooperates with public and private organizations leading to the development of technological standards (including mandatory safety standards), codes and methods of test; and provides technical advice and services to Government agencies upon request. The Institute consists of the following divisions and Centers:

Standards Application and Analysis — Electronic Technology — Center for Consumer Product Technology: Product Systems Analysis; Product Engineering — Center for Building Technology: Structures, Materials, and Life Safety; Building Environment; Technical Evaluation and Application — Center for Fire Research: Fire Science; Fire Safety Engineering.

THE INSTITUTE FOR COMPUTER SCIENCES AND TECHNOLOGY conducts research and provides technical services designed to aid Government agencies in improving cost effectiveness in the conduct of their programs through the selection, acquisition, and effective utilization of automatic data processing equipment; and serves as the principal focus within the executive branch for the development of Federal standards for automatic data processing equipment, techniques, and computer languages. The Institute consists of the following divisions:

Computer Services — Systems and Software — Computer Systems Engineering — Information Technology.

THE OFFICE FOR INFORMATION PROGRAMS promotes optimum dissemination and accessibility of scientific information generated within NBS and other agencies of the Federal Government; promotes the development of the National Standard Reference Data System and a system of information analysis centers dealing with the broader aspects of the National Measurement System; provides appropriate services to ensure that the NBS staff has optimum accessibility to the scientific information of the world. The Office consists of the following organizational units:

Office of Standard Reference Data — Office of Information Activities — Office of Technical Publications — Library — Office of International Relations — Office of International Standards.

---

[1] Headquarters and Laboratories at Gaithersburg, Maryland, unless otherwise noted; mailing address Washington, D.C. 20234.

[2] Located at Boulder, Colorado 80302.

Semiconductor Measurement Technology:
ARPA/NBS Workshop IV.
Surface Analysis for Silicon Devices

A. George Lieberman

Electronic Technology Division
Institute for Applied Technology
National Bureau of Standards
Washington, D.C. 20234

This activity was supported by
The Defense Advanced Research Projects Agency
under ARPA Order 2397, Program Code 5D10
and
The National Bureau of Standards
Washington, D.C. 20234

U.S. DEPARTMENT OF COMMERCE, Elliot L. Richardson, *Secretary*
James A. Baker, III, *Under Secretary*
Dr. Betsy Ancker-Johnson, *Assistant Secretary for Science and Technology*
NATIONAL BUREAU OF STANDARDS, Ernest Ambler, *Acting Director*

Issued March 1976

Library of Congress Cataloging in Publication Data
Main entry under title:

ARPA/NBS workshop IV.

(Semiconductor measurement technology) (NBS Special publication ; 400-23)
"Contains the proceedings of the ARPA/NBS workshop IV, Surface analysis for silicon devices, held at the National Bureau of Standards on April 23-24, 1975."
Supt. of Docs. no.: C 13.10:400-23.
1. Semiconductors—Testing—Congresses. 2. Silicon—Testing—Congresses. 3. Surfaces (Technology)—Congresses. 4. Spectrum analysis—Congresses. I. Lieberman, Alfred George, 1937- II. United States. National Bureau of Standards. III. Series. IV. Series: United States. National Bureau of Standards. Special publication ; 400-23.
QC100.U57 no. 400-23 [TK7871.85] 602'.1s [621.3815'2]
76-608043

National Bureau of Standards Special Publication 400-23

Nat. Bur. Stand. (U.S.), Spec. Publ. 400-23, 238 pages (Mar. 1976)

CODEN: XNBSAV

PREFACE

The ARPA/NBS Workshop IV, *Surface Analysis for Silicon Devices,* was held at the National Bureau of Standards on April 23-24, 1975 under the cosponsorship of the National Bureau of Standards and the Defense Advanced Research Projects Agency. It was the first meeting, on a national level, to address the applicability of modern surface measurement techniques to the analysis of semiconductor devices. Representatives from industrial, governmental and academic organizations concerned with device manufacture, analysis and instrument design participated in this workshop. Speakers were selected from among the finest and most active researchers in the field. The outcome was a large and enthusiastic workshop attendance. It is hoped that this report will convey the spirit of the workshop to those who could not attend.

A. George Lieberman
Editor

ABSTRACT

This report contains the proceedings of the ARPA/NBS Workshop IV, *Surface Analysis for Silicon Devices,* held at the National Bureau of Standards on April 23-24, 1975.

The Workshop, as part of an NBS program to develop measurement technology for the field of semiconductor devices, was held to discuss the present capabilities and future prospects of modern analytical beam techniques as applied to silicon, and associated insulator films and device structures. Of particular interest were the determination of impurity profiles, surface contamination, and interface characteristics. Techniques utilizing impinging electron, ion, neutral or photon beams were considered. The Workshop was directed at the analysts, the semiconductor manufacturers who use the analysts' results, and the instrument people who design and manufacture the analytical equipment. Transcripts of the discussions following each paper are also included within these proceedings.

Key words: Auger spectroscopy; depth profiles; electron beam induced imaging; ESCA; insulator films; interface characteristics; internal photoemission; ion scattering spectroscopy; nuclear resonance profiling; photodepopulation; photovoltaic imaging; Rutherford backscattering; SCANIIR; secondary ion mass spectroscopy; semiconductor devices; silicon; surface analysis; X-ray photoelectron spectroscopy.

TABLE OF CONTENTS

ION AND NEUTRAL BEAMS - TECHNIQUES AND APPLICATIONS

TABLE OF CONTENTS

PAGE

ELECTRON AND PHOTON BEAMS - TECHNIQUES AND APPLICATIONS

WELCOMING REMARKS

Judson C. French, Chief

Electronic Technology Division
National Bureau of Standards
Washington, D. C. 20234

Good morning. It is my pleasure this morning to welcome you on behalf of the National Bureau of Standards and our cosponsor, the Defense Advanced Research Projects Agency, to the Workshop on Surface Analysis for Silicon Devices.

This Workshop is the fourth in a series dedicated to the furtherance of the measurement technology needed by the semiconductor device industry in its attempt to provide to its customers products that are based on the most advanced technology yet have high reliability and the affordable costs which result from high yields.

These products are essential components in modern electronics, and they consequently play a vital role in the social and economic welfare of our Nation and in its defense. They are, therefore, a matter of considerable interest both to the Department of Commerce and to the Department of Defense, the parent organizations of the sponsors of these Workshops.

To those of you who are not in the semiconductor business, and in this Workshop in particular there are many such people, it may come as a surprise that there is any need for NBS and ARPA to carry on work in a field which is so technologically sophisticated and so innovative. The reason is that the sophistication and innovative abilities of the semiconductor industry have led to the development of new processes and new devices much faster than the measurement techniques for their control and characterization have been developed.

In the fifteen years that our NBS staff has worked with the semiconductor industry and its customers we have seen increasing need for improvements in practical methods of measurement for analysis, control, and specifications in this field. And we have learned that the Bureau can be especially helpful in this field because of its neutrality in evaluating measurement methods and associated technology, and because its charter encourages it to work in the area of generic measurement for industry-wide use and market-place application. This is an area where individual companies understandably find less incentive for extensive research than in areas leading to new and proprietary processes and designs.

As a result, the NBS Semiconductor Technology Program has been established, having as its goal the development and standardization of improved methods of measurement for use in specifying materials and devices and in control of device fabrication processes: methods that have been well documented and tested for technical adequacy, are of demonstrated precision of an industrially acceptable level, and are acceptable to both users and suppliers.

When such methods are used by the electronics industry, they are expected to provide a more consistent set of measured results and interpretations and, hence, lead to improved quality control and yield in the manufacturer's plant, and to improved reliability and economy in the customer's applications.

In recent years, ARPA has joined with us as a major sponsor of the program in order to provide a new approach to the solution of DoD problems in component reliability and availability, system costs, and system maintainability.

Our program now encompasses work on selected measurements ranging from those needed to characterize process materials; through those for photolithography, process control using test structures, bonding and die attachment, and hermeticity; on to thermal and electrical properties of finished devices.

Modern devices are dependent for their operation on the properties of extremely thin layers of silicon and oxides, and their interfaces. Performance demands, including those of reliability and radiation hardness, call for knowledge and manufacturing control of the chemical and physical makeup of these structures that pose requirements for sensitivity and spatial resolution far exceeding those provided by traditional analytical methods.

Thus, an exciting new area of interest in our Program is the subject of this Workshop: the determination of the present qualitative and quantitative capabilities, and the future prospects, of modern analytical beam techniques as applied to the analysis of silicon and associated insulator films and device structures.

Of particular interest are the determination of impurity profiles, surface contamination, and interface characteristics, using electron, ion, neutral particle, or photon beams.

Our initial work in this area has disclosed both great promise, and numerous problems in interpretation and quantification of the results of beam analysis methods. It has also disclosed that too little communication exists between many in the semiconductor industry who have need for the new techniques, the many expert analysts, and manufacturers of the analytical instruments.

It is the purpose of this Workshop to bring some of these people together to foster discussions between these three groups for the mutual benefit of all three.

I share the pleasure of your Chairman, George Lieberman, at seeing the large attendance of representatives of these groups. I hope that the report of the Workshop, when it is published, will carry your discussions to the many others who were unable to attend. The titles of the papers, and the stature of our speakers, promise most interesting and valuable presentations, and I encourage you to take advantage of the expertise of our speakers and of your colleagues in the audience in the discussions.

I would like to acknowledge the efforts of our Workshop Committee in making the arrangements for today's meeting: Dr. Lieberman, its chairman; Kathy Leedy and Harry Schafft, for coordination and publicity; and Sara Torrence, for the local arrangements.

I want to thank all of you, and especially our speakers, for attending and helping us to make this a useful Workshop. And now I will return the microphone and the conduct of the day's program to Dr. Lieberman. Again, thank you all.

NBS Special Publication 400-23, ARPA/NBS Workshop IV, Surface Analysis for Silicon Devices,
held at NBS, Gaithersburg, Maryland, April 23-24, 1975 (Issued March 1976)

INTRODUCTORY CONCEPTS FOR SILICON SURFACE ANALYSIS

A. George Lieberman

Electronic Technology Division
National Bureau of Standards
Washington, D. C. 20234

The planar silicon technology for semiconductor device manufacturing was first described in 1960. Since then, planar silicon technology has become the principal method for fabricating semiconductor devices and integrated circuits (ICs). The technique has now been developed to the extent that 3,000 to 10,000 MOS components can be manufactured on chip areas which only fifteen years before could hold no more than a dozen bipolar components. To meet today's component density requirements, on chips barely millimeters on a side, design rules have been met that call for micrometer linewidths and gate oxides less than 0.1 μm thick. In addition, most of the device physics is found to occur within nanometers from the silicon surface. The continuing trend toward larger scales of integration and microminiaturization has consequently increased the need for quantitative measurements in extremely shallow multilayer device structures and accounts for the growing interest in surface analysis for silicon devices.

Over the years, manufacturing techniques for control of the IC process have not substantially changed. Yet, it has been estimated that only three percent of the silicon entering the manufacturing process now ends in acceptable devices. New techniques are clearly called for to improve production yield and assure the quality of completed devices. Modern surface analysis can provide the IC manufacturer with the potential to identify, count, and locate, with monolayer precision, trace impurity atoms. For the device scientist, these analytical methods also allow determinations of chemical bonding, carrier trapping levels, and densities of states information. Several of the surface analysis techniques are already in successful use for IC failure analysis.

From among the myriad of surface spectroscopies which have been spawned over the past decade, a half dozen of the most promising techniques for the analysis of silicon device structures and associated materials were selected for workshop discussion. The determination of impurity profiles, surface contamination, and interface characteristics for IC process control were held foremost in mind. The instrumentation had also to be commercially available or capable of readily being constructed.

Referring to figure 1 we see that each spectroscopy employs a beam of primary particles to probe and interact with the impurity atoms on the device structure. A flux of secondary particles is detected which may, or may not, be the same as the primary particles. The difficulty in detecting neutrals has been reason to exclude this species as a viable secondary particle spectroscopy. The ion and neutral excitation spectroscopies on the right half of the diagram form a group distinct from the electron detection spectroscopies on the left. Of course, there are other spectroscopies, but they do not appear to meet the objectives of the workshop.

The ion and neutral excitation spectroscopies may be ranked in energy. At the low end, between 0.5 and 2 keV, is Ion Scattering Spectroscopy (ISS), while at the high end, from 0.5 to 3 MeV is Rutherford Backscattering Spectroscopy (RBS). Both spectroscopies measure the energy loss of the primary ion after it experiences an elastic binary collision with an impurity atom. The energy loss serves to identify the impurity atom through its mass. Because of its low energy, ISS is extremely surface sensitive. A most important aspect of RBS is that it is the only quantitative and essentially nondestructive spectroscopy for depth profiling available today.

RBS faces problems detecting light elements in heavier substrates, but here the complementary accelerator technique known as Nuclear Resonance Profiling (NRP) is of aid. The chief disadvantage of all these accelerator techniques is the cost and size of the equipment. However the increasing usage of ion accelerators for impurity implantation in device structures may eventually offset this.

At intermediate beam energies, from 1 to 20 keV, the impact of inert or reactive ions is effective in removing and ionizing surface material in a controllable manner. The method of Secondary Ion Mass Spectroscopy (SIMS) consists of determining the mass to charge ratio of these sputtered ions. SIMS is the most sensitive of all the depth profiling methods, but it suffers from orders of magnitude variation in sensitivity from one element to the next.

SCANIIR, an acronym for Surface Composition by Analysis of Neutral and Ion Impact Radiation, is the optical analogue of SIMS. SCANIIR utilizes the characteristic radiative relaxations of sputtered metastable ions to identify and quantify the amount of an element present on an investigated surface. The major advantage of this technique is its ability to use neutral beams to analyze insulating films under field-free conditions.

Auger Electron Spectroscopy, AES, is the most popular of the surface analysis methods. In conjunction with simultaneous sputter-etching it can be used to determine compositional depth profiles. Impurity elements are identified by the characteristic energies of their detected Auger electrons. Sensitivities vary by less than a factor of ten for the various elements, except for hydrogen and helium which cannot be detected. In addition to having superb depth resolution, AES is also capable of excellent lateral resolution in the plane of the specimen, e.g., when the focussed beam of a scanning electron microscope is used as the primary excitation.

The UV and X-ray Photoelectron Spectroscopies (UPS and XPS*) are becoming increasingly important for electronic materials analysis. UPS has been applied to study the effects of contaminants on surface potentials, and to study the trapping levels in the energy bandgap of insulators. Since UV photoelectrons originate from valence band states, or thereabouts, they are not element specific. On the other hand, the core level binding energies measured by XPS not only uniquely identify the parent atoms, but also contain information concerning its chemical environment. The chemical information contained in the XPS spectra is what makes this technique so useful.

Statements comparing sensitivities, detection limits, resolutions, sampling depths, etc., of the various spectroscopies must be tied to a particular material, instrument, measurement procedure, and the skill of the experimentalist. There is also a certain transmutability of the instrument parameters themselves, e.g., the ability to trade sensitivity for spectral resolution. It may be well to consider the definitions of sensitivity and detection limit used in evaluating a spectroscopy. These definitions are illustrated in figure 2 for a typical impurity calibration curve.

The sensitivity of an analytical technique refers to the slope of a calibration curve, i.e., the change in the output signal to the increment in material concentration. It is, so to speak, the gain of the instrument. By the output signal is meant the amplitude of the spectral peak less the background level. The background consists of all unwanted information which is correlated with the desired signal, and it is different from noise which is not correlated and, in principle, can be reduced to any desired level by averaging the signal over an ensemble of identical specimens or over a sufficently long period of time. The data acquisition time is, of course, limited in practice by the rate at which the surface deteriorates under the action of the probe or by contamination. Even under ultrahigh vacuum conditions, at pressures of 10^{-8} pascals ($\sim 10^{-10}$ Torr), a surface can become completely covered by deposited contamination in less than two hours.

The detection limit is a concept which is related to the sensitivity. The detection limit is defined as the minimum concentration of an impurity required to produce an observable signal with 95% confidence. The criterion in common use for whether a trace detection has occurred is that the signal count N must exceed the background count N_B by three times the square root of the background count ($N > N_B + 3\sqrt{N_B}$).

The detection limit of a surface analytical technique for a specified element is usually stated as being a fraction of a monolayer. A surface measurement should ideally sample only the very outermost layer of surface atoms, a depth of less than one nanometer. Silicon has a bulk atomic density of 5×10^{22} cm^{-3} and therefore a monolayer of coverage would contain about 10^{15} atoms per square centimeter of surface. Most surface measurements today sample depths of several nanometers with the result that impurity atoms residing below the surface, but within the sampling volume, are interpreted as belonging to the surface. Consequently, the detection limit for a surface analysis may appear to be either better or worse than it

---

[*] Also known as Electron Spectroscopy for Chemical Analysis (ESCA).

actually is, depending upon the technique, the sampling depth, and the particular impurity distribution. When a surface analytical technique is applied, together with some form of surface removal, for the purpose of measuring an impurity concentration - depth profile, it becomes appropriate to introduce bulk detection limits and to speak of volumetric concentrations. It follows that those surface analytical techniques employing the smallest sampling depths are capable of yielding concentration profiles displaying the greatest depth resolution and possibly the poorest bulk detection limits.

These concepts are not, of course, the only factors to be considered in evaluating a spectroscopy. One has only to examine a spectrometer manufacturer's specification sheet to realize how complex the choice of a technique or an instrument can be.

In summary, the evolution of high component density, planar silicon technology has forced us to look for new techniques to assist or replace the traditional process control methods. Microprobes of extreme sensitivity are being called for which can identify, quantify and locate impurity atoms at surfaces, interfaces and within thin films. Only a few commercially available surface analysis techniques have demonstrated their usefulness for studying silicon device structures and related material properties. These techniques will be examined at this workshop in light of their performance for analyzing silicon, silicon dioxide, and related materials.

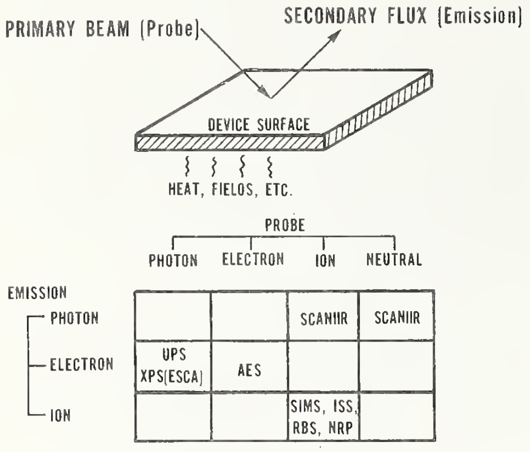

EMISSION \ PROBE	PHOTON	ELECTRON	ION	NEUTRAL
PHOTON			SCANIIR	SCANIIR
ELECTRON	UPS XPS(ESCA)	AES		
ION			SIMS, ISS, RBS, NRP	

Figure 1. The analysis of a surface by photon, electron, ion or neutral beams. The surface may be stressed to enhance the spectral information carried by the secondary emission. The primary and secondary particles need not be identical. A description of the techniques appears in the text.

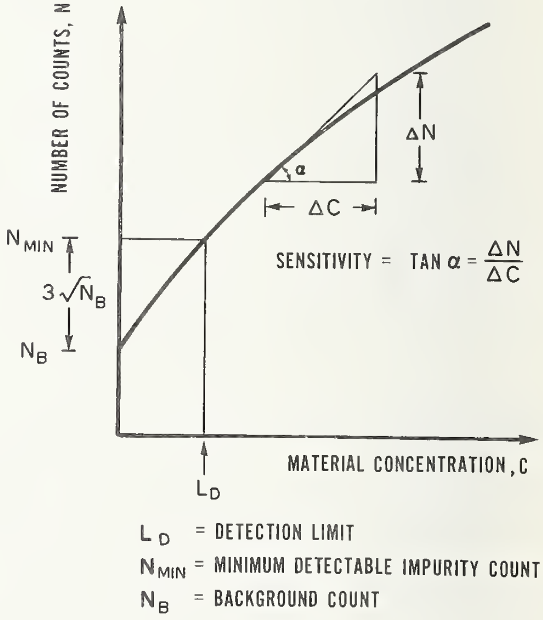

Figure 2. Definitions of sensitivity, detection limit, minimum detectable impurity level and background are illustrated for a typical impurity calibration curve.

NBS Special Publication 400-23, ARPA/NBS Workshop IV, Surface Analysis for Silicon Devices, held at NBS, Gaithersburg, Maryland, April 23-24, 1975 (Issued March 1976)

IDENTIFICATION OF INTEGRATED CIRCUIT PROCESS AREAS AMENABLE TO DIAGNOSIS AND CONTROL BY ANALYTICAL BEAM TECHNIQUES

Bruce E. Deal

Fairchild Camera and Instrument Corporation
Palo Alto, California 94304

ABSTRACT

The general process steps required to fabricate silicon integrated circuits are reviewed, and examples in each area are indicated where analytical beam techniques can be used for compositional analysis and process control. In some cases satisfactory methods of analysis have been established and are in current use, while in others new techniques need to be developed. Those characterizations related to device reliability and yield improvement are considered to be the most important; these include metallization, chip protection, and oxide charge control for reliability effects, and photomasking and cleaning in regards to yield considerations.

INTRODUCTION

Analytical beam techniques have been employed for a number of years to evaluate and control processes used to fabricate semiconductor devices and integrated circuits. As the structures of these devices and circuits have become more and more complex with increasing component densities, the requirements for more refined analytical techniques have increased accordingly. The purpose of this paper is to review areas of integrated circuit fabrication where such analytical beam techniques of analysis are important.

There are two general types of integrated circuits--MOS and bipolar. Examples of their structures are shown in Fig. 1. While specific process steps used to fabricate these circuits vary widely from product line to product line, some general process areas are common to all MOS or bipolar structures. These are as follows:

Silicon Substrate Preparation
Thermal Oxidation
Photomasking and Cleaning
Diffusion
Dielectric Deposition
Metallization
Chip Protection

In this paper we will discuss each of these general areas, and will indicate where problems in composition or structure may arise which can affect device properties or performance. We will give examples which show how some of these problems are being solved by the proper use of analytical beam techniques, and where, in other cases, additional work needs to be done. Due to space limitations, only one or two examples will be given for each process area.

Before discussing these possible problem areas, we should emphasize that many of today's bipolar integrated circuit structures are every bit as complicated as MOS-type circuits, and we can no longer say that MOS process control problems are more severe than those of bipolar circuits. Also, the formidable requirements for tools used in the analysis of integrated circuit structures produced today are demonstrated by the yearly increase of circuit complexity as shown in Fig. 2. These data were produced by Gordon Moore [1] and show that in 1975 the semiconductor industry can produce circuits containing more than 10,000 individual components on chips with areas not too much larger than those of discrete devices produced only fifteen years ago. Thus, the challenge to those involved with developing and carrying out materials analysis techniques is readily apparent.

DISCUSSION OF INTEGRATED CIRCUIT PROCESSING AREAS

(A) Silicon Substrate Preparation

Characterization and analysis of semiconductor substrates is an established procedure and includes several areas. The first is the original crystal as produced by various crystal growing techniques. Such properties as structure, impurities, dopant distribution and defects such as dislocations must be characterized and kept under suitable control. Next, the silicon surface after wafer slicing must be maintained free of contamination and particles. In addition, the surface should have the proper crystal orientation and be relatively free of stress. Finally, subsequent substrate processing steps such as buried collector preparation and epitaxial film deposition must be controlled. In the latter case, all considerations applicable to the original crystal bulk and surface apply, but in addition, analysis and control of the dopant profile become increasingly important.

As indicated above, methods of analysis used to characterize the properties of the silicon substrate are well known. Of course, as larger slices are used and more complex circuit structures are developed, the analytical techniques may have to be refined. Since this area of integrated circuit fabrication is probably under better control than the others, no specific examples will be presented here. However, the reader is referred to a general reference on the subject of surface characterization [2].

(B) Thermal Oxidation

Thermal silicon dioxide (SiO_2) is the basis for today's semiconductor devices and integrated circuits. It provides passivation for active device regions that is not equaled by other types of dielectric layers generally prepared by deposition techniques. The thermal oxidation kinetics and properties have been characterized in a satisfactory manner so that devices with predictable properties may be produced. Included in this characterization are the electrical properties as determined by the four types of oxide charges. These charges are Q_{ss}, the fixed oxide charge; N_{st}, fast interface states; Q_o, mobile ionic charge; and N_{ot}, radiation-induced charge. While the empirical dependence of these charges on processing variables is well known, a number of questions remain as to their exact origin and physical nature [3]. Indications of how these charges may be investigated using analytical beam techniques are as follows.

Figure 3 depicts a cross-section of a thermal silicon oxide as oxidation is proceeding. Also included in the figure is the general relationship for the thermal oxidation process. It can be noted that a thin oxide region at the SiO_2-Si interface is shown to contain partially ionized silicon. It is believed that the ionized or excess silicon in this region is the origin of Q_{ss}, the fixed oxide charge. However, investigators to date have not verified this origin and additional work needs to be done. An example of the type of analysis that can be employed is shown in Fig. 4. Here, an analysis of the Si/O ratio in a thermal oxide has been obtained using the ion backscattering technique [4]. Although it is not clear in the figure, the data indicate that a thin layer of about three atomic layers is present which contains a silicon rich oxide. This is compatible with the Q_{ss} origin model described above. However, it is clear that additional characterizations and analyses are required to provide a satisfactory understanding of this phenomenon.

The same questions arise regarding origin of N_{st}, the fast interface states. These states or charges may have a similar origin to Q_{ss}, but since they are in electrical communication with the silicon, they can respond to changes in surface potential. While much is known about Q_{ss} and N_{st}, the question of their origin is still quite thought-provoking and presents a challenge to those involved with beam analysis.

Similar questions may be asked about the physical nature of Q_o, mobile impurity ions. These ions, which include sodium, lithium, potassium, or hydrogen protons, have long been a source of instabilities in semiconductor device fabrication. A recent development has been the incorporation of a chlorine species in the oxidation process. This chlorine has been reported to "cure all ills" in areas of ionic instability, dielectric breakdown, junction leakage, fast state generation, and others. An example of a verified improvement is shown in Fig. 5 ,where MOS device drift is almost eliminated in two cases of sodium contamination [5]. Auger analysis is being used to determine some of the compositional properties of these chlorine-containing oxides as shown in Fig. 6, as reported by Chou et al [6]. However, many additional questions remain concerning ion instabilities, in general, and even effects of the analysis technique on the impurity profiles themselves have been noted. Thus, another challenge is presented to materials analysis scientists.

The identification of the origin and elimination of N_{ot}, the radiation induced charge is no exception to the discussion presented above. Much time and money have been expended on this subject over the past ten or more years, and many questions still remain. In Fig. 7, Gwyn [7] summarizes some of the different "cures" for radiation hole trapping in oxides. These proposed solutions include, optimizing oxidation conditions, incorporating species such as aluminum or chromium in the oxide, or even the use of mixed oxides or dielectrics. The need for developing analytical beam techniques for identification of radiation charge origin and elimination mechanisms is obvious, if we are to be able to produce MOS devices that will withstand radiation environments.

In addition to oxide charges, other areas of thermal oxidation that need to be controlled or better characterized are oxide integrity, complex oxide-silicon interfaces and dopant impurity redistribution. These will be briefly discussed in later sections.

(C) Photomasking and Cleaning

Of all the areas of integrated circuit fabrication, none has advanced as rapidly as the photomasking operation. This is demonstrated in Fig. 8, where a single MOS transistor of 1964 is pictured as an insert in a photo of a recently developed calculator chip. The latter, which contains about 10,000 individual transistors, is still not as densely packed as more advanced memory chips. The dimensional scales on the two devices in Fig. 8 are roughly equivalent; the larger circuit being about 150 x 180 mils.

The tremendous increase in complexity of today's circuits results in enormous problems related to carrying out the photomasking process as well as to the associated cleaning treatments. The use of analytical beam techniques for identifying and controlling contamination left over from these processes will become increasingly important. Likewise, methods need to be established for better characterization of the photoresist materials. In addition to electrical instability problems, the question of oxide integrity presents itself. In Fig. 9, Kern has provided an example of how two different types of resists may affect defect formation in the underlying oxides [8]. While the incentive for those involved in materials analysis may not be as obvious or the results as satisfying in this area, it is certain that the effects on device yield and reliability are more significant than in almost any other IC processing step.

(D) Diffusion

One of the oldest processes associated with silicon devices is that of dopant diffusion. Typically in the past, the source of dopants that are deposited on the silicon surface prior to diffusion into the silicon has been a gaseous species transported in a diffusion tube from solids (P_2O_5, B_2O_3), liquids ($POCl_3$) or gases (B_2H_6). More recently, other types of sources have been employed, such as doped vapor deposited dielectrics, spin-on oxides and ion implantation. In all cases, the main problem has been to determine the diffusion profile before, and more important, after the subsequent high temperature diffusion steps. Also, it has been important to know what percentage of the doping species is electrically active. Thus, many analytical techniques have been used for obtaining these profiles, as well as to determine anomalies and structural damage to the silicon. An example showing the importance of being able to determine dopant profiles is shown in Fig. 10, where the depth of a dopant's penetration during ion implantation is determined by the type of dielectric on the silicon surface [9].

Closely related to the diffusion process and requiring similar types of profile analysis are impurity gettering, and redistribution of dopants during oxidation. In the case of gettering, unwanted metallic impurities, such as copper, iron, nickel, and the like are removed by a complexing action at high temperatures with a species such as phosphosilicate glass. A knowledge of the distribution of these impurities before and after gettering is important. Likewise, the changing dopant profiles in the silicon due to redistribution during thermal oxidation must be known in order to end up with the proper device electrical properties. It has been difficult to accurately predict and verify redistribution profiles after just one oxidation treatment. When it is considered that today's integrated circuit processes employ many such treatments, the correct prediction and/or determination of dopant profiles is almost impossible. In Fig. 11, an example is shown where attempts are being made to calculate and determine profiles after just two oxidation steps [10]. It is obvious that much more work, both theoretical and analytical, needs to be done in this area.

Finally all of the above considerations discussed thus far must be put together and then the problems multiplied by some unknown factor when a three-dimensional aspect is considered. This is exemplified by the drawing in Fig. 12, which depicts a device structure employing an oxide or Isoplanar type of isolation. The interface between this oxide and the device silicon now can result in changes in orientation-dependent, oxide charge densities, as well as dopant impurity concentrations, all of which can severely degrade device properties. Furthermore, the difficulty in predicting these interface properties is exceeded only by the difficulty in analyzing them. So it is obvious that there will be plenty for the materials analysis scientist to do in cooperation with the device engineer, when this complex type of structure is considered.

(E) Dielectric Deposition

Vapor deposited dielectric films are generally used in conjunction with thermal oxides to provide additional improved device properties. These properties include impurity ion masking, increased voltage breakdown, gettering of impurities, and others. Dielectrics most commonly used for these applications are silicon nitride, silicon oxide, aluminum oxide and phosphosilicate glass. While the use of these deposited dielectrics provides improved characteristics, some adverse effects may result. One such effect is an electrical instability due to charge generation. Four general types of charge formation instabilities have been found to be associated with the combination of deposited dielectric films over thermal silicon oxides. These are indicated in Fig. 13. The degree of all these effects is dependent on the structural composition of the deposited dielectrics. Thus, the analysis and control of the film compositions and structures are very important. An example of this effect is shown in Fig. 14. Here, the electrical conductivity of a silicon nitride film is inversely proportional to the ratio of nitrogen to silicon in the film, the latter being a function of the reactant gas ratios during film formation [11]. The conductivity of the Si_3N_4 thus determines the degree of instability (c) in Fig. 13. The etch rate of the nitride film also is a function of its composition. Many other examples could be given which show the importance of being able to characterize the compositional and structural properties of deposited dielectric films, which can lead to adverse effects on device properties.

(F) Metallization

The metal interconnection system represents a key aspect of integrated circuit fabrication. This metal has typically been pure aluminum, but lately aluminum alloys have been used, as well as inert metals (Pt, Au), refractory metals (Mo, W) and, in the case of MOS circuits, polycrystalline silicon. In the latter case, the films are doped with phosphorus or boron to achieve the required conductivity. As integrated circuits have become more complex, the analysis and control of the metal interconnection systems have been accordingly more important. This has especially been the case with the addition of alloying constituents to the aluminum for improved electromigration resistance (Cu) and for reducing silicon substrate alloying effects (Si). An example of effects on the metal film properties due to the addition of these elements is shown in Fig. 15. Here, it is important to analyze and control the precipitate or cluster formation as well as nodule growth [12]. Another example where structural analysis of interconnections is important is that of polycrystalline silicon deposition, as shown in Fig. 16. In this case, X-ray analysis has been used to determine relative amounts of orientation textures which can affect both electrical properties as well as dopant diffusion kinetics [13]. It is felt that satisfactory techniques exist for charactizing these metal films, but that much more work is needed to monitor changes in film structure and composition during various heat treatments and even device operation. In the latter case, reliability aspects become important as chemical reactions occur between the metal films and the environment in the case of nonhermetic packages (see next section).

(G) Chip Protection

Very soon after integrated circuits were developed in the early 1960's, it was discovered that some sort of layer must be deposited over the metallized chip to protect the metal interconnections from mechanical damage during subsequent assembly procedures. Films used for this purpose were plastics, sedimented glasses, and vapor deposited oxides. Later it was found that this same type of chip-protecting film was required to prevent the metal from reacting with moisture and other gases which penetrated plastic packages. At the same time, it was difficult to obtain a film which exhibited all the necessary properties--physical, chemical and electrical--to provide the necessary protection. This is true to a large extent at the present time. One of the most common causes of reliability problems in plastic packaged integrated circuits is metal corrosion.

Many of the above problems result from improper analysis and control of the chip protection film, which quite often contains phosphorus. This phosphorus prevents cracking of the deposited silicon oxide film, but also can react with water to form phosphoric acid. This acid in turn is a common etchant for aluminum. Paulson and Kirk [14] have presented some curves showing optimum phosphorus concentrations for these films, and one of these is shown in Fig. 17. This example helps to point out the requirements for the determination of composition and structure of chip protection films. An additional difficulty is that of obtaining a proper depth profile of the constituents.

One last type of characterization that is very important in this area involves failure analysis. When integrated circuits are subjected to life tests or fail in actual use, the understanding of the failure mode is very important and may be accomplished by a carefully executed analysis. Such an analysis includes identification of reaction products, and analytical beam techniques can be used very effectively for this purpose.

CONCLUSIONS

In summary, we have reviewed the various processing steps of integrated circuit fabrication. In doing so, we have noted the many areas where analytical beam techniques can be used to provide a better control of these processes and the resulting device properties. Many such analyses are being successfully used today, while in some areas, new or improved methods must be developed. If priorities are to be stated, those areas of analysis related to device reliability should be listed first. These include chip protection, metallization and control of device electrical properties. Next in importance would be wafer sort yield. In this case, control and characterization of the photomasking and cleaning processes would undoubtedly be the most important factors, since this process area dominates yields of semiconductor integrated circuits today. Finally, it is important that the scientists who are responsible for developing and carrying out the analyses keep in close communication with the IC processing engineers, so that the problems that need to be solved are solved, and that our always limited resources are used most efficiently.

ACKNOWLEDGMENTS

The author wishes to thank A. J. Learn and R. C. McDonald for helpful discussions concerning various aspects of this paper.

REFERENCES

1. Moore, G. E., Private Communication.
2. *Characterization of Solid Surfaces,* P. F. Kane and G. B. Larrabee, Eds., (Plenum Press, New York 1974).
3. Deal, B. E., *J. Electrochem. Soc.* 121, 1986 (1974).
4. Sigmon, T. W., Chu, W. K., Lugujjo, E. and Mayer, J. W., *Appl. Phys. Lett.* 24, 105 (1974).
5. Kriegler, R. J. and Devenyi, T. F., *Proc. 11th Annual Reliability Physics Conf.,* Las Vegas, Nevada, April 3-5, 1973.
6. Chou, N. J., Osburn, C. M., van der Meulen, Y. J., and Hammer, R., *Appl. Phys. Lett.* 22, 380 (1973).
7. Gwyn, C. W., Sandia Laboratories Report No. SLA-73-0017, Jan. 1973.
8. Kern, W., *RCA Review* 34, 655 (1973).
9. Reddi, V. G. K. and Yu, A. Y. C., *Solid State Tech.*, 35, (Oct. 1972).
10. Margalit, S., Neugroschel, A. and Bar-lev, *IEEE Trans. Elec. Dev.* ED-19, 861 (1972).
11. Gyulai, J., Meyer, O., Mayer, J. W. and Rodriguez, V., *J. Appl. Phys.* 42, 451 (1971).
12. Learn, A. J., *Thin Solid Films* 20, 261 (1974).
13. Kamins, T. I. and Cass, T. R., *Thin Solid Films* 16, 147 (1973).
14. Paulson, W. M. and Kirk, R. W., *Proc. 12th Annual Reliability Phys. Conf.* Las Vegas, Nevada, April 2-4, 1974.

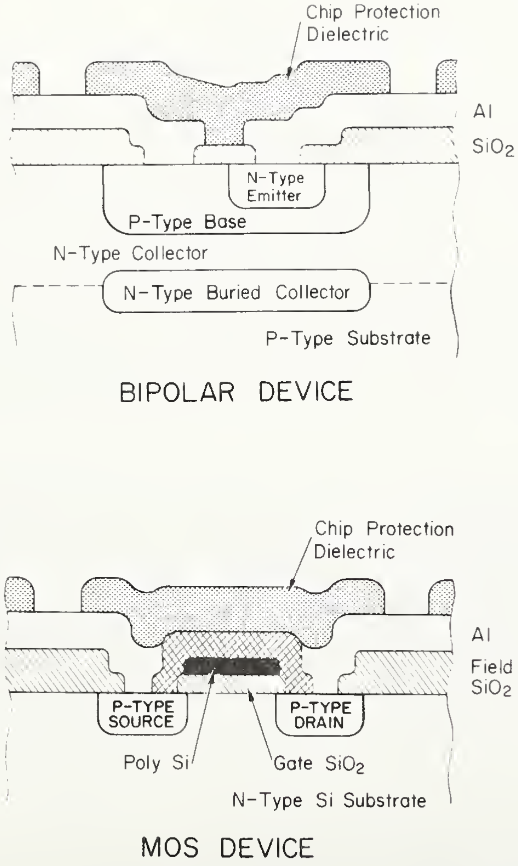

Figure 1. Representative cross-sections of two main types of semiconductor device structures.

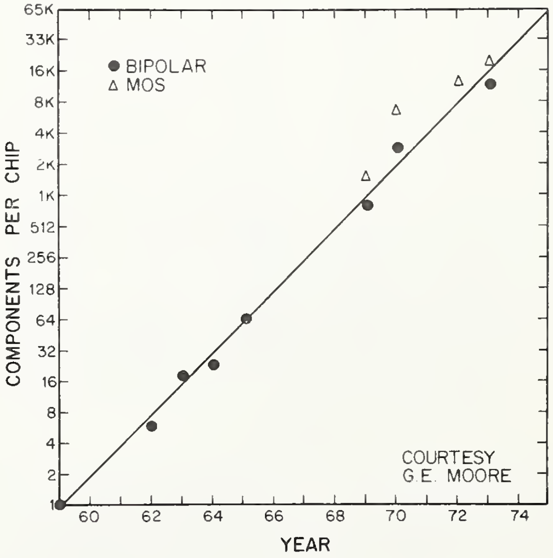

Figure 2. Complexity of silicon integrated circuits over the time period 1959-1975 (G. E. Moore, Ref. 1).

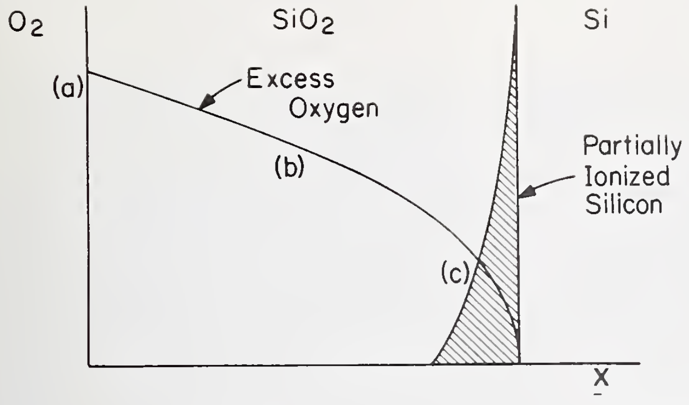

$$x_o^2 + Ax_o = B(t+\tau)$$

where: $A \equiv 2D(1/k + 1/h)$

$B \equiv 2DC^*/N_1$

$\tau \equiv$ Constant

For "large times,"

$$x_o^2 \simeq Bt$$

For "small times,"

$$x_o \simeq \frac{B}{A}(t+\tau)$$

Figure 3. Kinetics of the thermal oxidation of silicon, including the general relationship.

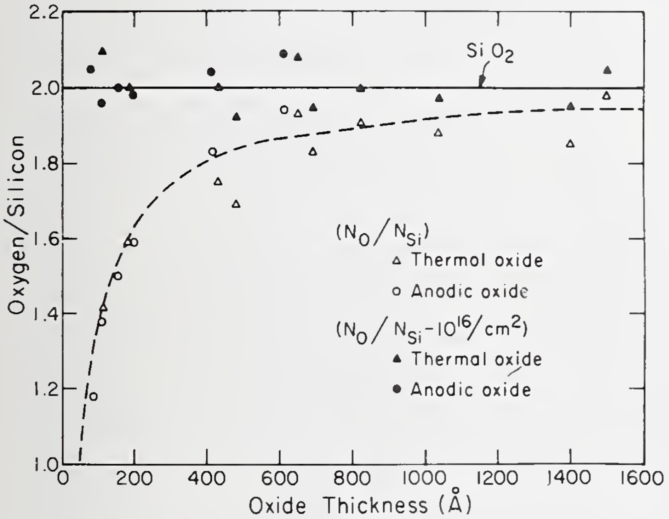

Figure 4. Ratio of oxygen to silicon vs. oxide thickness for thermal and anodic films (Sigmon et al., Ref. 4).

Figure 5. Time dependence of ΔV_{FB} under 6 V bias at 25°C for standard (~1200 Å) and HCl oxides (~1150 Å). (a) NaOH evaporated onto oxide surface, $N_{ion} \sim 0.8 \times 10^{12}/cm^2$. (b) aluminum evaporated from resistance heated tungsten filament; $N_{ion} \sim 1.6 \times 10^{12}/cm^2$ (Kriegler and Devenyi, Ref. 5).

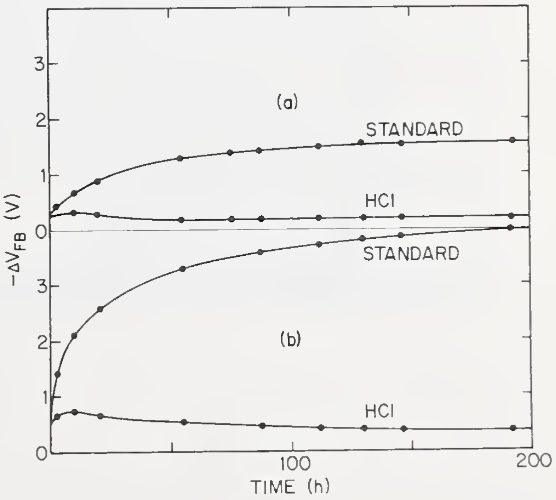

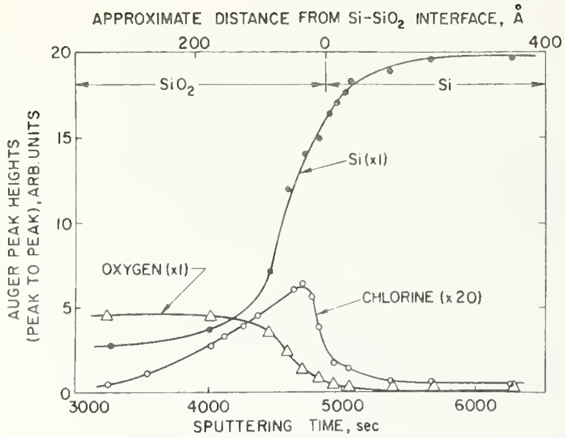

Figure 6. Cl profile in an HCl oxide determined by the sputter-etching technique (Chou et al., Ref. 6).

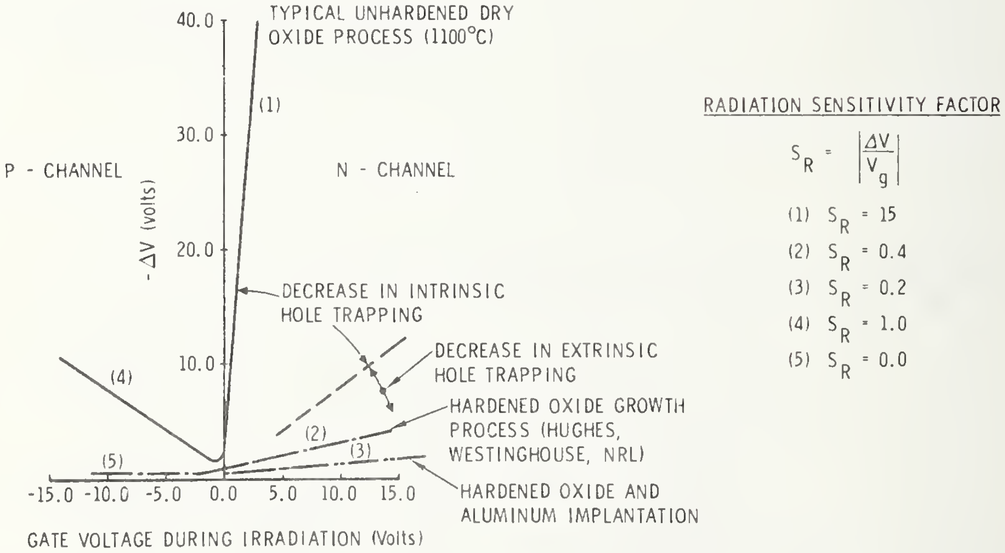

Figure 7. Radiation hardening of MOS devices (Gwyn, Ref. 7).

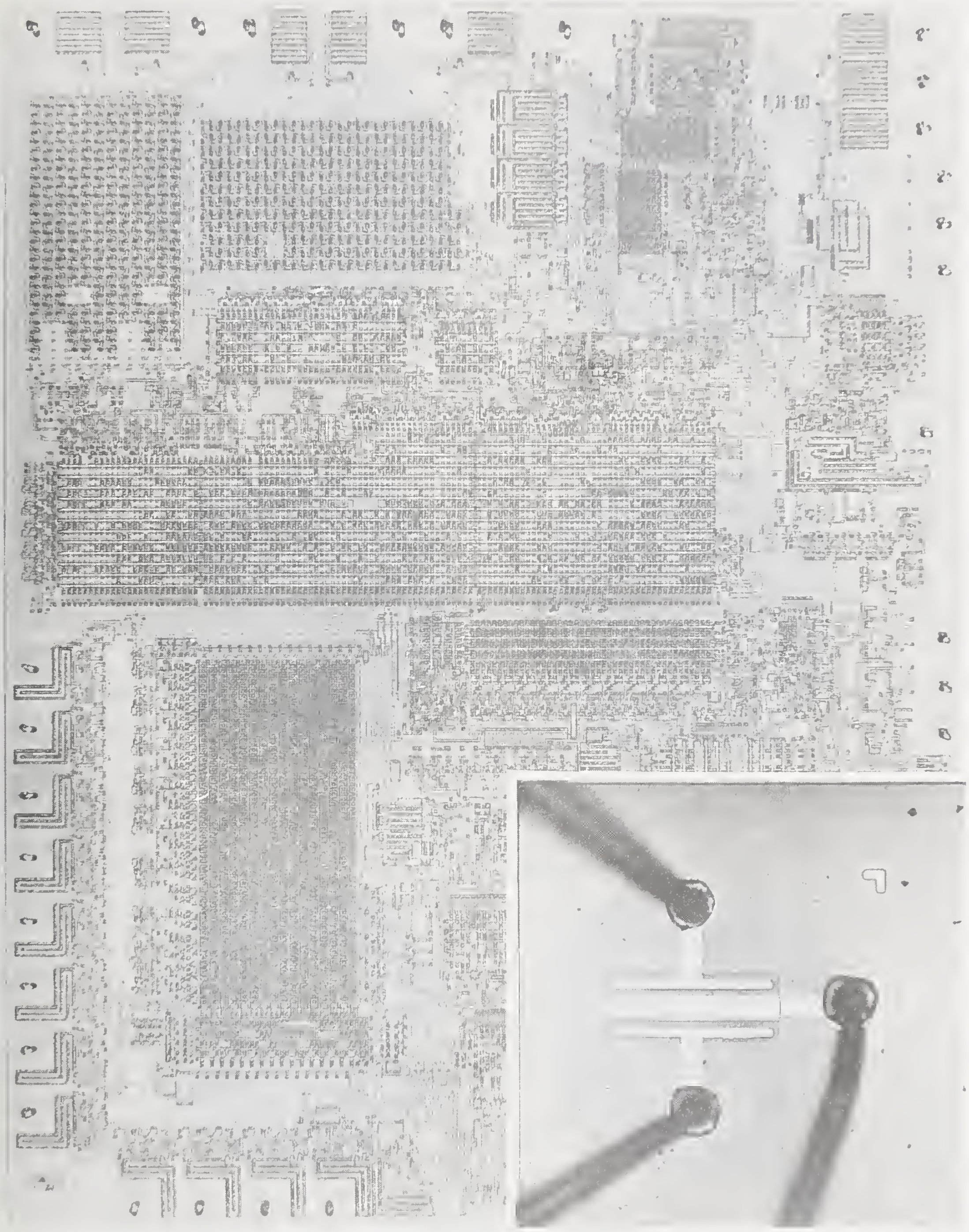

Figure 8. Comparison of early MOS transistors (1964) and present day calculator chip. Latter dimensions are 150 × 180 mils.

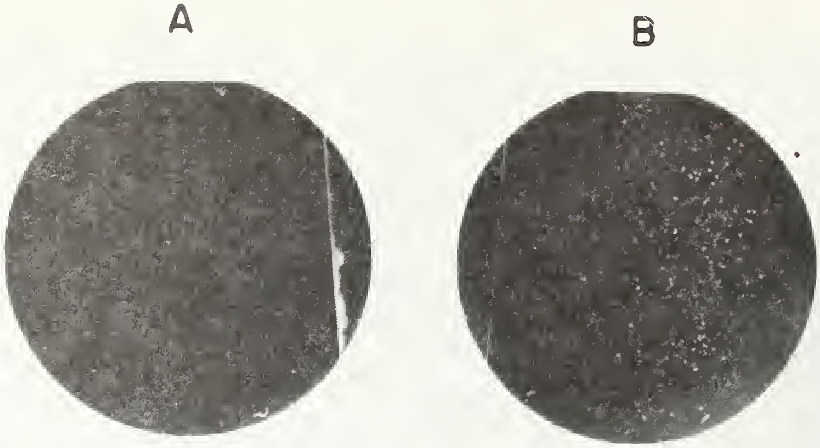

5min 5×10^5 V/cm

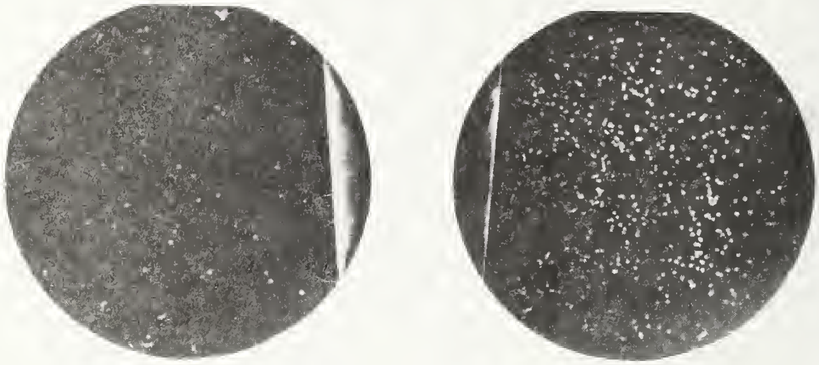

3min 1×10^6 V/cm

2 min 3×10^6 V/cm

Figure 9. Copper-decorated SiO_2 defects in two silicon wafers as seen after application of successively increasing oxide fields. The defects were caused by failure of two types of photoresist (A and B) on prolonged exposure to buffered HF (Kern, Ref. 8).

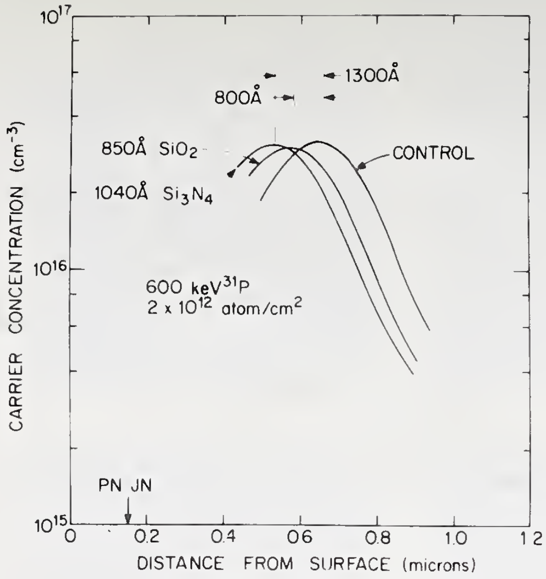

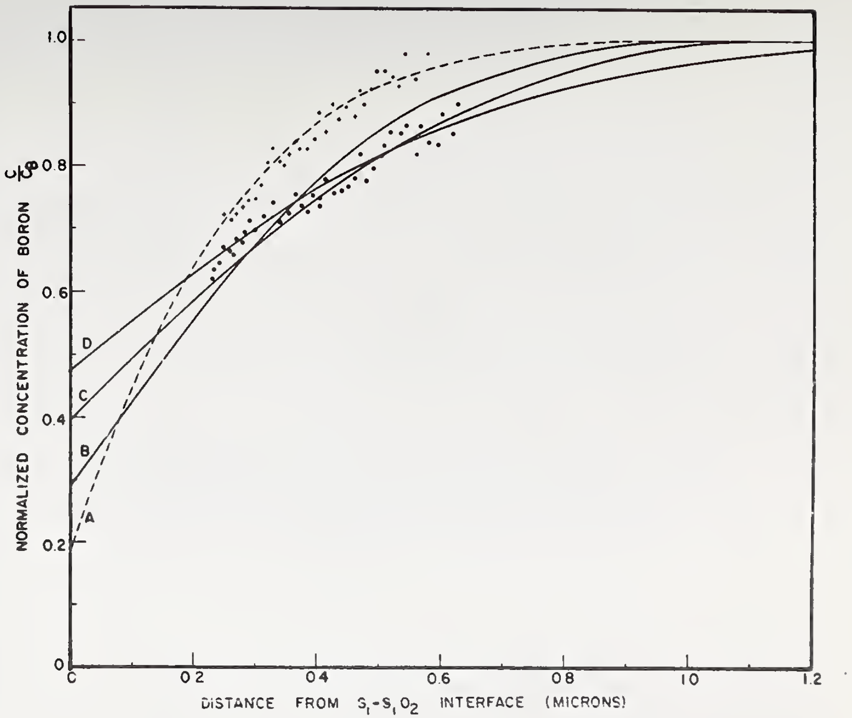

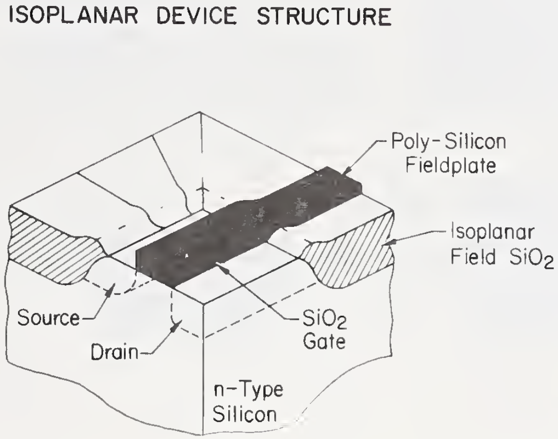

Figure 10. (upper left) Profiles resulting from 600 keV ^{31}P with (i) control: no film on Si, (ii) 850 Å of SiO_2 on Si and (iii) 1040 Å of Si_3N_4 on Si (Reddi and Yu, Ref. 9).

Figure 11. (upper right) Redistribution of boron after two step oxidation (wet-dry). Curve A: calculated distribution after first oxidation (1100°C, wet, x_o = 1 μm) (initial condition for second oxidation). Curve B: calculated redistribution after second oxidation (1200°C, dry, x_n = 500 Å). Curve C: calculated redistribution after second oxidation (1200°C, dry, x_n = 700 Å). Curve D: calculated redistribution after second oxidation (1200°C, dry x_n = 1000 Å). +++ measured distribution corresponding to curve A, ... measured redistribution corresponding to Curve D (Margalit et al., Ref. 10).

Figure 12. (left) Representative Isoplanar (oxide-isolated) MOS device structure.

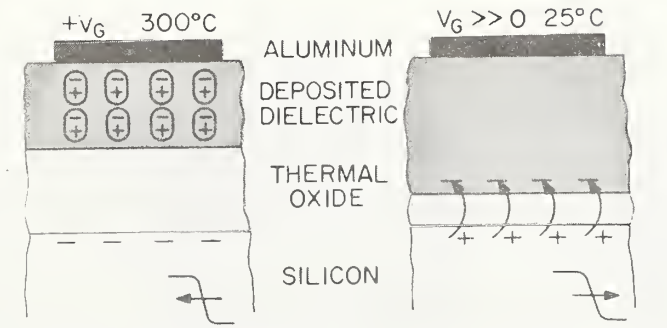

(a) POLARIZATION DUE TO DIPOLE ORIENTATION

(b) INTERFACE TRAPPING

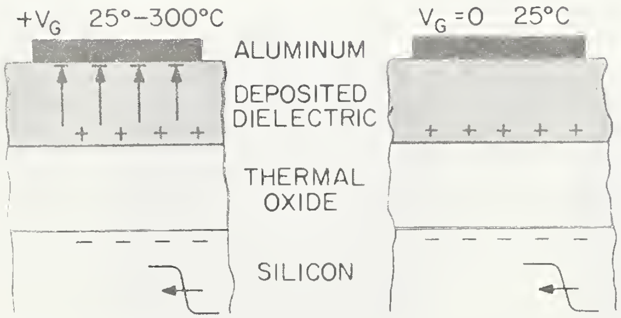

(c) POLARIZATION (OR TRAPPING) DUE TO CONDUCTIVITY DIFFERENCES

(d) INTERFACE CHARGE (AS DEPOSITED)

Figure 13. Four types of electrical instability or charge effects associated with MIOS structures.

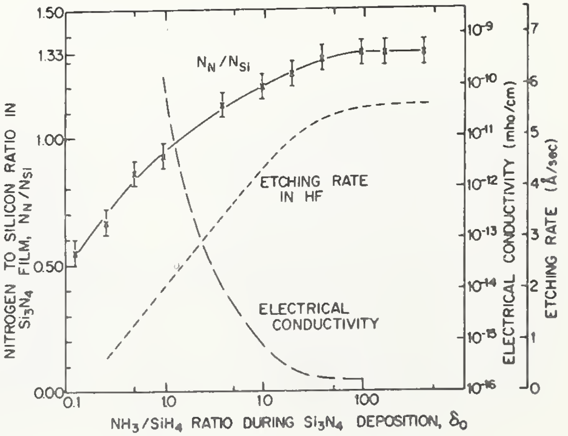

Figure 14. Relationship among silicon nitride film composition, etch rate, and electrical conductivity as influenced by NH_3/SiH_4 ratio during silicon nitride deposition (Gyulai et al., Ref. 11).

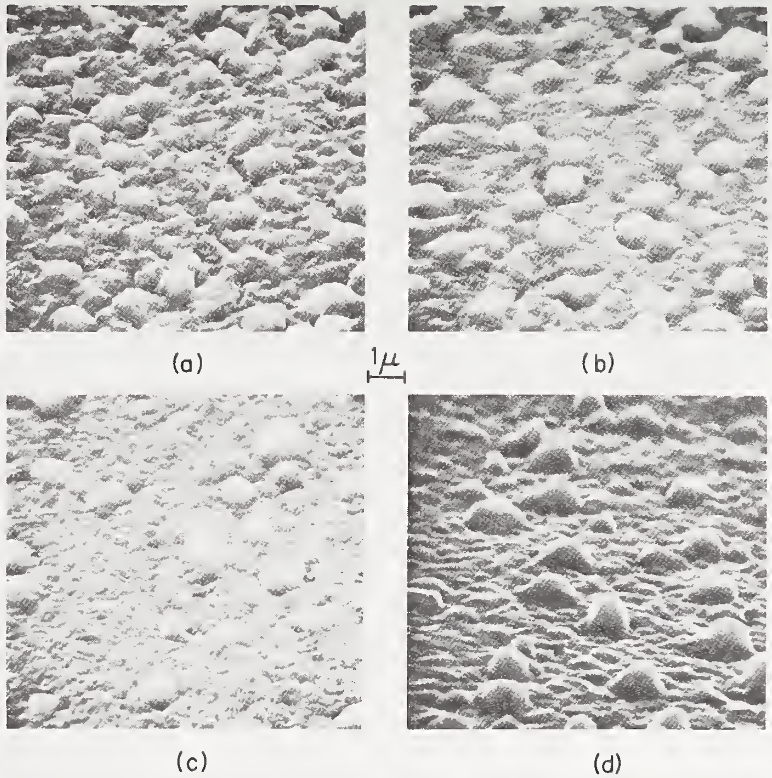

Figure 15. Scanning electron micrographs of aluminum alloy deposits with (a) 12% Cu, (b) 8% Cu, (c) 4% Cu, (d) 0% Cu; (a)-(c) 1.7% Si, (d) 2.5% Si (Learn, Ref. 12).

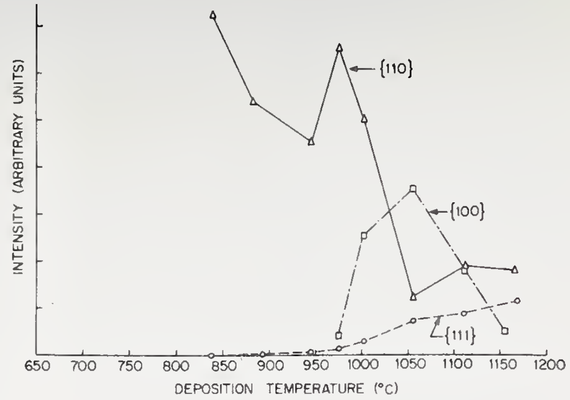

Figure 16. Relative amounts of (111), (110) and (100) texture in 5 µm thick polycrystalline silicon films (Kamins and Cass, Ref.13).

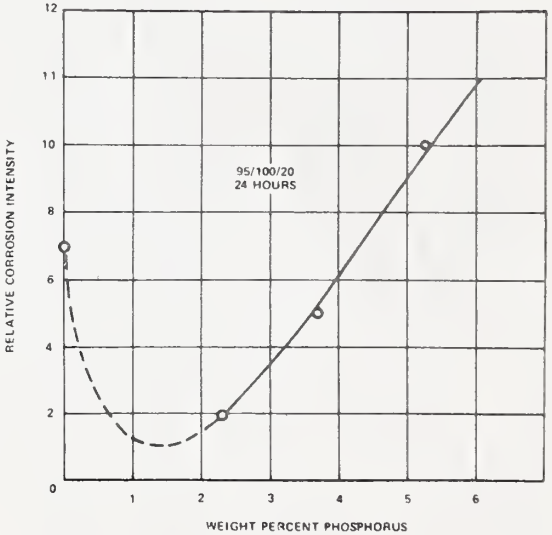

Figure 17. Relative corrosion intensity versus weight percent phosphorous after 24 hours at 95°C/100% RH/20 volts (Paulson and Kirk, Ref. 14).

DISCUSSION OF THE PAPER

Lieberman: I am particularly interested in the high energy backscattering data presented in your fourth slide for the silicon-silicon dioxide interface. You suggested that the O/Si stoichiometric offset was due to a silicon-rich transition layer several atomic layers thick. On the basis of this data alone, could not the excess silicon region have extended hundreds of angstroms into the oxide film.

Deal: I do not think it extends that far. Most of the change effects that we observe probably result from a region within 50 angstroms of this interface.

Lieberman: Another point is that the cross section for Rutherford backscattering is independent of the electronic screening and so this technique cannot be used to determine the ionization state of the excess silicon.

DiStefano: We, at IBM, have used field dependent internal photoemission to probe that interface down to 4 angstroms from the silicon and find no evidence of oxide non-stochiometry of large enough extent to perturb the conduction band of the SiO_2; i.e., the conduction band of the SiO_2 appears to be flat to within 0.02 eV up to 4 angstroms of the silicon surface. There may be a small amount of excess silicon but we cannot find any ionized silicon of consequence.

Deal: This is for a thermal oxide?

DiStefano: Yes.

NBS Special Publication 400-23, ARPA/NBS Workshop IV, Surface Analysis for Silicon Devices,
held at NBS, Gaithersburg, Maryland, April 23-24, 1975 (Issued March 1976)

LOW ENERGY ION SCATTERING SPECTROMETRY STUDIES OF Si, SiO_2, AND RELATED MATERIALS

William L. Harrington

RCA Laboratories
Princeton, New Jersey 08540

INTRODUCTION

Although low energy ion scattering spectrometry (ISS) has been described by several authors as a surface and in-depth analytical tool[1,2,3], characteristics of the method will be illustrated in this paper by using analytical examples relating to the topic of this workshop—Si, SiO_2, and related materials. After consideration of the technique in general, some fundamental studies of Si and the Si/SiO_2 interface will be discussed in which ISS is particularly suited.

METHOD

Figure 1 is a schematic diagram of the scattering process in which rare gas ions of mass M_1 and initial energy E_0 are scattered by surface atoms of mass M_2 in elastic, binary collisions. Although this ion-surface interaction results in the neutralization of about 99.9 percent of the incoming ions, a significant, measurable number survive as scattered ions, and the energy loss suffered by these ions can be related to the mass of the scattering center by the equation given at the bottom of the figure. At a lab scattering angle of 90° this equation reduces to the simple relation

$$E_1/E_0 = (M_2 - M_1)/M_2 + M_1)$$

where E_1 is the energy of the scattered ion and the other terms have been defined above. Since M_1 and E_0 are known quantities and one measures E_1 in the experiment, it is a simple matter to deduce M_2. The rare gas ions used are generally in the 1-3 keV energy range and will thus penetrate most solids on the order of 10-60 Å. Survival of these projectiles as scattered ions from a single collision, however, can be restricted almost entirely to the first average atomic layer and thus defines ISS as a true surface technique. Of course, bombarding a solid with such energetic ions also causes sputtering, and for this reason the technique naturally provides information as a function of depth.

To better put this technique in perspective with related methods, Figure 2 contrasts the principles just described with those of high energy backscattering and secondary ion mass spectroscopy (SIMS). High energy ISS uses MeV projectiles which penetrate thousands to tens of thousands of Å into a solid, and the energy loss suffered by the scattered particle (this particle does not have to remain ionized to be energy analyzed at these energies) is due not only to the mass of the scattering center, but its depth as well. It should be noted that this technique does not depend on the sputtering process for obtaining information in depth, and can thus be used very effectively to calibrate difficult, layered samples. SIMS, on the other hand, detects not the scattered ions, but those sputtered particles which escape the solid as ions. The sputtered ions are then extracted into a mass spectrometer and analyzed according to their mass/charge ratio. A point sometimes forgotten when comparing surface techniques is that SIMS data come from the sputtered species, which in the steady state are representative of the bulk sample composition. Low energy ISS and other techniques such as Auger Electron Spectroscopy analyze the surface that remains after sputtering, so that differential sputtering effects must be considered in the interpretation of data.

The instrumentation which in practice detects the low energy scattering event is commercially available from the 3M Company[4,5] and is schematically shown in Figure 3. Rare gas ions are formed in a filament ion source and accelerated toward the sample surface at energies between 500 and 3000 eV with a very small energy spread. The ions are focussed to a spot which is variable from about 1-3 mm in diameter (recent enhancements of the ion gun have reduced the beam size to 100 μm). This beam can be kept stationary for highest sensitivity with relatively poor depth resolution or rastered in combination with a small area detection gate for optimum resolution in depth. Ions that scatter from the sample surface at 90° enter a 127° electric sector for energy analysis and are detected with a channel electron multiplier operating in a pulse counting mode. A feature of great importance in this instrumentation is a charge neutralization filament located near the sample surface. Insulators, such as glass or thermal layers of SiO_2, which can be a problem for techniques employing high density ion or electron beams, are flooded with thermal electrons during ion bombardment with feedback regulation to keep the sample surface at a fixed potential near ground. The importance of sputtering with an uncharged surface will be demonstrated in some of the examples to follow, but the crucial point is to eliminate large electric field gradients across a sample to prevent migration of mobile ions.

The output from this technique is best described with the help of a pertinent example as shown in Figure 4. These are typical ISS spectra where the scattered response in counts/second is plotted vs. E_1/E_0, the ratio of scattered to initial ion energy as defined previously in Figure 1. The sample in this example is an alkali strontium silicate glass which is certainly a good insulator. With charge neutralization by the flood filament, however, no charging effects are noted. That is, the peaks fall at the same energy ratio as those obtained from a good conductor, and there is no evidence that mobile ions are affected by the sputtering beam. The top spectrum in this figure is that for a normal, untreated glass, and one can discern peaks for O, Na, Si, K, and Sr. The bottom spectrum is from the same glass after the application of a heat and voltage treatment with non-blocking contacts to move mobile ions into the glass[6,7]—only O and Si remain at the surface. A series of such spectra while continuing to sputter yields a concentration profile in depth as shown in Figure 5. Note the depletion and subsequent pile-up of Sr, the largest and least mobile of the ions, whereas Na, the most mobile species, is barely detected even at large distances from the surface. Potassium, having an intermediate mobility, shows an intermediate trend.

The magnitude of the scattered signal from an element in a given matrix is basically a function of three variables—(1) the geometric arrangement of atoms on a surface, i.e., does one atom shield another from the incoming beam?, (2) the extent of neutralization of the incident ions, and (3) the scattering cross section (the probability that scattering will occur) as a function of atomic number. Geometry, for most analytical problems concerning amorphous, non-oriented layers, is not critical; but for situations where the position of atoms is important, the one layer resolution of ISS can be used to an advantage. Although neutralization may vary from one surface to another, differential neutralization between elements in a given matrix would be expected to be a rather small factor. Relative scattering cross sections have been studied extensively, and certainly as a first approximation, one can correct elemental scattering data for this variable. Figure 6 is a plot of Bingham's differential cross sections[8] as a function of atomic number for 1500 eV[4] He^+ ions. Of course, there is a family of such curves for each initial energy and for each different probe ion. The magnitude of the correction implied by these data over the range of a light element such as O to a heavy element such as Pb is only about a factor of 6 as compared to several orders of magnitude correction for ion yields in the SIMS technique.

To illustrate this correction, Figure 7 shows a spectrum of glass used to form a liquid crystal cell. When a voltage is applied to specific areas of such a cell, the liquid crystal material sandwiched between the glass surfaces will align to produce visible contrast for displays. For this application the glass surface composition has been found to be important, and in some cases leads to liquid crystal misalignment. The spectrum shown in this figure was taken in an area of the cell which operated normally. The Na, Ca, O, and Si concentrations were calculated by subtracting a background for each peak and dividing the net peak height by the relative scattering cross section. A simple summing of all corrected signals and divisions to determine individual percentages produced very good agreement with the bulk composition as given by the manufacturer. Figure 8 is a similar spectrum taken in an area of the glass cell just a few mm away from that in Figure 7. In this case liquid crystal misalignment was a problem, and the surface composition of the glass, as determined from the same calculation procedure described previously, is completely different with very high concentrations of Na and Ca.

CRYSTALLOGRAPHIC ORIENTATIONS OF SINGLE CRYSTAL Si

Having established the characteristics of the method, it is instructive to describe the results of two ISS studies which focus on Si and the Si/SiO_2 interface.

The (111) and (100) surfaces of single crystal Si wafers are used extensively in Si devices and offer an excellent system for studying surface sensitivity and information depth of an analytical technique. In addition, for those techniques using sputtering to provide information as a function of depth, single crystal Si provides a sensitive means of evaluating damage to these surfaces from ion bombardment.

The detailed preparation of these surfaces has been described previously[9], but Figure 9 shows spectra of a typical surface as received—there is the expected small amount of residual oxide, some carbon, and F from the final HF etch. In order to obtain accurate ISS response on the pure Si surface, it was necessary to carefully sputter through this thin contamination layer to reach a clean Si surface, as shown in the right half of this figure.

If one considers the geometrical packing of Si atoms on the (111) and (100) surfaces, the surface atom density of (111) Si is 1.15 times greater than that of (100) Si. ISS responses for these two orientations are shown in Figure 10 as a function of several energies for both He^+ and Ne^+. The columns under the figures show the signal level for each orientation, and the last column is the calculated (111)/(100) ratio. For He^+ the observed ratio does not fall within the range of the true ratio until an energy of 1500-2500 eV is reached. Because the true ratio is observed at these higher energies, one can deduce that no detectable damage has been done to the crystal lattice by He bombardment. At low energies the ratio approaches unity because the low current density and very low sputter yield at these energies result in a situation where the surface is not kept clean during the scattering measurement. With such a contamination layer on the surfaces, the true Si response cannot be obtained. If the surface were first cleaned by sputtering with 1500 eV He^+, the ratios obtained with Ne^+ at 500 and 1500 eV are correct within the measurement precision. The slightly lower value at 500 eV could again be due to contamination since the higher Ne sputter yield was somewhat offset by a low current density of about 3 $\mu A/cm^2$. The low ratio at 2500 eV indicates that damage has been done to the crystal lattice. This damage is shown more clearly in Figure 11, where Ne^+ at 500, 1500, and 2500 eV was used to sputter the two surfaces until the oxide was removed. Each location sputtered was then examined with 1500 eV He^+ ions. The ratio at 500 eV is the same as that obtained with no Ne^+ sputtering, so that again there was no detectable damage. The ratios at 1500 and 2500 eV, however, become progressively smaller; and if one examines the individual Si responses, it is the (111) surface that remains stable and the (100) surface that becomes damaged and pushed into a configuration of higher surface density.

Even at these low energies lattice damage can result—especially in Si lattices of less than maximum density. Those techniques which obtain depth profile data by sputtering with heavy ions (O, Ne, Ar) at much higher energies are definitely causing damage to the surface being examined, and the possible effect of this damage on true concentration profiles must be kept in mind.

STOICHIOMETRY OF SiO_2 AND THE SiO_2/Si INTERFACE

The Si - SiO_2 system is a vital part of present semiconductor device technology as evidenced by the fact that this workshop has been organized on this topic. The thin region making up the Si/SiO_2 interface dominates many aspects of MOS behavior—surface states, surface charge, radiation damage, dielectric breakdown, etc.—and for this reason has received a great deal of attention by analytical techniques. High energy backscattering, in particular the work of Sigmon, Chu, Lugujjo, and Mayer[10], has reported a rapidly decreasing O/Si ratio as one measures thinner and thinner oxide films. This work is interpreted as showing excess Si near the interface which has been pulled out of the substrate lattice into the oxide during the initial stages of oxide growth. However, the limit of depth resolution by this technique is on the order of 200 Å, so that only integrated values over these thicknesses can be obtained, and thus the data can only infer the Si-rich interface.

The low energy scattering technique has such a well-defined, small information depth as illustrated previously in this presentation that the question of SiO_2 stoichiometry and the character of the SiO_2/Si interface can now be examined in much greater detail.

Assuming that excess Si does exist at the interface, it is inconceivable that these substrate atoms could move large distances into an oxide. For this reason an oxide thickness of about 1000 Å was chosen as an ISS standard for SiO_2. Certainly, in the outer few hundred Å of such a film, as shown in Figure 12, the O/Si ratio should be 2:1. In this and all the following figures the scattered response for O was multiplied by 1.72 as an empirical, relative scattering cross section correction, which for the 904 Å oxide in Figure 12 produces an O/Si ratio of 2. Figure 13 shows a complete profile of this same film after controllably etching down to a thickness of 498 Å (all these oxide thicknesses were measured by ellipsometry before ISS profiling). At this thickness the O/Si ratio is still 2 within the measurement precision, and it might be noted that at such oxide thicknesses, high energy ISS already reports a deviation from the 2:1 ratio. This etching procedure was continued for several steps, and down to 44 Å, as shown in Figure 14, the ratio at the surface is still 2. It is at this point that there is a slight indication in the Si response that might be direct evidence of excess Si at the interface.

Because it is difficult to controllably etch films much thinner than in Figure 14, the problem was then approached from the other direction—clean to bare Si and grow to known, measured thicknesses of 600°C oxide. At 7 Å, in Figure 15, the O signal had to be multiplied by 5 to show up effectively on the same scale as the other plots. At the maximum O level the O/Si ratio is only 0.3-0.4, in good agreement with some of the thinner oxides measured by high energy ISS. At these thicknesses the integration effect of the high energy technique is of little consequence. Figure 16 shows a large change when growth proceeds from 7 to 17 Å*, but in this experiment the ratio is still between 0.2 and 0.5 in the region of constant oxygen response. Again at 40 Å, as shown in Figure 17, the O/Si ratio is 2 near the surface and this profile agrees quite well with the 44 Å layer obtained by thick film growth and etching (Figure 14).

The results shown in Figure 18 were obtained after the installation of a beam raster/gated detector system. Such a modification gives the much needed improvement in depth resolution that was lacking with a stationary, Gaussian beam, and almost equally important allows a fine control over the sputter rate for obtaining detailed data on these very thin films. Over much of the film in this figure the O/Si ratio is again 2, but at the interface it is clear that the Si signal rises to a plateau before the O signal falls. It is this region of 10-20 Å that is established experimentally as Si-rich. Using the Si atom density of 7.9 x 10^{14} at/cm^2 in the thermal SiO_2 region as a point of calibration, one can calculate rather directly that the Si-rich plateau corresponds to a Si density of 9.4 x 10^{14} at/cm^2. Therefore, there is an excess Si density of 1.5 x 10^{14} at/cm^2 per monolayer which extends out from the interface 10-15 Å or about 3-4 molecular layers.

REFERENCES

1. Smith, D. P., Scattering of keV Ions from Solid Surfaces, *Proc. 15th Ann. Conf. on Mass Spectrometry and Allied Topics*, Denver, 1967.
2. Smith, D. P., Scattering of Low Energy Noble Gas Ions from Metal Surfaces, *J. Appl. Phys.* 38, 340-347 (1967).
3. Honig, R. E. and Harrington, W. L., Ion Scattering Spectrometry Below 10 keV, *Thin Solid Films* 19, 43-56 (1973).
4. Goff, R. F., Ion Scattering Spectrometry — A New Technique for Surface Composition Analysis, *Proc. 6th Natl. Conf. on Electron Probe Analysis*, Pittsburgh, 1971.
5. Goff, R. F., Ion Scattering Spectrometry, *J. Vac. Sci. Technol.* 10, 355-358 (1973).
6. Carlson, D. E., Ion Depletion of Glass at a Blocking Anode: I, Theory and Experimental Results for Alkali Silicate Glasses, *J. Am Ceramic. Soc.* 57(7), 291-294 (1974).
7. Carlson, D. E., Hang, K. W. and Stockdale, G. F., Ion Depletion of Glass at a Blocking Anode: II, Properties of Ion Depleted Glasses, *J. Am. Ceramic Soc.* 57(7), 295-300 (1974).
8. Bingham, F. W., Tabulation of Atomic Scattering Parameters Calculated Classically from a Screened Coulomb Potential, Sandia Research Rept. SC-RR-66-506, TID-4500-Physics, 1966.
9. Harrington, W. L. and Honig, R. E., Low Energy Ion Scattering Spectrometry of (111) and (100) Silicon, *Proc. 22nd Ann. Conf. on Mass Spectrometry and Allied Topics*, Philadelphia, 1974.
10. Sigmon, T. W., Chu, W. K., Lugujjo, E. and Mayer, J. W., Stoichiometry of Thin Silicon Oxide Layers of Silicon, *Appl. Phys. Lett.* 24, 105-107 (1974).

---

* Recent data on similar films obtained with the raster/gate system for better depth resolution indicate an O/Si ratio of 2 at the surface of films only 15 Å thick. This observation also establishes the extent of the Si-rich region as 10-15 Å.

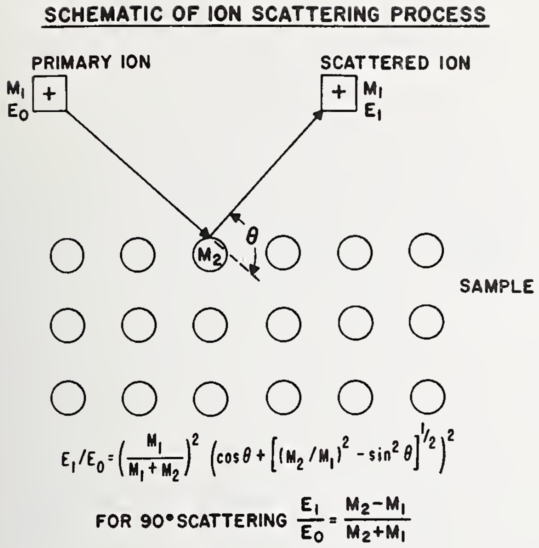

Figure 1. Schematic diagram and formulae of the ion scattering process.

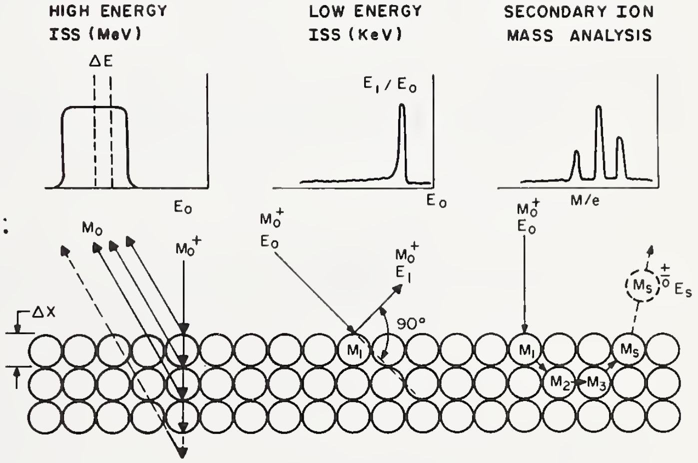

Figure 2. Comparison of high energy backscattering, low energy ISS and SIMS.

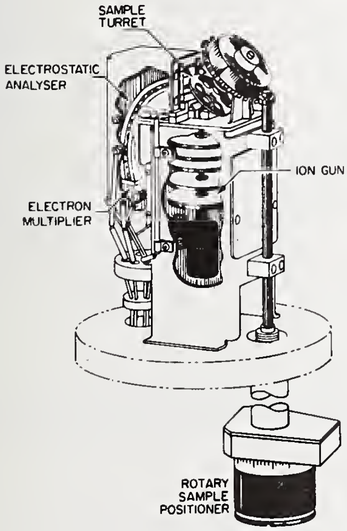

Figure 3. Schematic diagram of the 3M ion scattering spectrometer.

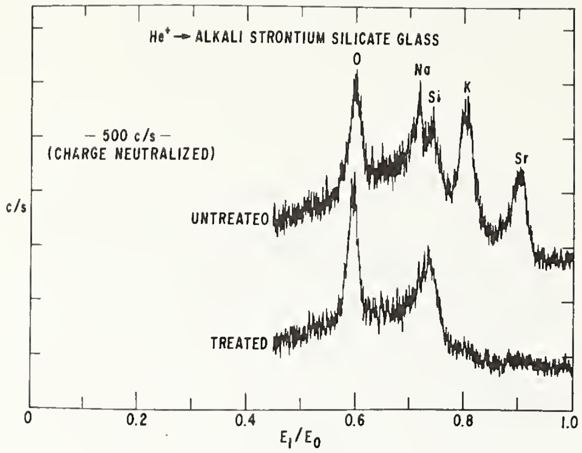

Figure 4. ISS spectra of 1500 eV He^+ ions scattered from alkali strontium silicate glass.

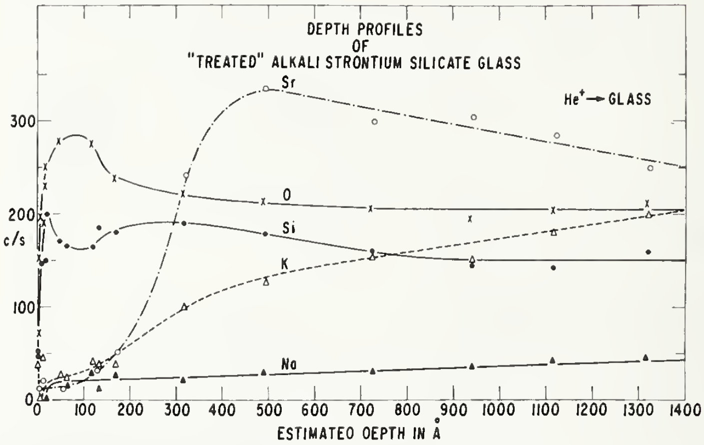

Figure 5. Depth profiles of "treated" alkali strontium glass.

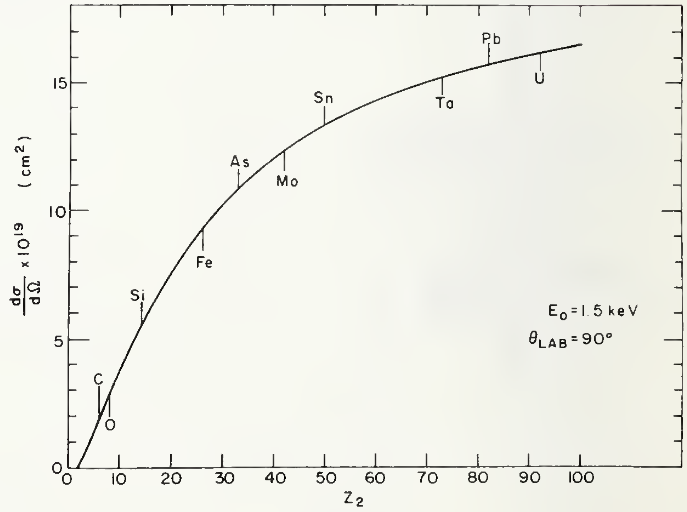

Figure 6. Differential scattering cross sections for $^4He^+$.

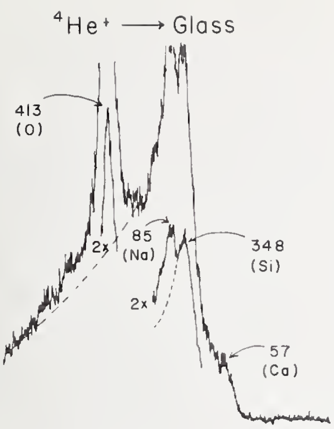

ELEMENT	C/S	σrel	C/S/σ	AT.% CALC.	AT.% GIVEN
Si	348	.545	638.5	26.4	25.2
O	413	.275	1501.8	62.1	60.4
Na	85	.415	204.8	8.5	9.0
Ca	57	.760	75.0	3.1	3.3
		Σ =	2420.1		

Figure 7. Relative scattering cross section correction applied to ISS data from a "normal" liquid crystal cell.

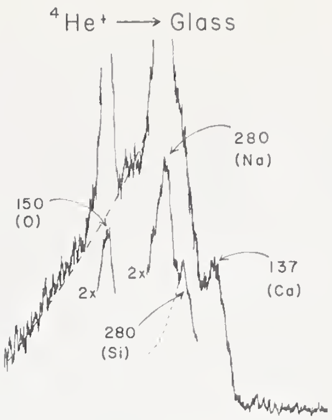

ELEMENT	AT.% CALC.
Si	26.8
O	28.5
Na	35.2
Ca	9.4

Figure 8. Calculated ISS composition from a "misaligned" liquid crystal cell.

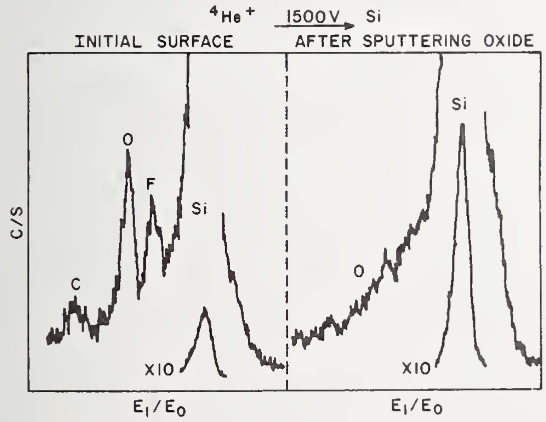

Figure 9. 1500 eV He^+ ISS spectra of a typical Si surface.

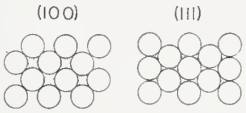

		(100)	(111)	(111)/(100) ATOM DENSITY RATIO 1.15
		c/s/nA	c/s/nA	
$^4He^+$	500V	1.02 ± 7.0%	0.98±3.8%	0.96±8.0%
	1500V	10.90 ± 0.9%	11.92±0.4%	1.09±1.0%
	2500V	14.56 ± 3.3%	17.32±4.5%	1.19 ± 5.5%
$^{20}Ne^+$	500V	9.48 ± 3.1%	10.47±2.6%	1.10 ± 4.0%
	1500V	11.25 ± 2.7%	13.28± 1.6%	1.18 ± 3.1%
	2500V	15.74 ± 2.6%	16.90±1.4%	1.07±2.9%

Figure 10. ISS Si responses from (111) and (100) Si surfaces.

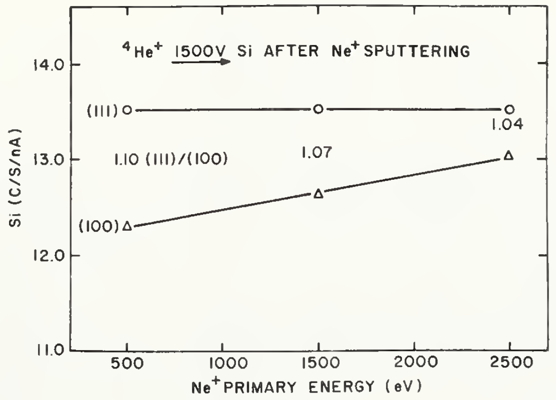

Figure 11. ISS Si responses showing lattice damage from Ne^+ bombardment.

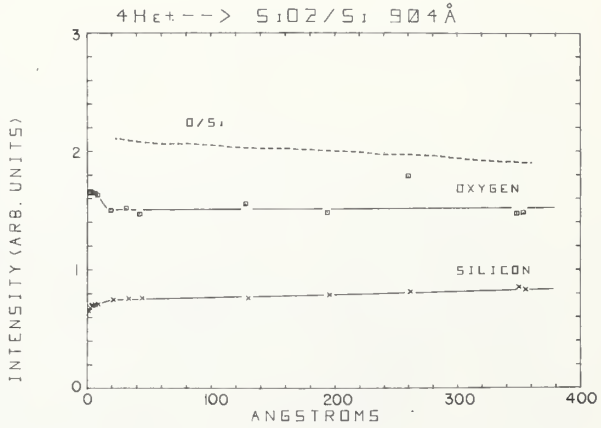

Figure 12. ISS responses from a 904 Å oxide layer on Si used as a standard for SiO_2.

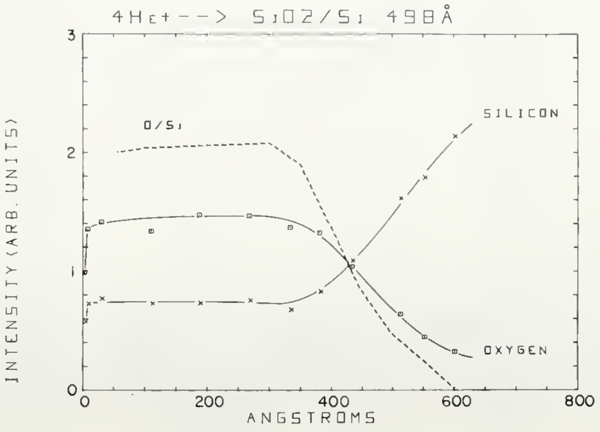

Figure 13. ISS depth profile of SiO_2/Si etched down to 498 Å.

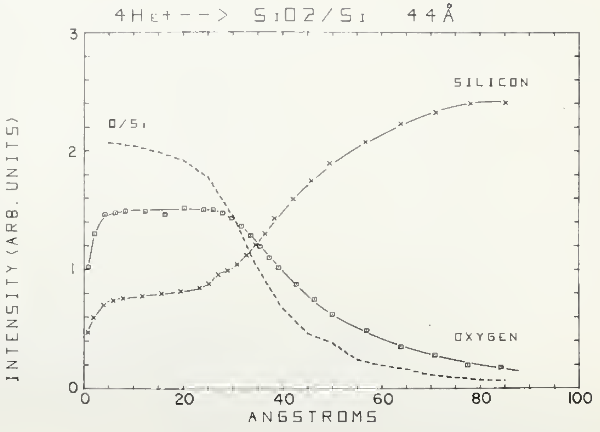

Figure 14. ISS depth profile of SiO_2/Si etched down to 44 Å.

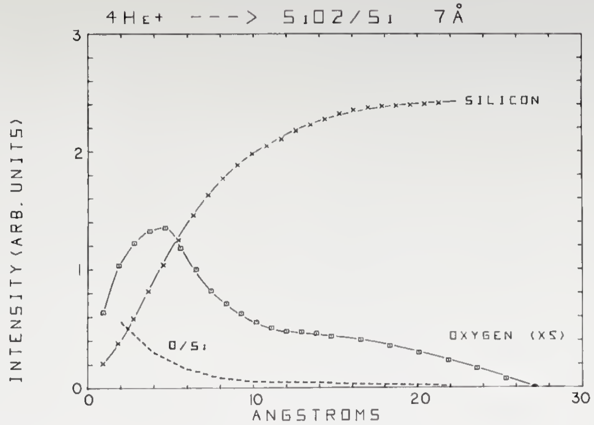

Figure 15. ISS depth profile of residual 7 Å oxide on "clean" Si.

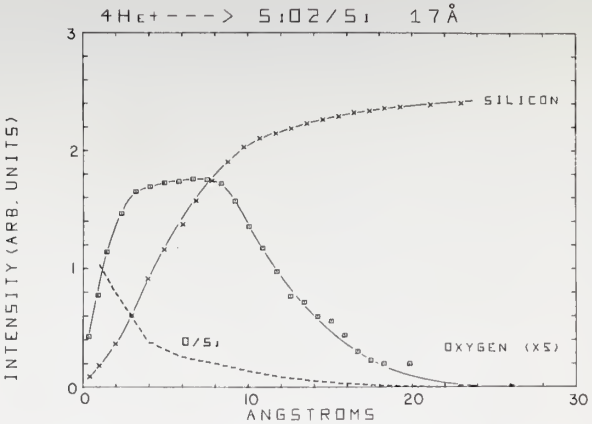

Figure 16. ISS depth profile of 17 Å oxide on Si grown at 600°C.

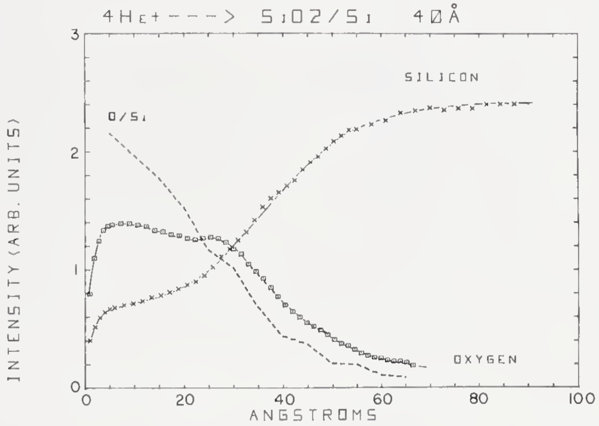

Figure 17. ISS depth profile of 40 Å oxide on Si grown at 600°C.

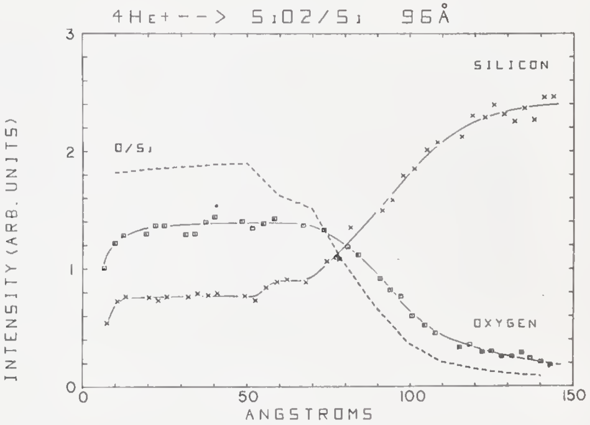

Figure 18. ISS depth profile of SiO_2/Si etched down to 96 Å. The step in the Si response corresponds to 1.5×10^{14} at/cm^2 excess Si per monolayer at the SiO_2/Si interface.

DISCUSSION OF THE PAPER

Participant: Do you have any measure of the excess silicon versus charge density via depth?

Harrington: No, I do not know what the charge density was on these films. This is very recent work and I am continuing on it. I am sure we will do measurements like that.

Johanessen: What is the penetration depth of the helium ions?

Harrington: The penetration depth is on the order of 10 to 60 Angstroms. I think it is probably about 20 Angstroms at 1.5 keV, however the scattering occurs only from the first surface layer.

Johanessen: Is that region distorted by the measurement?

Harrington: It is distorted somewhat, but with helium scattering the damage done by helium sputtering is very very slight and at this point we are basically observing the scattering before the damage has been done. In addition, I think the surfaces do reconstruct and certainly this is borne out by many of the LEED studies. I cannot give you a good explanation as to why we see so little damage in comparison to say reconstruction or this type of thing. The scattering seems to occur before the damage exists. Even if you are able to penetrate and sputter several atoms the signal remains constant.

Johanessen: Would you repeat the value you cited for the extent of the interface?

Harrington: The silicon signal seems to rise over roughly 10 to 20 Angstroms, which looks like about 3 molecular diameters for silicon dioxide. This is about as much as I can tell on such a thick film. I am also going to pursue this more.

DiStefano: Could you estimate the contribution of multiple scattering events to the penetration depth? It is possible that this could lead to a misinterpretation of the extent of the silicon dioxide/silicon interface.

Harrington: Because you are following both the oxygen signal and the silicon signal in a situation like this and you see one rise before the other falls I do not think that is really a possibility. The probability for the scattered particles to penetrate even several stomic thicknesses and emerge as ions from a single scattering event, and we can tell the difference between a single scattering event and a multiple scattering event, is very very small. I do not know whether to say it is a percent or less, I really do not know. The fact is that you can see density differences on (111) and (110) silicon surfaces. If the beam penetrated two layers for instance the density would be the same on the two surfaces; one is basically behind the other.

Participant: How were your samples prepared?

Harrington: The silicon surfaces as prepared were as finely polished and as free of damage as we could get them. They were finely polished, a thick oxide was grown on them at, I believe, 600° or 900°C and this thick oxide was removed by etching in order to get rid of all the damage basically.

Participant: What is the background vacuum level you are operating in?

Harrington: Backfilling is done to a static pressure of about 5 x 10^{-5} of argon or neon or helium, whichever you are using. The vacuum before backfilling is 10^{-9} and titanium sublimation pumping is in effect during the whole process.

NBS Special Publication 400-23, ARPA/NBS Workshop IV, Surface Analysis for Silicon Devices, held at NBS, Gaithersburg, Maryland, April 23-24, 1975 (Issued March 1976)

SURFACE ANALYSIS BY SECONDARY ION MASS SPECTROSCOPY TECHNIQUES

Robert D. Dobrott

Materials Characterization Laboratory
Texas Instruments Incorporated
Dallas, Texas 75222

The secondary ion mass spectrographic technique implies a source of primary ions, a source of secondary ions and a spectroscopic method of analyzing the latter. Figure 1 is an artist's conception illustrating the primary and secondary ions referred to in this presentation. The primary ions in the collimated column are normally generated from a gaseous ambient either by dc or rf fields or in separate sophisticated ion guns such as duoplasmatrons. These primary ions then collide with the solid surface which results in the sputter process which in turn gives rise to a plasma containing positive and negative ions, neutral atoms and molecules having the composition of the solid surface. These sputtered ions are the secondary ions which are analyzed by mass spectroscopy. Figure 1 also illustrates the 20 angstrom possible escape depth of a secondary ion which defines the minimum surface depth.

The remainder of this presentation will be restricted to the three types of commercially available instruments. Figure 2 is a schematic of the ARL QMAS system. Primary ions are generated in the duoplasmatron, accelerated to 10 kV in the gap between the anode and pickup electrode, and focused onto the sample by the primary lens. The sputtered secondary ions are accelerated by the sample voltage back through the extraction lens into a spherical electric sector where they are energy separated. The ions are then mass analyzed by a quadrupole mass spectrometer and detected by ion to electron conversion-scintillator-photomultiplier technique. The quadrupole mass analysis scheme is illustrated in figure 3. A dc field applied to opposite poles is superimposed with a radio frequency field. This oscillating field will then start the ions oscillating between the poles. At any specified frequency only ions of a given mass will undergo stable oscillation which is necessary for them to pass through the length of the field without being collected by the electrodes. The mass is selected by choice of both the dc field and the radio frequency field. Mass spectra are recorded by continuously varying both fields keeping their ratios constant. Figure 4 shows a portion of a 1 ppm boron doped silicon spectrum taken with this instrument.[2] The boron 10 peak shows that the sensitivity is well into the sub-ppm region. This spectrum also shows the mass resolution is sufficient for most inorganic analysis.

Figure 5 is a schematic of the Cameca ion microanalyzer. This instrument is unique in that it uses a magnetic prism for mass analysis which acts as an ion emission microscope as well as a microanalyzer. The primary ions are generated in the duoplasmatron and focused onto the sample. The secondary ions are accelerated and picked up by an electrostatic immersion lens. These ions are then mass or momentum analyzed in the first leg of the magnetic prism which has both radial and tranverse focusing properties. The ions are directed towards the electrostatic mirror where only ions with an energy below a preselected threshold are reflected back through the aperture into the second leg of the magnetic prism. This leg of the magnetic prism reproduces the single mass ion image of the specimen surface on the ion to electron image converter where the electrons can be used for fluorescing a screen, exposing a film or activating a scintillator for photomultiplier detection. A given mass can be preselected by using the appropriate magnetic field, or a complete mass spectra can be recorded by sweeping the magnetic field. Figure 6 is a photograph of this instrument. The ion-gun and sample are to the left of the magnetic prism, and the ion to electron converter, fluorescent screen and photomultiplier to the right.

Figure 7 shows the scheme of the third type of instrument. This is the block diagram of the ARL ion microprobe mass analyzer instrument. The primary ions are generated in the duoplasmatron and accelerated to the primary magnet where they are mass separated. The selected ions are then focused onto the sample with a condenser-objective electrostatic lens combination. The secondary ions are accelerated to the pickup electrode, focused by a retrofocal lens, energy analyzed with a spherical electric sector, and mass separated by the secondary magnet system. The mass of interest is allowed to pass through the slit where the ions are detected with the ion-electron conversion-scintillator-photomultiplier combination. Mass spectra are obtained by sweeping the magnetic field. Ion images of a preselected mass are obtained by rastering the primary beam on the sample and using the photomultiplier current output to modulate the brightness of a CRT by synchronizing the raster with the primary beam.

Figure 8 is a photograph of the ARL-IMMA instrument. This particular one is the instrument in our laboratory at Texas Instruments. The duoplasmation and primary magnet are to the right in the main console and the secondary ion analyzer system is to the left. The data collection system is interfaced to a Texas Instruments 960A computer (installed in the top rack on the left console). The 960A can drive a digital plotter which has been used to generate most of the data figures in this presentation.

This introduction to the instruments, which is by no means complete, is only intended to cover the general principles; let us go on to their application to surface analysis. No review of secondary ion mass spectroscopy would be complete without showing Anderson's famous figure 9 depicting the ion yield comparison between the kinetic and chemical ionization processes. The curve on the left is the ion yield of Al^+ as a function of sputter time (or depth). Note that the ion yield falls off dramatically as the surface oxide is sputtered away. The curve on the right is a repeat of the same experiment using O_2^+ as the sputter beam. Here the surface yield is high; then the yield takes a small dip, and then returns to the high surface point after about 40 seconds of sputtering. The conclusion is that in both cases the surface yield is primarily the result of chemical ionization (oxides) and in the Ar^+ case the mechanism quickly converts to kinetic ionization. For the O_2^+ beam the dip is related to a combination of kinetic and chemical ionization which becomes completely chemical when the sputtered depth reaches the original primary ion implant depth. This experiment has lead to the widespread use of oxygen as the primary ion sputter beam while maintaining a relative high partial pressure of oxygen near the sample surface.

Figure 10, also from Anderson's[1] work, shows the relative intensities of secondary ions obtained from pure metals using an O^- sputter beam. From this table Al appears to be the most intense, and noble metals represented by Au the least intense. This chart, even though taken from the pure metals, does correlate moderately well with the sensitivities determined for these elements in the silicon or silicon oxide matrix. However, for bulk type analysis in silicon, the ordinate is from 1 ppb to 10 ppm going from top to bottom. This illustrates that secondary ion mass spectroscopy is a very sensitive technique even when material quantities are small, as is the case in surface analysis.

Figure 11 is a series of spectra taken from a silicon surface with identical primary O_2^+ beam density, with the analyzed surface depth controlled by either rastering the primary beam or moving the sample. The calculated sputter rate for these spectra was about 50 Å/sec. As can be seen in these spectra, by far the most sensitive method in surface analysis is to move the sample and thereby constantly expose a fresh area to the primary beam. In this spectrum the carbon, hydrocarbon fragments, sodium, potassium and calcium peaks are quite pronounced. The 400 micron raster spectrum does show the same peaks but not nearly so intense. Also, note that the overall intensity is reduced, which tells us that the whole spectrum was recorded in the region between the surface and primary ion implant depth. The 50 micron and stationary spectra both suggest the surface is quite clean with only traces of Na and K appearing. I have not labeled the peaks on these spectra since the point I wish to make is the number of peaks and their relative intensity. However, if you care to do some quick mental exercises, I will remind you Si has 3 isotopes at mass 28, 29, and 30, and Si related peaks will always appear as groups of three to five peaks. Also, you may note that the SiO_2 group at mass 60 (spectra shifted to the right) are prominent in the 50 micron and static beam spectra. This, along with the higher intensity, tells us that the spectra were recorded after reaching the implant depth. This molecular spectra is characteristic of structural chemical bonding and has been investigated by several of my European colleagues for surface fingerprint spectra. Other techniques such as decreased beam intensity or faster recording could have been used to insure the surface wasn't sputtered away before the entire spectra was recorded, but it must be remembered that sensitivity is directly related to ions/sec delivered to the detector, and that a little integration goes a long way at the low end.

Figure 12 is the analysis of various fractions of a monolayer of Ag deposited on a Si surface. The monolayers were deposited by electroless deposition from an aqueous solution which contained ^{110}Ag tracer ions.[3] The coverage was then determined by gamma counting the tracer on the Si slice after deposition. The analysis was done with a 20 kV, 15 nanoamp, 10 micron, O_2^+ beam rastered to a 200 x 160 micron area. By electronic counter gating synchronized with the primary beam raster, the count acceptance area was restricted to the central 1/4 of the crater bottom. The depth assignments were made by measuring the total crater depth with optical interferometry and assuming a uniform sputter rate. This family of curves all show the same trend, a very intense surface peak rapidly falling off before the 50 angstroms depth, then increasing slightly as the primary ion implant depth is approached, and then taking a second sharp decrease to a constant level well above background. These shapes show that much of the surface Ag is knocked into the silicon by the primary ion beam, hence, the second rapid decline. This is bad if we were interested in a concentration depth profile, but actually beneficial in a surface analysis since it does contribute to detectability time for quantitative analysis. However, if we are struggling for quantitative analysis, which is every mass spectroscopist's impossible goal, we would like to minimize this knock-on effect even though it is only 1 part per hundred. Figure 13 is an attempt to reduce the knock on, or at least the depth, by lowering the primary ion energy. The general trend does show that the second sharp drop is indeed decreased as the energy is reduced. Only the 12 kV curve violates this trend and is probably in error. The actual depths for these curves were extremely difficult to measure and could easily be as much as 100% in error. One final point to note on these curves is that only the 20 kV curve shows a positive slope after the first surface drop. This results from the decreased sputter rate, with the lower energy beams allowing the ambient oxygen to keep a constant surface oxide throughout the analysis. Figure 14 is a closer look at the surface region as a function of primary ion energy. The set illustrates that even in the worst case at 20 kV, we will have collected about 90% of the integrated intensity before 50 angstroms have been sputtered away. Consequently, this illustrates that for quantitative surface analysis by secondary ion mass spectrometry, it will probably be for only one mass per area sputtered. If the area is limited such as on a small signal diode, this can be a severe limitation. However, on pilot slices, which encompasses most of my work, the problem is not limiting as it can be overcome by continual movement of the sample. Figure 15 is one last look at the curves as a function of primary ion energy. These are the same curves as Figure 13, but now the abscissa is plotted as a function of time. This set shows that for qualitative analysis, as much as 10 minutes was available to detect the Ag which was present at about 5% of a monolayer.

Figure 16 shows how quantitative the results shown back in Figure 12 were. The line is a least squares fit to the five points indicated. Each point represents the total integrated count under the respective curve, with the base line taken where the curve leveled off after the second sharp drop. This empirical calibration curve is very encouraging even though two of the low points are off by as much as 100%. No correction was made for ion pick-up efficiency by means of a matrix-ion and this is known to vary by as much as 50% from sample to sample. This study does show that given a set of standards, and I believe that bulk standards can be used, secondary ion mass spectroscopy surface analysis can be empirically quantitated, provided the surface impurity concentrations are not high enough to drastically alter the effective matrix which controls the ion yield efficiency.

Figure 17 turns the topic over to the analysis of SiO_2 surfaces, whereas up to now I have concentrated on silicon surfaces. This is a series of spectra taken under various conditions on a 10,000 angstrom thick oxide film. The oxide was not coated with a conductive film, as would be the normal practice for bulk or in depth analysis, since this would mask the surface of interest. As can be seen from this set of spectra the use of a positive beam on a naked sample gave only a few peaks, none of which are normal patterns expected from a SiO_2 matrix. The absence of a spectra is the result of a high positive charge buildup at the point of impact by both the positive ion beam and loss of secondary electrons. Also, without a conductive surface coating there is insufficient bias on the sample surface to accelerate and direct the secondary ions to the pickup electrode. The negative beam on the naked sample does show the silicon peaks but they are very weak. This does show that the secondary electron loss is compensated by the negative primary ion which allows the point of impact to come to an equilibrium state. The absence of the remainder of the spectrum here is entirely due to the absence of the accelerating sample bias. The two spectra on the right were taken through the open areas on a 300 mesh electron microscope copper grid which was electrically connected to the 1500 volt sample bias. The primary beam was rastered rapidly over both the copper bars and the openings. The theory is that the primary beam bombarding the copper emitted sufficient low energy secondary electrons, which neutralized the positive charge on the SiO_2 surface and provided the necessary secondary ion accelerating potential as well. These spectra do show that the mechanism works; both positive and negative beams give satisfactory spectra. However, these electroplate formed copper grids are not noted for their purity, so a much more pure grid must be employed to render meaningful results. Grids formed by e-beam evaporation of high purity Al or Au should be excellent. This discussion only applies to oxide films greater than 1500 angstroms thick. Thinner oxides behave the same as bare silicon. Therefore, when searching for the source of contaminants, such as furnace tubes, the oxide thickness should be kept below about 1200°C which just happens to be the gate oxide thickness of most MOS devices.

No presentation concerning oxide analysis would be complete without illustrating the mobile ion problem shown by Ron Baxter[4] in Figure 18. These profiles were taken on the same sample using both a positive and negative beam. The conclusion is that using a positive beam, the Na all moves to the interface and with a negative beam, it is all drawn to the surface. The grid technique may help this problem as well, but to date the grid itself has been the dominant source of sodium.

To summarize this presentation, a look at secondary ion mass spectroscopy with respect to five criteria for surface analysis is in order.

1. Accuracy of Chemical Analysis

   The qualitative analysis was shown to be very good and the Ag experiment showed quantitative potential is fair.

2. Surface Sensitivity

   The sensitivity has been shown to be as good as a few ppm.

3. Non-Destructive Analysis

   The method is totally surface destructive.

4. Selected Area Chemical Analysis

   Can be very good depending upon instrument.

5. Experimental Complexity

   Secondary ion mass spectroscopy is one of the most complex analytical techniques in use.

Therefore, for surface analysis, secondary ion mass spectroscopy has not yet reached the ideal, but it has demonstrated itself to be one of the more powerful techniques.

REFERENCES

1. Anderson, C. A., *International Journal of Mass Spectrometry and Ion Physics* 2, 61 (1969).

2. Fralick, R. D., and Roden, H. J., ASMS Committee VII Workshop, 22nd Annual ASMS Conference, Philadelphia, (May 1974).

3. Larrabee, G. B., unpublished work, Texas Instruments Incorporated, Dallas, Texas.

4. Hughes, H. L., Baxter, R. D., and Phillips, B., *IEEE Trans. Nucl. Sci.* NS-19, 256 (1972).

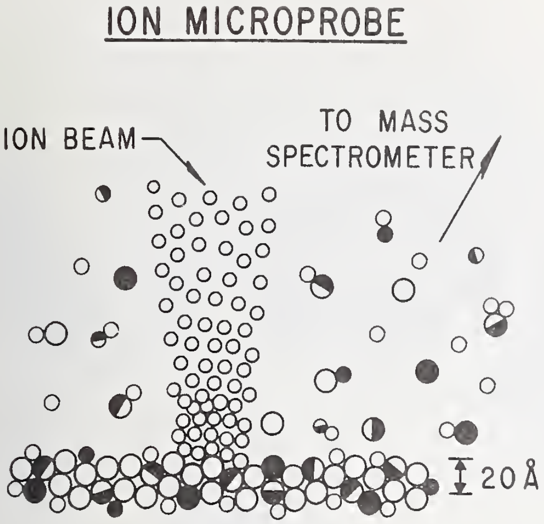

Figure 1. Artist's conception of the secondary ion production process.

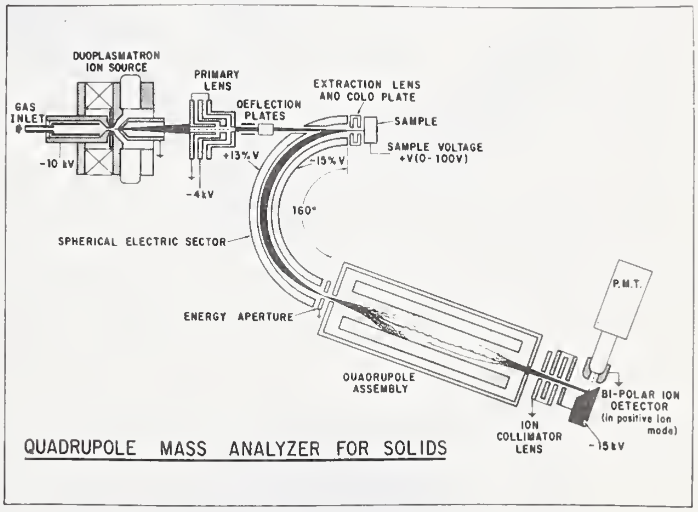

Figure 2. Block diagram of the ARL QMAS system.

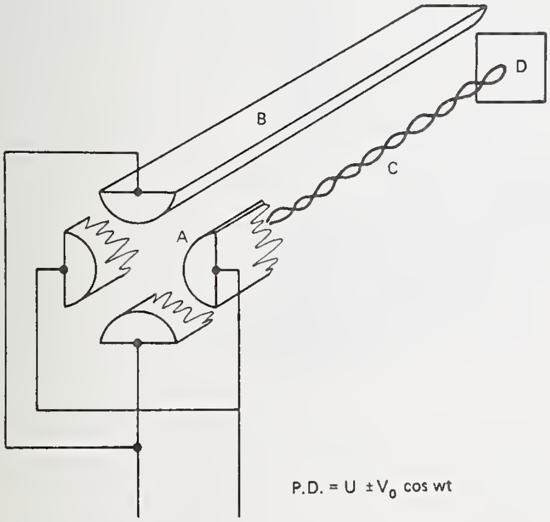

Figure 3. Quadrupole mass analyzer scheme.

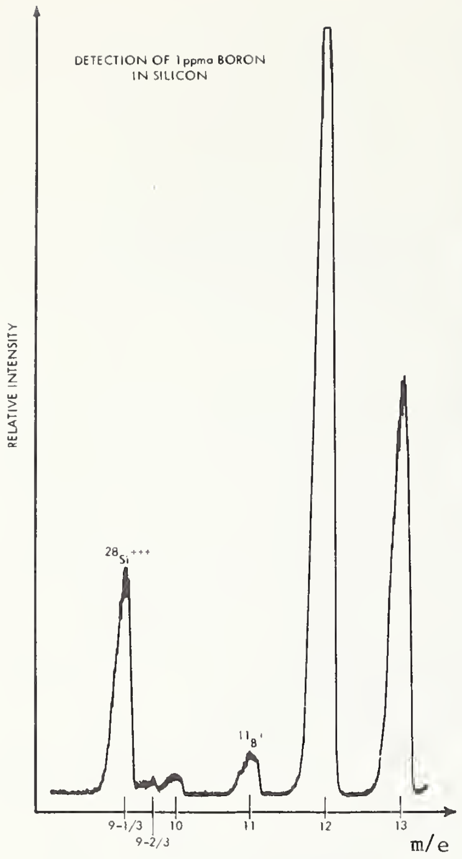

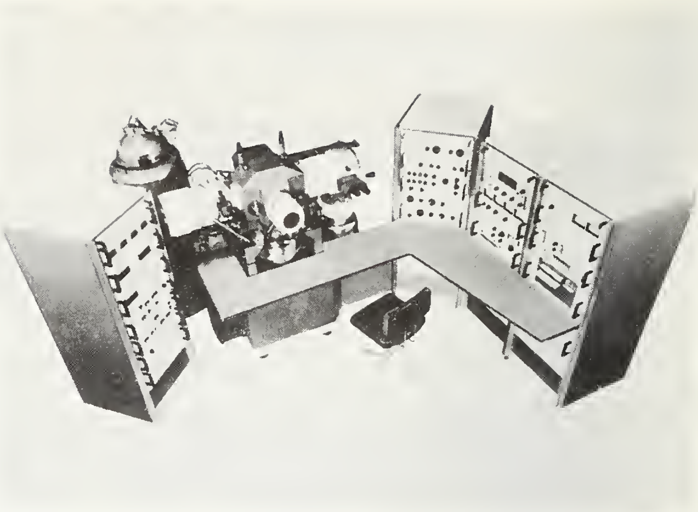

Figure 6. Photograph of the Cameca ion microanalyser.

Figure 4. Portion of mass spectrum of 1 ppm B doped Si taken with the ARL QMAS system.

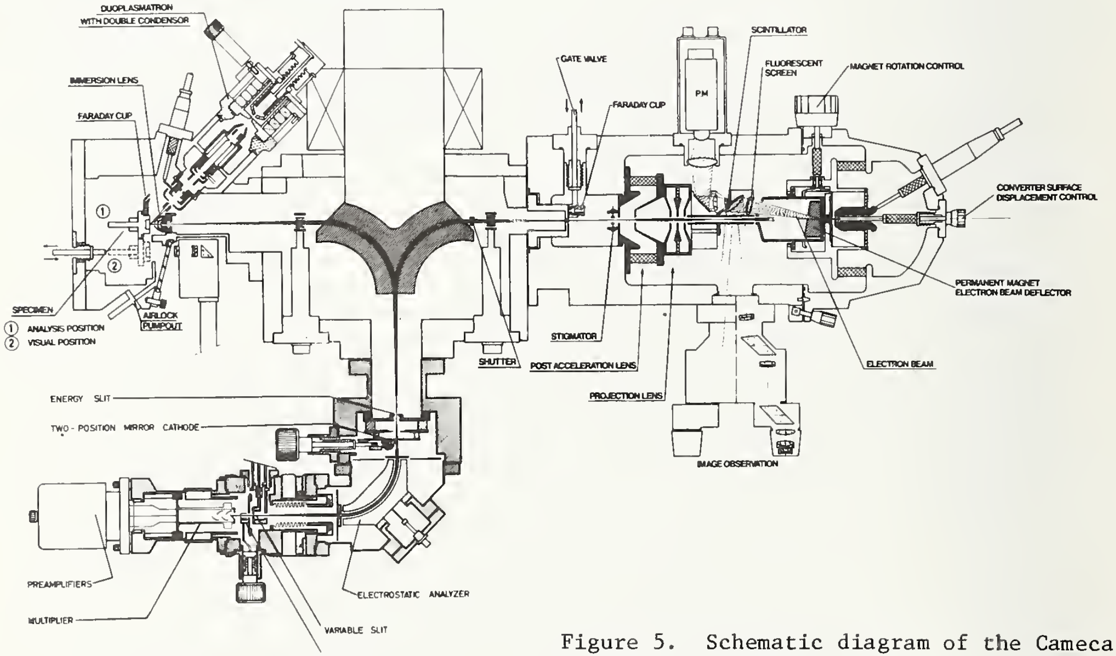

Figure 5. Schematic diagram of the Cameca ion microanalyzer.

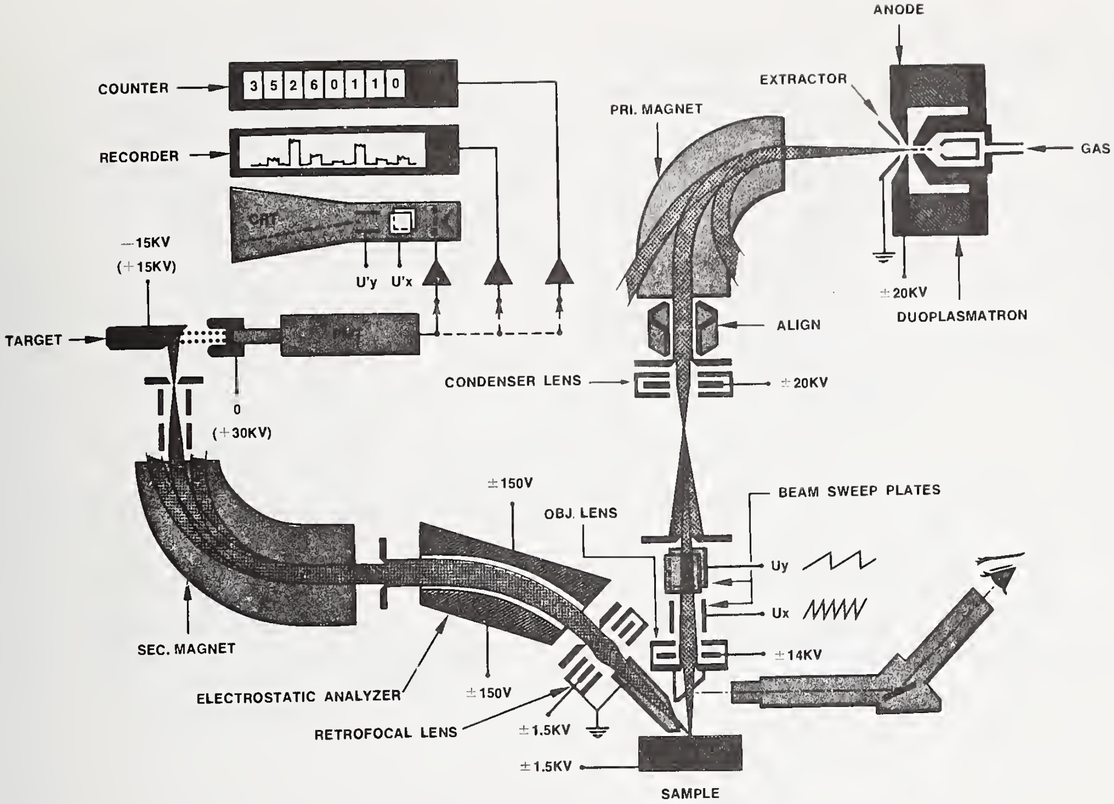

Figure 7. Schematic diagram of the ARL IMMA.

Figure 8. Photograph of the ARL IMMA at Texas Instruments Incorporated.

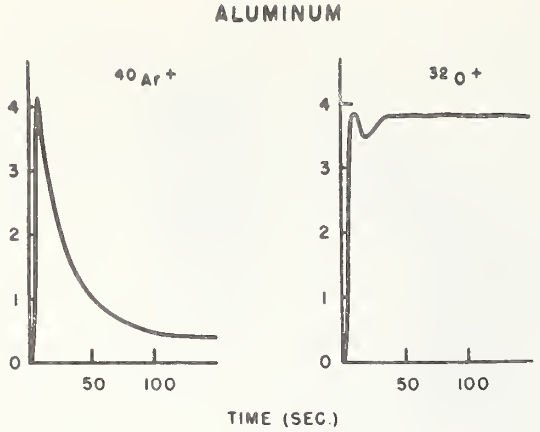

Figure 9. Sputter yield comparison for kinetic and chemical ionization mechanism.
Accel. potential 11 KV
Sample current 4 × 10^{-9} A
Probe size 20 μm^2

Figure 10 (below). Relative yield of some positive ion intensities from pure metals.

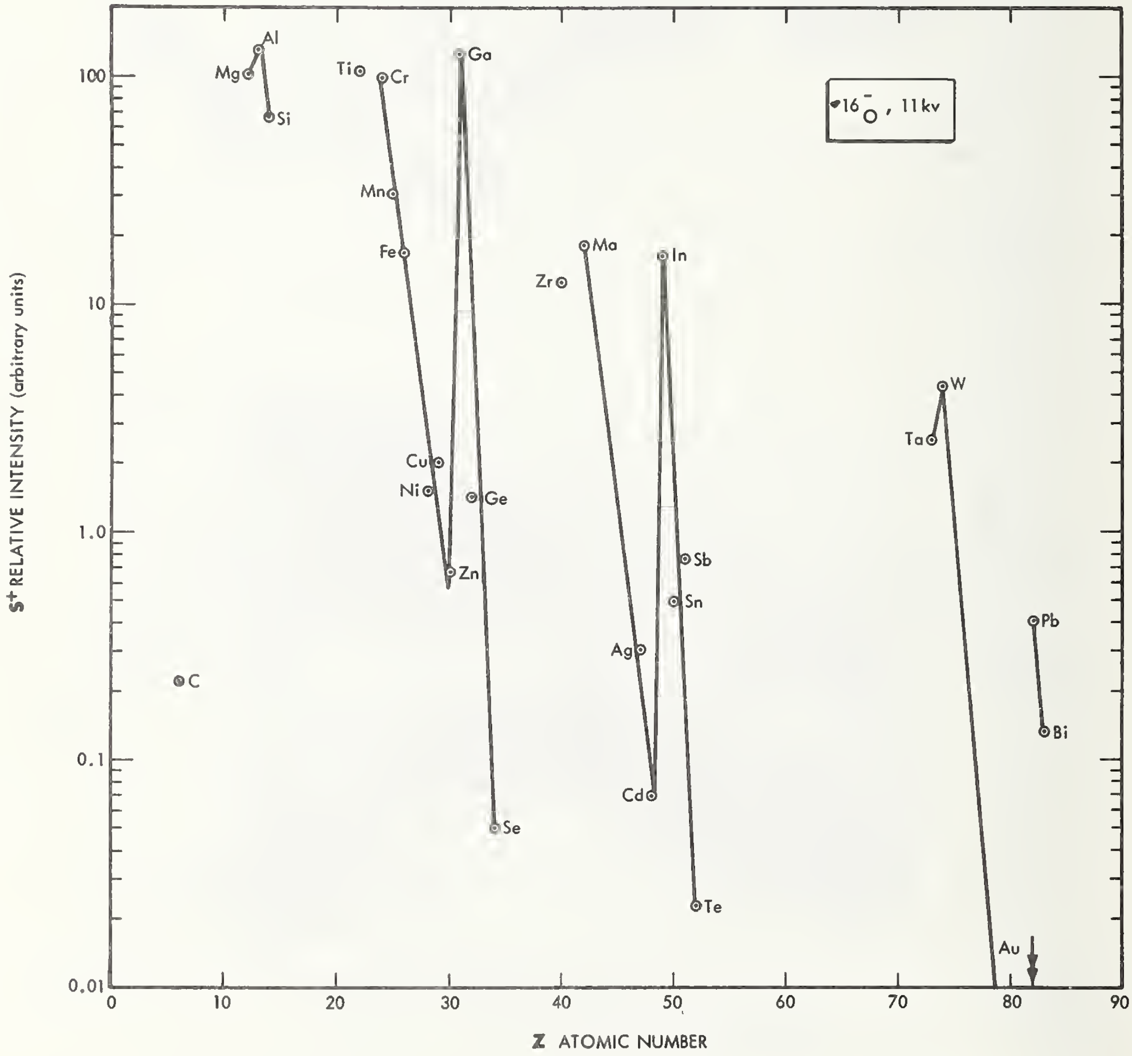

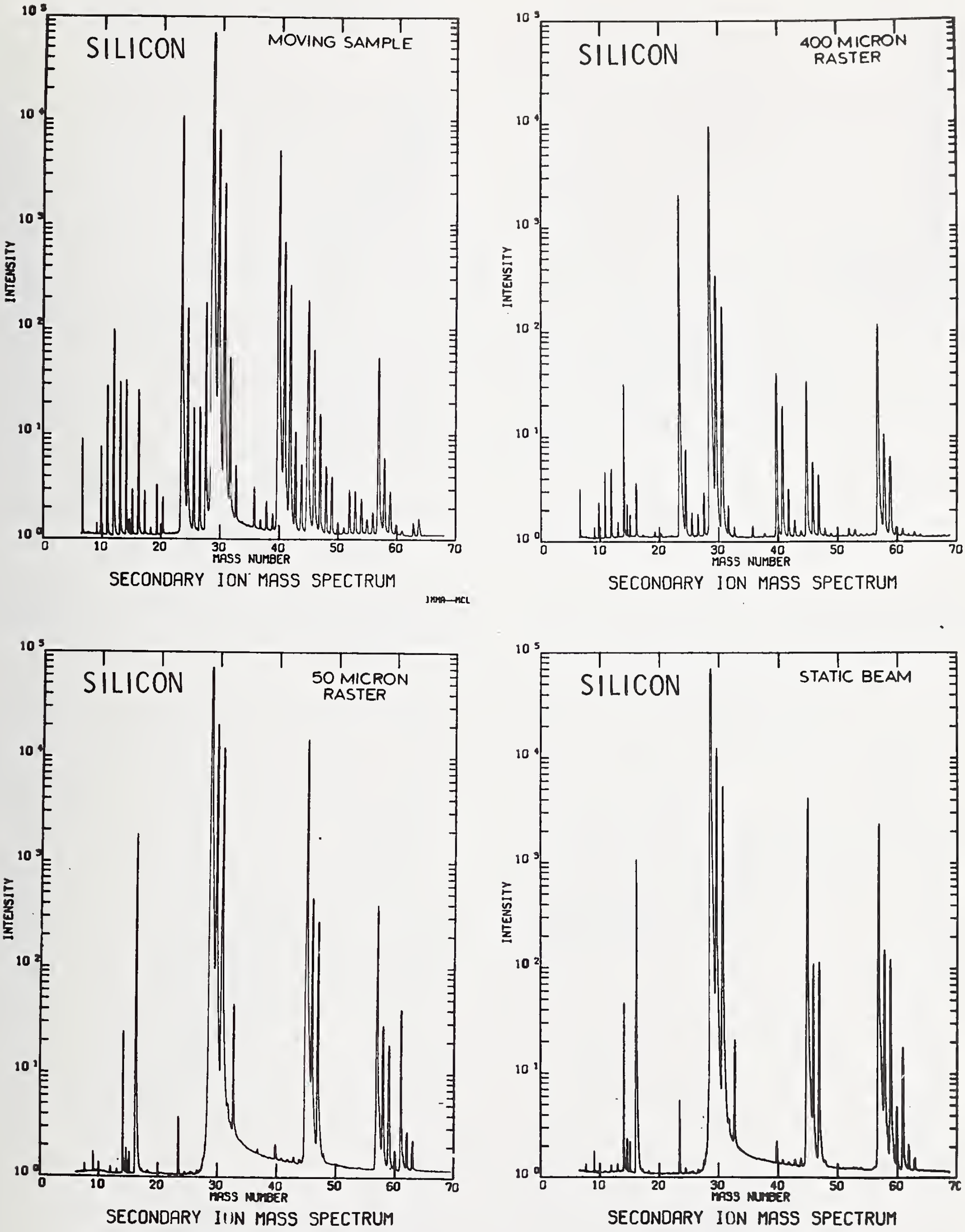

Figure 11. Surface spectra of Si as a function of depth consumed.

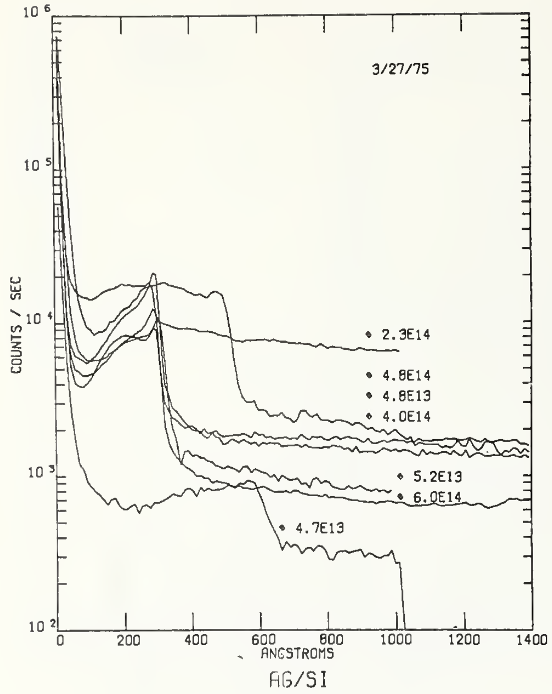

Figure 12. Ag on Si surface and depth profile ion intensity as a function of monolayer coverage.

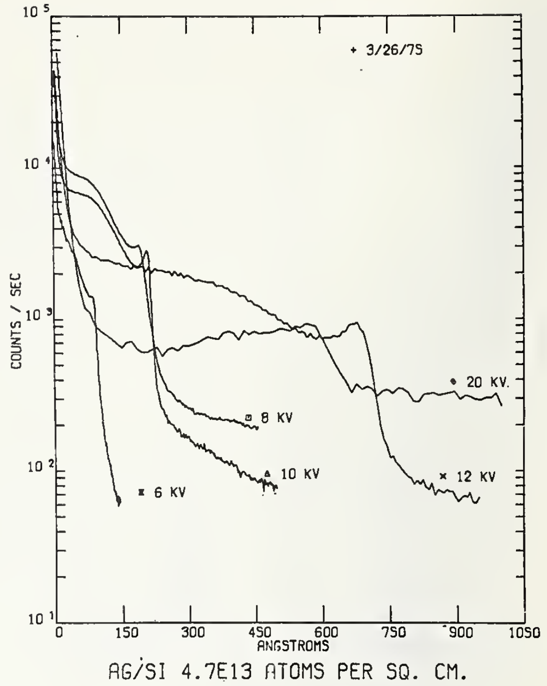

Figure 13. Ag on Si surface and depth profile ion intensity as a function of primary ion energy.

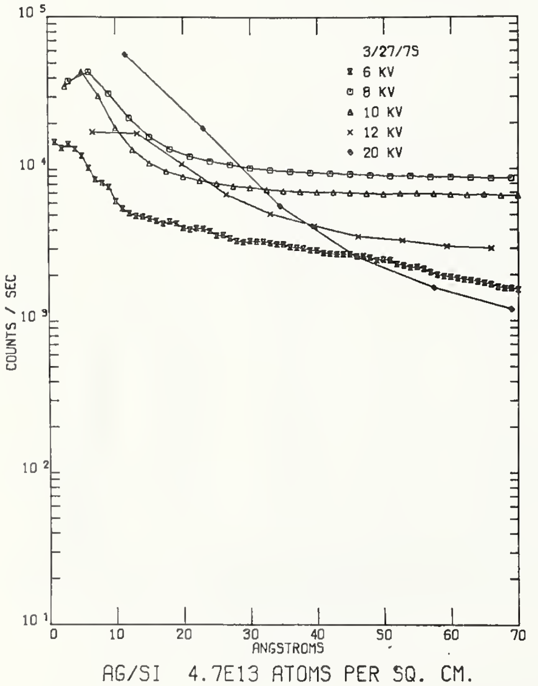

Figure 14. Surface expand view of figure 13.

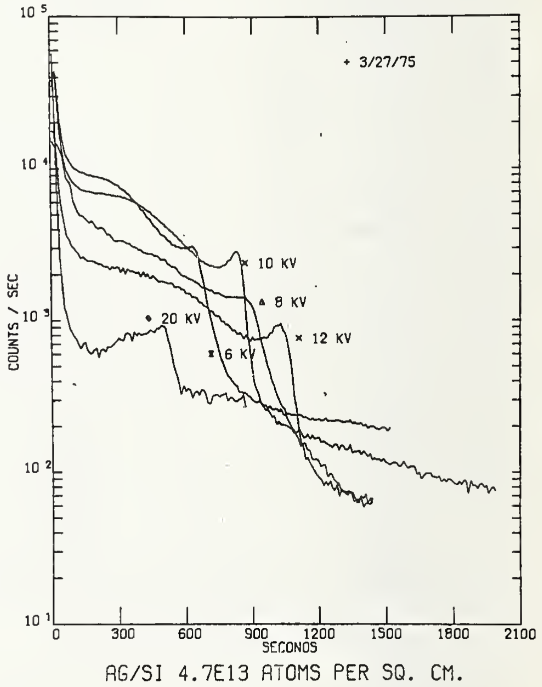

Figure 15. Ag on Si surface and sputter time dependent ion intensity as a function of primary energy.

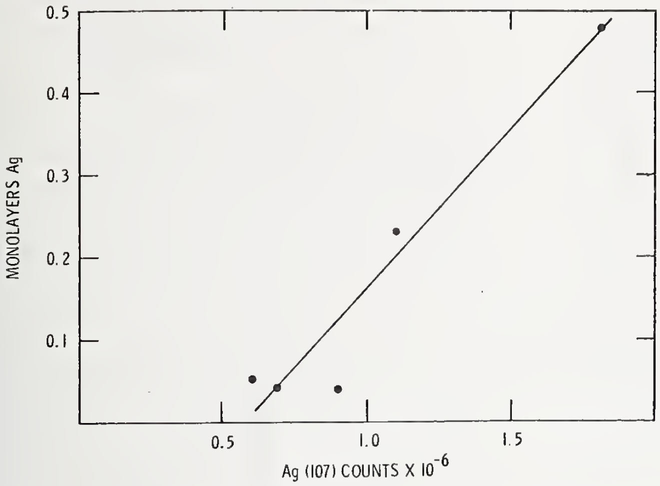

Figure 16. Empirical quantitative curve for monolayer Ag on Si surfaces.

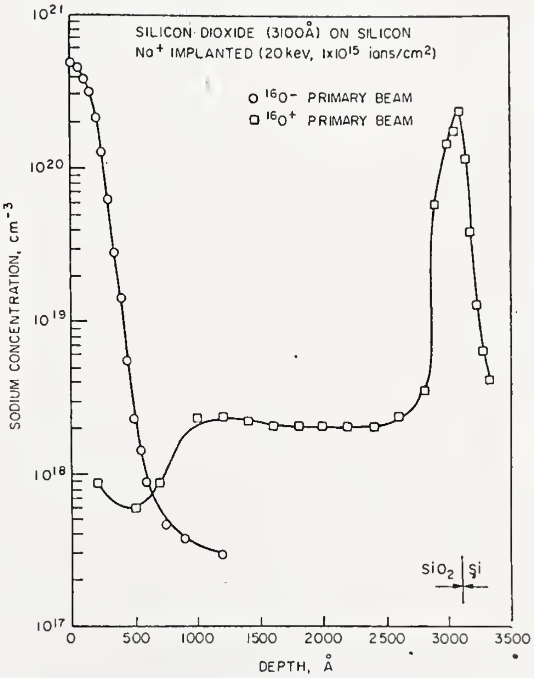

Figure 18. Na profiles in SiO_2 taken with positive and negative primary beams.

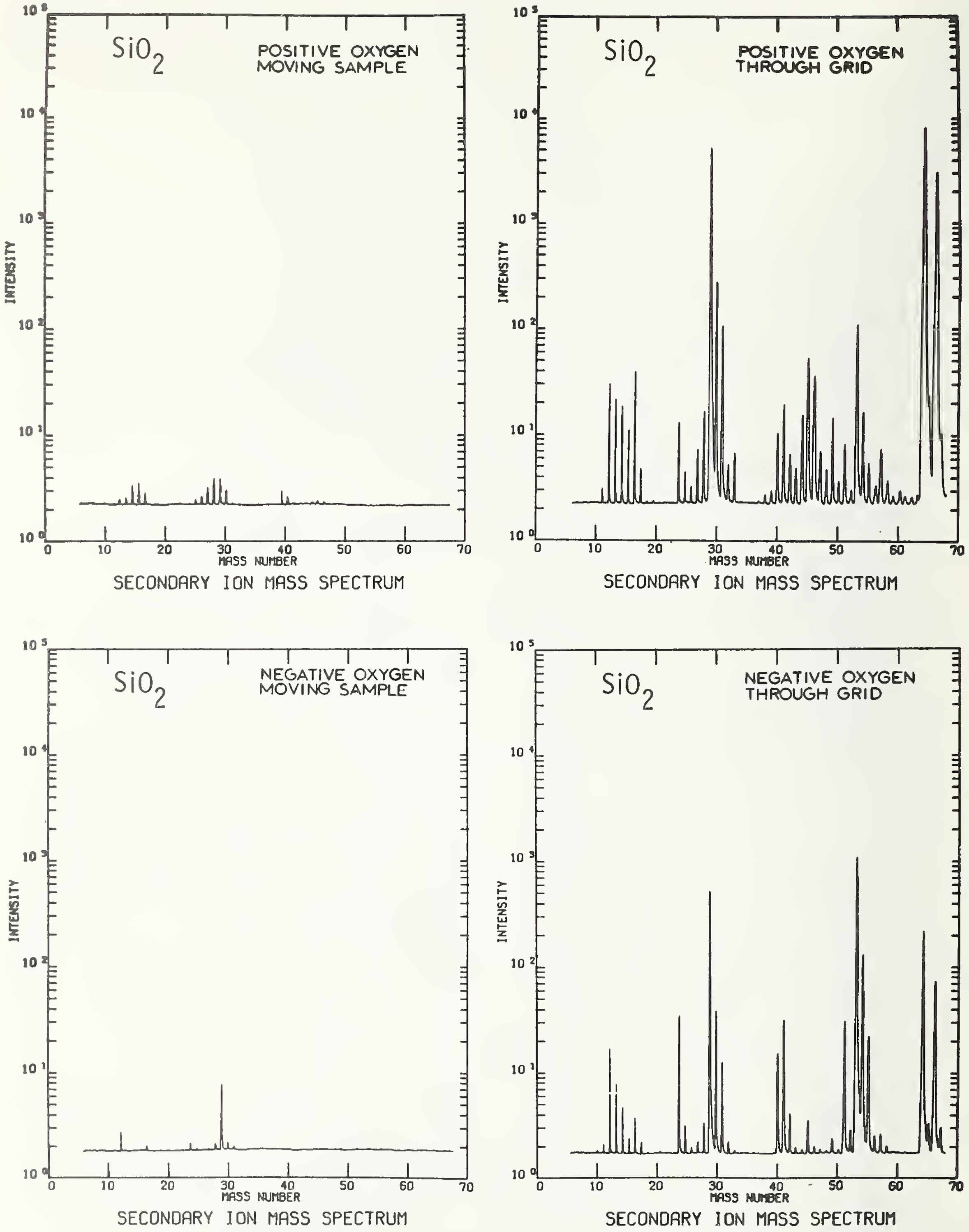

Figure 17. Surface mass spectra of uncoated SiO_2 surfaces and mass spectra taken through a 300 mesh grid.

DISCUSSION OF THE PAPER

Participant: I did not understand what you said concerning the appearance of the SiO_2 peaks in the silicon.

Dobrott: The SiO_2 peak appeared in the silicon analysis after the initial oxide surface was removed simply because I was analyzing the silicon dioxide formed at the implant depth of the primary oxygen beam.

Participant: Could you have avoided that problem by using ^{18}O instead of ^{16}O as the primary ion?

Dobrott: There was no mass interference problem. I made that observation to point out the sample depth at which that particular spectrum was gathered.

Morabito: Should not that dip in the SiO_2 profile, due to the primary oxygen implant, be accompanied by a corresponding dip in the silver signal?

Dobrott: The silver profiles determined at lower primary ion energies did not really dip, they went down and never regained; probably because of the proximity of the initial implant depth and the surface. The higher energy profiles dipped and recovered probably due to the implantation process.

Participant: In the silver case did you assume the silver was uniform, or could it have formed islands, or what?

Dobrott: We assumed that there was a uniform deposition of silver. The analysis was done to see if we could correlate the known amount of low temperature electroless deposited silver on the surface with what we get when we sputter it all away, and to see how quickly this could be done. Yes, the silver could have formed islands, we do not know that it did not.

NBS Special Publication 400-23, ARPA/NBS Workshop IV, Surface Analysis for Silicon Devices, held at NBS, Gaithersburg, Maryland, April 23-24, 1975 (Issued March 1976)

SOME EFFECTS LIMITING SIMS DEPTH PROFILE ANALYSIS AND METHODS FOR IMPROVEMENT

Robert K. Lewis

Cameca Instruments, Inc.
Elmsford, New York 10523

INTRODUCTION

Secondary ion mass spectrometry (SIMS) has proven to be a very attractive method for obtaining surface and bulk concentrations of materials used in semiconductor device technology. The popularity of SIMS has resulted primarily from the fact that the method has the sensitivity necessary to detect doping level concentrations, namely 10^{+15} to 10^{+17} atoms/cm^3, and the ability to produce depth profiles at these concentration levels.[1,2] The disadvantage of being a destructive method is readily offset by the inherent depth analysis capability which results from the sputtering action of the primary beam. It is this depth profiling capability, in fact, that has provided the principal interest in SIMS for analyzing semiconductor material and the technique is now widely used for characterizing these materials. However, there are problems with SIMS depth profiling which must be taken into consideration. This paper discusses some of the effects which have been encountered and tend to limit the usefulness of the technique and describes methods to minimize them. These effects have been summarized in Table I.

DEPTH RESOLUTION

To achieve good depth resolution it is obvious that the surface of the crater bottom must be maintained as flat as possible. With normal or non-normal incidence of the primary beam a high degree of flatness can be easily maintained by rastering the beam. Schematic diagrams of craters produced by non-rastered and rastered beams are shown in Figure 1 and Figure 2. Figure 1 shows that with a non-rastered beam, 250μm in diameter, incident at 45° (this is approximately the bombarding angle in the Cameca IMS 300 instrument used for this study), and a gaussian distribution, the flatness variation over a typical selected area (50μm) is approximately 200 Å. This is adequate for many depth profiles. However, if the beam is rastered as shown in Figure 2, the flatness over the area selected for analysis can be greatly improved. We have established that the variation in flatness can be less than 40 Å over an area of 100μm to depths of about 1,000 Å by bombarding amorphous Ta_2O_5 and using the technique of observing the variation in color of fringes produced in white light.[1] This would give a value of less than 5% for the variation in depth divided by the total depth sputtered. This value is consistent with the R value found by Werner[3].

It is clear that ions sputtered from the crater wall must be rejected to have good depth resolution. This is easily accomplished in the Cameca ion microscope by mechanically aperturing in an image plane or in an ion probe by electronic gating (turning off the secondary detector when the primary beam is on the crater wall). Mechanical aperturing is shown schematically in Figures 1, 2, and 16. With electronic gating the primary beam must be kept smaller than that required with mechanical aperturing. This tends to limit the maximum average beam density obtainable and consequently the maximum sputtering rate available with ion probes.

If the sample surface does not sputter away evenly because of a lateral variation in sputtering rate, the depth resolution will suffer accordingly. Lateral variation in sputtering rate results from different lattice orientations encountered by the primary beam from grain to grain in polycrystalline material or from different lattice structures when different phases are encountered. For this reason the depth resolution attainable in such material is usually only ten to twenty percent of the total depth sputtered. Continuously rotating the sample while sputtering could reduce the lattice orientation effect; however, no commercial instruments presently provide this capability. When lateral differences in orientation or in phase are encountered the use of an oxygen leak can sometimes minimize the variation in sputtering rate.

Channeling (lattice effects) in SIMS have been described by Slodzian and Bernheim[4]. This is a variation in ion yield that occurs when the incident beam traverses transparent and opaque directions in the lattice. A plot of secondary ion intensity versus the angle of rotation is shown in Figure 3. Fortunately, this effect is only a second order effect so it is generally not a problem in depth profiling. However, it is important to be aware of the fact that it can cause errors especially when comparing samples. A method of minimizing the effect is to bombard the surface with a stream of oxygen (oxygen leak). This produces a less severe variation in ion intensity with orientation as shown by the dotted line in Figure 3. Slodzian has pointed out that the effectiveness of the oxygen leak is determined by whether the surface oxide formed is crystalline or amorphous.

"Knock on" is the redistribution that occurs from the physical driving in and sub atomic mixing of the atoms being analyzed. The effect has been shown by McHugh[5] analyzing Ta_2O_5 which had an approximately 50 Å thick phosphorous layer located 230 Å below the surface. His results are shown in Figure 4. The effect is significant only at high primary bombardment voltages (above about five kilovolts). The effect would be less, of course, at a higher angle of incidence. The angle of incidence can be changed for non-normal incident primary beams by changing the polarity of the primary beam. The combinations positive primary-positive secondary and negative primary-negative secondary give the highest angles of incidence.

DETECTION SENSITIVITY

One of the most serious problems encountered in SIMS is the mass interference from the complex polyatomic species produced by the secondary ion process. These species are formed from the clusters of the matrix atoms formed by the sputtering action of the beam (e.g., M, M_2, M_3,...) and combinations with the primary ion when a reactive gas such as oxygen is used (e.g., MO, MO_2,...M_2O, M_2O_2, ...etc.).

Typical spectra produced when bombarding silicon with a reactive gas (oxygen) is shown in Figure 5 due to Evans[6]. It can be seen that the problem of mass interference is more severe at the higher masses. This is just the opposite of the ion production process in spark source mass spectrometry (SSMS) where the interferences are more concentrated in the lower mass region of the mass spectrum. This is because in the spark source the energy available is much higher which breaks up the clusters and creates many multiply charged ion species.

The simplest method for minimizing mass interference from the polyatomic species is to take advantage of the large differences in energy distribution between the polyatomic and monatomic species. These distributions are shown in Figure 6 which is from Satiewicz[7]. It can be seen that the complex polyatomic species can be rejected perferentially over the monatomic species by rejecting the low energy ions.

The low energy ions may be rejected in the Cameca instrument by using the low energy discriminator (L.E.D.) shown in Figure 7 or by appropriate adjustment of the electrostatic analyzer when the double focusing arrangement shown in Figure 8 is used. Rejection of the low energy ions with the ESA is possible because the double focusing geometry used has a first order direction focus position such that slits can be used to precisely define the energy limits accepted. The SIMS instruments designed by Herzog et. al. (GCA)[8] and Tamura et. al. (Hitachi)[9] have this feature while the ion probe SIMS instruments described by Liebl (ARL)[10] and Banner et. al. (AEL)[11] do not.

The attenuation of the silicon polyatomics in the spectra shown in Figure 5 with increasing attenuation of the parent monatomic peak using the L.E.D. on the Cameca instrument is shown in Figure 9. A typical application of the L.E.D. is shown in Figure 10. Here the detection of arsenic using the AsO^- species has been improved by one order of magnitude. An equally important use of the L.E.D. is the removal of tails on the low energy side of a mass peak. The presence of these tails can cause a serious loss in abundance sensitivity (and therefore detection sensitivity) on the low mass side of intense peaks. This is shown for the detection of copper and zinc in gallium arsenide in Figure 11. These tails result from the post ionization of the neutral species leaving the sample. This "kinetic" emission process has been described by Blaise and Slodzian[12]. It is not necessary to attenuate the intensity of the peak to eliminate the low energy tails with the L.E.D.

A second and more elegant method for eliminating interference from polyatomic ion species is the use of high mass resolution. The method of obtaining high mass resolution on the Cameca instrument is shown in Figure 8. Here the normal imaging mode path, that is prism - mirror - prism, is interrupted and the beam is allowed to pass through a hole in the mirror (the mirror being displaced) into a sperical electrostatic analyzer (ESA). This combination of an ESA with the first magnetic deflection is an inverted Nier-Johnson double focusing configuration. With this analyzer mass resolutions over 5000 have been achieved. It is possible with high mass resolution to completely separate the interfering polyatomic mass peak $^{27}Al_2$ from the ^{54}Fe peak as shown in Figure 12 because of the mass differences that occur. Some typical elements, the possibly polyatomic interferences, and the mass resolution required to resolve the doublet are listed in Table II. The separation of the $^{75}As/^{29}Si^{30}SiO$ doublet at the peak and lower limit of the distribution, for arsenic ion implanted into silicon, is shown in Figure 13.

A second effect limiting detection sensitivity is the contamination of the surface from the ambient gas molecules in the vacuum system. At pressures around 10^{-7} to 10^{-8} torr, which is the typical vacuum level in commercial SIMS instruments, it can be readily demonstrated that the low current densities present in the beam periphery produce an artificially high background signal. This is because the influx of ambient gas molecules now competes with the primary beam and react with the surface where they are sputtered away producing various interfering ion species. Low beam densities will always be present at the periphery of an ion probe. In addition there is a significant flux of neutral atoms (neutralized ions) over a large area outside the bombarded region that also sputter the target surface and produce ions from the ambient gas as shown by McHugh[13] in Figure 14. A cold plate near the sample surface will minimize the hydrocarbon contamination, but it will not eliminate it and it will have little or no effect on oxygen, nitrogen and CO_2. The effect is shown dramatically using the Cameca instrument by bombarding aluminum with a beam of nonreactive ions (Ar^+). By keeping the beam diameter less than the field of view (225μm) it is possible to see the effects of low primary beam density at the periphery of the beam on the fluorescent screen as shown in Figure 15. At the periphery there is a marked increase in the secondary ion intensity due to an ion yield enhancement (chemical effect) from the reactive ambient gas. By mechanically aperturing as shown in Figure 16 and selecting areas approximately 50μm in diameter at the center (Area A) and the periphery (Area B) the spectra shown in Figure 17 were produced. It is obviously impossible to achieve a low background signal without rejecting this ambient contribution. The only methods that have been demonstrated to be effective in eliminating the ambient contamination are lowering the vacuum below 10^{-9} Torr as Benninghoven[14] has shown which unfortunately is impractical in commercial SIMS instruments or the ions produced outside the area of high beam density can be eliminated by the mechanical aperturing technique. However, there is no way to avoid this effect with the electronic gating technique used with ion probes.

A third effect which can limit detection sensitivity is the phenomena of resputtering. This effect is observed when material in high concentration near the surface at the edge of the crater is sputtered and the neutral particles are scattered in some manner into the analyzed area at the crater bottom. This is essentially a second order effect. It can be kept below the detection limits by using crater diameters much larger than the area analyzed. Evaporating non mass interfering metal (e.g. gold) on the surface prior to depth profiling can also be helpful.

ACCURACY

The most serious effects limiting the accuracy of a depth profile are those limiting the uniformity of the ion yield of the element being measured or a reference element (e.g. a matrix element) used for normalization. Any marked change in concentration of a reactive element such as boron, carbon or oxygen can change the ion yield of elements associated with it. This effect is shown in Figure 18 where phosphorous enhances the yield of the tantalum ion. It is important to determine if such species are present by in-depth mass spectral analysis whenever possible, and, if present, to measure the depth profile of the reactive species simultaneously with the element of interest. This also applies to any element being measured for normalization purposes. Sometimes it is useful to check for the presence of a reactive element by using an inert gas as the primary beam (e.g. argon) which does not enhance the matrix greatly increasing the contrast.

Whenever a reactive primary beam is used there can be a marked change in the ion yield over the first few hundred angstroms of sputtered material (15kV bombardment) due to the implantation effect of the primary beam as described by Lewis et. al.[15]. The effect is shown in Figure 19 where pure silicon was bombarded with O^- primary ions and positive secondary ions of oxygen and silicon measured together. This ion yield variation results from the fact that the implanted primary oxygen ion is first concentrated at a depth below the surface as shown schematically in Figure 20. Until the sputtering front reaches this depth there will be a variation in ion yield of all elements which are enhanced by the primary ion. The effect is minimized by keeping the bombardment voltage low (below 5kV) and can be essentially eliminated by the use of an oxygen leak as shown in Figure 21.

Variations in sputtering rate with depth can cause errors in depth measurements if the variations are not taken into consideration in the sputtering rate calibrations used to establish the depth scale. Often measurement of a matrix species and normalization against this signal will take care of small sputtering rate variations due to beam density changes. However, variations due to phase changes in the sample must be determined by depth measurements outside the instrument. If sufficient thicknesses of the material in the individual phases are available (a few hundred angstroms) it is possible to make their depth calibrations with a Talystep. If larger thicknesses (a few thousand angstroms) are available it is more convenient to make the measurements with a light microscope equipped with a Michelson interferometer.

It is not unusual to encounter a situation where what appears to be a variation in depth (shown for aluminum in the thin film depth profiles shown in Figure 22) is actually a variation in lateral distribution as shown in the ion image of Figure 23. This variation may be real or a result of variations in the lateral sputtering rate. The lateral distribution effect is observed most often at metal - metal oxide interfaces or thin film metallizations. It is difficult to minimize this effect. However, its presence can usually be taken into account by observing a series of ion images with depth.

One of the major concerns in all depth profiling work is whether the element of interest is being redistributed by the bombardment process. This is the case of the "knock on" phenomena described above, which was described as a second order process. The only first order redistribution effect observed to date has been for the analysis of sodium in silicon dioxide layers. This redistribution occurs whenever a potential is applied to the surface. The sodium migrates (within milliseconds) to the SiO_2/Si interface or to the sample surface depending on whether the potential applied at the sample surface is positive or negative as shown in Figure 24. It is questionable whether an accurate profile of sodium in SiO_2 can be obtained at all since even neutral atom bombardment will release secondary electrons and charge the surface. The surface to substrate potential must not exceed a few tenths of a volt while the profile is being measured. Fortunately this ion mobilization phenomena appears to be a problem only for the case of sodium in silicon dioxide. No other documented instances are known to this author.

References

1. Morabito, J. M., and Lewis, R. K., *Anal. Chem.* 45, 869 (1973).
2. Kofkner, W. K., Werner, H. W., Oosthoek, D. E., and de Grefte, H. A. M., *Rad. Effects* 17, 88 (1973).
3. Werner, H. W., *Acta Electronica* 18, 51 (1975).
4. Slodzian, G., and Bernheim, G., *Int. J. Mass Spectrom. Ion Physics* (1975).
5. McHugh, J. A., *Rad. Effects* (1973).
6. Blattner, R. J., Baker, J. E., and Evans, Jr., C. A., *Anal. Chem.* 46, 2171 (1974).
7. Satkiewicz, R. G., Air Force Technical Report, AFAL TR-69-322 (1970).
8. Herzog, R. F. K., Poshchenrieder, W. P., Ruedenauer, F. G. and Satkiewicz, F. G., *Proc. Fifteenth Annual Conf. Mass Spectrometry and Allied Topics*, Denver, Colorado, May 1967, p. 301.
9. Tamura, H., Kondo, T. and Doi, H., Advances in Mass Spectrometry, Quayle, Ed., (Inst. of Petroleum, London, 1971), Vol. V., p. 441.
10. Liebl, H., *J. Appl. Phys.* 38, 5277 (1967).
11. Banner, A. E., and Stimpson, B. P., *Vacuum* 24, 511 (1975).
12. Blaise, G., and Slodzian, G., *J. Phys.* 31, 93 (1970).
13. McHugh, J. A., to be published.
14. Benninghoven, A., *Surf. Sci.* 28, 541 (1971).
15. Lewis, R. K., Morabito, J. M., and Tsai, J. C. C., *Appl. Phys. Lett.* 23, 260 (1973).

TABLE I

Parameter	Limiting Effect	Order	Method of Minimizing	Figure
Depth Resolution	Uneveness of crater bottom	1	Rastering primary beam	1,2
	Contributions from crater wall	1	Electronic gating or mechanical aperturing	1,2
	Lateral variation in sputtering rate	1	Rotate sample Oxygen leak	
	Channeling and "knock on"	2	Oxygen leak Lower primary ion voltage and/or increase the incident angle	5
Detection Sensitivity	Mass interference from polyatomics	1	Low energy discrimination High mass resolution	8
	Surface contamination from the ambient gas	1	Mechanical aperturing Operate in vacuum 10^{-9} torr	16
	Resputtering	2	Coat sample surface, e.g. gold Keep crater walls far from area analyzed	
Accuracy	Variations in ion yield	1	Oxygen Leak Monitor distribution of reactive elements in depth	21
	Variations in sputtering rate	1	Intermediate depth measurements	
	Variations in lateral distribution	1	Ion imaging	
	Redistribution	*	Keep surface charge neutral	

* Large effect for sodium in SiO_2, no other similar instances have been reported.

TABLE II

MASS RESOLUTION REQUIRED TO SEPARATE DOUBLETS OF TYPICAL INTERFERING POLYATOMIC ION SPECIES IN SIMS

Nominal Mass	Species	M/ΔM
14	$^{14}N/^{28}Si^{++}$	1,000
27	$^{11}B^{16}O/^{27}Al$	1,200
48	$^{24}Mg_2/^{48}Ti$	2,200
54	$^{27}Al_2/^{54}Fe$	2,300
56	$^{24}MgO_2/^{56}Fe$	1,400
56	$^{28}Si_2/^{56}Fe$	3,000
59	$^{27}Al^{16}O_2/^{59}Co$	1,500
60	$^{28}Si^{16}O_2/^{60}Ni$	1,700
64	$^{48}Ti^{16}O/^{64}Zn$	4,700
75	$^{29}Si^{30}SiO/^{75}As$	3,200

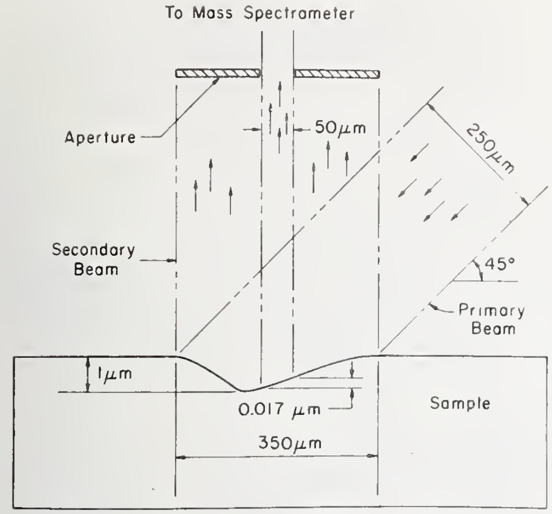

Figure 1. Crater produced by unrastered primary ion beam.

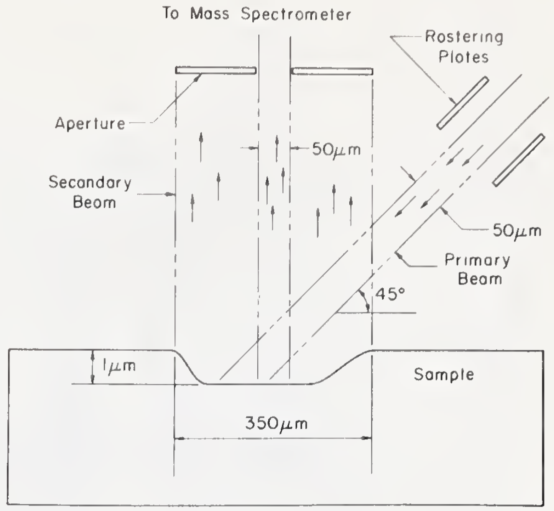

Figure 2. Crater produced by rastered primary ion beam.

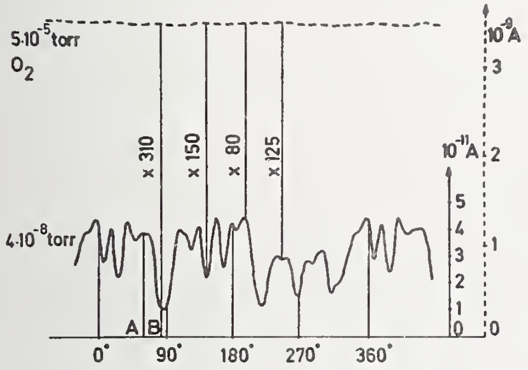

Figure 3. Variation in ion yield with different orientations of primary beam.

Figure 4. "Knock on" redistribution from ion bombardment.

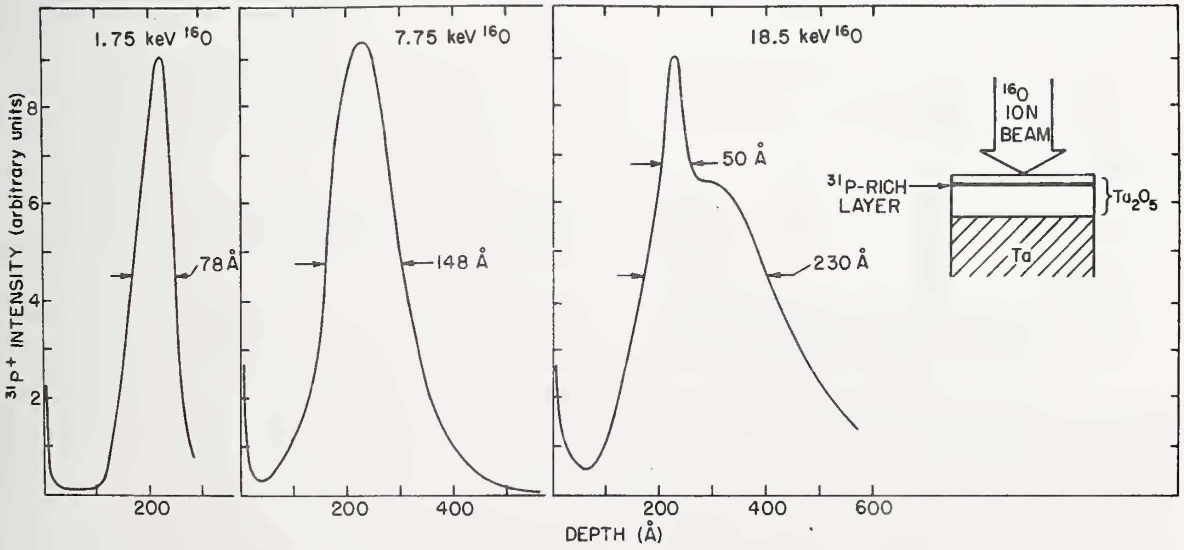

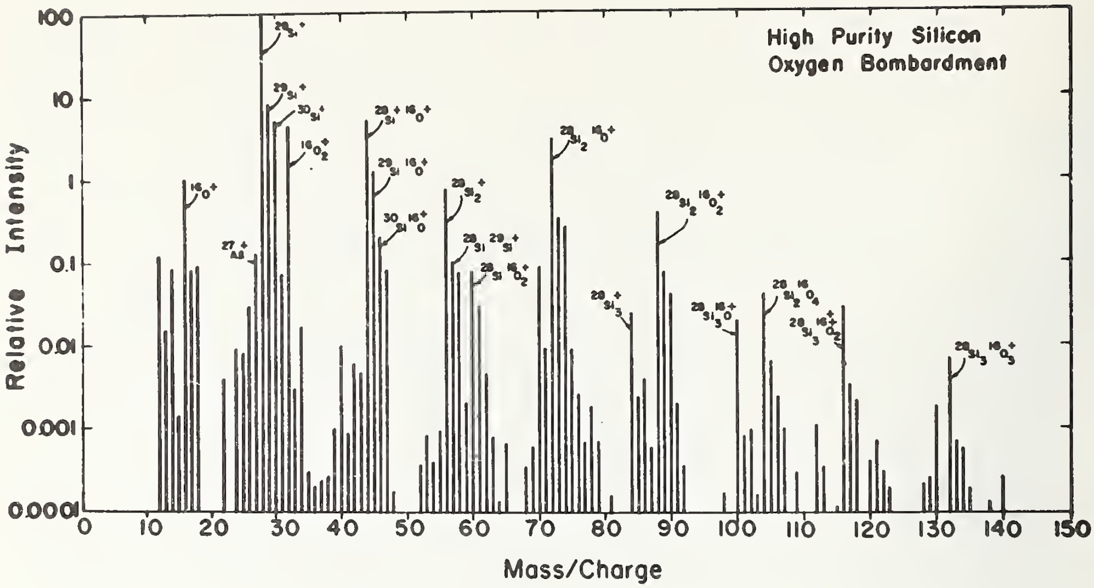

Figure 5. Mass spectra of silicon polyatomics.

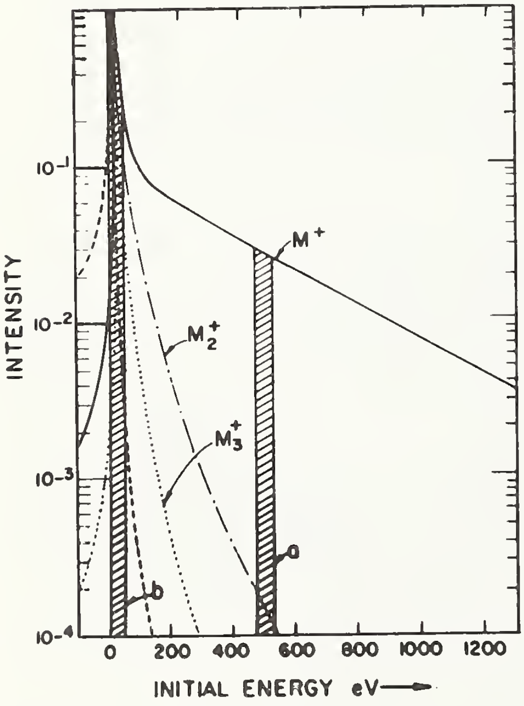

Figure 6. Energy distribution of polyatomics.

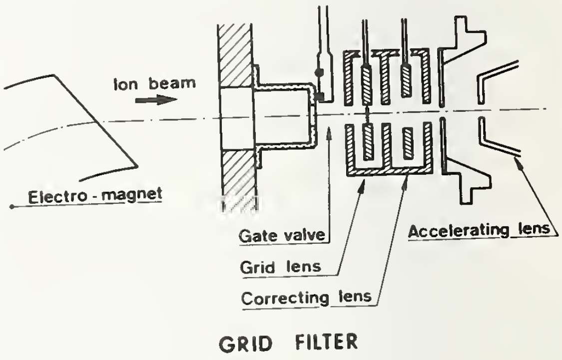

Figure 7. Low energy discriminator grid filter on the Cameca IMS.

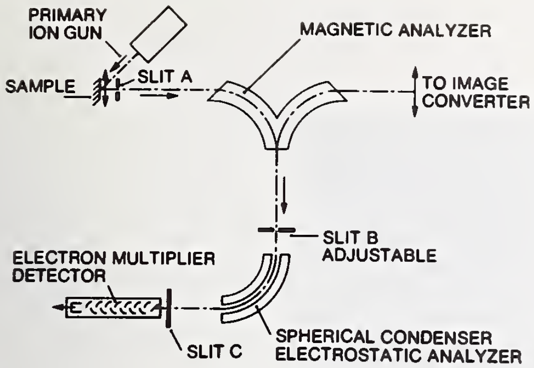

Figure 8. Double focusing ion optics accessory for the Cameca IMS.

Figure 9. Attenuation of positive secondary silicon molecular ion species with low energy discrimination.

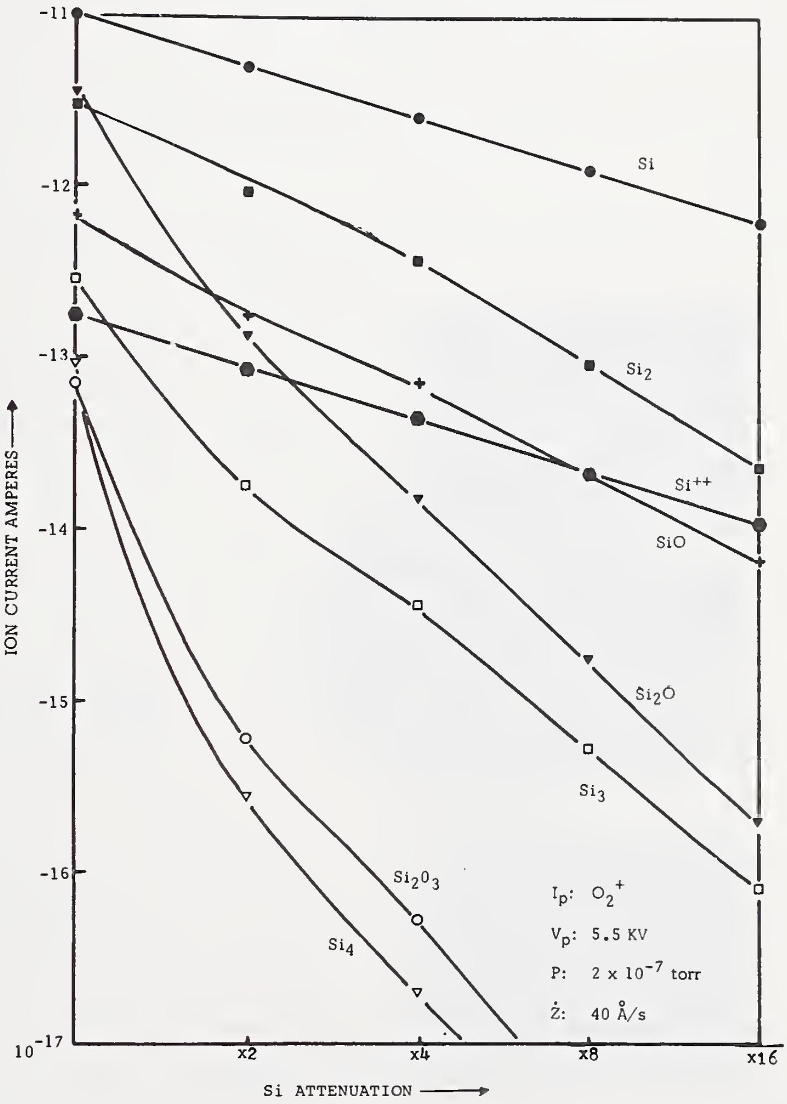

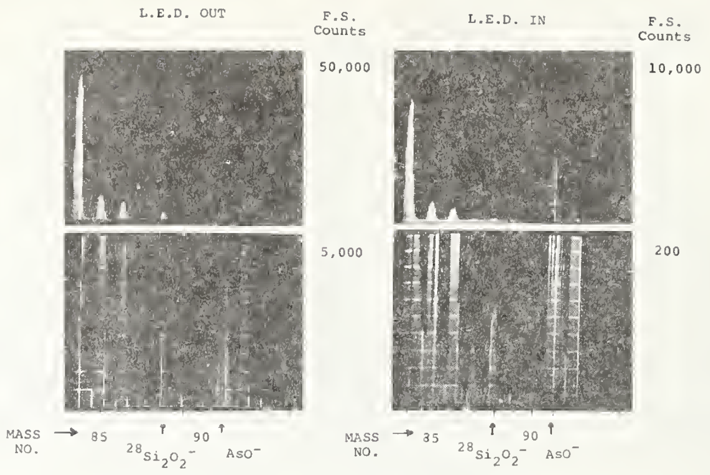

Figure 10. Attenuation of the $Si_2O_2^-$ interference with AsO^- using low energy discrimination.

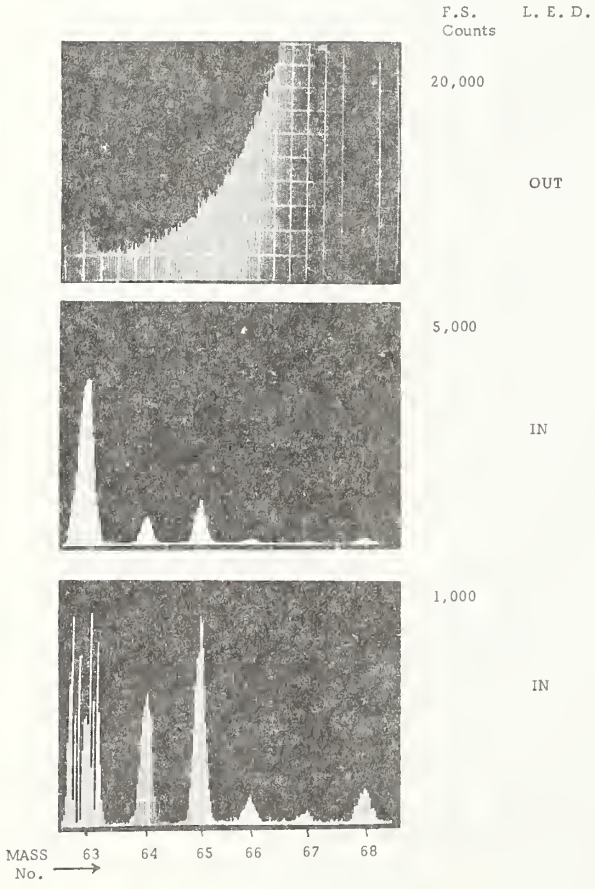

Figure 11. Attenuation of low energy tails from gallium in gallium arsenide interfering with the detection of copper and zinc.

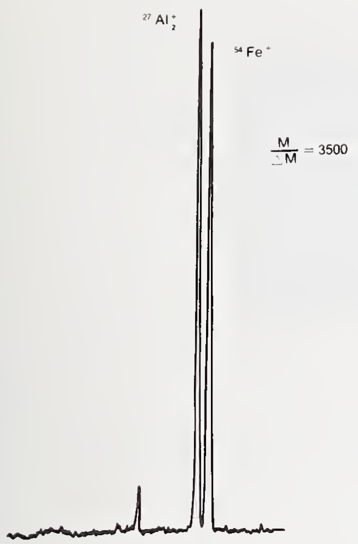

Figure 12. The separation of the aluminum dimer from the iron 54 isotope using high mass resolution.

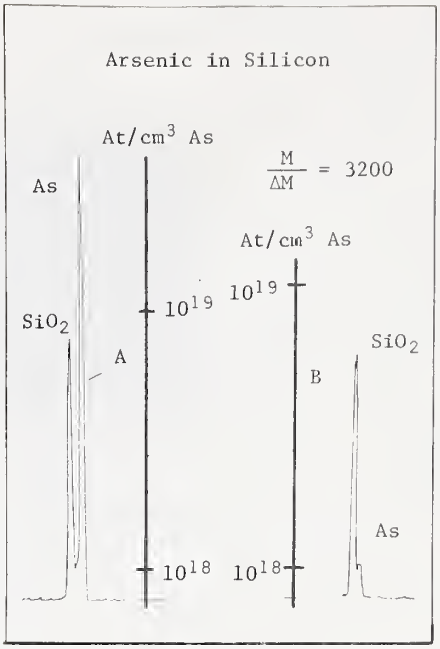

Figure 13. Separation of arsenic from SiO$_2$ at the peak and tail of an arsenic ion implantation profile.

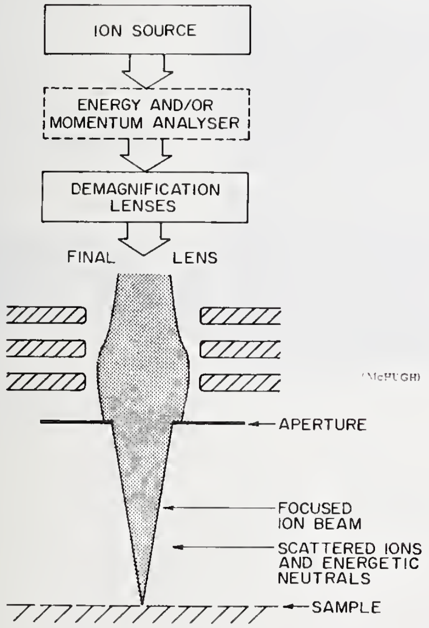

Figure 14. Schematic of neutral bombardment associated with an ion probe.

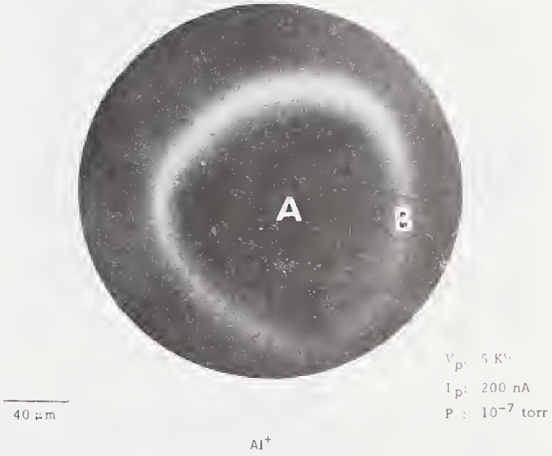

Figure 15. Enhancement of the aluminum ion yield at the periphery of an argon beam bombarding aluminum.

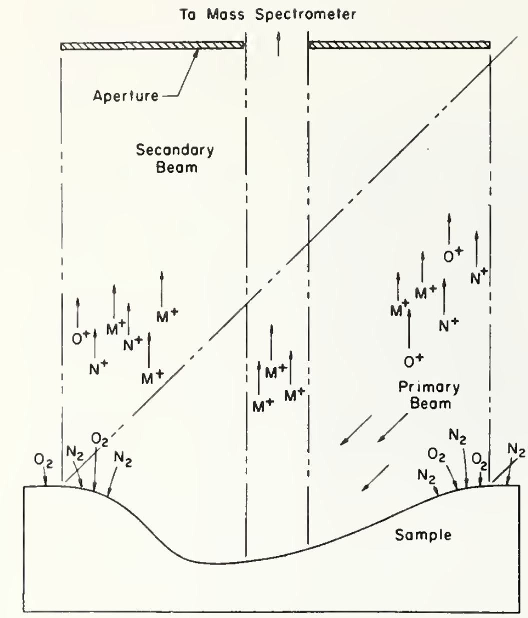

Figure 16. Mechanical aperturing in a secondary ion image plane to eliminate contributions from periphery of the ion probe and neutral bombardment.

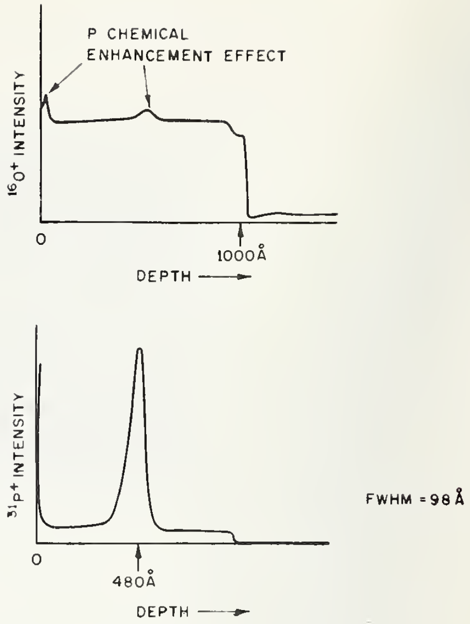

Figure 18. Phosphorous enhancement of tantalum signal in Ta_2O_5.

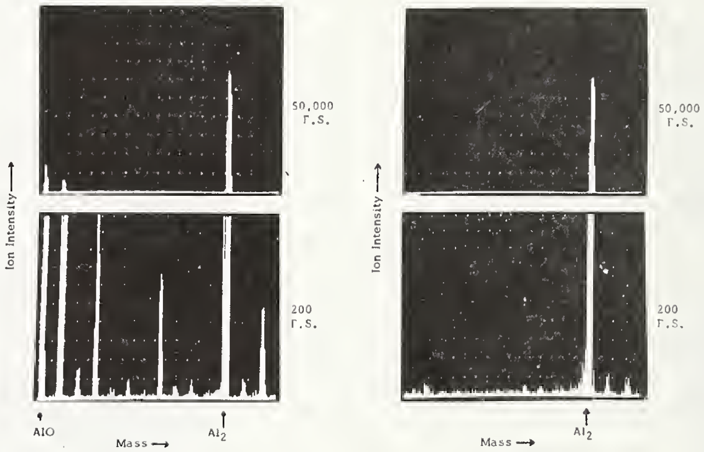

Periphery Center

Figure 17. Mass spectra for mass range 43 to 56 at periphery and center of primary beam probe on pure aluminum.

Pri: A^+ Sec: + P: 3×10^{-8} Torr

I_p : 8×10^{-8}A ϕ_A : 70 μm

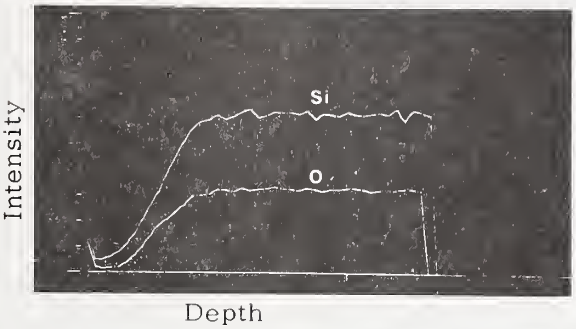

Figure 19. Depth profiles of silicon and oxygen in pure silicon bombarded with oxygen.

I_p: O^-, V_p: 15 kV, P: 10^{-17} Torr

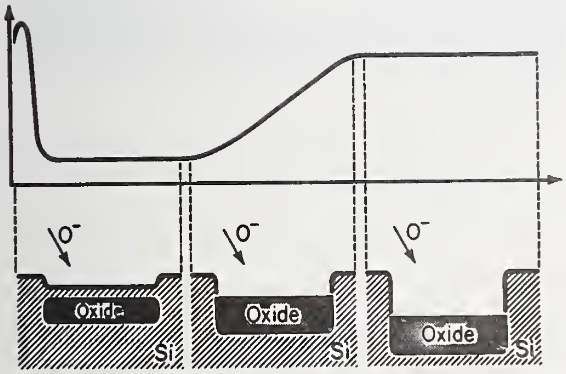

Figure 20. Primary oxygen beam implantation depth profile.

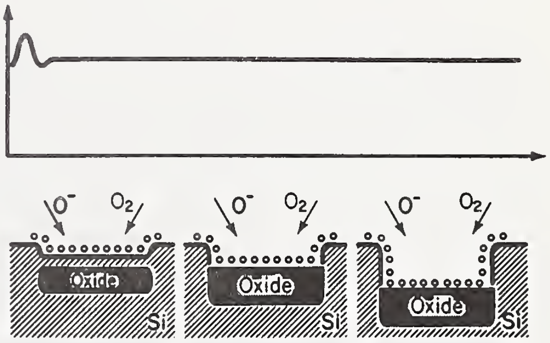

Figure 21. Primary oxygen beam implantation depth profile with oxygen leak.

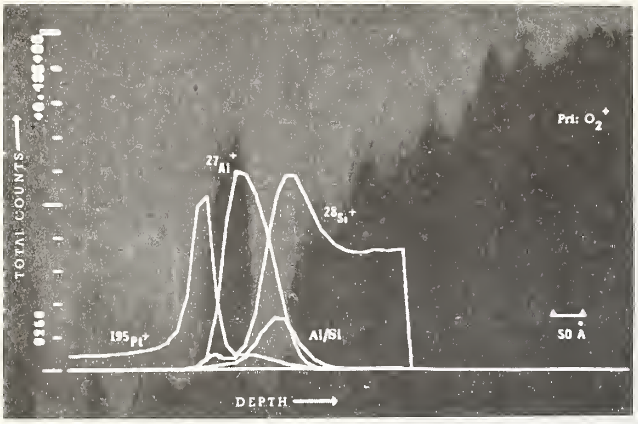

Figure 22. Depth profiles of platinum - aluminum thin films sputtered onto silicon.

Figure 23. Aluminum ion image of platinum - aluminum thin film sputtered onto silicon at Al/Si interface.

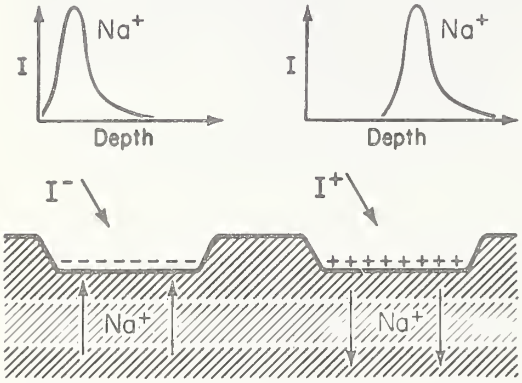

Figure 24. Schematic diagram of sodium redistribution in SiO_2 with applied fields.

DISCUSSION OF THE PAPER

Hurd: How does the SIMS profiling technique compare to other profiling techniques, such as NAA, spreading resistance, or the four point probe techniques?

Lewis: Actually I should probably refer you to one of the people who has used SIMS and those other techniques, Joe Tsai could tell you more.

Tsai: Our results show very good correlation as a matter of fact.

Morabito: Another point is that the SIMS technique can measure the electrically inactive as well as active species.

Lewis: The electrical techniques only measure the concentration of electrically active impurities whereas SIMS measures the actual chemical concentration. I should also say something about the speed of analysis. A typical SIMS profile can be obtained in a matter of minutes, but your spreading resistance measurement takes how long?

Participant: About a day or so.

Lewis: Right. So I think it is important to point this out. You can, in a day, do easily 40 or 50 SIMS depth profiles. While the high performance SIMS instruments are quite expensive, the speed of analysis also has to be taken in consideration. This is one thing I like to point out when SIMS analysis is compared to electron probe analysis. At the same concentration level SIMS can typically do analysis five to ten times faster. This can readily offset the difference in cost of these machines. The real interest to semiconductor people, however, is that SIMS has the sensitivity to detect the dopant concentration levels and I do not know of any other technique that does as well.

Harrington: You can also tell what the dopant species is, whether it is boron, or aluminum, or phosphorous. With the electrical techniques you are only guessing.

Lewis: Right, we are identifying the species and, as a matter of fact, we are correlating this information with other possible electrically or nonelectrically active species, so the information that you gather this way is considerably more useful.

DiStefano: What sort of total spatial resolution do you obtain with your SIMS technique?

Lewis: The depth resolution can be a few tens of angstroms if you are dealing with single crystal silicon. But there are many limiting effects. Usually we do not like to quote a depth resolution capability better than 10% of the depth sputtered because of sputtering artifacts. However, in silicon you are usually working with a very ideal situation and much better resolutions can be obtained.

DiStefano: If you sample a large area you could obtain a resolution of 10 Å, but for a smaller area you obviously would have to sample a greater depth. What combinations of sampled area and sampled depth are attainable?

Lewis: You must always take into consideration the amount of material sputtered and the ionization efficiency of the particular species you are looking at. As the area is made smaller and smaller you must sputter to greater depths to get enough ions to achieve an adequate precision. I am talking about a bulk analysis now. In a concentration gradient this does not really apply. The answer is that the lateral spatial resolution is about a half a micron in bulk analyses. However, this is not a practical area to use for a depth profile. A practical limit to depth resolution for a depth profile is a few tens of angstroms for an area 100 μm or so in diameter.

NBS Special Publication 400-23, ARPA/NBS Workshop IV, Surface Analysis for Silicon Devices,
held at NBS, Gaithersburg, Maryland, April 23-24, 1975 (Issued March 1976)

Qualitative Assessment of Ion Erosion Damage by Means of Electron Channeling Patterns

Dale E. Newbury

Analytical Chemistry Division
Institute for Materials Research
National Bureau of Standards
Washington, D. C. 20234

In secondary ion mass spectrometry (SIMS), the sample is bombarded with energetic ions, usually in the range 5 to 30 keV. These primary ions impart their energy to the atoms of the sample via inelastic processes, resulting in the sputtering of atoms lying at or near the surface. The ionized fraction of these sputtered atoms, the secondary ions, are then mass analyzed, forming the basis of this spectrometry.

Concomitant with the sputtering of atoms is the damage to the sample produced by the primary ion — solid interaction along the entire range of primary ions. Lattice defects such as vacancies and interstitials are created by the displacement of atoms from lattice sites due to energy imparted by the primary ion collisions. The effect of ion bombardment is to degrade the crystal perfection. Such degradation occurs in a shallow layer near the sample surface, the depth of which is governed by the range of the primary ions. Typically, this range will be of the order of 50 nm or less for the ions, for example, Ar^+, O_2^+, O^+, N_2^+, N^+, O^-, and the beam energies used in SIMS and other surface analysis techniques which make use of ion bombardment for erosion.[1]

Assessment of the damage induced by ion bombardment is possible by use of the electron channeling pattern technique in the scanning electron microscope (SEM).[2,3,4] Briefly, electron channeling contrast is obtained in SEM because of the influence of the periodic structure of a crystal on the initial electron-specimen interaction. The electron channeling pattern (ECP) is generated by varying the beam incidence angle relative to the crystal through the scanning action. The emitted or absorbed electron current varies depending on the angle between the beam and the crystal lattice. The information carried by electron channeling contrast is confined to a region within 50 nm of the surface since elastic scattering of the beam electrons rapidly randomizes and decollimates the beam with depth. Moreover, the ECP has been found to be sensitive to imperfections in the crystal.[5,6] ECP's can be obtained from areas of 10 μm diameter or less and, thus, the technique offers the possibility of assessing the crystal perfection of shallow layers with micrometer resolution.

In the present study, the ECP technique has been used to qualitatively assess the damage induced in a silicon crystal by the ion bombardment in an SIMS instrument. The ion bombardment conditions used were: $^{16}O^-$ primary ions, beam energy 18.5 keV, beam current 10 nA, beam astigmatically focused and scanned in an area 50 μm × 50 μm for 1000 seconds. The resulting eroded crater is shown in figure 1. A region of constant current density was obtained over most of the scanned area, as evidenced by the uniform erosion (figure 1, region I) observed by an optical interference pattern. An ion flux of $2.5 \times 10^{18}/cm^2$ passed through this region. The astigmatically focused beam produced a gradation in ion flux at the edge of the crater (figure 1, region II). ECP's were obtained from the original crystal surface, the region of limited ion bombardment (region II) and the center of the crater by translating the specimen under the beam. The ECP from the original surface, figure 2, shows the fine detail and strong line definition characteristic of highly perfect crystal. The ECP obtained from the region of limited ion bombardment, figure 3, with identical SEM operating conditions as those used to generate figure 2, is greatly degraded. The ECP from the center of the pit was totally lost, indicating that as far as the electron channeling effect is concerned, the specimen is amorphous.

Additional experiments are being carried out to relate ECP quality to the defect concentration. However, from the present qualitative comparison of an ion bombarded region with the original crystal, it is clear that ion erosion leaves behind a severely degraded surface layer. This fact must be considered when questions of solute mobility during analysis or of the physical nature of the region under analysis are important.

References

1. Carter, G., and Colligon, J. S., *Ion Bombardment of Solids*, pp. 151-156 (Elsevier, New York, 1968).

2. Booker, G. R., *Modern Diffraction and Imaging Techniques in Material Science*, Amelinckx, S., et al., ed., pp. 613-653 (North Holland Publishing Company, Amsterdam, The Netherlands, 1970).

3. Newbury, D. E. in SEM/1974, *Proceedings of the 7th Annual SEM Symposium*, Johari, O., ed., IITRI, Chicago, Illinois, 1974, pp. 1047-1054.

4. Goldstein, J. I., Yakowitz, H., Newbury, D. E., Lifshin, E., Colby, J., and Coleman, J., *Practical Scanning Electron Microscopy*, pp. 150-179 (Plenum Press, New York, 1975).

5. Schulson, E. M., van Essen, C. G., and Joy, D. C. in SEM/1969, *Proceedings of the 2nd Annual SEM Symposium*, Johari, O., ed., IITRI, Chicago, Illinois, 1969, pp. 47-55.

6. Wolf, E. D., and Hunsperger, R. G. in SEM/1970, *Proceedings of the 3rd Annual SEM Symposium*, Johari, O., ed., IITRI, Chicago, Illinois, 1970, pp. 457-463.

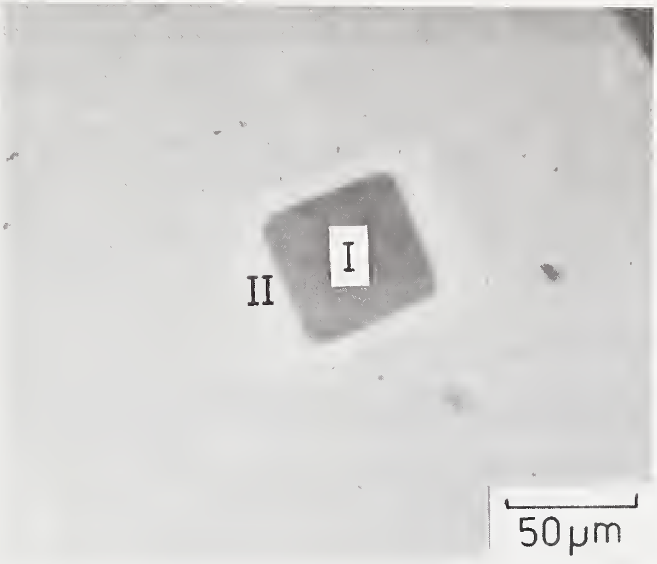

Figure 1. Optical micrograph of ion eroded crater. Region I is uniformly bombarded; Region II is lightly bombarded.

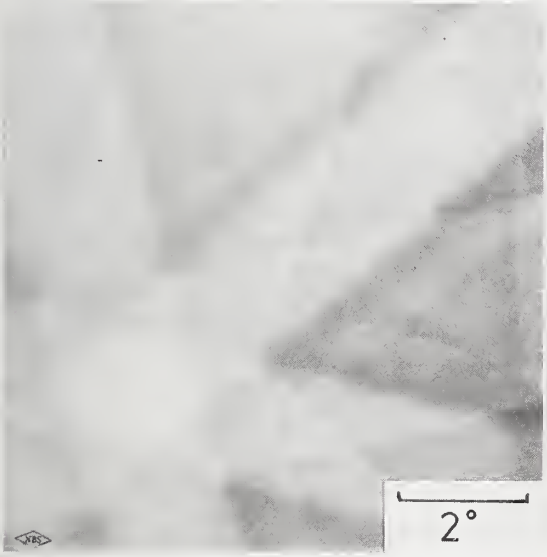

Figure 2. Electron channeling pattern obtained from original crystal surface prior to ion bombardment.

Figure 3. Electron channeling pattern from edge of crater region (Region II in figure 1).

NBS Special Publication 400-23, ARPA/NBS Workshop IV, Surface Analysis for Silicon Devices,
held at NBS, Gaithersburg, Maryland, April 23-24, 1975 (Issued March 1976)

THE EFFECT OF SPECIMEN COOLING ON THE MIGRATION OF SODIUM IN THIN FILM SiO_2

Bradway F. Phillips
Naval Weapons Support Center
Electron Optics Laboratory
Crane, Indiana 47522

Alfred E. Austin
Battelle Columbus Labs
Columbus, Ohio 43201

Harold L. Hughes
Naval Research Laboratory
Washington, D.C. 20375

INTRODUCTION

Being able to profile element concentration changes as a function of depth in thin film oxide structures, particularly SiO_2, is of vital concern to the understanding of MOS device characteristics. Early in the development of techniques to measure these element profiles directly using the ion probe, it was shown that both Na and K were mobilized by the primary ion beam while Al and P were essentially undisturbed by the charge built up in the thin SiO_2 film [1], [2], [3]. This discovery helped to explain how a number of widely varying results could be obtained on specimens which were supposedly identical in preparation since K and Na were moving through the SiO_2 films quite readily. This effect was causing Na and K surface contamination to show up at different points remote from the surface, particularly at the SiO_2 - Si interface.

EXPERIMENTAL CONCEPT

As a step toward providing better data on Na distributions in SiO_2 a number of possible experiments were proposed, including:
A. Use a primary ion beam with a low ionization potential compared to the O^-, O_2^+ or Ar^+ beam used regularly.
B. Increase or decrease the primary ion energy greatly compared to the nominal 5.5 keV O_2^+ or Ar^+ ions or 14.5 keV O^- ions used in the Cameca IMS 300.
C. Cool the specimen as near to liquid nitrogen temperatures as possible to slow down the "drift" of Na under the surface charge built up with ion bombardment.

It was felt that all of these experiments were important but that choice C was best suited to the study we wished to make. Therefore, a liquid nitrogen dewar and specimen holder were constructed to fit the specimen cooler port of the Cameca IMS 300. The specimen holder was designed to hold specimens 0.010 to 0.020 inch thick, 3/8 inch wide, and up to 1.5 inches long, and included a translation mechanism to go to any spot in a vertical line across these specimens. This allowed us to load three 3/8 inch square silicon slices, in addition to the copper grid pressed into aluminum for aligning the instrument and making sure the secondary ion optics were properly focussed. Specimen cooling rates and ultimate temperatures were measured several times, and the averaged temperature value obtained at the spot being analyzed was -180°C.

EXPERIMENTAL RESULTS AND ANALYSIS

As a reference to the work which lead to this study we see the results of profiling the Na distribution in SiO_2 at room temperature in figure 1, which was mentioned previously today in Bob Dobrott's talk and which is typical of analyses we were seeing in 1970, 1971, and early 1972. According to the predictions of the LSS theory we would expect the sodium to peak at 350 Å from the surface and obviously it is not doing that. Therefore, for our first room temperature and low temperature experiments we chose a series of specimens, which ranged from as-grown oxides to samples containing several levels of aluminum implantation and residual sodium. Results of these analyses are presented in table 1. First, we have an as-grown oxide analyzed at -180°C, in which 27% of the sodium concentrated at the SiO_2-Si interface; then at room temperature, where 70% of the sodium concentrated at the interface. The remainder of the specimens are aluminum implantations performed at 20 and 25 keV ranging in three steps from 4×10^{15} to 6.8×10^{12} atoms per square centimeter total dose. As we can see with the lower implant dose, NRR 371, we have at -180°C the smallest amount of sodium (32%) moving to the SiO_2-Si interface of this group of specimens. However, as we go to the higher dose specimen, NRR 372, 45% of the sodium moves and at the much higher dose, NRR 437, 46% of the sodium moves, where at room temperature these values are 75, 88, and 90% respectively. So we can see that there is a definite effect produced by using the low temperature specimen holder. As an example of the profiles obtained, figure 2 shows the results of analyzing an as-grown oxide at room temperature. The silicon secondary ion yield changes by several orders of magnitude as the interface is penetrated. At all points in the specimen except at the SiO_2-Si interface the sodium profile shows a count rate which is essentially at the background noise level of the instrument.

In figure 3 we see the results of cooling the same specimen to -180°C and this analysis demonstrates that the drift of sodium is retarded. The instrumental conditions were kept exactly the same in both cases. Here we see that when the specimen is cooled the sodium does not move rapidly to the SiO_2-Si interface during analysis, but is retarded; in fact, the sodium concentration is two orders of magnitude higher throughout the oxide in the spot analyzed on the cooled specimen than it is in the spot analyzed at room temperature. Although this technique does not yet give the true sodium profile, it does give some encouragement to continue on this path of analysis, and table 2 describes the next set of specimens which were prepared. The first specimen, JR1C, the as-grown oxide control sample, was cut up and used as a base material for all of the sodium ion implants which ranged from 3.2×10^{14} to 1.4×10^{15} atoms per square centimeter total dose; some of which were annealed at 200 or 900°C. The results obtained on these samples are tabulated in table 3. In specimen JR1C analyzed at 25°C with the O^- beam, 100% of the sodium appears at the surface of the oxide; at -180°C with the O^- beam, 97.5% of the sodium appears at the surface. Therefore, we see that in the control specimen essentially all of the sodium is present at the surface of the oxide as contamination. The next experiment on JR1C using the O_2^+ beam demonstrates that we still have a fair amount of the sodium mobilized both at 25°C and at -180°C. At 25°C, 10% of the sodium is at the surface and 89% is at the SiO_2-Si interface. Going to -180°C on the same sample, we see that 54% is on the surface of the oxide, 26% at the interface, and 20% is included within the bulk oxide. So we have retarded the movement of the sodium although we do not feel that we have a perfect profile yet. Working with specimen JR1A1, which was implanted to 3.2×10^{14} atoms per centimeter and annealed at 200°C, we see that there is a very small amount of the sodium at the surface in both the -180°C and the 25°C specimens. Most of the sodium has gone to the interface. We interpret this as being caused primarily by the ion induced channels from the implantation process and by the fact that the 200°C treatment does not anneal out these channels. We still have an inducement for the sodium to move, even though we have cooled the sample. JR1A2 has been annealed at 900°C for 30 minutes, and in this case we see at -180°C that 29% of the sodium is on the surface. 65% is at the interface. Essentially the same appearance was seen at 25°C, showing that there must have been some prior movement of the sodium at room temperature and then at 900 or 200°C before we did the analyses.

In order to show the differences a little bit more clearly we have made up differential plots between the work done at room temperature and the work done at low temperature. Figure 4 shows the results obtained with a differential plot of JR1C, our control specimen. This plot demonstrates that cooling holds some Na at the surface of the SiO_2, retards its diffusion through the SiO_2, and greatly reduces the pileup at the SiO_2-Si interface. In figure 5 we are looking at the JR1A1, which is an implanted and low temperature-annealed sample. We see that there is a sizeable portion of the sodium present which is retained at the surface by cooling the specimen during analysis.

In the sodium profile through the sample there is a large decrease in the peak right before going into the silicon substrate and some reproducible small peaks as you sputter into the silicon itself that must be caused by interface states and the differences in sodium activity between 25°C and -180°C. In figure 6 we are looking at the differential plot of JR1A2, which was annealed at 900°C for 30 minutes. Here we see somewhat the same results as with JR1A1 except that there is a wide peak of the sodium at the surface compared to the specimen analyzed at room temperature and a very deep valley when we get close to the interface. The integrated sodium intensities of the two JR1A2 specimens were 26,000 and 29,800 counts, compared to 54,000 and 44,000 for the JR1A1 specimens. This difference may be due to the loss of sodium from the surface during the high temperature annealing process. Such loss caused by diffusion of sodium to the surface and partial escape into the furnace atmosphere would also account for the increased surface concentrations of sodium in the JR1A2 specimens, 22 to 29% compared to 6 to 7% of the JR1A1 specimens. That the sodium concentration at the surfaces of the JR1A1 specimens is lower than would be expected for the shallow 200 A range suggests that the sodium ions may be driven into the SiO_2-Si interface by surface charging during the ion implantation.

A run on the JR1A1 specimen with O^- primary beam at -180°C showed a high but continuously decreasing sodium concentration through the oxide, and no sodium at the SiO_2-Si interface. As with the control, the high-energy O^- beam apparently makes the sodium more mobile in the oxide. We see in our third example, JR1A2, a fairly uniform distribution of the sodium throughout the SiO_2, with the peak reduced at the interface and a peak showing at the surface. Therefore, we can conclude that when a specimen which has little implantation damage is analyzed at -180°C, we can get a much better profile of the sodium which we would say does exist on the surface of the SiO_2 as contamination from the growth technique, and throughout the oxide from the implantation, than we can at room temperature.

SUMMARY

In summary the following points have been established.

1. A liquid nitrogen-cooled specimen holder was fabricated for a Cameca IMS 300.

2. Cooling thin-film SiO_2 specimens does retard the diffusion of Na during ion probe analyses.

Although it does not give a perfect profile, such cooling is a step in the direction of attaining sodium profiles that are reproducible and real.

3. The interactions of primary beam energy and species, ion implantation dose and energy, annealing temperature, and a variety of other factors not yet known, combine to affect the Na profiles obtained and to improve or degrade the benefits of cooling the specimens.

ACKNOWLEDGEMENTS

We would like to acknowledge the contributions of Mr. Ronald Baxter of Leeds and Northrop Company, North Wales, Pennsylvania in the design and initiation of these experiments, and the sponsorship of the Defense Nuclear Agency under subtask Z99QAXTD033, work unit 51, work unit title, "Radiation Resistant MOS Technology," technical monitor, Mr. H. L. Hughes, of the U. S. Naval Research Laboratory.

REFERENCES

1. H. L. Hughes, R. D. Baxter, and B. F. Phillips, *IEEE Trans. Nuc. Sci.* NS-19, 256 (1972).

2. D. V. McCaughan, and V. T. Murphy, *IEEE Trans. Nuc. Sci.* NS-19, 249 (1972).

3. R. D. Baxter, *Investigation of Thermally Grown SiO_2 by Ion Microanalysis,* Battelle Memorial Institute (1971).

TABLE 1

Na DISTRIBUTIONS AT -180°C VS 25°C[(a)]

Specimen	Ion Implantation	% Na at SiO_2/Si Interface -180 C	% Na at SiO_2/Si Interface 25 C
NRL-434	None	27	70
NRL-436	25 keV Al to 4×10^{15} cm^{-2}	46	90
NRL-371	20 keV Al to 6.8×10^{12} cm^{-2}	32	75
NRL-372	20 keV Al to 5×10^{13} cm^{-2}	45	88

(a) Sputtering by O_2^+ primary beam

TABLE 2

SPECIMENS FOR Na DISTRIBUTION MEASUREMENT AT BOTH 25°C AND -180°C

1) JRIC - as grown

2) JR1A1 - Implant 10 keV Na^{23} to 3.2×10^{14} cm^{-2} annealed 200 C 30 minutes

3) JR1A2 - Implant 10 keV Na^{23} to 3.2×10^{14} cm^{-2} annealed 900 C 30 minutes

4) JR1B1 - Implant 30 keV Na^{23} to 1.0×10^{15} cm^{-2} annealed 200 C 30 minutes

5) JR1B2 - Implant 30 keV Na^{23} to 1.0×10^{15} cm^{-2} annealed 900 C 30 minutes

TABLE 3

Na DISTRIBUTIONS AT -180 C VS 25 C

Specimen	Temp. C	Primary Beam	Percent of Na in			Si
			Surface of Oxide	Bulk Oxide	SiO_2/Si (interface)	
JR1C	25	O^-	100			
JR1C	-180	O^-	97.5			
JR1C	25	O_2^+	10.7	0.23	89	
JR1C	-180	O_2^+	54	20	26	
JR1A1	25	O_2^+	7.2	2.3	90.5	
JR1A1	-180	O_2^+	6	24	70	
JR1A2	25	O_2^+	22	1	77	
JR1A2	-180	O_2^+	29	6	65	
JR1B1	25	O_2^+	5	6	74	15
JR1B1	-180	O_2^+	3	64	26	7
JR1B2	25	O_2^+	21	4	74	1
JR1B2	-180	O_2^+	25	40	34	1

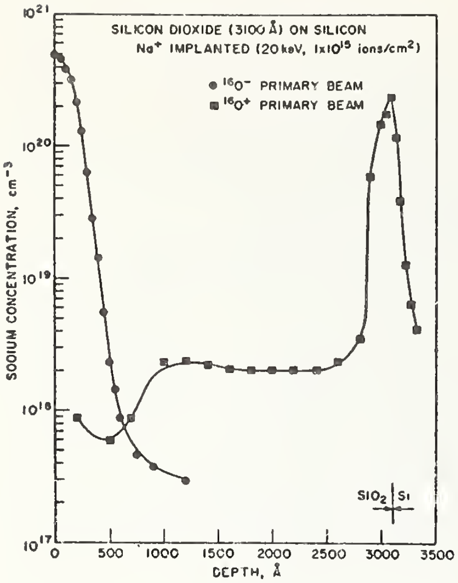

Figure 1. Sodium profiles of a sodium - implanted silicon dioxide film for both $^{16}O^+$ and $^{16}O^-$.

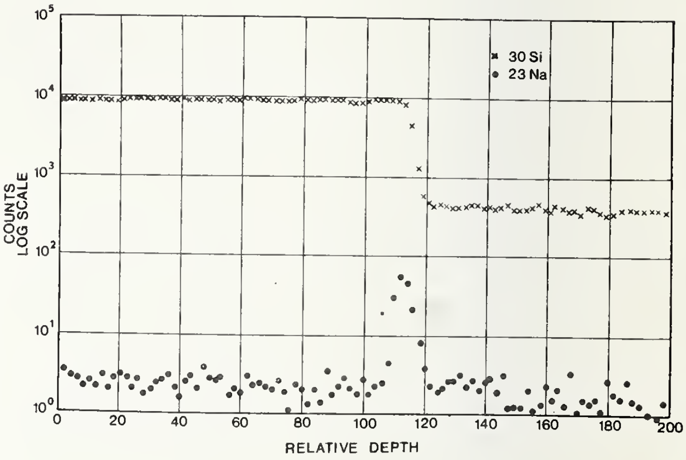

Figure 2. Sodium profile at 25°C of an as-grown oxide.

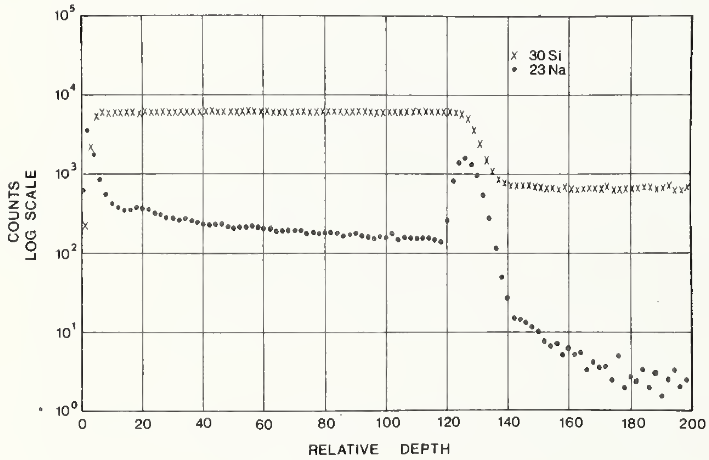

Figure 3. Sodium profile at -180°C of the same specimen as in figure 2.

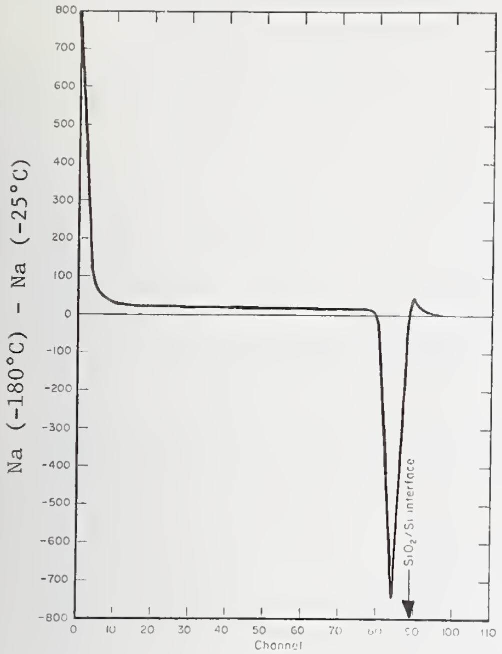

Figure 4. Plot of Na (-180°C) - Na (25°C) distribution in JR1C.

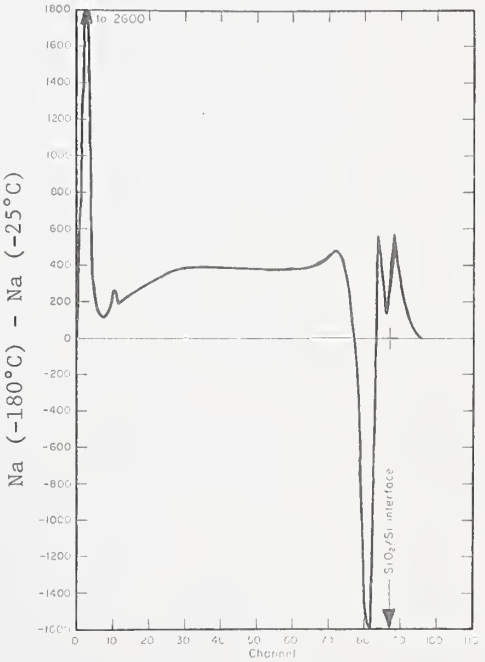

Figure 5. Plot of Na (-180°C) - Na (25°C) distribution in JR1A1.

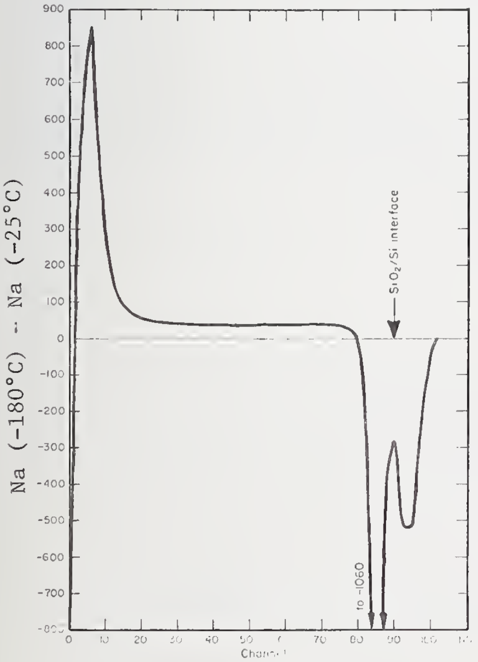

Figure 6. Plot of Na (-180°C) - Na (25°C) distribution in JR1A2.

DISCUSSION OF THE PAPER

Participant: What was your primary beam current density?

Phillips: The primary ion beam intensity was approximately 250 nanoamps rastered out to cover an 800 micron square.

Cock: For one of your samples you postulated that the sodium motion was enhanced by dislocations. Would you could elaborate on that model.

Phillips: I would say that at the 200°C anneal, you have not removed the channels that are caused by the ion implantation process itself. At the 900°C anneal you have removed some of the channels but you have also mobilized the sodium. Data, which we did not present today, using the picture mode in the Cameca IMS 300 to study the location of the sodium after a 200°C anneal and after a 900°C anneal shows the difference. At 900°C you have mobilized the sodium and you actually have it diffusing back through the channels to the surface and escaping into the furnace atmosphere, making your total sodium content in the entire oxide half as large as it is with the 200°C anneal.

Cock: I see, so this is a dislocation in the oxide structure.

Phillips: Yes. If you implant sodium to a high enough intensity in the oxide structure, somewhere around 1 x 10^{15} atoms per square centimeter, you can provide a state in the SiO_2 which is of such a high energy that the silicon and sodium, - in fact, all ions - coming off the specimen from a section extending from the surface to close to the depth at which the maximum of the implantation peak should occur, are of such a high energy compared to the secondary ion band pass of the instrument that you do not see any secondary ions. So you know that you are producing an extremely strained state in the SiO_2 film that does shift even your secondary-ion energy distribution.

Participant: The temperature of 180°C that you quote is, I gather, a bulk sample temperature.

Phillips: That is correct. The microtemperature at the sputtering spot has not been determined. The temperature at which the sputtering actually takes place, or the plasma in which the ions are produced, would be significant for the theory devised by Dr. C. A. Andersen. The bulk temperature has been determined to be 180°C.

Participant: Although the temperature at the sputtering location has not been determined do you have any idea of approximately how large of a difference you might expect?

Phillips: Well, in the plasma itself, or at the place at which the sputtering is occurring, the temperature is several thousands of degree Kelvin.

Evans: You are talking of the plasma or electronic temperature, not the thermal temperature. The thermal rise at the surface due to ion bombardment is only of the order of 5 to 50°C above the bulk sample temperature. The plasma "temperatures" are thermal spikes: they last the order of 10^{-12} seconds; they are not a temperature in the true sense, they are an electronic temperature.

Phillips: The temperature rise is extremely small because we are dealing with a fairly heat-conductive medium, silicon, and a fairly thin film of SiO_2 with a massive heat sink compared to the size of the sample. So I would say that even going through the SiO_2 there would be an extremely small temperature rise in the local area surrounding the sputtering; of the order of a few degrees at the most.

NBS Special Publication 400-23, ARPA/NBS Workshop IV, Surface Analysis for Silicon Devices,
held at NBS, Gaithersburg, Maryland, April 23-24, 1975 (Issued March 1976)

SILICON-ON-SAPPHIRE IMPURITY ANALYSIS*

D. Howard Phillips

Electronics Research Division
Rockwell International Corporation
Anaheim, California 92803

INTRODUCTION

The presence of undesirable impurities had detrimental effects on both the electrical and radiation performance of silicon-on-sapphire (SOS) integrated circuits. Conversely, device electrical and radiation characteristics can be improved by minimizing the number and types of impurities in SOS films.

Ion microprobe mass analysis (IMMA) techniques are being utilized for impurity analyses in a program associated with the development of a radiation-hardened CMOS/SOS (complementary MOS on sapphire) technology. From an applications point of view, four goals have been established for this program. The first is to improve lot-to-lot repeatability; the second is to improve wafer-to-wafer repeatability; the third is to improve the electrical stability of the devices (i.e., the bias-temperature stability of threshold voltage); and the fourth is to improve the radiation stability of the devices.

IMPURITY SOURCES

One source of contaminants is the sapphire substrate. Impurities are sometimes added during the growth process to minimize crystal defects such as twinning.

A second source of impurities is the epitaxial film itself. During the epitaxial film growth process, impurities come from silane, hydrogen carrier gas, and dopant gases.

A potential major source of impurities is the processing steps that are used during the wafer fabrication process.

MASS-ANALYSIS SILICON IMPURITY DATA

Figure 1 shows recent data comparing silicon-on-sapphire films with an epitaxial silicon layer on bulk silicon. The shaded areas indicate the impurity concentration measured in silicon films on a sapphire substrate grown using the Czochralski process. The unshaded lines on the bar graph indicate the impurity concentrations that were measured on epitaxial films grown on bulk silicon. The data are plotted as a function of elemental impurities versus the relative concentration, where each increment on the horizontal axis indicates an order-of-magnitude change in impurity concentration.

These data show that aluminum concentrations in silicon-on-sapphire are orders of magnitude greater than aluminum concentrations in bulk silicon. In the case of sapphire (Al_2O_3), there is more aluminum present in the system to act as a potential contaminant, either from top-side diffusion or from backside diffusion out of the sapphire substrate.

Another very important observation from these data is a consideration of sodium content. Sodium and potassium are known sources of electrical instability in MOS transistors. Compared to bulk silicon, typical silicon on sapphire contains much higher sodium concentrations. The data in Figure 1 show very little difference between silicon-on-sapphire epitaxial films and bulk silicon epitaxial films, in terms of potassium impurity concentration.

DIFFUSION PROFILES IN SILICON ON SAPPHIRE

IMMA analysis techniques are being used in the analysis of intentional dopants. Figure 2 shows phosphorous concentration as a function of diffusion drive-in time. The drive-in time at 1,000 degrees centigrate was varied from 0 to 15, 30, 60 and 80 minutes. Initially (at T = 0), phosphorous was concentrated close to the surface. Following high-temperature processing, the profiles changed as shown in Figure 2. We typically use silicon-on-sapphire material with a silicon epitaxial thickness in the range from 0.8 to 1.0 micron. For typical wafer-processing thermal cycles, phosphorous diffuses completely through the silicon-on-sapphire film. The diffusion coefficient in sapphire is very low and phosphorous does not diffuse through the silicon-sapphire interface. The sapphire interface acts as a diffusion stop causing phosphorous to remain in the silicon film.

---

* Partially sponsored by USAF/AFCRL (Contract F19628-75-C-0108) and by Rockwell International Corporation (IR&D).

MASS ANALYSIS DATA ACQUISITION

Figure 3 illustrates the instrument used to obtain impurity data presented in Figures 1 and 2. The ion microprobe mass analyzer generates an ionized beam that is swept electrostatically both in the Y direction and the X direction in much the same manner that a TV raster is generated. The ion source is allowed to impinge on the sample of interest. Beam diameters can be adjusted from 2 microns to 500 microns. The rate at which the surface is eroded depends on several experimental factors, i.e., the ion source, the intensity of the ion beam, the energy of the ion beam and the nature of the sample that is being analyzed. Erosion rates vary over a range from less than one angstrom per second up to 1000 angstroms per second. The secondary ions are analyzed electrostatically (momentum) and magnetically (mass-to-charge ratio). The ions impinge on a target where an electron beam is produced. The electron beam generates light in the scintillator, and this light is coupled to a photomultiplier tube. The signals from the photomultiplier tube can be recorded and displayed in several ways. One way is to record them on a CRT which utilizes the signal from the photomultiplier tube for Z axis modulation. CRT Y and X signals are derived from the waveforms used to deflect the primary ion beam. Data can also be recorded on a strip-chart recorder by using the signal from the photomultiplier tube to modulate the Y axis of the recorder. Data can be recorded by using a scaler to count pulses from the photomultiplier tube. Data can be recorded in the MHz range without significant data loss due to scaler dead time.

SPECTROCHEMICAL-ANALYSIS SAPPHIRE IMPURITY DATA

Table I lists data showing impurity levels in the sapphire substrate, rather than the silicon film. These data were obtained using spectrochemical analysis techniques rather than the ion microprobe mass analysis technique just described. These data were obtained by using Crystal Systems sapphire which was grown using the gradient furnace technique. The gradient furnace technique is one of three techniques that is used commercially to grow sapphire crystals that can be used to fabricate silicon-on-sapphire integrated circuits. Table I compares pre-1971 sapphire impurity data with data for the improved process that is being used at this time by Crystal Systems in the growth of gradient furnace sapphire. The number of impurities present to a significant extent are greater for the improved process, but the impurity concentrations, in general, are much less than for the sapphire-growth process used by Crystal Systems prior to 1971.

MATERIAL COMPARISON AND DATA CORRELATION

Considering the different analysis techniques that have been used to analyze both sapphire and silicon films, data correlation is needed. Figure 4 indicates some of the work that is being done to correlate the data that have been accumulated. Data are being obtained for three types of sapphire substrates—Czochralski-grown sapphire substrates fabricated by Union Carbide, ribbon sapphire substrates fabricated by Tyco, and gradient-furnace sapphire substrates fabricated by Crystal Systems. These sapphire substrate growth techniques are quite different, and preliminary indications are that the impurity concentrations are quite different for these three techniques.

Figure 4 describes a correlation study that is being performed as a cooperative effort with NBS and Rockwell participating in the data acquisition activities. This study includes the analysis of silicon-on-sapphire wafers from three sources. Each wafer will be divided into halves. One-half of the sapphire wafer will be analyzed using the flame emission spectrometry techniques in use at the National Bureau of Standards. The other half of the wafer will be analyzed by Rockwell using the ARL-IMMA analysis technique. An attempt will be made to correlate the results of these two measurement methods with the objective of learning more about the sapphire substrates and the silicon epitaxial films, and using that information in our attempts to improve the material characteristics and the device electrical and radiation characteristics. Wafers from the same lot will be used in integrated circuit fabrication. These integrated circuits will be characterized to determine the electrical characteristics and the radiation performance of SOS integrated-circuit devices. The data from the integrated circuit fabrication and test activities will also be correlated with the analysis of the SOS starting material using the flame emission spectrometry and IMMA analysis techniques. At the same time, we have other silicon-on-sapphire integrated-circuit fabrication and characterization programs that are continually providing additional data that can be used for correlation.

SUMMARY AND CONCLUSIONS

Unintentional impurities in silicon-on-sapphire films and substrates are relatively high, based on mass analysis data. Concentrations of the unintentional impurities are equal to, or greater than, the dopant concentration of the most lightly doped region of the semiconductor.

There is a significant difference between the impurity concentrations in typical SOS devices or SOS wafers as compared to bulk silicon wafers.

Preliminary data indicate that there is a good deal of impurity-concentration variability depending upon the sapphire source and the sapphire growth technique. In addition, considerable lot-to-lot and wafer-to-wafer variability has been observed in silicon films and has been attributed to growth conditions and device fabrication methods, as well as impurity concentration variations.

TABLE 1

SPECTROCHEMICAL ANALYSIS
CRYSTAL SYSTEMS SAPPHIRE DATA

GRADIENT-FURNACE SAPPHIRE

IMPROVED PROCESS (1971-1975)

Element	Concentration (ppm)	Element	Concentration (ppm)
Cr	0.4	N	3
Cu	2	F	0.3
Fe	B	Na	3
Mg	0.3	P	0.05
Mo	1	K	3
Ti	0.3	Ca	0.7
Y	0.5	V	0.04
Sc	4	Mn	0.7
Ce	6	Ni	0.2
B	0.02	Zn	0.6

Nominal detection limit = 0.05 ppma.

EARLY PROCESS (PRE-1971)

ELEMENT	CONCENTRATION (ppm)
Cr	1
Cu	10
Fe	1
Mg	1
Mo	10-100
Pb	1
Si	10-100
Ti	10-100

Elements sought and not detected (<0.05 ppma):
Ag, As, Au, B, Ba, Be, Bi, Ca, Cd, Co, Ga, Ge, Hf, Hg, In, Ir,K, Li, Mn, Na, Nb,Ni, Ds, P, Pd, Pt, Rb, Re, Rh, Ru, Sb, Sn, Sr, Ta, Te, Ti, V, W, Zn, Zr.

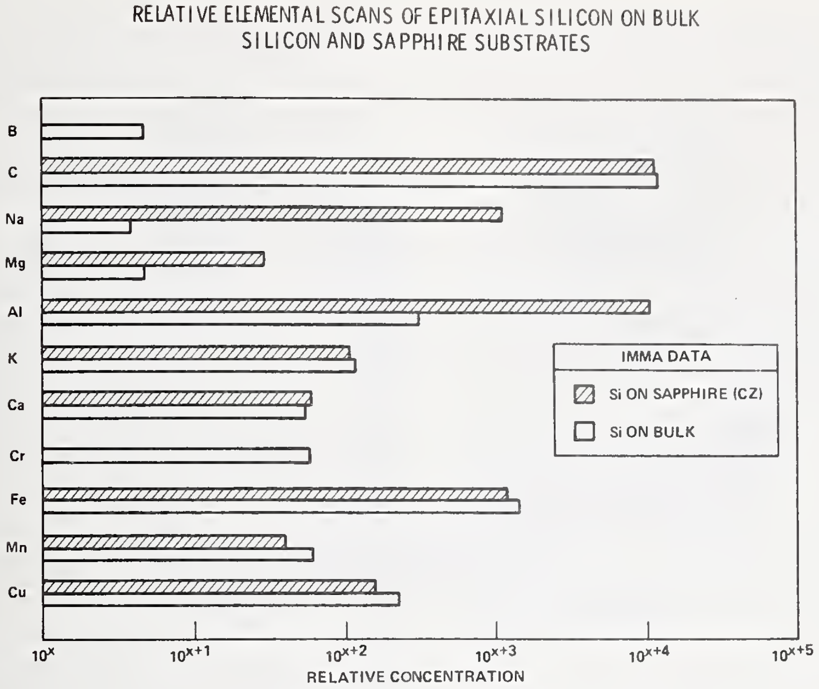
RELATIVE ELEMENTAL SCANS OF EPITAXIAL SILICON ON BULK SILICON AND SAPPHIRE SUBSTRATES

Figure 1. Relative elemental scans of epitaxial silicon on bulk silicon and sapphire substrates.

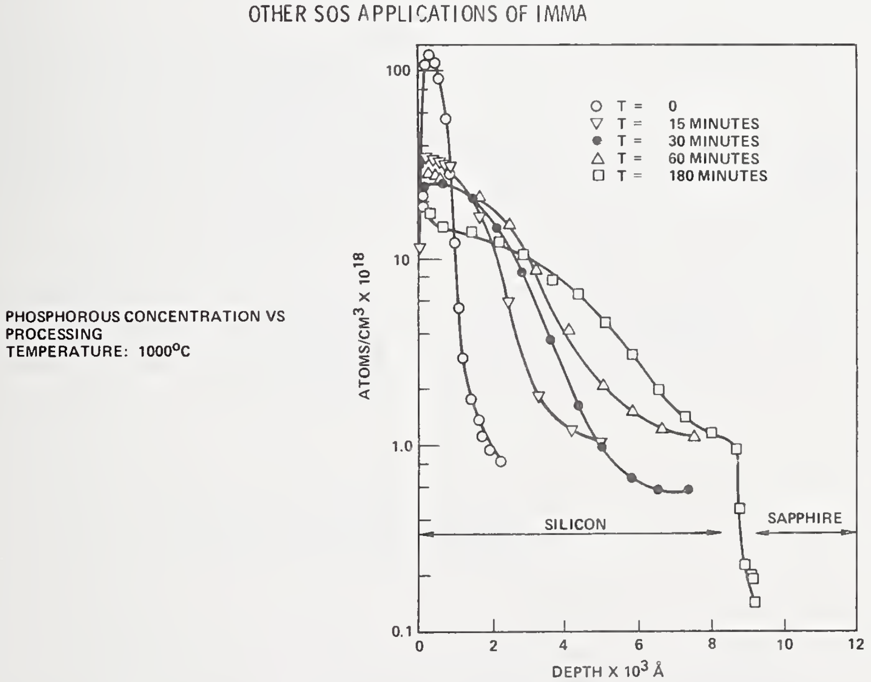
OTHER SOS APPLICATIONS OF IMMA

PHOSPHOROUS CONCENTRATION VS PROCESSING TEMPERATURE: 1000°C

Figure 2. Phosphorous diffusion profiles in silicon on sapphire.

ION MICROPROBE MASS ANALYZER (IMMA)

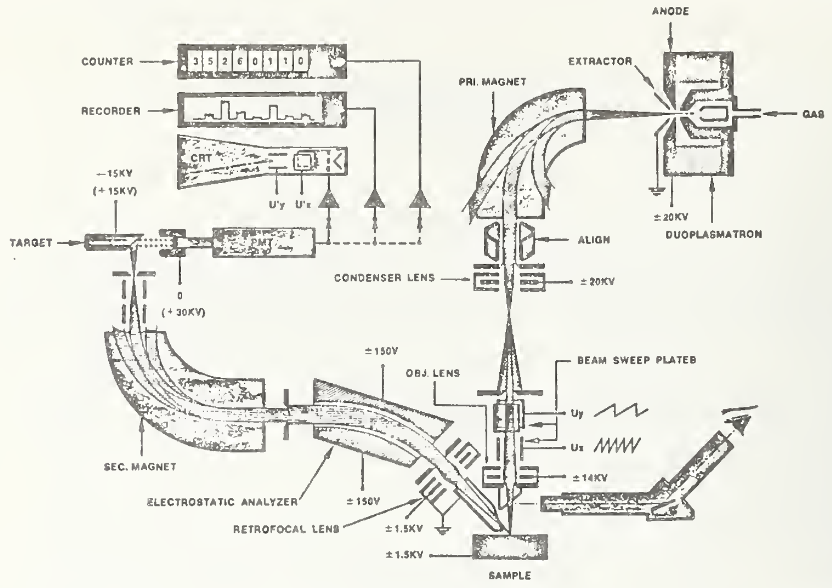

Figure 3. Ion microprobe mass analyzer (IMMA).

CORRELATION

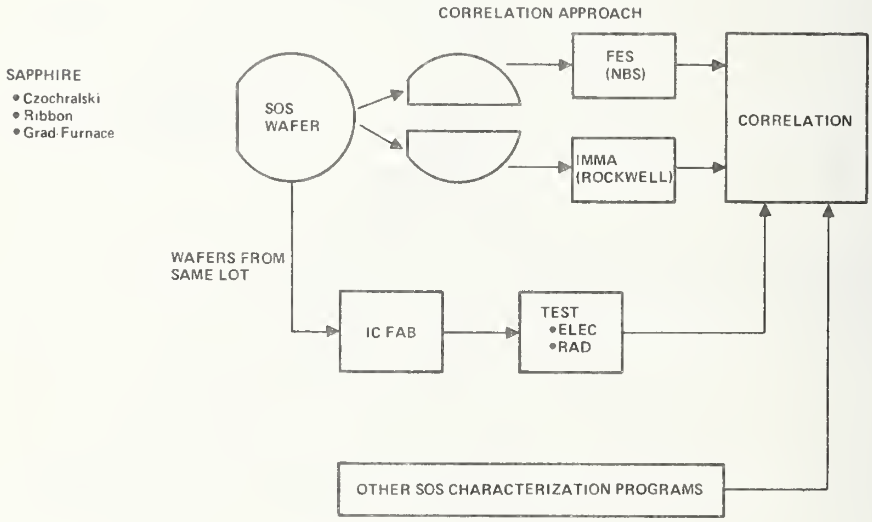

Figure 4. Material comparison and data correlation.

DISCUSSION OF THE PAPER

Participant: I have a comment and a question. Without having seen your original spectrum of the epitaxial silicon/bulk silicon composite, what I suggest is that your detection of species such as chromium, manganese, iron and copper may in reality be the following: at mass 52, since you have a large carbon peak, it could be SiC_2^+; at mass 55 instead of manganese you may have AlSi; at mass 56 you may have Si_2, and since you have a large sodium peak this may not be out of the question, and at mass 63, 65 the polyatomic peak SiCl. Now if your energy bandwidth is broad, you are going to be in trouble with polyatomic species, and therefore I suggest you look once again to the possibility of interferences.

The question is the following: In the profiling of phosphorus and silicon how do you discriminate between SiH at mass 31 and ^{31}P especially at low concentrations?

Phillips: Your comments are well taken. Although I cannot give you a comprehensive answer to your question, the need for correlation experiments is recognized. As I indicated, mass analysis impurity data are being correlated with impurity data from flame emission spectroscopy measurements.

Morabito: If you did not have this chemical technique you would not know from the SIMS technique what these impurities are because of these mass resolution problems. Although we have looked at phosphorus and silicon and it is not impossible to resolve SiH^+ from P^+. The technique there is to look at the PO^- species.

Dobrott: I have a few comments on applications with the IMMA. At that phosphorus level the SiH is nearly completely absent from the spectra provided the coldplate was run to gather most of the water. The SiH will not get you into trouble until you get much below the $10^{17}/cm^3$ region for phosphorus. The mass 52 which you identified as Cr could be SiC_2, however if that were the case you would see a much stronger mass 40 peak and also the mass 50 peak of Cr would be absent. You are probably perfectly right that mass 56 corresponds to iron because if you had much Al you would mask the iron 54. However, again, the intensity of molecular species is down considerably from what the monotonic species is, so you could get some feel of iron. Now when it comes to the copper of mass 63 and 65, it is true that silicon 28, together with chlorine 35 and 37 would dominate at 63 and 65, and unfortunately as nature would have it, the isotope ratio is about the same as what you would expect for copper. But it is unbelievable to me that he could take an epitaxial grown silicon and have enough chlorine incorporated into it that it would combine with the silicon and still come out to anything detectable by the IMMA.

The only other comment that I have is more or less a question. It was stated that the concentration level of anything which was not detected was below 0.05 ppma. I do not believe that this value is quite correct since a considerable number of noble ions were present. I would say the correct value that I would put on that with confidence is less than 10 parts per million unless you did specific long term counting on those particular ions.

Phillips: One comment on chromium and titanium. Often times those two elements are intentionally added to the melt during sapphire growth for the purpose of minimizing the number of defects in the crystal as it is grown. It has been experimentally observed that the number of twins per unit volume can be reduced if either or both of those two elements are added in reasonably large trace quantities.

NBS Special Publication 400-23, ARPA/NBS Workshop IV, Surface Analysis for Silicon Devices,
held at NBS, Gaithersburg, Maryland, April 23-24, 1975 (Issued March 1976)

SURFACE COMPOSITION BY ANALYSIS OF IMPACT RADIATION

Clark W. White
Bell Laboratories
Murray Hill, New Jersey 07974

Several speakers at this conference will discuss analysis techniques that are based on phenomena that occur when the low energy ions impact on solids. These include the techniques of low energy ion backscattering and secondary ion mass analysis, both of which utilize beams of low energy ions to bombard the surface of interest. In addition to the backscattering of the ion projectile and the secondary emission of positive and negative ions, one also observes the production of intense optical radiation in the low energy particle-solid collision process. In collaboration with Norman Tolk and Douglas Simms, we have been studying the radiation that is produced in collisions of low energy ions and neutral atoms with solids. These studies give fundamental information on the low energy particle-solid collision phenomena and at the same time provides us with the basis for a sensitive technique to identify the constituents of the surface and near surface regions. The radiation that will be discussed is produced as a result of the sputtering process and, therefore, if sputtering is being used for any purpose these optical signals and the optical information can then be used to serve as a monitor for the sputtering process.

Figure 1 schematically illustrates the type of experimental apparatus which has been used in this work. This apparatus produces beams of ions or neutral atoms of well-defined energy in the energy range from about 50 eV to about 8 keV. The neutral beam is used to impact on insulating surfaces to avoid any problems that are associated with charge accumulation on the nonconducting target. In the target chamber, the target to be bombarded is oriented with the surface normal making an angle of from 45 to 60 degrees with respect to the beam direction, and photons that are produced in the collision process pass through a quartz window and are focused by a quartz lens into a small, fast monochrometer. The monochrometer and the photomultiplier are used to record the spectral distribution of radiation that is produced in the collision process and single photon counting techniques are used for sensitive radiation detection.

Table 1 lists at least three possible sources or mechanisms for producing optical radiation in the low-energy collision region. First of all, there is radiation from excited states of atoms and molecules that have been sputtered off the surface. Basically, interaction of the beam with a solid results in sputtering of atoms and molecules off the surface. A significant portion of the sputtered fragments leave the solid in excited electronic states which then decay and give rise to lines and bands that are characteristic of surface constituents including surface contaminants. Secondly, there is radiation from excited states of backscattered beam particles. This obviously gives information on the quantum mechanical states of the backscattered projectiles. Then, finally, there is radiation which results from the excitation of the electrons in the solid. These, in general, are observed to be very broad continuum of radiation which are produced most efficiently by high velocity projectiles impinging on insulating targets. The radiative continuum that are observed here are localized to the solid and result from the transfer of projectile energy to the electrons in the solid. This gives rise to the creation of electron-hole pairs which then produce the radiative continuum upon recombination. The first mechanism provides the basis for a technique to identify surface constituents. This is the technique which we call the SCANIIR technique which stands for Surface Composition by Analysis of Neutral and Ion Impact Radiation. As an analysis technique this method is very sensitive to the first few monolayers of the solid. The spectrum of radiation that one obtains is relatively simple and uncomplicated, but there are effects due to nonradiative de-excitation processes that one has to be aware of.

Figure 2 shows examples of the spectrum of radiation that are produced when argon ions at an energy of 4 keV impinge on surfaces of copper and nickel. The prominent lines that are shown in these two spectra arise from low lying excited states of neutral copper and neutral nickel. Therefore, we are detecting the sputtering of neutral atoms from the surface by detecting the radiation that they emit when they leave the surface. In addition to radiation from copper and nickel, we also see radiation from common surface contaminants such as sodium, from the sodium D lines, as well as organic contaminants from a molecular band that arises from an excited state of the CH molecule. There is also radiation from hydrogen, which presumably results from either the fragmentation of the organic contaminants or possibly water vapor. The molecular band from the CH molecule is the most intense radiative feature that is seen from any of the common organic contaminants, and it serves as a unique fingerprint to identify specifically the fact that one has organic contamination on a surface. We have used this on numerous occasions to look for such things as photoresist residues on elemental surfaces.

Figure 3 shows results that were obtained using the neutral beam on three insulating targets: sapphire, lithium fluoride, and fused quartz. The optical lines that are shown here arise from low lying excited states of aluminum, lithium and silicon, respectively. The widths of all of these lines, at least the prominent ones, have been measured to be less than or equal to the instrumental resolution (∿1 Å) and this reinforces the conclusion that these lines originate from atoms which are radiating after they leave the surface. Experimentally we find that the photon production efficiency is substantially greater for these insulating targets than in the case of metal targets. In the case of metals, a typical prominent line will be produced with an efficiency of approximately 10^{-4} to 10^{-5} photons produced per incident projectile. In the case of insulators, these same optical lines are produced with an efficiency that is measured to be some two to three orders of magnitude higher.

A plausible explanation for the large difference in the excitation efficiency on metal and insulating targets can be found by considering the effects of nonradiative de-excitation. When an atom is in the vicinity of a solid, there are nonradiative electronic processes which result from the interaction of the excited atom with the solid which can very efficiently compete with radiative decay of the excited atomic states. In general, there are two basic types of nonradiative processes, and they are illustrated schematically in Fig. 4. This shows a potential well diagram that is appropriate to a metal with an excited atom located a distance S away from the surface. If the excited atomic state lies above the Fermi level, then the excited atomic electron can tunnel through the potential barrier into one of the unoccupied levels. This is a one electron resonance tunneling process and is known as resonance ionization. However, if the excited atomic state lies below the Fermi level (Case B), then tunneling is prohibited since the levels are filled. Even in that case the excitation energy can still be transferred nonradiatively to one of the available electrons in the solid and the electron from the solid may or may not appear as a secondary electron; it depends on the excitation energy of the atomic state and the depth in the well from which the upper electron was drawn. This is a two electron nonradiative process and is known as Auger de-excitation.

For both of these processes the nonradiative de-excitation rate is a very strong function of the distance of the excited atom from the surface, and it can be shown that these processes will preferentially de-excite those excited atoms which leave the surface with low velocities. This leaves only the small fraction ejected at higher velocities to efficiently contribute to the radiation. However, the band structure of a typical insulator is such that in many cases these nonradiative processes are not energetically allowed. Under these conditions, then, we expect to see radiation from all excited sputtered atoms even those that leave the surface with low velocities. We believe then that this accounts, at least in part, for the very large difference in the optical excitation that one commonly observes on insulating targets as compared to metal targets.

A good example of the effects of these nonradiative processes is illustrated in Fig. 5 where we have profiled a composite structure consisting of a 1200 angstrom thick film of SiO_2 on an infinite thickness of silicon. We have done this by measuring the intensity of a prominent silicon optical line as a function of the bombardment time. These measurements have been normalized to unity and then plotted on a logarithmic scale. The location of the SiO_2 silicon interface region is determined by that time at which the very rapid decrease in the intensity of the silicon optical line occurs. We see a factor of 50 reduction in the intensity of this optical line as we sputter from the SiO_2 film into the silicon substrate. The explanation for the results of Fig. 5 follows from the consideration of Fig. 6. Figure 6 shows the same type of potential well diagram, this time appropriate to an excited silicon atom in the vicinity of a silicon target and an SiO_2 target. As illustrated here, only in the case of the silicon substrate are the nonradiative de-excitation processes energetically allowed. Therefore in the silicon case, we expect to see radiation contributed efficiently only by those atoms which are leaving the silicon target with high velocities; only those atoms that lie in the high velocity tail. In the case of SiO_2, because of the very large 8 or 9 eV bandgap it is energetically impossible for these nonradiative processes to take place. Under those conditions we expect to see radiation from all excited sputtered atoms, even those that leave the surface with low velocities. And we believe that this accounts for the large difference in the optical intensity from SiO_2 as compared to silicon.

This model basically says there should be a substantial difference in the velocity distribution of the radiating atoms, and you might expect to see this reflected in the width of the optical emission line due simply to the Doppler effect, i.e., the Doppler broadening of the emission lines. Experimental results are shown in Fig. 7 where we have measured the emission line profiles for the same optical line in the case of the SiO_2 target and in the case of the silicon target. These measurements were done at higher bombarding energies, a bombarding energy of 80 keV, and they were done in second order to enhance any possible differences in the emission line profiles. In the case of the SiO_2 target we measure an emission line that has a full width at half maximum of about 1 Å, which is the instrumental resolution that we are using for these measurements. Under the exact same experimental conditions from the silicon substrate, we measure a full width at half maximum of about 5 Å. Since the instrumental resolution is the same 1 Å then most of the width of the optical line from the silicon target is real and this definitely indicates that there is a substantial difference in the velocity distribution of the radiating atoms. Experimentally, we find that the effects of these nonradiative processes can be minimized by either using oxygen as a bombarding projectile or by purposely backfilling the target chamber with oxygen gas. These, of course, are techniques that historically have been used in secondary ion mass analysis for essentially the same purposes and they drastically reduce the effects of the nonradiative processes in the optical emission.

To use this optical technique to identify the constitutents in the near-surface region of unknown solids, the procedure that we use is to simply impact the surface with the projectile beam, record the spectral distribution of the radiation, and identify the prominent lines and bands. A typical result is shown in Fig. 8. This shows the spectrum of radiation that was produced when nitrogen molecules impinged on two silica targets containing various oxide impurities. These two spectra were produced using an equivalent neutral current of about $1x10^{-6}$ amps/cm^2 and it took about 20 minutes to accumulate this data. We are using a scanning monochromator and therefore the full wavelength range must be scanned. By identifying the prominent lines that are shown in Fig. 8, one can show that there are common oxide impurities such as sodium, aluminum, and calcium in both of these. However, in one sample we have substantial optical lines from elements such as magnesium and iron, and those are not seen with any intensity in the other sample.

An indication of the sensitivity of the optical technique was obtained by using SiO_2 samples containing oxide impurities which were distributed homogeneously at known concentrations in the SiO_2 matrix. These samples were impacted with a beam of neutral atoms and the signal to noise ratio of the most prominent optical line from each impurity was measured. The detection limit for each impurity was estimated from the known impurity concentration and the measured signal to noise ratio. Table 2 summarizes results for some 10 or 12 oxide impurities in SiO_2. The left hand column of Table 2 lists the oxide impurities which were present in several different SiO_2 samples, and the right hand column gives the detection limit for the corresponding impurity. The numbers in the right hand column of Table 2 refer to the weight fraction of the oxide impurity which is necessary to be seen with a signal/noise ratio of one to one. An integration time of 10 secs was used and the particle flux was approximately $1x10^{-6}$ amps/cm^2. These results were obtained using a monochromator to isolate the prominent optical line characteristic of each impurity. However, if one is willing to use a narrow band interference filter to isolate the prominent optical lines, then 2 orders of magnitude improvement can be expected simply because this increases the photon collection efficiency by 2 orders of magnitude.

One other way that we have used to estimate detection limits is to use substrates which contain impurities distributed on the surface at known concentrations. Figure 9 shows results that were obtained using silicon samples which had chromium purposely deposited on the surface. For these measurements chromium was deposited on the surface of three silicon wafers at different concentrations and each of these samples was measured by 2 MeV Rutherford backscattering to give the chromium concentration. These range from approximately $2x10^{16}$ to $2x10^{14}$ chromium atoms per square centimeter. The samples were then put into the apparatus and the intensity of the prominent chromium optical line was measured as a function of bombardment time. The sample with 2×10^{16} chromium atoms/cm^2 was almost infinitely thick during the time scale of these measurements. For the sample that had 2×10^{14} atoms/cm^2, the chromium optical line was observed with a peak signal to noise ratio of approximately 200 to 1. The noise level was approximately 20 counts per second. Since the chromium coverage is about one-tenth of a monolayer on the silicon surface then one might expect to see 5 parts in 10^4 of a monolayer of chromium on silicon, and that could be improved also by using a narrow band interference filter.

One can also use this technique to provide depth profile information. Figure 10 shows the profile of a composite structure consisting of a layer of SiO_2, on Al_2O_3, on SiO_2, on an infinite thickness of silicon. These results were obtained by measuring the intensity of a silicon and an aluminum optical line as a function of bombardment time. In Fig. 10 you can easily distinguish the three different interface regions, but this is not a particularly good example because we obviously have problems related to the cratering phenomena. Presumably that is the reason that the aluminum optical intensity does not decrease to the noise level. Nevertheless, I think this example illustrates the potential for the optical technique and it certainly shows, for example, that if ion etching is being used for any purpose and you are interested in milling away a given layer to an interface region, then detection of the optical radiation produced in the collision process provides an in situ method to know when to turn off the beam.

One other possible application for this optical technique is to measure the range of implanted ions in silicon dioxide. Figure 11 shows some very preliminary results for an aluminum implant into silicon dioxide. The implantation dose was 10^{15} aluminum ions per square centimeter at an energy of 25 keV. This sample was then profiled by measuring the intensity of the aluminum optical line and the silicon optical line as a function of bombardment time. The time at which the rapid decrease in the silicon optical line occurs is a measure of the SiO_2/silicon interface region. If the initial film thickness is known, then the film thickness and time can be used to measure the sputtering rate for the conditions under which the experiment was performed. Knowing the sputtering rate, you can then determine the depth of the peak in the distribution of the implanted aluminum, which in this case is about 350 Å. From the full width at half maximum you can estimate the projected standard deviation which in this case is about 160 Å. The gaussian profile that one would expect is not indicated in Fig. 11. It has been fit and there is very little deviation until you get into the wings of the distribution and then it does start to deviate somewhat from the gaussian profile presumably due to effects associated with recoil implantation.

I would like to conclude by indicating the results of an experiment that was done to determine how impurity profiles of a mobile species such as sodium, which we have already heard about this morning, can be modified as a result of several different types of heavy particle bombardment. These experiments were done in collaboration with Richard Kushner and D. V. McCaughan. Previous work by these two had shown that if one took SiO_2 films on silicon, purposely coated on the outside surface with sodium, and bombarded the contaminated film with positive ions, then a large fraction of the sodium which was initially on the surface of the SiO_2 film was transferred as a result of the bombardment to the SiO_2-silicon interface region. They observed that up to 10 to 20% of all the sodium could be driven through the oxide film to the interface, simply as a result of the low energy ion bombardment. They attributed this transport to effects associated with the neutralization of the incoming ion at the SiO_2 surface. This, of course, gives rise to a positive charge on the outside surface which then provides a source of driving electric field to move the sodium to the interface. The experiment we did was to compare sodium transport in SiO_2 films subjected to ion and neutral particle bombardment. The results are shown in Fig. 12. The films that were used in this work were 5,000 angstrom SiO_2 films on silicon, purposely contaminated on the outside surface with approximately 10^{14} sodium atoms/cm^2; the sodium contained ^{22}Na as a radio tracer. The slices were then bombarded with nitrogen ions at 2 keV, nitrogen neutrals at 2 keV, and a third case was to use nitrogen ions at 2 keV but to flood the surface of the SiO_2 film with thermal electrons from a heated filament during bombardment. This was done in an effort to keep the surface neutral during bombardment. Each film was impacted with a particle dose of $\sim 10^{15}$ heavy particles/cm^2. Following bombardment, the sodium profile in the film was determined using planar etch and radio tracer counting techniques, i.e., counting the etching solutions for the ^{22}Na removed in a given etching step. The profile results are given in Fig. 12. In the case of ion bombardment we observed that sodium is left distributed throughout the oxide and is piled up very near to the interface region, certainly within the last 500 Å of the interface region. In the ion bombardment case, approximately 10% of all the sodium that was initially on the surface was moved through the oxide film to the interface. Under the conditions of neutral particle bombardment, we cannot detect any sodium in the SiO_2-silicon interface region. After removing a few hundred angstroms of the SiO_2 film, there is very little or no sodium observed above the detection limit for the radio tracer technique which is approximately 7×10^{14} Na atoms/cm^3. Therefore in neutral bombardment there is no detectable sodium at the interface, and this is substantially less, by at least 3 orders of magnitude, than in the case of the ion bombardment. The case of using nitrogen ions with the surface flooded with thermal electrons is an intermediate case. The sodium at the interface is down by almost two order of magnitude compared to the case of positive ion bombardment, but this is substantially above that which was observed in the case of the neutral particle bombardment. This work was done using 2 keV ions or neutral molecules of nitrogen and the targets were at room temperature. Other work, using argon as a bombarding projectile, gave essentially the same results. This work therefore suggests that using neutral particles for bombardment may substantially reduce problems associated with ion induced mobile impurity transport in SiO_2 films. However, a word of caution is in order. In our work a particle dose of $\sim 10^{15}/cm^2$ was used. However, much greater doses, 10^{17}-$10^{18}/cm^2$, are required to profile a film of a few thousand angstroms, and it is dangerous to extrapolate our results to that dose range.

In conclusion, I want to emphasize that the study of optical radiation produced in particle-solid collisions provides fundamental information on particle-solid interactions and serves as the basis for a technique to identify constituents and contaminants on surfaces. This radiation is produced in the sputtering process and the optical information is available for a variety of diagnostic purposes in any type of sputtering experiment.

TABLE 1

SOURCES OF OPTICAL RADIATION IN PARTICLE - SOLID COLLISIONS

1. Radiation from excited states of sputtered surface constituents.
2. Radiation from excited states of backscattered beam particles.
3. Radiation resulting from the excitation of electrons in the solid.

TABLE 2

SCANIIR DETECTION SENSITIVITIES IN SiO_2

Element	Sensitivity
Al	7×10^{-5}
Fe	8×10^{-4}
Ca	2×10^{-5}
Mg	1×10^{-4}
K	8×10^{-4}
Na	3×10^{-5}
Rb	7×10^{-5}
Li	1×10^{-5}
Sr	7×10^{-5}
Ba	8×10^{-5}
Mn	1×10^{-4}
Ti	1×10^{-3}
Be	4×10^{-5}

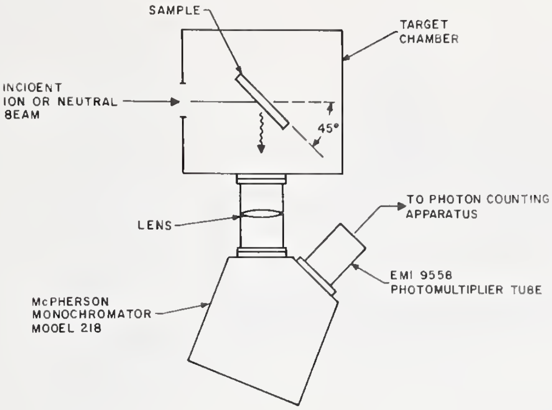

Figure 1. SCANIIR Surface Analysis Apparatus.

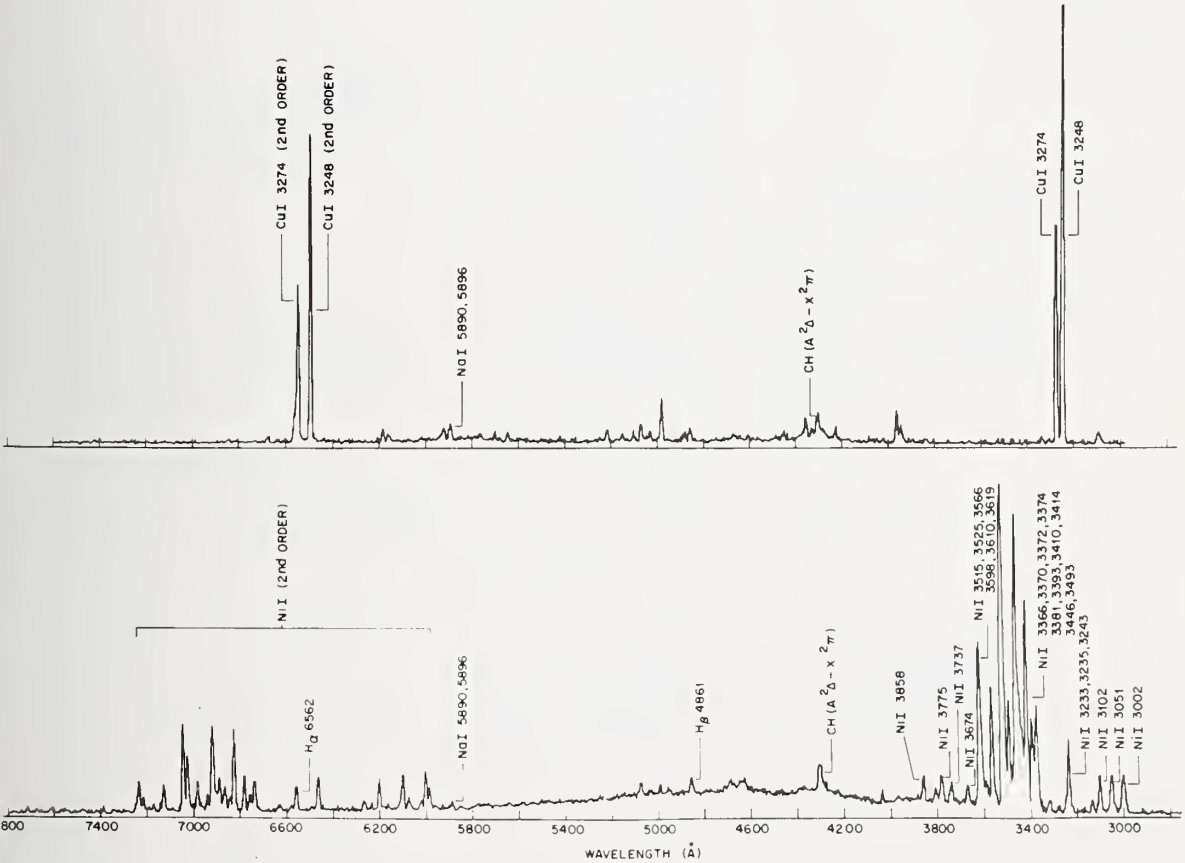

Figure 2. Spectra of radiation produced by the impact of Ar^+ (4 keV) on copper (top) and nickel (bottom). Lines arising from neutral Cu, Ni and various contaminants are identified by element and wavelength.

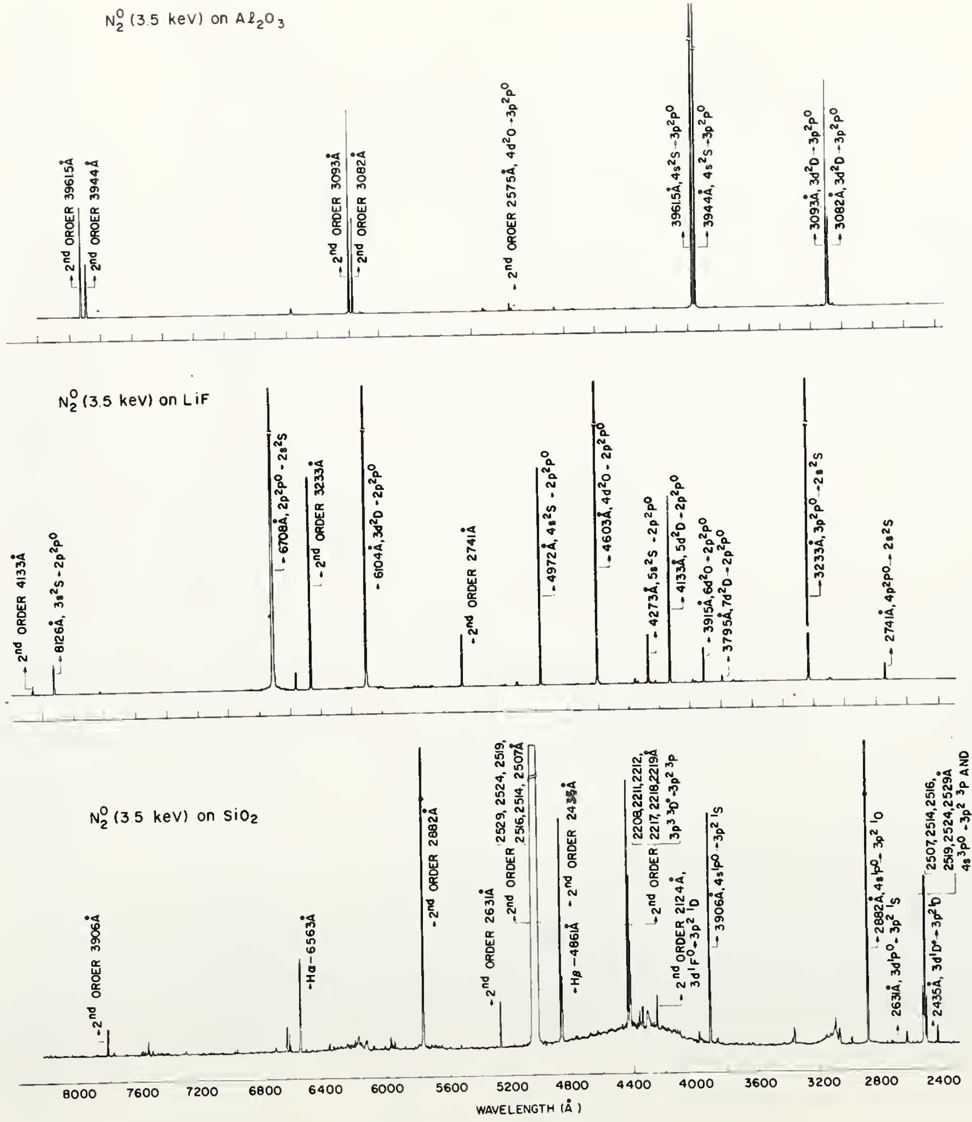

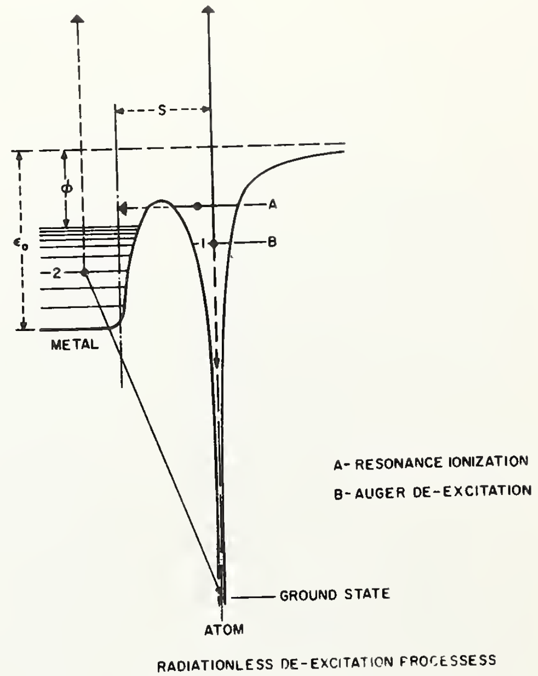

Figure 4. Energy level diagram showing possible nonradiative de-excitation processes.

Figure 3. Spectra of radiation produced by the impact of $N_2°$ (3.5 keV) on Al_2O_3, LiF, on SiO_2. The prominent lines arise from excited states of neutral Al, Li, Si and are identified by wavelength.

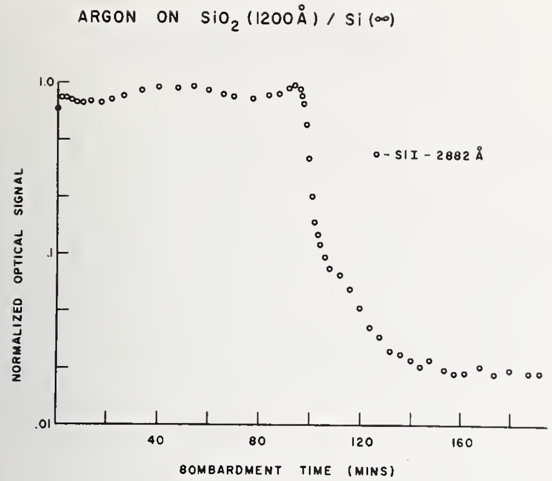

Figure 5. Profile of SiO_2 (1200 Å) on Si (∞). Intensity of SiI-2882 Å line is plotted on a logarithmic scale as a function of bombardment time. A current density of ∿ 10 $\mu A/cm^2$ was used for these measurements.

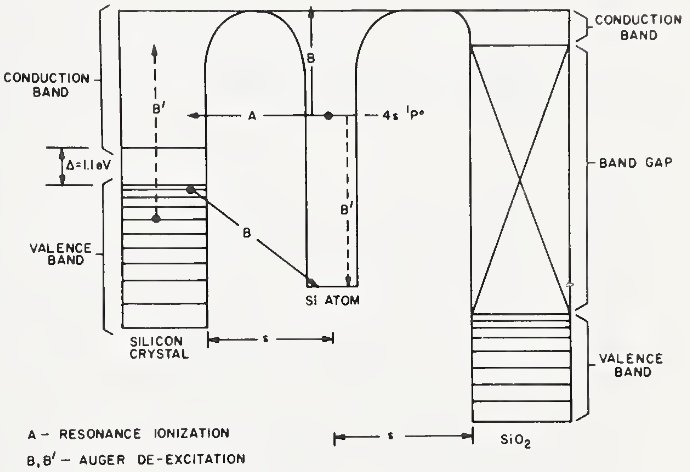

Figure 6. Energy level diagram for excited Si atom ($4s^1P^0$ state) near silicon and SiO_2 surface.

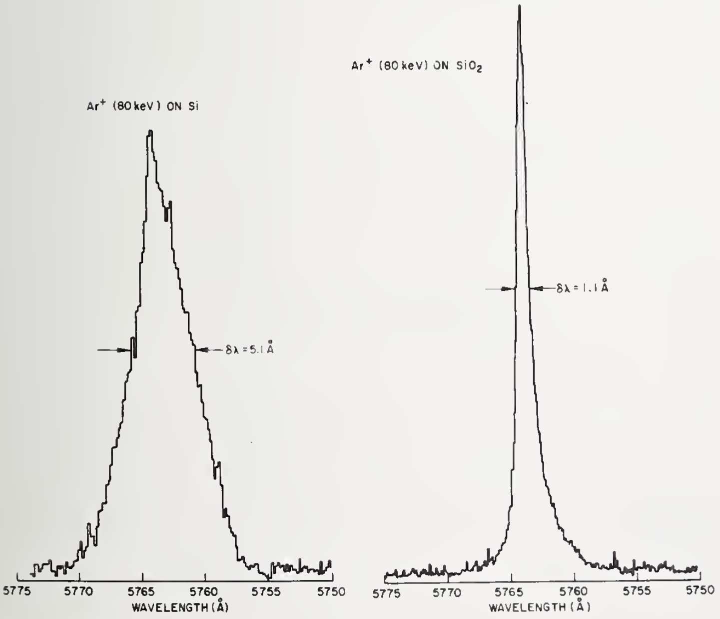

Figure 7. Emission line profiles of SiI-2882 Å from silicon and SiO_2.

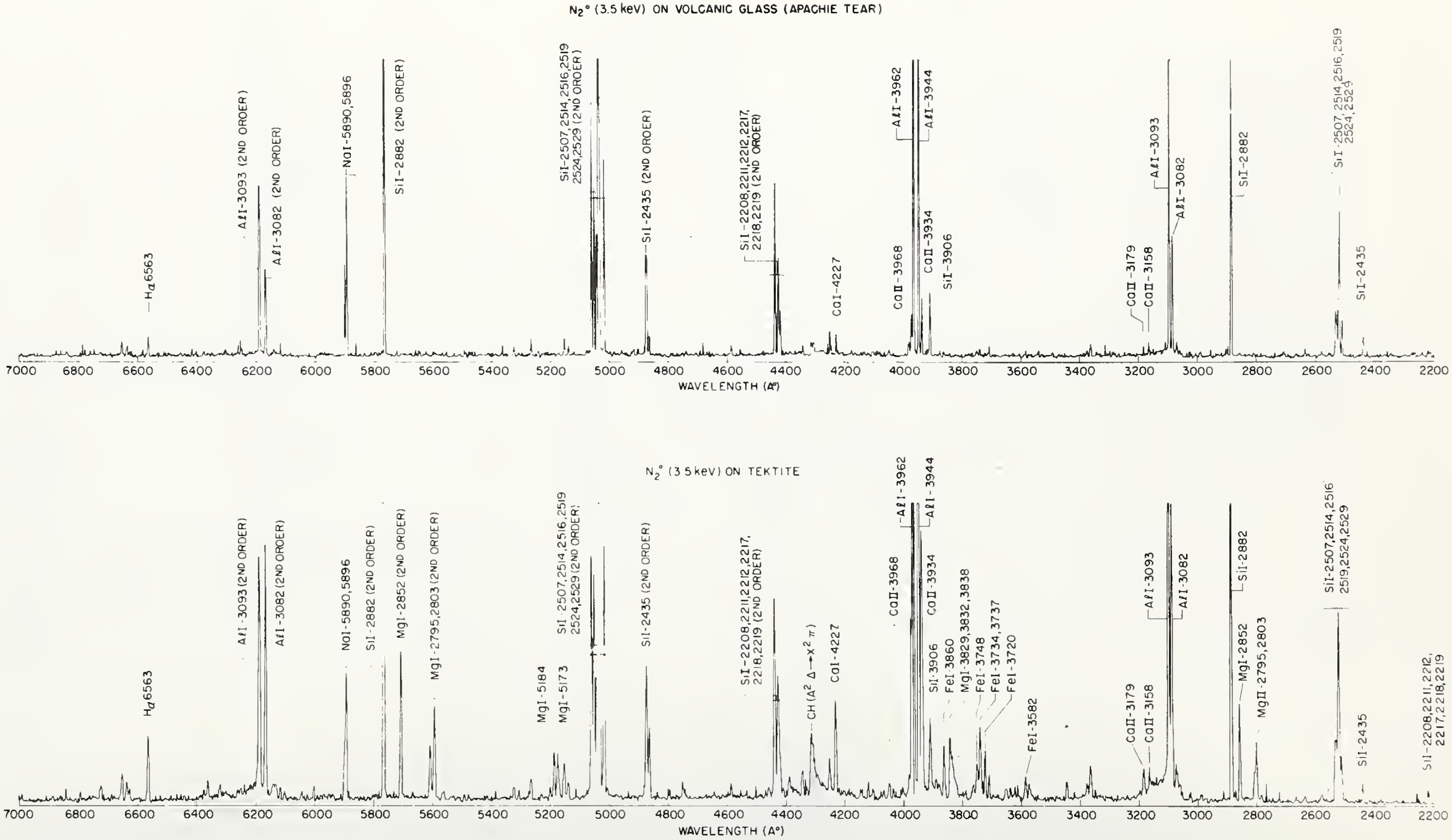

Figure 8. Spectra of radiation produced by N_2° (3.5 keV) impact on volcanic glass and tektite. Prominent lines are identified by element and wavelength.

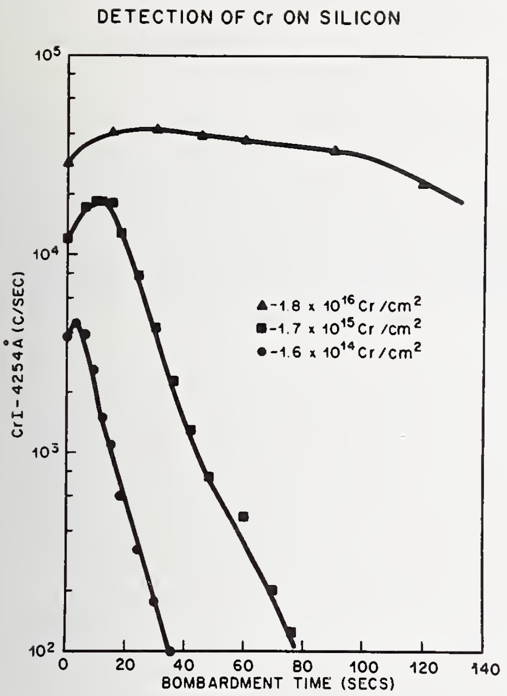

Figure 9. Detection of Cr on silicon. Measurements were made as a function of bombardment time using Ar$^+$ (8 keV), 4×10^{-6} amps/cm^2).

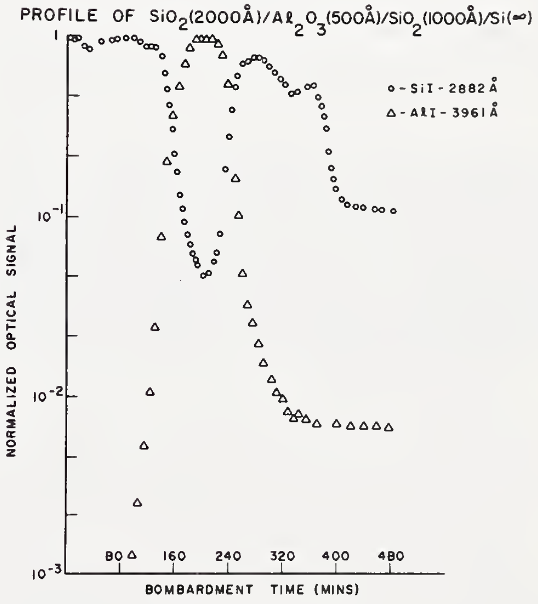

Figure 10. Profile of SiO_2 (2000 Å)/Al_2O_3 (500 Å)/SiO_2/(1000 Å)/Si (∞). Measurements were made using Ar$^+$ (5 keV).

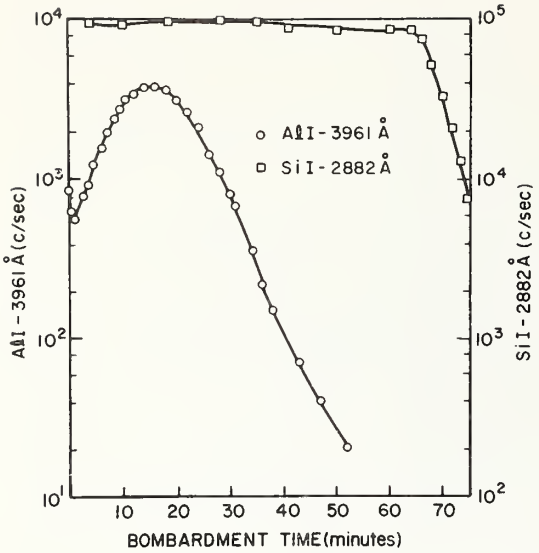

Figure 11. Profile of Al^+ (25 keV, 10^{15} ions/cm^2) implanted in SiO_2 (1500 Å thick). Aluminum and silicon optical lines were measured as a function of bombardment time. Profiling was accomplished using Ar^+ (8 keV, $\sim 5 \times 10^{-6}$ amps/cm^2) bombardment.

Figure 12. Sodium profiles produced by bombardment of SiO_2/Si. Initial sodium surface concentration on the SiO_2 surface was $10^{14}/cm^2$. Each sample was impacted with a dose of 10^{15} heavy particles/cm^2. The sodium profile following bombardment was determined by planar etch and radio tracer counting techniques.

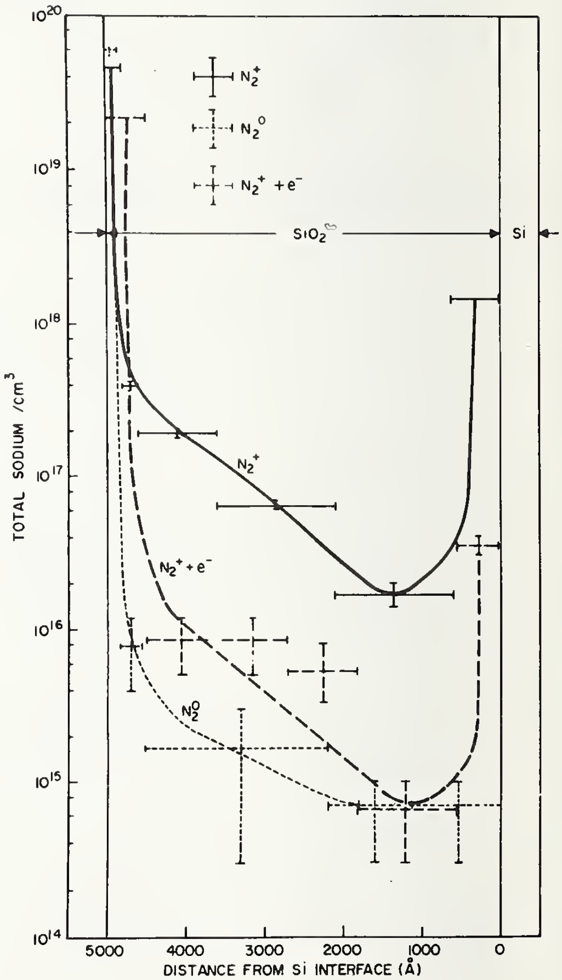

DISCUSSION OF THE PAPER

Participant: I wonder if you could comment on the detectability of hydrogen?

White: Hydrogen is definitely detectable; no question about it. In fact we have difficulty in getting rid of it. Our vacuums are typically of the order of 10^{-8} Torr, and under those conditions, one has difficulty getting rid of the hydrogen.

Participant: How does the photon production efficiency depend on the primary beam kinetic energy.

White: In the case of metal targets it is a very rapidly decreasing function of energy as you go toward lower energies. From a metal target, in fact, we have been able to see radiation down to about 300 or 400 eV primary energy using an argon projectile. In the case of the insulators, we do not know where the threshold is. It is below 50 eV for actually producing this radiation. It appears to rise linearly with energy and then apparently flattens out somewhere between one kilovolt and 1.5 kilovolts. In the case of the metals it continues to rise and does not peak until you get up into the range of about 10 to 12 keV.

Participant: How do you measure the particle beam current for a neutral beam?

White: You can do that in one of two ways. One of the detectors that we use is a bolometer, where basically you measure the temperature rise. This is calibrated against an ion beam of known current. But you can also measure particle current by using the photons that come from a metal surface because when a low energy ion impinges on a metal, the ion is actually neutralized several angstroms in front of the surface before the close-in sputtering encounter takes place. Therefore it does not matter whether you start with an ion or a neutral at infinity. By the time the sputtering encounter takes place, the incident projectile is, for the most part, neutralized. On the other hand photons are produced as a result of the sputtering encounter. And therefore the photon production efficiency from a metal target is essentially independent of the charge state of the incident projectile. And, thus, you can use a metal target and calibrate it in terms of its photon production efficiency using an ion beam of known energy and known current. Then by charge exchanging the ion beam and deflecting the ions out of the way to let the fast neutrals come into the target chamber you can use the photon count rate that the neutral beam produces on that same metal surface as a means of determining the neutral particle flux. Both of these techniques work very well.

Lin: As we understand, the sputter ion yield varies very much for elements in different matrices. How about the photon yields of elements in different matrices? This is very vital to the capability of the depth profile technique you described before.

White: The answer is that there are definite substantial variations in the photon yields as a function of different matrices. Impurities in a metal, for example, sodium impurities in metals, appear to have a different photon production efficiency than they do in a good insulator. How severe these problems really are at this point I honestly do not know. I do not know whether you see the gigantic variations that you see in secondary ion yields or not, but you do see variations.

Lin: Do you, then, expect it to be proportional to these sputter ion yields?

White: Not in all cases, no, definitely not. Other work that we are doing now shows that there are definite differences between the photon yields and the secondary ion yields, at least in some cases, and we are trying to understand that right now.

Feigel: Is the instrumentation as simple and as straightforward as you have shown or do you have your magic or money buried in there somewhere?

White: I can give a yes or no type answer to that. The apparatus that I am using has a lot of money invested in it. The reason is that it was designed to be a general purpose accelerator. It was built to study gas phase atomic collision processes and particle-solid collision processes. However, this radiation can be produced for as little money as you need to generate an ion beam, and then how you use the information is obviously up to you. You can go to some very complex photon detection schemes if you want to try to cover all possibilities. If you are interested in looking specifically for a given element, you can isolate optical lines from all of the elements of interest by using narrow band interference filters. These can be purchased for something like $200, a photomultiplier cost you $500, and then you have either got to count photons or you have to dc record. For specific applications, if you are interested in getting to an interface region, you should be able to do that unbelievably cheap. You may even be able to do it by eye, or using a solar cell type detector.

Harrington: Both ion and neutral beams will give secondary electrons and charged surfaces. Evidently from your experience, this is a second order effect in charging surfaces. Would you care to comment on that?

White: You can, under the conditions of neutral bombardment drive a lot of the sodium through an SiO_2 film to an interface if you put a collector in front of the target and collect the negative charge that comes off the bombarded surface. By biasing the collector to a certain voltage, you can control, or at least roughly control, what the surface potential will be on the bombarded surface. Now, our experience has been that if the collector is biased to approximately 100 V, you can then begin to see significant effects associated with driving sodium through the oxide. However, if you are not purposely collecting the secondary electrons that are emitted from the surface, then I do not expect that the bombarded surface is going to increase to a potential which is any greater than the average energy of the secondary electrons. This, I think is of the order of just a few volts, approximately 4 or 5 volts. Therefore, I think that this would be the only driving field that you would have, at least under the conditions that we have seen. This does not appear to be enough to give us sodium transport.

Participant: Do you have any techniques for reducing the cratering effect of neutral beams?

White: No. The only technique that we have is to narrow down the field of view of the optical detection system to the point where we are looking at a very small region. And then we hope that we are in the middle of the bombarded region. However, you can play games. We produce neutral beams by accelerating positive ions up to the desired energy and then partially neutralizing the ions by resonant charge transfer in their own gas. Resonant charge transfer is an atomic process in which there is very little momentum transfer so the resulting neutral has essentially the same energy and direction as the initial fast ion. If the apertures in the charge exchange region are opened up, then a certain amount of rastering of the ion beam before it goes through the charge exchange region is possible. By this technique a certain amount of rastering of the neutral beam is possible. But we have not done that yet and we have no plans to do it.

Participant: Have you looked for, or have you seen, any effects of damage while profiling implanted impurities?

White: No, as a matter of fact we have not. We have just gotten into the implantation business and we definitely have not looked for topography changes in the bombarded region yet. That is obviously something we should be doing, and in the future we will be. But in terms of the ion implantation profiles, we have done so few of them at this point that it is really meaningless to talk about them.

NBS Special Publication 400-23, ARPA/NBS Workshop IV, Surface Analysis for Silicon Devices, held at NBS, Gaithersburg, Maryland, April 23-24, 1975 (Issued March 1976)

NUCLEAR RESONANCE AND BACKSCATTERING SURFACE ANALYSIS OF SILICON AND RELATED INSULATORS*

Kenneth L. Dunning

Naval Research Laboratory
Washington, D.C. 20375

INTRODUCTION

Methods for surface analysis which are based on nuclear reactions and scattering generally require more complex and expensive apparatus than do other methods considered at this workshop and, in addition, are more limited with respect to the number of host-impurity combinations that can be profitably examined. On the other hand, these methods have some distinctive features which make them very useful in investigations pertaining to the technology of silicon and related insulators. For example, distributions of sodium in thin layers of silicon dioxide on silicon substrates can be accurately and repeatedly profiled; such measurements cannot be made by means of methods which sputter away the specimen in the depth-profiling process.

Two of the most useful nuclear methods for quantitative surface analysis are: nuclear resonance profiling and Rutherford backscattering. This paper is concerned with the principles and applications of these methods, with emphasis on the first since it is less familiar, and with the discussion of the second confined mainly to a recently-introduced improvement in the depth resolution very near the surface. These methods can be used to measure impurity depth-concentration profiles with depth resolution of the order of tens of angstroms (very near the surface). In interior regions, depth resolution is poorer, changing roughly as the square root of the depth. The depth scale is based upon the average rate of energy loss of the bombarding particles as they penetrate the specimen. This basis for the establishment of depth scales is better understood and provides greater reproducibility than do methods based upon sputtering rates. Although charged particles with energies in the neighborhood of one million electron volts do alter the crystalline structure of solids which they penetrate, their effect upon the distribution of elements is generally negligible and can be investigated by repeatedly measuring a particular depth-concentration profile.

References [1] through [3] are concerned with materials analysis by means of nuclear reactions in general; references [4] through [8] are specialized to nuclear resonance reactions; reference [9] is a recent review of backscattering and nuclear-reaction analysis methods.

INTERACTION OF ONE-MeV PROTONS WITH SILICON

The sketch of Figure 1 is intended as an aid to a brief review of the way charged particles with energies in the neighborhood of 1 MeV interact with silicon. For definiteness, protons are taken to be the incident particles; remarks on the interaction of alpha particles (which are commonly used for Rutherford backscattering analyses) will be inserted as the discussion proceeds. The sketch represents a layer of silicon 1,000 Å thick. As the protons penetrate the layer, they lose energy in a large number of small-angle inelastic scatterings depicted at the top of the figure. The average loss of 1-MeV protons traversing 1,000 Å of silicon will be 4 keV; the energy loss is linear with the depth of penetration and, hence, the depth can be conveniently measured in terms of this energy loss. Energy loss serves as a basis for a depth scale in both nuclear resonance profiling and Rutherford backscattering. As the protons pass through the silicon layer, they excite and ionize the atoms of silicon, losing a few electron volts in each interaction, and emerge in essentially the same direction in which they entered. At these velocities, a proton may occasionally pick up an electron but more than 99% of the time it is simply a stripped hydrogen nucleus. If the protons were to enter as hydrogen atoms, they would be stripped almost immediately and proceed as stripped nuclei. Alpha particles penetrating matter behave in a very similar way; however, the rate of energy loss with depth for 1-MeV α particles is about 7 times as great as for 1-MeV protons. This is an advantage in measuring depth by means of energy loss.

---

* This research was partially supported by the Defense Nuclear Agency under subtask Z99QAXTA007, work unit 52, work unit title "Electronic Transport and Trapping in Thin-Film Oxides."

Although the average loss for 1-MeV protons traversing the layer is 4 keV, the losses of individual particles will be distributed about this average in a predictable way. For penetration depths of the order of tens of keV, these loss distributions are Gaussian shaped; for small penetrations, the loss distributions are asymmetric about the mean but can still be predicted with great accuracy by means, for example, of the theory of P. V. Vavilov [11]. The full width at half maximum of the energy loss distribution of the protons emerging from the layer of silicon depicted is about 2.8 keV. It is this phenomenon of energy-loss fluctuations which is the chief source of depth resolution degradation in nuclear resonance profiling and Rutherford backscattering. The process represented at the middle of the sketch of Figure 1 is that of large-angle scattering. If this large-angle scattering occurs because of the Coulomb field interactions and not because of nuclear interactions, we call it Rutherford scattering. The probability for the occurrence of this process in a layer of the type illustrated is much less than the first process described but sufficient so that detectors can be located to measure the number and the energies of the scattered particles and this information used to establish quantitative depth-concentration profiles.

A third process of interest is illustrated at the bottom of the sketch; a proton is captured into the nucleus of one of the target atoms to form a compound nucleus of a new atomic species. Many different modes of decay of the compound nucleus are possible; two are illustrated. The decay mode in which a gamma ray is emitted is very useful for nuclear resonance profiling but that in which a nucleon is emitted can also be used. The probability for nuclear capture is often an extremely sharp function of the energy of the incident protons and the process is sometimes described as resonance capture.

PRINCIPLES AND APPLICATIONS OF NUCLEAR RESONANCE PROFILING

It is convenient to present the principles of nuclear resonance profiling with an example which makes use of a sharp resonance in the $^{27}Al(p,\gamma)^{28}Si$ reaction at a proton energy of 991.9 keV. The sketch of figure 2 shows a proton beam incident upon a silicon target which has a layer of aluminum atoms at the surface and another at a depth of 500 Å. A depth scale in angstroms is shown at the top of the target and at the bottom of the target is a depth scale in keV of the energy loss for the proton beam as it penetrates the target. The resonance in this reaction is very sharp having a full width at half maximum of 0.10 keV. If the proton energy is advanced in small steps from 1/2 keV below resonance energy to about 6 keV above resonance energy and a fraction of the gamma rays from the target is counted by means of a sodium iodide detector (with an energy window 9 to 12 MeV) for a fixed number of protons on target at each energy step, a gamma-ray yield curve of the kind illustrated in the lower half of the sketch will be obtained.

To understand the role of the resonance, consider the interior target layer containing aluminum atoms. When the bombarding energy is 2 keV above resonance, the most probable energy loss for the protons that have arrived in this layer is 2 keV; thus, the protons in this layer are very near resonance energy. Most of the protons to the left of this layer are above resonance energy and those to the right are below resonance energy. The first peak in the gamma-ray yield curve is associated with the first layer in the target containing aluminum atoms. The first peak is higher and narrower than the second peak because there are more aluminum atoms in the first layer than in the interior layer and there is less energy-loss straggling. The area under the gamma-ray yield curve is proportional to the number of aluminum atoms in the layer. The abscissa scale on the gamma-ray yield curve is a measure of the incident proton energy in keV above resonance energy. The figure has been drawn so that the abscissa scales of keV energy loss and incident proton energy above resonance are numerically equal. The yield curve, when plotted as a function of bombarding energy above resonance, provides an approximate depth-concentration profile. It is not a perfect depth-concentration profile because the incident proton beam has a small but finite width to its energy distribution and the resonance also has a small but finite energy width. The most serious impediment to precision is the statistical fluctuation in the energy loss of the protons as they penetrate the solid, that is, energy-loss straggling. This straggling becomes more pronounced with depth, increasing approximately as the square root of the depth of penetration.

Although the approximate profile provided by the yield curve is often accurate enough for some purposes, a much more exact profile can be obtained with the help of the following equation which describes the yield $Y(E_b)$ as a function of the bombarding proton energy, E_b [10].

$$Y(E_b) = \mathrm{Const} \int\int\int \sigma(E)\, g(E_i,E_b)\, w(E_i-E,\bar{\Delta})\, C(\bar{\Delta})\, dE\, dE_i\, d\bar{\Delta}$$

where $\sigma(E)$ is the cross section for the $^{27}Al(p,\gamma)^{28}Si$ reaction in the vicinity of the resonance (Breit-Wigner formula), $g(E_i,E_b)$ is the beam-energy distribution, $w(E_i-E,\bar{\Delta})$ is the energy-loss distribution which gives the probability that for a depth in the target for which the average energy loss is $\bar{\Delta}$, the exact energy loss is E_i-E, and $C(\bar{\Delta})$ is the concentration function. That is, the protons which are in an energy bin of width dE_i at E_i before entering the target have the probability, w, of being degraded into energy bin of width dE at E in the neighborhood of resonance energy on their way to the target layer of width $d\bar{\Delta}$ at depth $\bar{\Delta}$. The beam-energy distribution depends upon the characteristics of the beam-energy analyzer and, for the case at hand, the energy-loss distributions can be calculated by the theory of P. V. Vavilov [11,12].

One point of view that may be helpful is to think of performing the integration with respect to E_i first. This would give a new function of E and $\bar{\Delta}$. This proton energy distribution in the target broadens with depth, making the uncertainty for the calculated yield greater in interior regions than at the surface. Note that an additional integration with respect to E_b will give the area under the yield curve, this area is proportional to the total number of aluminum atoms represented by the profile. The foregoing equation may be used to calculate, to within a constant, ordinates on the gamma-ray yield curve if the concentration function, $C(\bar{\Delta})$ is known. The constant can be determined from a measurement of the yield from a homogeneous target of known thickness. If a yield curve is measured for a target with an unknown concentration profile, we can equate the experimental yield to the right-hand side of the equation but are then faced with the task of extracting the concentration function. Since the measured gamma-ray yield curve is an approximation of $C(\Delta)$, we may construct a trial function, calculate the yield function, and compare it with the experimental yield curve. If the comparison is not satisfactory, the comparison may be used as a guide to construct a new trial concentration function and the process iterated until satisfactory agreement between the calculated yield and experimental yield is obtained. With the aid of a digital computer to make the calculations and plot the experimental yield curve, the calculated yield curve, and the concentration function, a very satisfactory representation of the concentration function can be obtained with a few iterations.

Figure 3 illustrates results obtained with the procedure described for a target which was made by depositing 600 Å of aluminum oxide on a silicon substrate. A gamma-ray yield curve was then measured by counting the gamma rays as the bombarding energy was advanced in small steps from below resonance to 10 keV above resonance; these data are represented by the circles. The concentration function of the aluminum in the oxide is represented by the solid line. The calculated gamma-ray yield curve is represented by the triangles. The fact that the yield rises before the profile (near resonance) is due to the finite widths of the resonance and the incident beam-energy distribution. The "spike" at resonance is due to the asymmetry of the energy-loss distributions. The divergence of the calculated and experimental yield curves from the profile near the back face is due to the energy-loss straggling.

The area under the experimental curve is proportional to the number of aluminum atoms represented by the profile. The constant of proportionality can be easily obtained and experience has shown that the number of atoms represented by the profile can be determined with an accuracy of about 5%. This determination does not depend upon the shape of the beam, the shape of the resonance, or the effects of energy-loss straggling.

Figure 4 shows a profile for an unknown sample determined by this method. The sample was made by implanting 60-keV aluminum into silicon carbide and then annealing at a temperature of 1400°C. The sample was profiled before annealing and it was found the profile had a Gaussian shape with a peak at about 700 Å. The annealing drastically altered the profile, bringing aluminum to the surface region. A comparison of areas showed that there is much less aluminum in the region of the profile than there was before the annealing. The width of the spike in the profile at the face of the target is about 20 Å at half height. This gives some idea of what the depth resolution can be at the very face of the target. In interior regions, it is poorer than this due to energy-loss straggling. If such a spike concentration were located in the interior of the target then the yield curve representing it would be smeared out; the accuracy to which the profile could be constructed depends upon the depth at which the spike occurs and upon the statistical uncertainty of the experimental data.

It is feasible to profile sodium in thin silicon dioxide layers by means of this method. Reproducible profiles have been obtained for sodium in thin layers of silicon dioxide on silicon, both for test structures which have thin gold layers on the silicon dioxide surface and for test structures which have no metallic layer. There is, however, a limit to the fluence of protons which can be passed through the silicon dioxide layer without disturbing the sodium distribution. Figure 5 shows the results of measurements on a test structure consisting of 3,000 Å of silicon dioxide on a silicon substrate with a 175-Å layer of gold evaporated onto the surface of the silicon dioxide. Prior to the deposition of the gold surface layer, the structure was implanted with 60-keV sodium to a fluence of 10^{15} atoms/cm^2. The profile represented by the solid line was obtained for the as-prepared structure. It was re-measured to insure that the measurement process did not alter the profile. The specimen was then irradiated with 13-keV electrons (with the gold at +30 V relative to the silicon) to a fluence of 10^{13}/cm^2, the profile measured, and then re-measured to insure reproducibility. The electron irradiation has caused a migration of the sodium from the region profiled. It appears that some sodium has moved deeper into the specimen and that sodium has migrated through the gold film on the surface of the silicon dioxide. However, there is the possibility, of sodium contamination to the gold surface during the electron irradiation. These data are presented simply to demonstrate the profiling technique.

PRINCIPLES AND APPLICATIONS OF RUTHERFORD BACKSCATTERING SURFACE ANALYSIS

Much has been written concerning the application of Rutherford backscattering to the analysis of surfaces [2,9].Nuclear resonances are not used in this method to improve the depth resolution as was done in the previously discussed method. Instead, the depth scale is established on the basis of the energy loss of the incident charged particle (usually an α particle) in its trip to the scattering atom in the solid being analyzed and, after scattering, to the detector. In some situations, scattering can be enhanced by nuclear resonances but this is generally avoided so that the cross section for scattering can be computed from the Rutherford formula. The method is best suited to the profiling of heavy impurity atoms in light hosts.

The principles upon which the method is based can be quickly reviewed by referring to figure 6. Mono-energetic α particles (typically in the range 1 to 3 MeV) are shown incident from the right upon a target consisting of an aluminum oxide substrate covered by a thin nickel film which is, in turn, covered with a thin gold film. Scattered particles are usually detected by a semiconductor detector shown at the upper right. The voltage pulses from such a detector are proportional to the energy of the scattered particle. If these pulses are sorted by a pulse-height analyzer and displayed on an oscilloscope, a pulse-height (energy) spectrum such as that displayed in the lower part of the diagram is obtained. The energy, E_o, of the incident particles is an upper limit to the energy of the scattered particles. The high-energy side of the peak in the scattered spectrum marked Au is due to the scattering from the surface of the gold since the gold atoms are the heaviest atoms in the target and the incident particles have lost very little or no energy in the target before being scattered (billiard-ball kinematics). Alpha particles that are scattered from the interior of the gold film lose energy on the way to the scattering center and again on the way to the detector by small-angle inelastic scattering such as that discussed in connection with figure 1. Thus, if there are no atoms in the target which have nearly the same mass as the gold atoms, a peak will be formed in the scattered spectrum whose height is proportional to the number of gold atoms/cm^2 and whose width is proportional to the thickness of the gold layer. A similar peak appears in the scattering spectrum due to the presence of the nickel. The α particles scattered from nickel all have lower energies than any particle scattered from gold because the nickel atoms are not as heavy as the gold atoms and, in addition, the incident particle must lose energy in the gold layer before any scattering from the nickel can take place. Since the aluminum oxide substrate is considered to be very thick relative to the nickel and gold layers, the α particles scattered from aluminum atoms form a continuum which extends essentially to zero energy and, similarly, the contribution to the backscattered spectrum from the oxygen appears on top of this continuum. The signal-to-background ratio is much better for the heavy elements than for the oxygen. Since the cross section for scattering can be calculated from the Rutherford formula, and the rate of energy loss of the α particles in various materials has been measured and cataloged [13], the data in the scattered spectrum may be used to construct a quantitative depth-concentration profile.

The depth resolution for the method just described is determined by the finite energy width of the incident α-particle energy distribution, the energy-loss straggling in the target, and the energy-loss straggling introduced by the detector. The energy loss in such detectors is usually in the range 10 to 15 keV with the width of the energy-loss distribution being in the neighborhood of 10 keV; this can cause an uncertainty in the depth scale at the face of the target, typically, in the neighborhood of 100 Å.

There are a few laboratories where the semiconductor detector in a scattering apparatus has been replaced by a magnetic spectrometer which determines the energy of the scattered particle without introducing energy loss. Figure 7 shows such an arrangement which has been developed and tested by Dr. J. K. Hirvonen and his colleagues at the Naval Research Laboratory. The spectrometer can be rotated about a verticle axis and positioned to accept a certain fraction of the particles scattered from a target. Of the particles scattered, those within a small range of momentum (determined by the strength of the magnetic field which is perpendicular to the paper) will pass through the spectrometer and be detected in a position-sensitive detector in the image plane of the spectrometer. The voltage pulses from this detector are routed to a pulse-height analysis system. The energy coordinate of the contribution of a particle to the scattered-particle spectrum is determined by the position at which the particle strikes the detector which is located in the image plane of the spectrometer. With this arrangement, one obtains only a small part of the semiconductor energy spectrum but the degradation of depth resolution introduced is an order-of-magnitude smaller than that introduced by a semiconductor detector.

In order to measure the effect of the scattered-particle detector on the depth resolution, it is useful to have a very thin target of heavy atoms. The data of figure 8 were obtained with a target made by depositing gold onto silicon dioxide to an average thickness of one monolayer. However, gold deposited in such thin layers tends to form "islands" which means that some of the incident 2-MeV α particles were scattered by several monolayers of gold. At any rate, we have a target which is quite thin.

The upper part of figure 8 shows a spectrum obtained with a semiconductor detector. The left half of the spectrum is due to the silicon and oxygen and is not of interest. At the high-energy end of the spectrum is the contribution from the gold, a peak with a full width at half maximum of 16 keV. This width is due almost entirely to the energy-loss straggling in the semiconductor detector. The spectrum at the lower right of the figure was obtained with the magnetic spectrometer. The full width at half maximum of the peak is now 5 keV and less than half of this is due to the uncertainty in the scattered energy due to the spectrometer arrangement which is about 2 keV and corresponds to an uncertainty in the depth scale of a depth-concentration profile of about 25 Å. Thus, the depth resolution that may now be achieved with Rutherford backscattering at the surface of a specimen is comparable to that illustrated in figure 4 with nuclear resonance profiling.

The magnetic spectrometer arrangement has another advantage; it passes scattered particles whose energies fall only within a narrow band, whereas the semiconductor detector sees a much larger number of particles per unit of time. This results in a higher background in the semiconductor detector scattered spectrum due to pulse "pileup" and degrades the detection level. The "spectrum" at the lower left of figure 8 was obtained by bombarding a silicon dioxide target with no gold layer. Although five times as many incident α particles were used in this case as were used to obtain the spectrum at the lower right, not a single event was recorded in the 40-keV region spanned by the abscissa. If one count had been recorded, the detection limit for the gold would be 10^{10} atoms/cm^2. The detection limit with the semiconductor detector is about 10^{12} gold atoms/cm^2. Thus we see that we can expect a depth resolution very near the surface of about 25 Å with a detection limit of less than 10^{10} atoms/cm^2 with this spectrometer arrangement for a target that is free from contaminating atoms with atomic weights near that of gold.

CONCLUSION

Some of the more important features of the two discussed methods of obtaining depth-concentration profiles can be summarized and compared as follows.

(1) Both methods discussed are nondestructive in the sense that the atoms struck are not moved very far (at least almost never). However, the probing ions do move the struck atoms from their lattice sites far enough to degrade the crystalline structure.

(2) Repeated measurements can be made on the same test specimen and these measurements can be interspersed with various other processes such as annealing and irradiation.

(3) Depth scales do not depend upon surface-removal techniques and can be very accurate.

(4) The total number of atoms represented by a profile can be determined, often to accuracies better than 5%.

(5) The apparatus for these methods is complex and, hence, these methods are suitable only for some problems related to the silicon-device development and production. They can be very useful in support of the development of measurement technology which, in turn, can be more directly and easily applied to device problems.

(6) The number of host-impurity combinations that can be analyzed is limited and detection limits vary from 10^{10} atoms/cm^2 upwards. The nuclear resonance profiling method is isotope specific and useful for light impurities in any kind of substrate that does not have interfering resonances. The Rutherford backscattering method is best for impurities that are heavier than the host impurity.

ACKNOWLEDGEMENTS

Support of this work by the Defense Nuclear Agency is gratefully acknowledged. The part of this report dealing with Rutherford backscattering is based on the work of Dr. James K. Hirvonen, Naval Research Laboratory. Contributions of Mr. Harold Hughes, Naval Research Laboratory, to the work are gratefully acknowledged. The experimental work with accelerated ions was carried out with the 5-MV Van de Graaff accelerator of the Ion Beam Applications Branch, Radiation Technology Division, Naval Research Laboratory, with assistance from the staff. Dr. E. A. Wolicki provided helpful comments and suggestions.

REFERENCES

1. Amsel, G., Nadai, J., D'Artemare, E., David, D., Girard, E., and Noulin, J., *Nucl. Instr. Meth.* 92, 481 (1971).
2. Wolicki, E., *Nuclear and Ion Beam Techniques for Surface and Near-Surface Analysis*, NRL Report #7477, (December 13, 1972).
3. Wolicki, E., *Surface Analysis Using Nuclear Reactions in New Uses of Low Energy Accelerators*, (Plenum Publication Corporation, New York, to be published).
4. Möller, E., and Starfelt, N. *Nucl. Instr. Meth.* 50, 225 (1967).
5. Witton, J., and Mitchell, L., *Can. Jour. Phys.* 49, 1125 (1971).
6. Bernett, M. K., Butler, J. W., Wolicki, E. A., and Zisman, W. A., *J. Appl. Phys.* 42, 5826 (1971).
7. Dunning, K., and Hughes, H., *IEEE Trans. Nucl. Sci.* NS-19, 243 (1972).
8. Dunning, K., Hubler, G., Comas, J., Lucke, W., and Hughes, H., *Thin Solid Films* 19, 145 (1973).
9. Chu, W., Mayer, J., Nicollet, M., Buck, T., Amsel, G., and Eisen, F., *Thin Solid Films* 17, 1 (1973).
10. Gove, H., *Nuclear Reactions*, p. 293, Endt and Demeur, Eds. (North Holland Publishing Co., Amsterdam, The Netherlands 1959).
11. Vavilov, P., *Zh. Eksp. Teor. Fiz.* 32, 320 (1957); *Transl. JETP* 5, 749 (1957).
12. Seltzer, S., and Berger, J., *Nuclear Sciences Report 39*, p. 187, National Academy of Sciences - National Research Council, Washington, D. C. (1964).
13. Williamson, C., Boujot, J., and Picard, J., *Tables of Range and Stopping Power of Chemical Elements for Charged Particles of Energy 0.5 to 500 MeV*, Report CEA-R-3042, Centre d'Etudes Nucleaires de Saclay, France (1966).

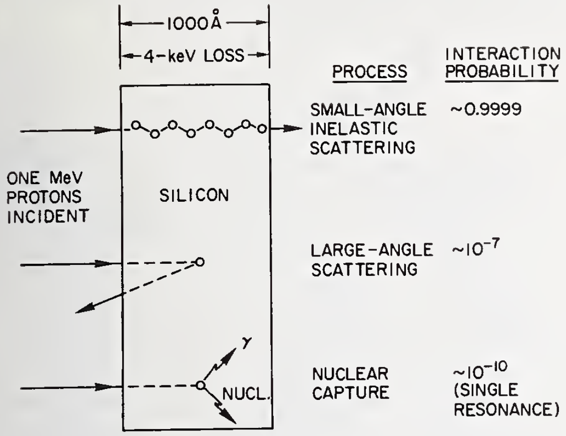

Figure 1. Sketch illustrating the interaction of 1-MeV protons in a 1,000 Å thick slab of silicon.

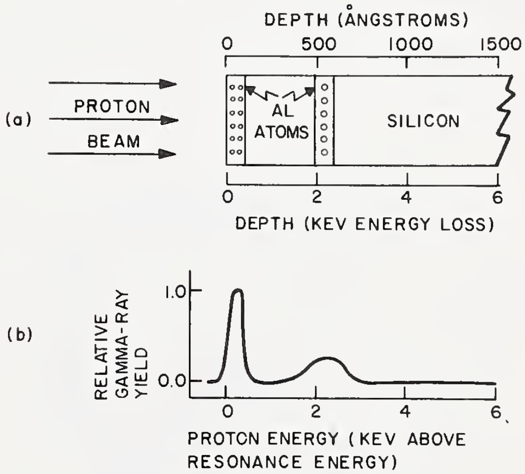

Figure 2. Diagram illustrating the relationships between depth-concentration profiles and yield curves.

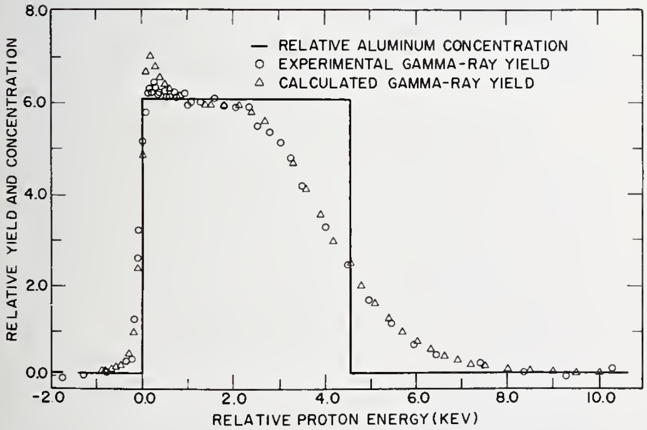

Figure 3. Experimental yield, calculated yield, and "profile" for an Al_2O_3 target 4.6-keV (600 Å) thick.

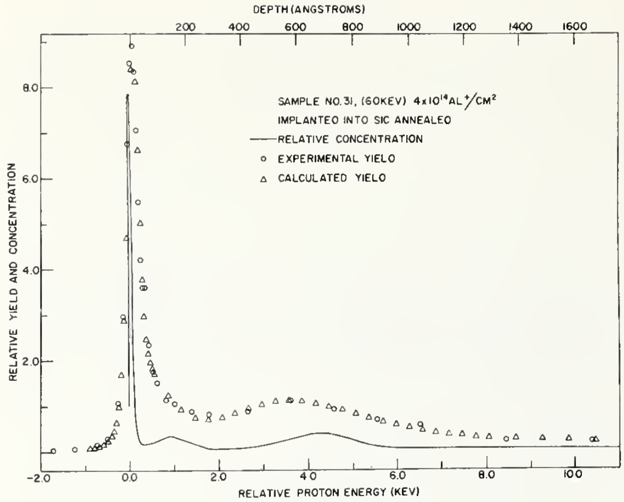

Figure 4. Profile, experimental yield, and calculated yield for SiC implanted to a fluence of 4 × 10^{14}Al atoms/cm^2 at an energy of 60 keV and then annealed at 1400° C.

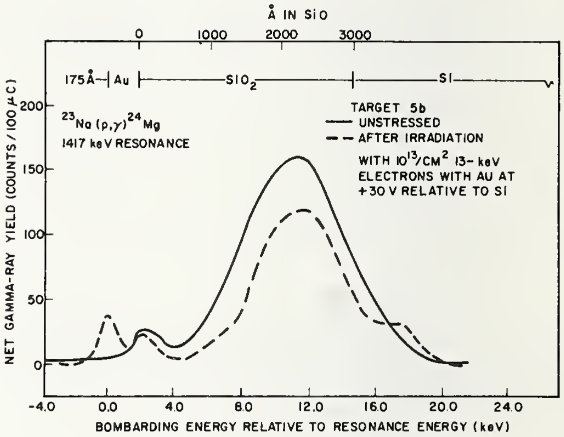

Figure 5. Depth-concentration profiles for sodium implanted at an energy of 60 keV to a fluence of 10^{15}/cm^2 into an Au/SiO$_2$/Si test structure. The solid line shows the measured yield curve for the as-prepared specimen; the dashed curve shows the yield curve after the specimen has been irradiated with 13 keV electrons to a fluence of 10^{13}/cm^2 with the gold layer at +30 V relative to the Si during the irradiation.

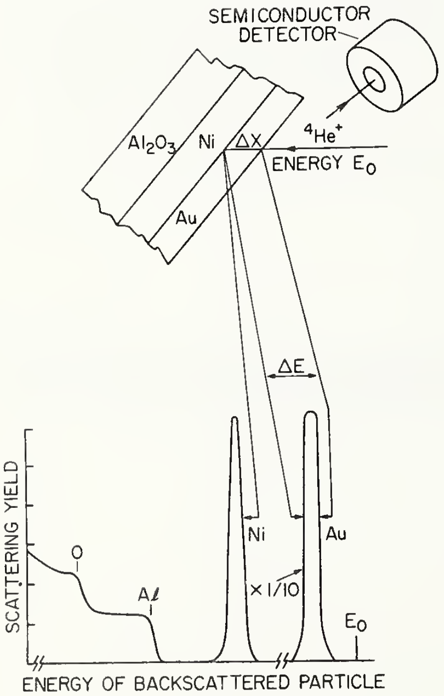

Figure 6. Diagram illustrating the Rutherford backscattering method for obtaining depth-concentration profiles.

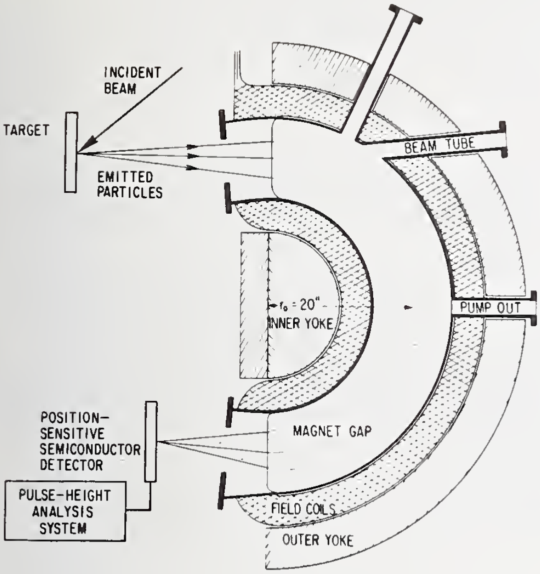

Figure 7. Diagram illustrating the use of a charged-particle magnetic spectrometer in the detection leg of a Rutherford backscattering apparatus.

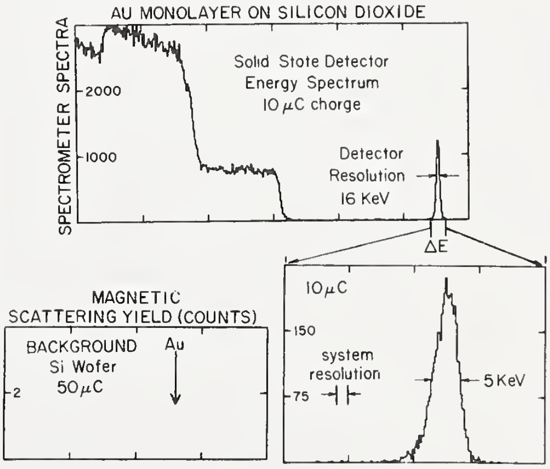

Figure 8. Rutherford backscattering spectra illustrating the superiority of a magnetic spectrometer over a semiconductor detector in the detection leg of a Rutherford backscattering apparatus. The spectrum at the top was obtained from a very thin layer of gold on silicon dioxide with a semiconductor detector; the gold peak at the right hand side of the spectrum has a full width at half maximum of 16-keV. The lower-right spectrum was taken with a magnetic spectrometer; only the gold peak is shown and it has a full width at half maximum of 5 keV, less than half of which is introduced by the detection system. The lower left "spectrum" is for a silicon dioxide target with no gold layer and the magnetic spectrometer and shows that with five times as many incident α particles as for the lower-right spectrum, no background counts were registered.

DISCUSSION OF THE PAPER

Harrington: The magnetic spectrometer that you use depends, of course, on ions coming from the surface. From what depths can these reflected particles originate and still be ions? Are not most of the particles from, say, the silicon substrate coming back as neutrals?

Dunning: At this energy many particles come off as charged particles and so I would say one can analyze at least to micron depths.

Harrington: I was under the impression that most of the particles were coming out as neutrals from those depths. Are they still ionized?

Dunning: My impression is that, at MeV energies, as soon as an ion enters a solid it is almost entirely stripped. It will pick up a little charge and loose a little charge as it goes through but we always think of ions at MeV energies as being almost completely stripped.

Dobrott: You showed us a profile of a sodium ion implanted oxide. You told us that the sodium flux was $10^{15}/cm^2$ but do you happen to remember at what energy the implant was made?

Dunning: The energy for the sodium implant I think was 60 keV.

Dobrott: Then the actual peak that you did see was probably a little bit deep for the theoretical projected range of the sodium in the SiO_2.

Dunning: It is not exactly according to theory but I think it is not far off.

Dobrott: The peak was shown to fall between two thousand and twenty-five hundred Angstroms into the sample, and that is pretty deep.

Dunning: No, I would say that that was fairly near the theoretical peak.

NBS Special Publication 400-23, ARPA/NBS Workshop IV, Surface Analysis for Silicon Devices, held at NBS, Gaithersburg, Maryland, April 23-24, 1975 (Issued March 1976)

APPLICATIONS OF SCANNING AUGER SPECTROSCOPY (SAM) TO THE SILICON INTEGRATED CIRCUIT (SIC) TECHNOLOGY

Joseph M. Morabito

Bell Laboratories
Allentown, Pennsylvania 18103

I. INTRODUCTION

Auger electron spectroscopy is a technique based on the emission and energy analysis of secondary electrons produced by a high energy (3-10 keV) electron beam. The energy of a small fraction of the secondary electrons can be related to the core levels of a target atom; these electrons, the Auger electrons, have an escape depth in the range of approximately 5 to 20 Å, making Auger electron spectroscopy a truly surface sensitive technique which can detect all elements with exception of H and He down to approximately 10^{12} atoms per centimeter squared or .1 atom percent. The technique, in principle, is nondestructive; but electron beam damage and electron beam desorption effects can occur. In combination with insitu ion sputtering, in-depth profile analysis can be obtained and by the use of multiplexing, several elements can be monitored while sputtering through the film. By the use of finely focussed electron beams, or optical methods, selected area surface analysis can also be obtained, which is very important when analyzing actual integrated circuits. Quantitative analysis is also possible along with Auger imaging, which provides a surface distribution map of the impurities on the surface.

II. INSTRUMENTATION

Figure 1 shows some of the basic components and associated electronics of the commercially available PHI scanning Auger microprobe.(1) This consists of an electron gun used to excite the Auger electrons and a spectrometer for energy analysis. Electrons of a well-defined energy are focussed on the exit aperture of the spectrometer and enter an electron multiplier where they are detected by phase sensitive detection using a lock-in amplifier. The electron gun consists of 4 basic components; a tungsten triode source, condenser and objective lenses, and deflection plates. Its operation is somewhat similar to a scanning electron microscope. The condenser lens and the objective lens are used to demagnify the crossover formed by the triode source. The deflection plates are used to raster the beam over the sample. Electron beam spot sizes down to approximately 5 microns can be obtained and the beam currents possible are in the range of 10 nanoamps to 10 microamps. To locate areas of interest on the sample, absorbed current micrographs or secondary electron micrographs are used. Useful magnification is about 1,000 X.

Line scans and Auger imaging provide information on the variations of surface impurities. The Auger imaging is obtained by rastering the primary electron beam and intensity modulating the z axis of a CRT. Table I shows the minimum time constant required for the analysis of 10 and 1 atom percent, corresponding to signal-to-noise ratios of 10 to 1 and 100 to 1, as a function of varying beam size (in μm^2) for current densities of 10^{-7} amps per micron squared and 10^{-6} amps per micron squared. A practical limit on the lock-in amplifier is approximately 10 seconds. This is due to amplifier drift. This limit is reached at 1 atom percent for a beam area of approximately 10 microns squared for a current density of 10^{-7} A/μm^2. If the current density is increased from 10^{-7} to 10^{-6} A/μm^2, this limit of 1 atom percent is reached at a beam area of approximately 1 micron squared. Beam areas in the range of 20 to approximately 1 μm^2 are very useful in the analysis of actual integrated circuits. As the beam size is decreased, the time that it takes to do the analysis increases, and this time is inversely proportional to the beam current. Current densities in the 10^{-7} A/μm^2 range can be obtained, as shown by the work of Brandis(2), with the tungsten triode source down to approximately 1 micron squared. Current densities in the range to 10^{-6} can only be obtained with a lanthium hexaboride source, which is a brighter source. However, at these beam current densities there is a possibility of beam desorption and beam damage effects, particularly in the case of insulators.

III. MODES OF OPERATION

The Auger technique, like SIMS, has basically three modes of operation: a) Auger spectra, b) Auger images and c) in-depth profile analysis. These three modes of operation (illustrated in Figure 2) provide a truly three-dimensional microchemical analysis. Auger spectra are used to detect and identify surface impurities and impurities in the bulk of the sample. Spectral interferences are less of a problem in Auger Spectroscopy than in SIMS, but they can occur since the inherent energy spread of Auger electrons is such that it is difficult to resolve peaks that are within 1 or 2 eV of each other. When this becomes a problem, the best solution is to add an X-ray source and to obtain photoelectron or ESCA spectra. Some of the unique features of the ESCA technique have been described in the literature.(3) One of its unique features is that it can provide information on chemical environment, but it is also possible to occasionally obtain information on chemical environment using the Auger spectra.(4,5,6) This information is contained in peak energy shifts, changes in peak shape, and in fine structure on the low energy side of the peak. Figure 3 shows Auger spectra which were obtained on a silicon nitride layer of a silicon diode array. The spectrum at top is the spectrum obtained prior to sputtering. Prior to sputtering the silicon is partially present in oxide form(5) and the low energy silicon transistion is occurring at approximately 78 eV. After sputtering we have removed the oxide, the silicon is now no longer present as oxide and its energy has shifted from 78 eV to approximately 90 eV which is a shift of 12 eV. In the case of pure silicon the low energy peak occurs at 92 eV. Although such changes in the Auger spectra are often rather difficult to interpret, they do provide a fingerprint like the SIMS spectra of the chemical environment.

A lateral resolution of approximately 0.5 microns has been demonstrated(2) in Auger imaging. Auger imaging does not require sample consumption, but is limited to approximately 1 atom percent concentration.

Auger profiling is particularly useful when monitoring concentration from the surface into the bulk of a thin film, or when the extent and amount of interdiffusion in multilayer film is of interest. Figure 4 shows an Auger profile of a titanium-copper-nickel-gold (TCNA) thin film system(7) after 4 hours of 350°C. The copper and nickel have completely diffused through the gold layer and are present on the surface as oxides. The metal oxides can interfere, for example, with TC bonding to this system.(7) Copper is present throughout the nickel diffusion barrier layer and has also diffused into the titanium glue layer. The depth resolution possible with Auger profiling is primarily limited by artifacts inherent in the sputtering process. In polycrystalline films the depth resolution is in the range of 10 to 30 percent of the thickness removed by sputtering.(8) Some of the problems inherent in sputtering are: First, the possibility of differential sputtering; this is particularly true in the case of alloys.(9) It is not always possible to eliminate, but it can be minimized by the use, when possible, of higher energy (larger escape depth Auger electrons) because these transitions are less sensitive to the change in surface composition(9) which results from differential sputtering. Next, the recoil or "knock on" phenomenon(10); this is an effect whereby lattice atoms are pushed deeper into the solid during the sputtering process. It is a cumulative affect, i.e., a function of film thickness. This can sometimes be minimized by the use of low energy primary ions in the range of around 500 eV to about 2 KeV. There is also a possibility of the redeposition of sputtered atoms. This can be avoided by careful instrument alignment. Topographical changes can also occur during the sputtering operation. The best way to avoid these is to use smooth substrates when possible. And, finally, probably one of the worst problems, a varying sputtering rate throughout the film due to changes in composition or changes in the alloying that occurred during the interdiffusion process. This greatly complicates the assignment of an accurate depth scale. Accurate depth scales are important when extracting diffusion coefficients from Auger profiles.(8,11) However, the work of Dahlgren and McClanahan(12) has shown, in the case of alloys where the solute is about 10 atom percent or greater, that the lower sputtering yield element actually controls the sputtering rate. By using this fact, it is often possible to assign a rather accurate depth scale from measurements of sputtering rate (z) and time.(8)

IV. STATUS OF QUANTITATIVE ANALYSIS

There are essentially three methods of performing quantitative Auger analysis. Method A is a method based on the use of standards prepared by techniques such as ion implantation,(13) reactive sputtering,(14) and controlled doping.(15) Method B is the use of pure elemental samples and sensitivity factors with an equation of the following form:

$$C_i = \frac{I_i/A^j_{rel}}{\sum_{j=1}^{m} I_j/A^j_{rel}} \qquad (1)$$

where C_i is the concentration of element i, I_i is the measured Auger peak height, A^j_{rel} is the relative Auger yield of element i referenced or normalized to some matrix element, and j is a running index summed over all the elements present in the sample. Method C is a technique which is independent of any standards - called the first order approximation method.(16) Generalized models, e.g., models such as those used for quantitative analysis using the electron microprobe(17) or SIMS(18) technique, do not at the present time exist for Auger electron spectroscopy. The major reason for this is that we do not have an accurate data base on the ionization cross sections, the escape depths, or on the backscattering correction. Other reasons include: the sputtering artifacts mentioned and the fact that it is difficult to perform background correction procedures in Auger spectroscopy. Figure 5 shows a calibration curve(15) obtained on samples which were prepared by bulk doping. With these calibration curves it is possible to measure the concentration of phosphorus and boron in silicon. This data also establishes the detectability limits for these dopants in silicon. In this case, the detectability limits for boron and for phosphorus in silicon is approximately 8×10^{18} atoms per cubic centimeter. Method B has been successfully applied to numerous multicomponent systems.(8,19) The first order approximation method does not depend on standards, but is based primarily on the fact that the Auger yield is determined primarily by the ionization cross section (Φ), the transmission of the spectrometer (η), and the Auger escape depth (d). Work to date has shown that the ionization cross section (Φ) is proportional to one over the square of the Auger energy, at least for K and L transitions. For the CMA analyzer, the transmission (η) is linear with energy. Escape depths (d) in a range of 100-1,000 eV appear to be proportional to the square root of the energy. The product, $\Phi\eta d$, is therefore proportional to one over the square root of the energy. We can use this fact to estimate the Auger yield or sensitivity factors. Table II shows some of the results using this method for magnesium oxide, copper oxide, cadmium sulfide, gallium phosphide, and potassium chloride. The results are quite good, particularly since no corrections(9) for sputtering artifacts have been made.

Table III shows a comparison between the bulk detectability limits of Auger and SIMS for the common dopants in silicon and for the light element in tantalum. In general, the detectability limits for Auger are in the range of 10^{19} and 10^{20} - which is much less sensitive with regard to bulk detectability limits than SIMS, which can detect boron down to 10^{14} atoms/cm^3. It is very important to be able to detect concentrations in the range of 10^{17} -10^{14} in the case of transistor fabrication. This is just not possible at the present time with Auger electron spectroscopy. Possible ways to increase the sensitivity of Auger electron spectroscopy are: 1) increase the transmission (η) of the spectrometer; 2) improve the detection scheme, e.g., the use of multichannel analyzer, data smoothing techniques, deconvolution, background correction, integration techniques, etc.; 3) signal processing - analog averaging or digital averaging;* 4) use a different source to excite the Auger electron. Some possibilities include high energy proton sources and ions. With these sources the background could be lower.

V. APPLICATIONS OF SCANNING AUGER MICROPROBE IN SILICON INTEGRATED CIRCUIT (SIC) FABRICATION

a) Analyses Of Contaminated Gold Beam Leads

Gold beam leads are used to attach SIC's to gold metallized ceramic. Any contamination of these leads or of the gold on the ceramic can prevent intimate gold-to-gold contact, which results in unreliable bonding. Figure 6 shows an Auger spectrum and absorbed current micrograph of a contaminated beam lead. The beam lead is ∿ 4 mils in width. The bright lower line on the micrograph indicates that most of the beam current is absorbed by the conducting beam lead which appears dark. The major surface contaminants are carbon and oxygen with trace amounts of copper, sodium, and silicon. Although the high energy gold transition is detectable, the low energy gold transition at 69 eV is not. This low energy gold transition has an escape depth of ∿ 5 Å and is completely attenuated by the carbon layer. The carbon layer does not, however, completely attenuate the high energy gold transition at 2,017 eV, which has an escape depth of ∿ 20 Å. This suggests that the carbon layer is no greater than 20 Å in thickness. The carbon Auger image obtained showed the carbon to be homogeneous across the surface, but the copper and silicon Auger images suggest a heterogeneous distribution for these elements. Figure 7 shows the in-depth profile of carbon. As the carbon film is removed by sputtering, the intensity of the low energy gold transition increases.

The thickness of the carbon layer can be calculated by the following expression(20)

$$\frac{I_c}{I_{Au}} = \frac{I^\circ_c}{I^\circ_{Au}} \left[\exp\left(\frac{x_c}{d_{Au}}\right) - \exp\left(x_c \frac{d_c - d_{Au}}{d_c d_{Au}}\right) \right] \quad (2)$$

---

* This is not a very practical approach since a factor 10 increase in sensitivity would require a factor 100 increase in analysis time.

where I_c/I_{Au} is the measured carbon peak height normalized to the high energy (2,017 eV) gold peak, and I°_c/I°_{Au} is the ratio of the 272 eV carbon Auger peak height to the 2,017 eV peak height for carbon and gold in the pure state. x_c is the thickness of the carbon layer, d_c is the escape depth of the carbon 272 eV Auger electrons and d_{Au} is the escape depth of the 2,017 eV gold Auger electrons. Equation 2 can be simplified to

$$x_c = d_{Au} \ln\left(\frac{I_c/I_{Au}}{I^\circ_c/I^\circ_{Au}}\right) \qquad (3)$$

which has been plotted for d_{Au} equal to 4, 6, and 10 Å in Figure 8. These curves can then be used to estimate the thickness of the carbon layer from the data shown in Figure 6. The thickness of the carbon layer for $I_c/I_{Au} = 35.2$ is in the range of 8 Å (for d_{Au} = 4 Å) to 20 Å (for d_{Au} = 10 Å). It is doubtful that this amount of carbon could seriously interfere with bonding. Therefore, the carbon layer is most probably polymerized by the high energy electron beam, leaving behind a carbon layer of reduced thickness. There is, in addition, the possibility of beam desorption of some of the carbon present on the surface during analysis. Therefore, the actual thickness of the contamination layer prior to electron beam excitation is perhaps a factor 5 higher, i.e., in the range of 40 to 100 Å, which would definitely inhibit bonding.

b) Analysis of Contaminated Gold Plated Ceramic

Figure 9 shows the Auger results obtained on a gold plated ceramic after pre-bond cleaning. Pre-bond cleaning which includes a heat treatment of 120°C for 1 hour has increased the Cu (920 eV),Au (239 eV) and Ag (354 eV)/Au (239 eV) ratios from an average of .36 to 1.24 for the "as-received" sample to .49 and 1.70 respectively. This increase is due to diffusion from the bulk via grain boundaries. There is also a large increase in the oxygen peak. The large increase in oxygen suggests that these impurities are present as oxides. There is, however, no characteristic change in the Auger spectra of Figure 9 (e.g., peak energy shifts, additional plasma loss peaks) which can be used to verify that oxidation has actually occurred, but Schon(21) has recently used X-ray induced Auger emission and photoelectron spectroscopy to identify the presence of Cu, Cu_2O and CuO. Unfortunately, the energy resolution required(21) is beyond the capability of most spectrometers used in Auger electron spectroscopy.

The surface concentration of Ag and Cu varied in the range of 1 to 4 at. %. This magnitude is consistent with the fact that 50 ppm (at. %) in the bulk, if completely concentrated within the first 10 Å of the surface, would correspond to 4.95 at. % and to 9.9 at. %. The above calculations were made for a gold bonding pad with an area of 2.25×10^{-2} cm^2 and a gold thickness of 10^{-4} cm or 1 μm. Figure 10 shows the calculated surface concentration, C_S^{cal}, which would result if all of the bulk impurities should concentrate within the first 10 Å of the surface. The bulk concentration was varied from 5 to 300 ppm (at. %). Although it is highly improbable that all or even most of the bulk impurities will concentrate on the surface after processing prior to bonding, a fraction (α) of the impurities will, and this fraction can be measured by quantitative Auger analysis.

The presence of Sn (Figure 9) is apparently due to inadvertent contamination introduced during pre-bond cleaning, but the Cu and Ag are codeposited during plating. A regression analysis (shown in Figure 11) of the bonding and Auger data showed the correlation between the presence of Ag, Cu, O, and Sn on the surface and poor bonding to be 0.74. The impurities present in the bulk are therefore segregating to the surface during thermal processing, oxidize, and act as barriers to intimate gold-to-gold contact.

c) SAM Analysis of Laser Debris On Ti-Pd-Au Resonator Electrodes

The frequencies of Ti-Pd-Au resonator electrodes can be raised by vaporizing portions of mass from the resonator electrode.(22) Using the focussed beam from a Q-switched Nd:YaG laser (λ = 1.06 μm), a series of 25 μm diameter holes on approximately 125 μm centers are vaporized as shown in Figure 12. When nominal frequency has been reached, laser trimming is terminated. The use of an on-line computer and optical beam steering techniques permit raster scanning by which each resonator is adjusted in three successive passes. In this manner the effects of thermal shock can be minimized and the adjustment control is as precise as the vacuum operation (± 12 Hz). All initial filter electrical requirements can be met; i.e., adequate control over resonator frequencies can be exercised. However, since the laser machining involves the melting and evaporation of material from the acoustically active region of the resonator, the enhancement of long-term aging might result from this operation.

A pair of thin film electrodes which form the resonator region are composed of Ti-Pd-Au tri-metal thin films. As the focussed laser pulse strikes the top electrode, a small hole is produced, and material from this region is melted and evaporated. Most material is evaporated; however, some material melts, pulls away and forms a lip surrounding the hole. Other material is ejected and redeposited in the immediate vicinity of the hole. An additional problem is encountered since the quartz substrate is only 200 μm thick. When the laser beam strikes the top electrode, it vaporizes in a matter of a few nanoseconds.(23) The pulse width of the Q-switched TaG laser is approximately 300 nanoseconds. After the top electrode is vaporized there is still sufficient beam energy to vaporize a hole in the bottom electrode (Figure 12 - 'laser exit') even though the beam is defocussed and scattered by two 'rough' quartz surfaces. The vaporization of the bottom electrode is markedly different from that of the top electrode, as the Ti layer next to the quartz is vaporized first while the outer Pd-Au layers are still momentarily intact. The diameter of the laser exit hole is (15 μm) considerably smaller than that produced on the top electrode (25 μm). SEM micrographs (Figure 12) were taken of both laser entrance and exit holes. The entrance hole has a minimal lip formation and shows no obvious damage to the substrate. The laser exit hole has a somewhat larger lip formation, but again no obvious damage to the substrate can be seen.

Figure 13 (insert) shows an adsorbed current image of entrance laser machined craters. The bright line across the micrograph indicates the dynamic position of the primary electron beam which is within a beam diameter (∿ 5 μm) of the laser hole. The point analyses obtained in the vicinity of the crater defined by the bright line is also shown in Figure 13. The selected area analysis showed that Ti, Pd, and Si (in the form of SiO_2) are present in the vicinity of the crater, but are <u>not</u> present about ∿ 50 μm away from the craters as shown in Figure 14. Carbon, an ubiquitous contaminant present in cleaning solvents and laboratory air, is present over the entire surface. S and Cl, which are common impurities in Pd(24) and Ti(25), are also detected (see Figure 13). The impurities Cl and S are also common impurities in the solvents used in cleaning (such as trichloroethylene, acetone and ethyl alcohol). The intensity of the Ti, Si and Pd peaks varied in the vicinity of each crater. This is attributed to pulse-to-pulse variation in laser intensity and in point-to-point variations in beam attenuation in focussing lens. The laser is operated at power levels which are near threshold values to initiate vaporization; thus, small differences in power levels could easily account for the observed hole-to-hole variations. Auger images of Ti and Pd could be taken in the vicinity of the craters, but surface charging due to exposed quartz (SiO_2) at the bottom of the crater prevented the taking of well-defined images at that region. The images obtained in the vicinity of the crater prior to charging indicated that the Ti-Pd debris layer is uniform and extends approximately 25 μm beyond the crater. This fact and the fact that the high energy gold transitions (approximately 20 Å escape depth) were also detected indicates that the debris surrounding the crater is on the order of 20 Å in thickness. It is also possible to determine from Auger data that the titanium debris is completely oxidized, since the oxidation of titanium has a definite effect on the titanium LMM Auger triplet (387, 418, 460 eV). The 418 eV transition is the most sensitive to oxidation and will decrease in amplitude relative to the 387 eV peak, which is smaller in amplitude for <u>unoxidized</u> titanium.(25,26) Selected area in-depth profile analysis showed that the entire titanium debris layer was oxidized; i.e., the amplitude of the 387 eV Ti transition was larger than the 418 eV Ti transition and the oxygen peak (510 eV) was also high. Removal by insitu on sputtering of the debris layer (∿ 20 Å) showed complete absence of the 387 and 415 eV Ti peaks, which also was accompanied by almost complete attenuation of the oxygen peak.

The analysis in the vicinity of the <u>exit</u> laser machined holes was very similar to that previously discussed for the entrance holes. The Ti-Pd debris again extended approximately 25 μm around the exit crater. Thus, from the debris distribution analysis, the laser exit hole did not exhibit different characteristics.

VI. <u>SUMMARY</u>

Auger electron spectroscopy is capable of three-dimensional selected area analysis. Of the techniques described in this monograph, with the possible exception of SIMS, it is the only analytical technique which can perform a selected area analysis on dimensions which are of interest in integrated circuit processing. Quantitative analysis is possible by means of calibration standards, pure standards, and a first order approximation method. Detectability limits are in the range of 0.1 atom percent.

Future possibilities include the development of techniques to increase the sensitivity of Auger electron spectroscopy, the commercial availability of instrumentation which combine Auger with SIMS and ESCA, and the development and routine use of ∿0.5 µm electron beam sizes with sufficient current for practical analysis times.

REFERENCES

1. Physical Electronics, Inc., Eden Prairie, Minnesota.
2. Brandis, E. K., *Proc. of Ninth Annual Conf. Microbeam Analysis Soc.*, Ottawa, Canada, 45A, July 22-26, 1974.
3. *Electron Spectroscopy,* D. A. Shirley, Ed., (North Holland Publishing Company, Amsterdam, The Netherlands, 1972).
4. Bassett, P. J., and Gallon, T. E., *J. Electron Spectroscopy and Related Phenomena* 2, 101 (1973).
5. Amelio, G. F., *Surf. Sci.* 22, 301 (1970).
6. Grant, J. T., and Haas, T. W., *Surf. Sci.* 24, 332 (1971).
7. Morabito, J. M., Thomas, J. H., and Lesh, N. G., to be published in special issue of *IEEE Parts, Hybrids, and Packaging.*
8. Hall, P. M., Morabito, J. M., and Poate, J. M., to be published in *Thin Solid Films.*
9. Shimizu, H., Ono, M., and Nakayama, K., *Surf. Sci.* 36, 817 (1973).
10. Schulz, F., Wittmaack, K., and Maul, J., *Rad. Effects* 18, 211 (1973).
11. Hall, P. M., and Morabito, J. M., to be published in *Surf. Sci.*
12. Dahlgren, S. D., and McClanahan, E. D, *J. Appl. Phys.* 43, No. 4, 1514 (1972).
13. Morabito, J. M., and Tsai, J. C. C., *Surf. Sci.* 33, 422 (1972).
14. Morabito, J. M., *Anal. Chem.* 46, 189 (1974).
15. Thomas, J. M., and Morabito, J. M., *Surf. Sci.* 41, 629 (1974).
16. Morabito, J. M., *Surf. Sci.* 49, 318 (1975).
17. Castaing, R., These de Doctorat, Universite de Paris (1951), Publication Onera (1955).
18. Anderson, C. A., and Hinthorne, J. R., *Anal. Chem.* 45, 1421 (1973).
19. Palmberg, P. W., paper presented at *Symposium on Surface and Near Surface Chemical Characterization,* Am. Inst. Metal. Engrs., Toronto, May 18-22, (1975).
20. Holloway, P. H., to be published.
21. Schon, G., *Surf. Sci.* 35, 96 (1973).
22. Hokanson, J. L., and Unger, B. A., *J. Appl. Phys.* 40, 3157 (1969).
23. Masumura, R. A., and Achter, M. R., *Appl. Phys. Lett.* 16, 395 (1970).
24. Tracy, J. C., and Palmberg, P. W., *J. Chem. Phys.* 5, 852 (1969).
25. Bishop, H. E., Riviere, J. C., and Coad, J. P., *Surf. Sci.* 24, 1 (1971).
26. Morabito, J. M., *Thin Solid Films* 19, 21 (1971).

TABLE I

THE MINIMUN TIME CONSTANT, τ_{MIN} REQUIRED FOR AUGER SURFACE ANALYSIS AS A FUNCTION OF BEAM SIZE (μm^2) FOR A CONSTANT CURRENT DENSITY (j)

$j = 10^{-7}\ A/\mu m^2$

		A	A	A	A
		$10^3 \mu m^2$	$10^2 \mu m^2$	$10\ \mu m^2$	$1\ \mu m^2$
S/N	C(at %)	τ_{MIN}	τ_{MIN}	τ_{MIN}	τ_{MIN}
10/1	10	1×10^{-2} SEC.	.1 SEC.	1 SEC.	10 SEC.
100/1	1	.1 SEC.	1 SEC.	10 SEC.	100 SEC.

$j = 10^{-6}\ A/\mu m^2$

		A	A	A	A
		$10^3 \mu m^2$	$10^2 \mu m^2$	$10\ \mu m^2$	$1\ \mu m^2$
S/N	C(at %)	$\tau_{MIN.}$	$\tau_{MIN.}$	$\tau_{MIN.}$	$\tau_{MIN.}$
10/1	10	1×10^{-3} SEC.	.01 SEC.	.1 SEC.	1 SEC.
100/1	1	.01 SEC.	.1 SEC.	1 SEC.	10 SEC.

$\tau_{MIN.} \propto \frac{1}{JA}$ OR $\frac{1}{i_B}$

TABLE II

CALCULATED COMPOSITIONS OF COMPOUND STANDARDS

SAMPLE	A_{Rel}	CALCULATED COMPOSITION*
MgO	1.50	56 at. % O 44 at. % Mg
Cu_2O	1.34	35 at. % O 65 at. % Cu
CdS	1.57	48.5 at. % S 51.5 at. % Cd
GaP	2.99	47 at. % P 53 at. % Ga
KCl	1.18	47.4 at. % Cl 52.6 at. % K

*ALL DATA (EXCEPT MgO) WERE TAKEN WHILE SPUTTERING.

TABLE III

COMPARISON OF BULK SENSITIVITY LIMITS FOR P, B, AND As IN SILICON AND FOR N, O, C IN TANTALUM USING AES AND SIMS

ELEMENT	TECHNIQUE	DETECTABILITY LIMIT
N, O, C	AES	10^{19} atoms/cm^3
N	SIMS	10^{19} atoms/cm^3
C, O	SIMS	10^{17} atoms/cm^3
P, B	AES	10^{19} atoms/cm^3
As	AES	10^{20} atoms/cm^3
B	SIMS	10^{14} atoms/cm^3
P	SIMS	10^{17} atoms/cm^3
As	SIMS	10^{18} atoms/cm^3

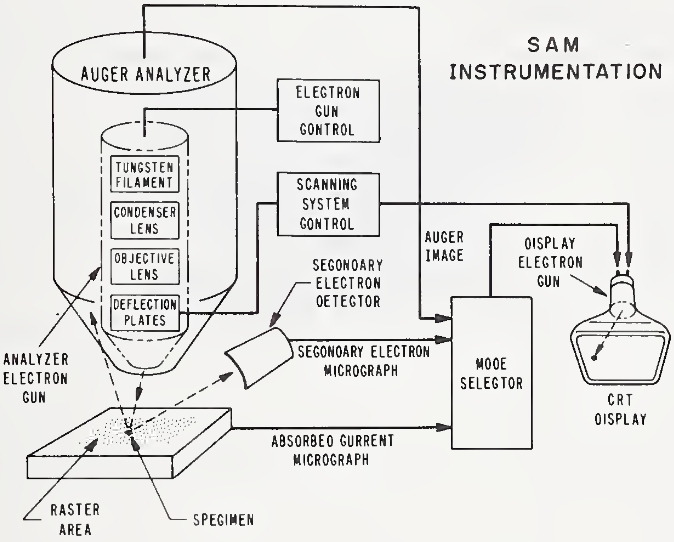

Figure 1. Schematic of SAM instrumentation.

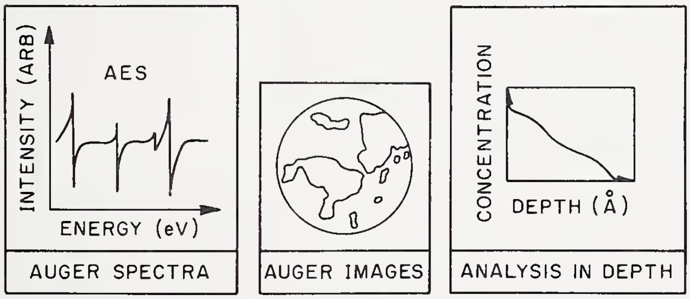

Figure 2. Modes of operation for AES.

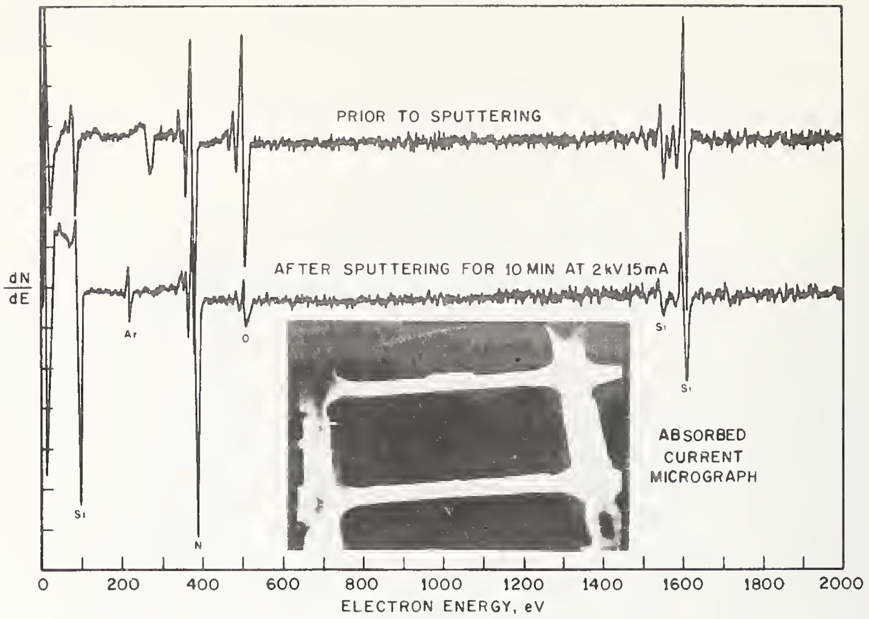

Figure 3. SAM analysis of a silicon nitride passivated layer of a "good" diode prior to and after sputtering. N ∿ 55 at.% or Si_3N_4.

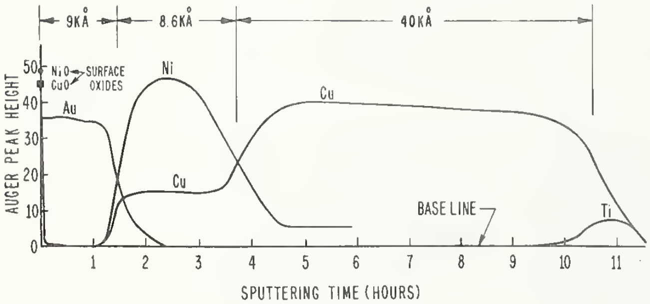

Figure 4. Auger in-depth profile of TCNA after 4 hours at 350° C.

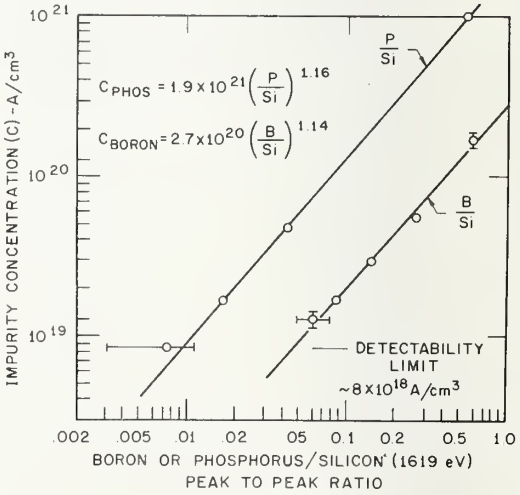

Figure 5. Auger calibration curves for B and P in silicon.

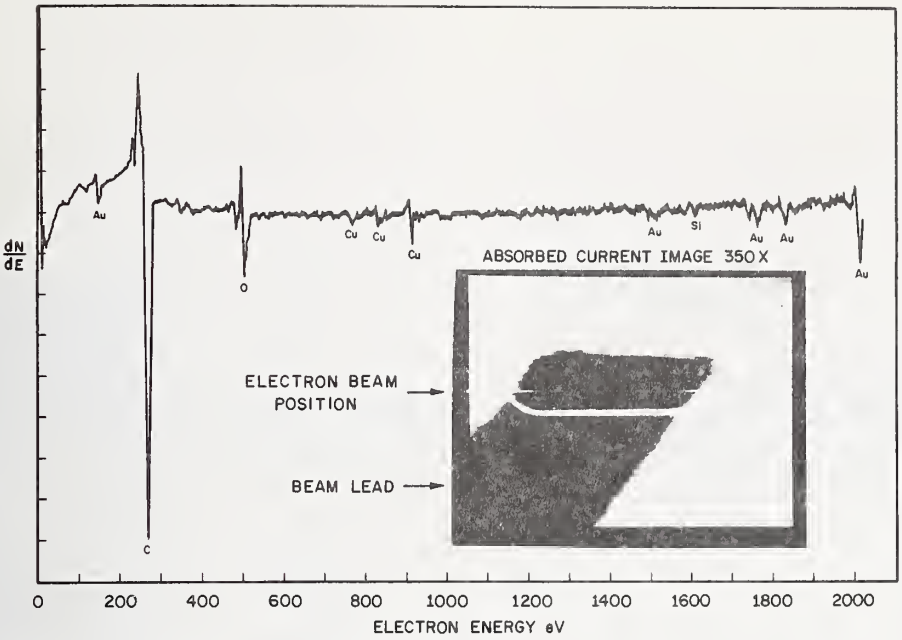

Figure 6. Auger spectrum and absorbed current image of contaminated beam lead prior to in-situ ion sputtering.

Figure 7. In-depth profile of a carbon contaminated beam lead.

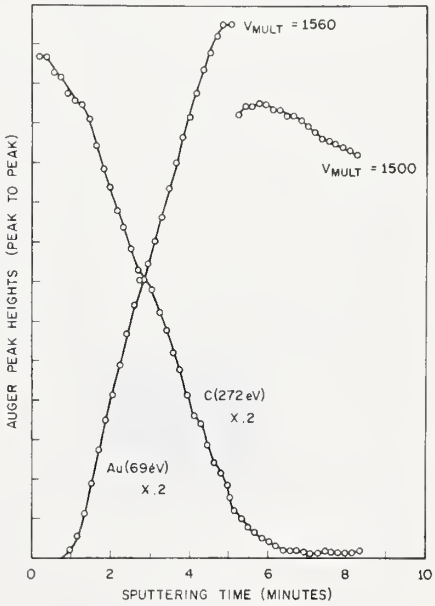

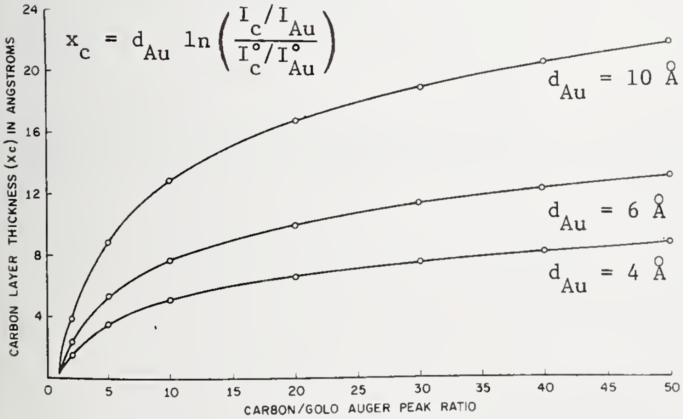

Figure 8. Carbon layer thickness vs. the normalized Auger peak heights (C/Au) for carbon escape depths (d_c) of 4 Å, 6 Å and 10 Å.

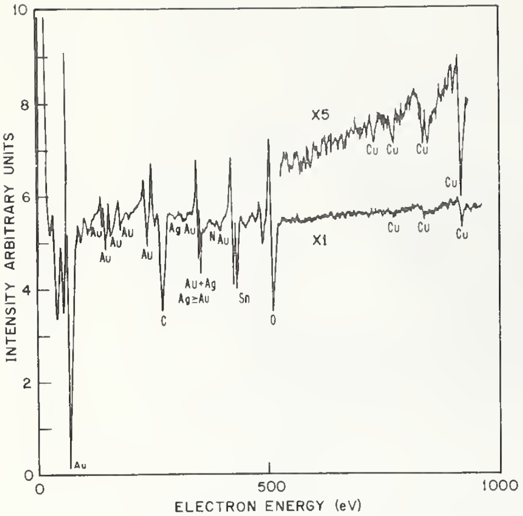

Figure 9. Auger analysis after pre-bond cleaning of gold plated ceramic.

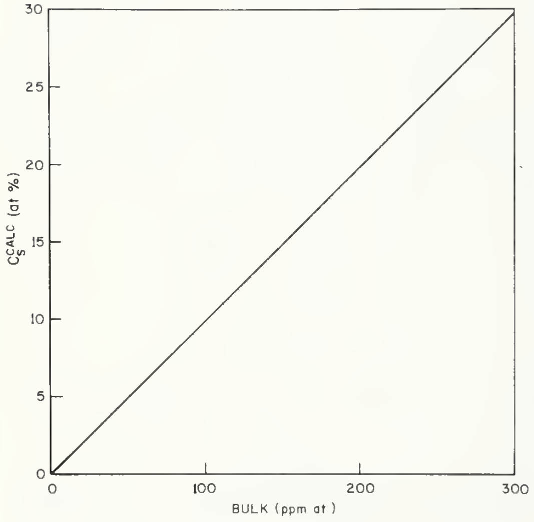

Figure 10. Calculated surface concentration (C_s^{calc}) assuming complete segration to the surface as a function of bulk concentration (ppm at.).

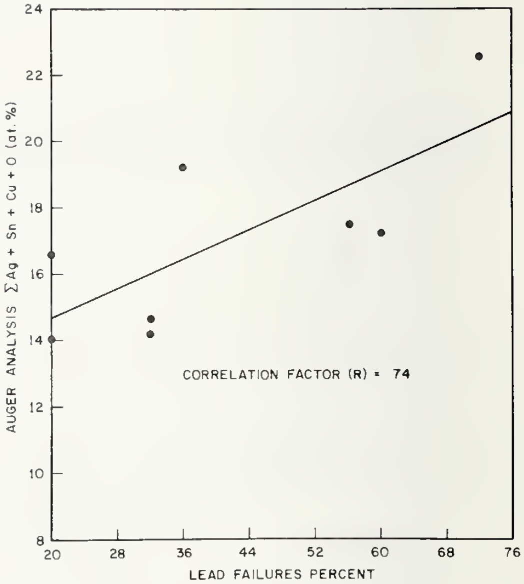

Figure 11. Regression analysis of Auger data vs. lead failures (percent).

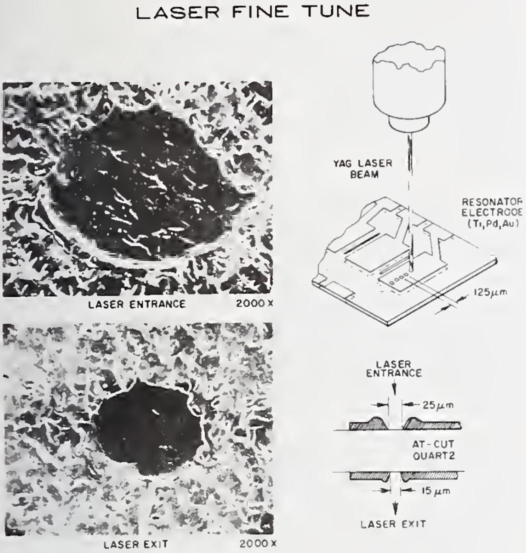

Figure 12. Schematic of laser fine tune process. SEM of laser entrance hole shows minimal lip formation and absence of substrate damage. SEM of laser exit hole shows smaller hole with somewhat larger lip formation, but no damage to substrate.

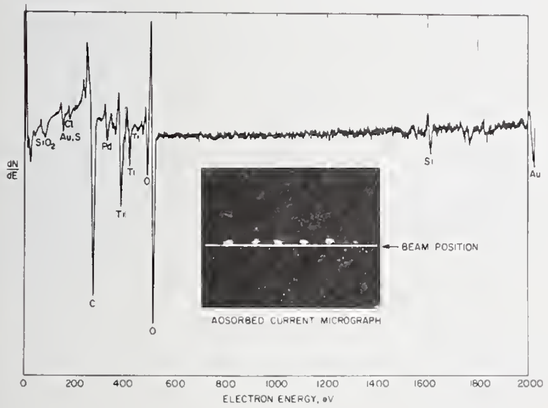

Figure 13. Absorbed current image (insert) and SAM spectrum in vicinity of laser machined holes.

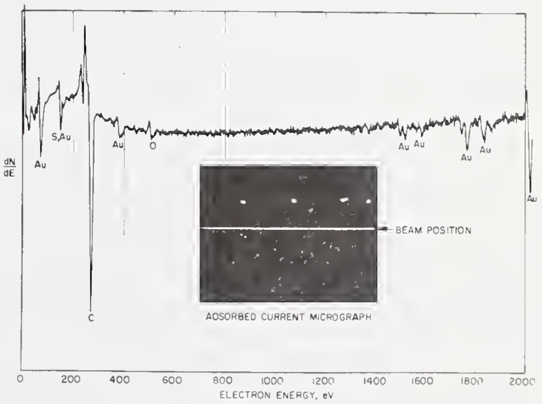

Figure 14. Absorbed current image (insert) and SAM spectrum away from laser machined region.

DISCUSSION OF THE PAPER

Participant: I wonder if you could clarify exactly which of the impurities was causing the beam lead bond failures? Was it the carbon, the silver, the tin, or the copper - and how did they manage to get all those impurities in that gold?

Morabito: At different times, different impurities were causing the bond failures. For the example I showed, it was primarily the carbonaceous material. Now various cleaning techniques can be used to remove the carbonaceous material. When this is done there is a possibility that other impurities can start to have an effect. As far as the metallic impurities are concerned, other people have been able to identify that during the plating operation impurities such as copper, iron and silver are codeposited. Silver is actually a part of the gold cyanide solution. These impurities will rapidly diffuse to the surface. In fact, for a certain dimension of beam lead (for example 5,000 Å in thickness and so many angstroms in width) you could actually calculate that 100 ppm of copper in the bulk relocated on the surface would represent a 10 atom percent concentration. This could have a drastic effect on TC bonding and it does.

Dobrott: Would you care to comment on the fact that all the Auger spectra showed gold but were conspicuously absent of sodium or potassium. Could you comment on the sensitivity of Auger spectroscopy these elements?

Morabito: I can show you many spectra where we do see sodium. The one unique thing about sodium is that it is very rapidly beam desorbed. Anyone doing Auger spectroscopy has seen sodium; not routinely, but very often. Carbon is perhaps the more routine. I do not really expect sodium to have any affect on bonding. The sensitivities of Auger, as indicated, are not as high as those of SIMS. I am really talking seriously when I say 0.1 atom percent is about the very best Auger can do.

Participant: Where does your contamination come from?

Thomas: Very often you find carbon on top of the gold surface. The explanation which is often given is that carbon diffused to the gold surface very readily, even though there is only a small amount of carbon present in the bulk. Even at moderately low temperatures it can come to the surface. Even if there is no hydrocarbon contamination you will see some carbon on top of the gold.

I would also like to agree with you about the bonding problem. The most frequently recurring problem is really due to the oxides of copper, nickel or iron, rather than the carbon. All of our experiments show that carbon is not really a bonding problem as such, if it is less than 20-25 Å thick, as you said. The real problems are nickel oxide, copper oxide, or iron oxide. Some of the leads have gold plate on copper; the copper can then diffuse through the gold. The copper can also be codeposited in the gold plate, as in your case. There are many possibilities, however carbon is not a problem as far as I can see.

Morabito: In my particular case, the carbon did not come from the plating film.

Whitford: Many semiconductor manufacturers use, as part of their processing, the technique called low temperature ashing, they also do etching work with it. It has been used by the connector industry when they want a good bond and a hermetic seal to glass, rubber or polymer. Just a quick spritz for about 5 minutes in a nitrogen atmosphere at room temperature in a RF plasma insures the bond and takes off any carbon films or any materials that have diffused to the surface. I know the technique has been used in some electron microscopy work instead of ion sputtering to clean surfaces, and it is a lot cheaper too.

Morabito: We are very familiar with that technique.

NBS Special Publication 400-23, ARPA/NBS Workshop IV, Surface Analysis for Silicon Devices,
held at NBS, Gaithersburg, Maryland, April 23-24, 1975 (Issued March 1976)

USE OF AUGER ELECTRON SPECTROSCOPY TO DETERMINE THE STRUCTURE OF SILICON OXIDE FILMS

J. S. Johannessen† and W. E. Spicer

Stanford Electronics Laboratories
Stanford University
Stanford, California 94305

and

Y. E. Strausser

Varian Associates
Palo Alto, California 94305

In the present paper we present experimental results on phase separation in unsaturated silicon oxides[1] and the chemical structure of the SiO_2-Si interface.[2]

The chemical structure of SiO_x is a controversial subject which has received considerable attention in the past. From interpretation of experimental observations, two chemical structure models have emerged. These models are commonly referred to as the microscopic mixture model[3] and the random bonding model.[4]

The microscopic mixture model (MMM) states that unsaturated silicon oxides SiO_x, where $0 < x < 2$ is a stoichiometry factor, are phase separated mixtures of amorphous Si and amorphous SiO_2. Interpretation of radial distribution functions of films of SiO_x give support to this model.[3,5]

Optical reflectance data from unsaturated silicon oxides are interpreted in terms of the random bonding model (RBM)[4], which states that the local atomic arrangement in SiO_x is statistically distributed among five coordinations of Si atoms.

Figure 1 shows how these two models predict the relative amount in each coordination C_z as a function of sample stoichiometry, given by x.[3] The MMM is represented by the broken line. The RBM, represented by full drawn curves, is based on a statistical distribution of tetrahedra of the type Si - $(Si_{z-1}\, O_{5-z})$, where z = 1, 2, 3, 4, 5. The relative amount in each coordination C_z is determined by the overall stoichiometry, as shown in figure 1. Both models are identical for x = 0 and x = 2.

In the present paper we present experimental evidence of phase separation of SiO_2 and Si in unsaturated silicon oxides of stoichiometry SiO_x, where $x < 2$. We make use of high energy resolution Auger electron spectroscopy (AES) in a study of evaporated films of SiO_x and thermally grown SiO_2. Significant chemical structure effects are observed in both the LVV and KLL series of Auger transitions. However, we limit the discussion to the Si_{KLL} spectra because these spectra reflect directly the effect of the changes in the local atomic arrangement around each silicon atom as a result of changes in the overall stoichiometry.

Chemical structure effects or chemical shifts are well known from XPS and ESCA analysis of oxidized silicon[6] and evaporated films of silicon oxide[7], and appear as a 3-4 eV shift in the binding energy of the Si(2p) energy level. We see similar chemical shifts in the silicon $KL_{2,3}L_{2,3}$ Auger transition as indicated in figure 2. In figure 2 we show two experimental transition energies 1618 eV corresponding to elemental silicon x = 0, and 1611 eV corresponding to silicon in SiO_2, x = 2. The straight line between these two values gives an indication of the expected chemical shift in the silicon $KL_{2,3}L_{2,3}$ transition energy as the local coordination around each silicon atom changes. We use the extrapolated Auger transition energies in figure 2 and the coordination factors in figure 1 to calculate the energy dependence of the silicon $KL_{2,3}L_{2,3}$ Auger transition of the two structural models. The result for two stoichiometries is shown in figure 3 where we, for convenience, have chosen a Lorentzian shape of each of the Auger transitions. The half width in this case is slightly less than the experimental half width. The broken curves are the contribution from each of the separate silicon coordinations. There is a pronounced difference between the two models. The MMM shows two distinct Auger transitions, where the peak-to-peak heights depend on overall stoichiometry. The RBM, shows one

---

† On leave from Electronics Research Laboratory (ELAB), University of Trondheim, Norwegian Institute of Technology, Norway.

broadened peak, whose peak-to-peak height and energy position depends on the stoichiometry factor x.

In figure 4 we show a series of experimental Si_{KLL} spectra obtained from a thermally grown oxide x = 2, and from evaporated oxide films $1.2 \leq x \leq 1.9$. The Si (100) substrate is used as reference x = 0. Notice that the spectra for x = 0 and x = 2 are similar, but displaced in energy by $\Delta E \sim 7$ eV. This is the chemical shift due to change in local coordination of the silicon atom. Similar shifts are reported for oxidized silicon.[8] The Auger spectra for intermediate values of x are significantly different. This is particularly pronounced for the lowest value of x, which show two distinct transitions of 1611 eV and 1618 eV. We were not able to obtain SiO, probably due to a finite O_2 background during deposition at 10^{-7} Torr. The experimental conditions are described elsewhere.[9] The stoichiometry factor x is estimated using the O_{KLL} peak-to-peak height normalized to the thermally grown oxide.

The experimental results presently in figure 4 strongly support the MMM, as can be seen when compared with figure 3. Based on the above discussion and our experimental data we are led to the conclusion that unsaturated silicon oxides SiO_x, where $0 < x < 2$, are phase separated and best described by the microscopic mixture model.

We have also performed chemical depth profiling of thermally grown SiO_2 on Si (100). In figure 5 is shown a typical depth profile of an oxide grown to a thickness of 1000 Å at 1200 Å in dry O_2. After oxidation the sample was annealed in dry N_2 and slowly pulled from the furnace. Figure 5 is obtained by automatic multiplexing of the peak-to-peak heights of the O_{KLL} (502 eV), Si_{KLL} (1611-1618 eV), and Si_{LVV} (78-92 eV) Auger transitions.[10] The data points to the left of the origin are steady state values before the onset of the 1 keV Argon ion beam. The small step in the O_{KLL} and Si_{LVV} transitions is most probably due to removal of surface contaminants such as water vapor and carbon. The depth profile of figure 5 shows a uniform SiO_2 film, except in the interface region when there is a dip in the silicon $KL_{2,3}L_{2,3}$ peak-to-peak height. The reason for this dip is clearly shown in the actual real time Auger spectra plotted above the depth profile. The numerals indicate the position of the spectra in the interface region of the SiO_2-Si depth profile.

There are two characteristic features of the depth profile near the interface. Firstly, the Si_{KLL} transition "sees" the interface before the O_{KLL} and Si_{LVV} transitions, and secondly it "sees" a broader interface than the two other transitions. These features are related to the escape depth of the Auger electrons and to the nature of the KLL and LVV Auger transitions.[2]

When the electron escape depth[6,11] is accounted for, we find that the width of the SiO_2-Si interface is on the order of 35-50 Å wide. Interface broadening by the ion beam is estimated to be on the order of 10 to 15 Å.[2] Hence, we are left with a "real" interface width on the order of 20-30 Å. In the interface region, the average stoichiometry is SiO_x, $x < 2$, and the material appears to be phase separated in a similar manner as unsaturated silicon oxides.

In conclusion, we mention that we have made the first observation of chemical shifts in the silicon $KL_{2,3}L_{2,3}$ Auger transition in unsaturated silicon oxide films. We interpret our results in terms of a microscopic mixture of SiO_2 and Si. Chemical depth profiles through thermally grown SiO_2 on Si (100) show a phase separated SiO_2-Si interface of finite width on the order of 20-30 Å. We believe that the positive oxide charge observed in MOS-devices[12], are confined to the connective regions between the two phases at the interface, SiO_2 and Si, respectively.

ACKNOWLEDGEMENTS

Work in part supported by Army Research Office, Contract No. DAHC 0474 G 0215. One of us (J.S.J.) has been partly supported by ELAB and the Royal Norwegian Council for Scientific and Industrial Research.

REFERENCES

1. Johannessen, J. S., Spicer, W. E., and Strausser, Y. E., to be published.

2. Johannessen, J. S., Spicer, W. E., and Strausser, Y. E., to be published.

3. Temkin, R. J., *J. Non-Cryst. Solids* 17, 215 (1975).

4. Phillips, H. R., *J. Non-Cryst. Solids*, 8-10, 627 (1972).

5. Coleman, M. V., and Thomas, A. J. D., *Phys. Stat. Sol.* 22, 593 (1967).

6. Flitsch, R., and Raider, S. I., *J. Vac. Sci. Technol.* 12, 305 (1975).

7. Hollinger, G., Tousset, J., and Tran Ming Due, *Tetrahedrally Bonded Amorphous Semiconductors*, M. H. Brodsky, S. Kirkpatrick, S. and D. Weatre, Eds., p. 102 (Am. Inst. Phys., New York, 1974).

8. Wagner, C. D., *Anal. Chem.* 47, 1201 (1975).

9. Strausser, Y. E., and Johannessen, J. S., An Auger Electron Spectroscopy Study of Silicon Spectra From Silicon Monoxide, Silicon Dioxide and Silicon Nitride, ARPA/NBS Workshop IV, *Surface Analysis for Silicon Devices*, A. G. Lieberman, Ed., NBS Spec. Publ. 400-23 (March 1976).

10. The notation Si_{LVV} is used to show that the LVV spectrum of silicon oxides is composed of molecular orbitals originating both from Si-Si bonds and Si-O bonds.

11. Lindau, I., and Spicer, W. E., *J. Elec. Spectr.* 3, 409 (1974).

12. Deal, B. E., *J. Electrochem. Soc.* 121, 198C (1974).

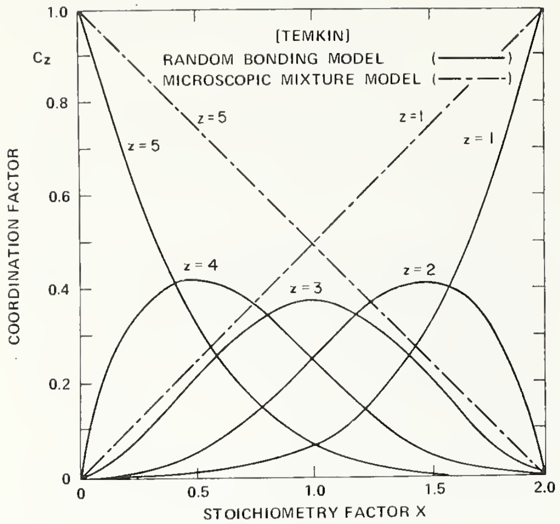

Figure 1. The relative amount C_z in each coordination Si-(Si_{z-1} O_{5-z}) is shown as functions of x the stoichiometry factor of silicon oxides. The broken line represents the microscopic mixture model (MMM) and the full drawn curves represent the random bonding model (RBM).

Figure 2. The energy of the $\mathrm{Si}_{KL_{2,3}L_{2,3}}$ Auger transition is plotted as function of x the stoichiometry factor of silicon oxides. The two circles are experimental values. Also shown is the calculated excess charge on the silicon atom, according to the Pauling electronegativity theory. The straight line behavior is an approximation.

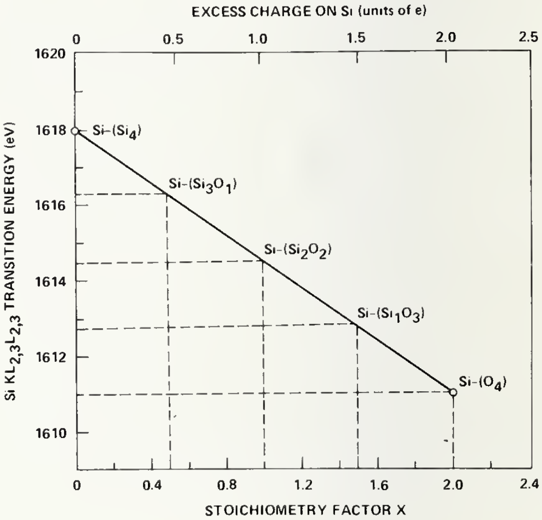

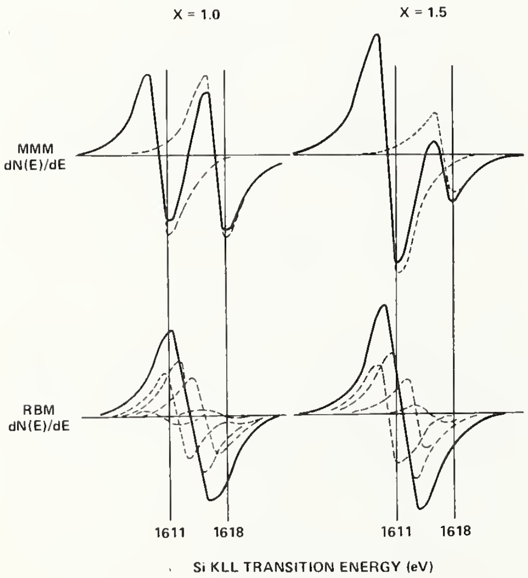

Figure 3. Model calculation of the $\mathrm{Si}_{KL_{2,3}L_{2,3}}$ Auger transition in two unsaturated silicon oxides, x = 1.0 and x = 1.5, according to the microscopic mixture model (MMM) and the random bonding model (RBM). The density of the material is not corrected for in these calculations.

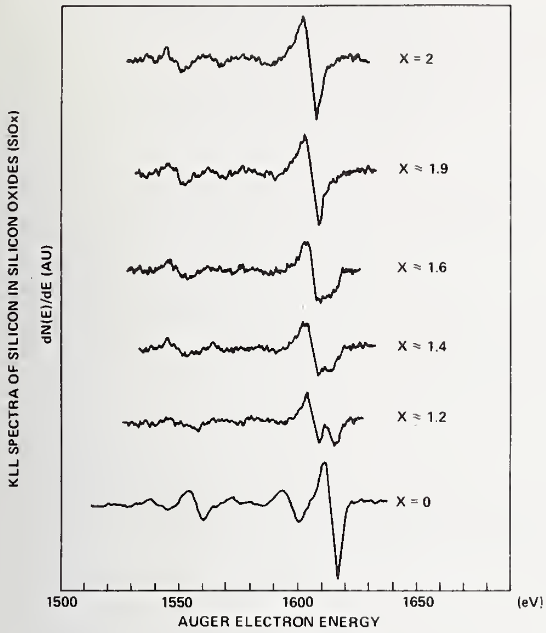

Figure 4. Experimental Si$_{KLL}$ spectra of silicon oxides. Thermally grown oxide is denoted by x = 2. Vacuum deposited silicon oxides are x = 1.9, 1.6, 1.4, and 1.2. The silicon (100) substrate is used as reference for x = 0.

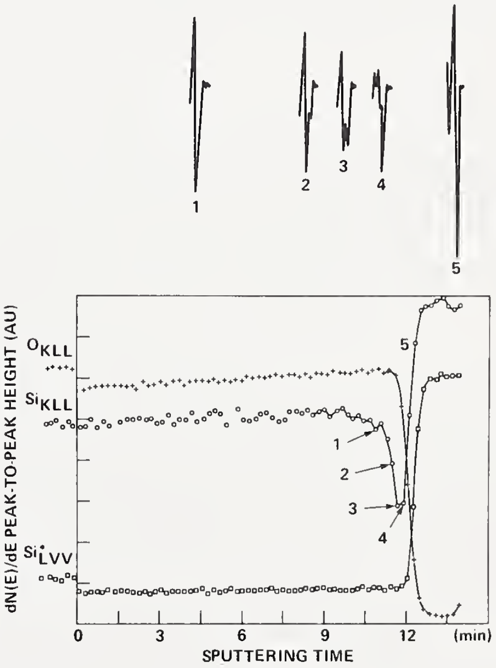

Figure 5. Chemical depth profile through 1000 Å thick thermally grown SiO$_2$ on Si (100) substrate. Above the depth profile is shown the change in the Si$_{KL_{2,3}L_{2,3}}$ transistion in the interface region between the dioxide and the substrate.

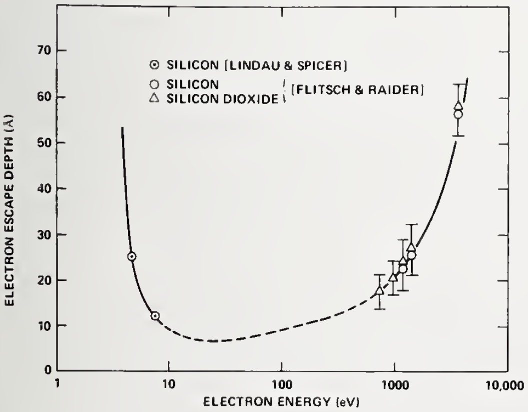

Figure 6. The energy dependence of the electron escape depth in Si and SiO$_2$. The broken part of the curve is an extrapolation by the authors. The data are collected from the literature (6,11).

NBS Special Publication 400-23, ARPA/NBS Workshop IV, Surface Analysis for Silicon Devices, held at NBS, Gaithersburg, Maryland, April 23-24, 1975 (Issued March 1976)

AN AUGER ELECTRON SPECTROSCOPY STUDY OF SILICON SPECTRA FROM SILICON MONOXIDE, SILICON DIOXIDE, AND SILICON NITRIDE

Y. E. Strausser

Varian Associates
Palo Alto, California 94305

and

J. S. Johannessen*

Stanford Electronics Laboratories
Stanford University
Stanford, California 94305

INTRODUCTION

AES, in conjunction with ion sputtering, is of great value in semiconductor technology, for determining impurity doping profiles and chemical stoichiometry of overgrown layers on semiconductors. The technologically most important overgrown layers today are silicon oxides and silicon nitride on silicon substrates. The electronic properties of these insulating films are strongly dependent on their stoichiometry. Only small deviations from SiO_2 stoichiometry of vacuum deposited silicon oxide is detrimental to its properties as an insulating layer [1].

The general purpose of the work reported in this paper is to explore the use of AES and ion sputtering in determining the chemical states of these overlayers, the relative amounts in each chemical state, and how this is changed by the AES measurement itself.

Particular emphasis is put on chemical structure effects, electron beam distortion of the sample composition and ion beam effects during simultaneous ion-sputter etching. By chemical structure effects we mean all of the changes that occur in the silicon Auger spectra as a result of the chemical environment of the Si atoms.

It is well known from photo-electron spectroscopy (PES) of silicon and silicon oxides that both the valence band spectra and the core levels are effected by the presence of an oxide layer on silicon [2, 3, 4]. Similar "chemical shifts" are also observed in Auger spectra of silicon in a large variety of chemical environments [5].

The chemical structure effects may be grossly understood on a basis of charge transfer according to the Pauling electronegativity theory [6], although the details of the structure of the valence bands of silicon oxide and silicon nitride are determined by the chemical bonds.

EXPERIMENTAL

In the present analysis we have used an Auger spectrometer with a CMA of high energy resolution, in conjunction with argon ion sputtering for depth profiling of the oxide and nitride films. The samples investigated are pure silicon, silicon oxides and silicon nitride on silicon (100) substrates of n-type doping ($1 < \rho < 5$ Ω cm).

Experimental Apparatus

The measurements reported in this paper were made in a Varian Auger spectrometer. This system uses a cylindrical mirror analyzer (CMA) with an energy resolution of 0.25% and a transmission of > 8% of the electrons emitted from the sample. The primary electron beam was produced by an electron gun mounted inside the inner cylinder of the CMA. It is capable of producing electron beams at energies up to 10 keV and with diameter less than 5 μ. The important system parameters used in these measurements were as follows:

a) Si LVV, N KLL and O KLL spectra: All of these spectra were obtained using a primary electron beam of 5 μA total current at 2 keV. The electron beam diameter was < 20 μm FWHM. The sample holder used held the samples so that there was an angle of 30° between the sample surface normal and the axis of the CMA. The modulation used to obtain the differential spectra was equivalent to 1 eV peak-to-peak. The sweep rate and the lock-in-amplifier time constant were varied in such a way that we always

---

* Permanent Address: Electronics Research Laboratory, Norwegian Institute of Technology, University of Trondheim, Trondheim, Norway

swept $\leq$ 1 eV per time constant.

b) Si KLL spectra: These spectra were taken with a primary electron beam energy of 4.5 keV and a current of 5 μA. The beam diameter was < 15 μm FWHM. In these spectra, a modulation equivalent to 2 eV peak-to-peak was used. The other parameters were the same as in a).

There are two other features of the electron gun which are important to these measurements. First, the use of the scanning sample positioner, normally used to scan the electron beam to make absorbed current images, enabled us to record spectra while the electron beam was being scanned over small, well defined areas of the sample. In this way, we could control the average beam current density incident on the sample and obtain data on the effect of total electron beam exposure. Additionally, this removed the effect of the current density distribution through the electron beam.

The second important feature of the electron gun is the existence of a deflection plate between the two lenses of the gun which permits one to electronically chop the primary electron beam. Pulsing the electron beam then makes it possible to directly record the energy distribution curves under the same conditions as the derivative spectra were taken.

The ion gun used in the profiling measurements produces a beam with ion current densities from 0 to > 200 μA/cm^2 at energies up to 3 keV. As in the case of the electron gun, the ion beam can be scanned over well defined areas of the sample to provide control of the ion beam current density and to remove crater shape effects. The geometry used resulted in an angle of 53.5° between the ion beam and the sample surface normal.

Sample Preparation

Saturated silicon oxides (SiO_2) were grown by thermal oxidation of Si in a dry O_2 atmosphere at temperatures between 1000°C and 1200°C, in the thickness range from 250 Å to 1000 Å. Slow and fast cooling in, and without, a protective N_2 atmosphere was used. Non-saturated silicon oxides SiO_X, where $0 < X < 2$, were vapor deposited in a residual oxygen atmosphere ranging from 10^{-7} Torr to 10^{-4} Torr, on silicon (100) substrates held at 210°C or 240°C. The thickness of the SiO_X films has been kept approximately constant at 1000 Å. The silicon nitride films were grown by CVD at approximately 750°C for a large variation of silane to ammonia ratio. All samples have been exposed to air for at least several hours before each AES analysis. All the overgrown layers discussed in this paper are X-ray amorphous. That is, they possess no long range crystalline order.

CHEMICAL STRUCTURE EFFECTS

We have observed pronounced chemical structure effects in the Auger spectra of silicon in compounds such as silicon oxides and silicon nitride. By chemical structure effects, we mean all of the changes that occur in the Auger spectra of Si due to changes in the chemical environment of silicon atoms in the compounds.

We have studied the KLL and LVV series of Auger transitions in pure silicon, and of silicon oxides, and silicon nitride grown on Si (100) surfaces. The presentation and discussion of the results will be divided into three parts. First, we discuss Si (100) spectra, then silicon oxides of stoichiometry SiO_X, where $0 < X \leq 2$, and finally we deal with silicon nitride, Si_3N_4.

Pure Silicon

AES spectra of silicon are well known, hence we shall only briefly discuss the characteristic features of the KLL and LVV series of transitions and relate them to the electronic structure of silicon. The gross features of the band-structure of silicon are determined by the local tetrahedral coordination of each Si atom, and the co-valent Si-Si bonds, giving no net charge on any individual Si atom (according to the Pauling charge transfer theory).

The series of peaks in the KLL spectrum of Si is shown in Figure 1a and 1b, where the Auger current, I_A, is differentiated with respect to the energy E in Figure 1a, and Figure 1b is a plot of I_A versus electron energy (the background current has been subtracted). There are three distinct peaks in the I_A spectrum one at 1562 eV corresponding to KL_1L_2 transitions, one at 1602 eV corresponding to KL_2L_2 transitions, and one at 1618 eV corresponding to KL_3L_3 transitions, in good agreement with theoretical predictions [7].

The LVV spectrum of silicon is most commonly presented in differentiated form (dI_A/dE), showing a strong peak at 92 eV [8]. In Figure 2 are shown both dI_A/dE (a) and I_A (b) as a function of energy for a silicon sample where the natural oxide has been removed by argon ion-sputtering. The spectrum shown in Figure 2 is composed of $L_{2,3}VV$ transitions at higher energies and $L_1L_{2,3}V$ transitions at the low energy side of the spectrum. Detailed analysis and identification of the different transitions is difficult due to the complexity of the silicon valence band. However, some of the characteristic features of the valence band are reflected in the LVV series of Auger transitions. Using Kane's density of state calculations [9], by assigning the binding energies $V_1 = 3$ eV, $V_2 = 4$ eV, $V_3 = 7$ eV, and $V_4 = 10$ eV to the four major peaks in the density of states, and using the binding energies $E_{L1} = 148.7$ eV and $E_{L2.3} = 99.2$ eV, we are able to give a crude identification of the features of LVV Auger spectrum of Si. This is the same approach as that of Maguire [10]. The major peak in Figure 2b, at 88 eV, is due to $L_{2,3}V_1V_1$ transitions, while the minor peak is due to $L_{2,3}V_4V_4$ transitions at 72 eV. The shoulder between these peaks is largely $L_{2,3}V_3V_3$ transitions at 79 eV. The two small pieces of structure on the low energy side are $L_1L_{2,3}V_{1,2}$ transitions at $\sim$ 41 eV and $L_1L_{2,3}V_{3,4}$ transitions at $\sim$ 35 eV. The details of the LVV spectrum are amplified by differentiation w.r.t. energy as shown in Figure 2a.

Silicon Oxides

Silicon oxides and oxidized silicon have been subject to extensive studies in the past, both by AES and photoelectron spectroscopy (PES) [2, 3, 11]. However, most of the work has been focused on either silicon dioxide or oxygen chemisorbed on clean silicon. In this paper, we report on results of studies of thermally grown silicon oxide of stoichiometry SiO_2, and evaporated films of stoichiometry SiO_X, $1 \lesssim X \lesssim 2$.

In Figure 3, we show a series of Si LVV spectra of silicon oxides (a), and oxygen KLL spectra (b) for the corresponding compounds. The stoichiometry of the samples was determined using the amount of oxygen present in the films, as indicated by the peak-to-peak heights of Figure 3 (b). The oxygen spectra of Figure 3 (b) indicate that oxygen is present in only one chemical state, namely as a bridge between two silicon atoms [12]. Furthermore, the coordination of oxygen determines the major features of the LVV spectrum through the density of states in the valence band of silicon oxides. The two major peaks in the LVV spectra of silicon at 64 eV and 78 eV are associated with transitions from bonding and non-bonding molecular orbitals of the Si-O-Si (Si_2O) quasi-molecule. The transition probabilities are apparently determined by the oxygen 2p predominance of these orbitals. The peak appearing at 92 eV is due to the presence of "free" silicon, i.e., silicon coordinated by four nearest silicon neighbors. A small amount of "free" silicon in silicon oxides is in this case produced by ion sputter cleaning. In fact, 500 Å of material had been removed before the AES spectra were taken.

It is important to understand that the ratio of the peak-to-peak heights of the 78 eV and 92 eV peaks in the $\frac{dN}{dE}$ spectra does not give, directly, the ratio of the concentrations of Si bound to O to the concentration of Si bound to Si ("free" Si). Observation of the N (E) spectrum shows that the peaks at 64 eV and 78 eV are very broad whereas the 92 eV peak is narrow, with a very sharp high energy edge. This, of course, results in a large negative excursion on the 92 eV $\frac{dN}{dE}$ peak without the corresponding large number of electrons in the peak. In fact, N (E) spectra corresponding to a condition like that shown in the $\frac{dN}{dE}$ spectra of Figure 3 will show the 92 eV peak to be only a small, although sharp, step on the high energy side of the large, broad 78 eV peak. This does not, however, prohibit the calibration of the LVV spectrum to determine the relative concentrations of these two states of Si. On the other hand, the KLL spectra give much more obvious and direct information about the relative concentrations of the different chemical states of Si.

The local atomic arrangement around the silicon atoms is shown by the Si KLL spectra in Figure 4, for silicon oxides of varying stoichiometry. For $X = 2$ (SiO_2) there appears a well defined $KL_{2,3}L_{2,3}$ peak at 1611 eV, associated with Si-(O_4) coordination. For $X \overset{=}{\sim} 1.8$ there appears a small shoulder above 1611 eV, and for $X \overset{=}{\sim} 1.3$ a broad peak occurs at 1616 eV. This peak may be associated with silicon tetrahedra of the type Si - ($Si_y\ O_{4-y}$), where $y \neq 0, 4$. However, upon electron exposure a single peak emerges at 1618 eV corresponding to Si - (Si_4) tetrahedra (or "free" silicon).

Silicon Nitride

In Figure 5a and b, we show silicon nitride Auger spectra in the energy range between 25 eV and 525 eV. Figure 5a is the spectrum from a sample exposed to atmosphere. Note the presence of carbon and oxygen KLL transitions, the large silicon nitride LVV peak at 85 eV, and the small silicon oxide peak at 64 eV. Removal of carbon and oxygen by ion-sputter etching results in the clean silicon nitride spectrum shown in Figure 5b. It is interesting to note that oxygen is associated with silicon oxide in the contaminated surface, and that removal of silicon oxide results in a "free" silicon peak at 92 eV, while there is no observable change in the 382 eV N KLL peak. This indicates that nitrogen exists only in one chemical state associated with a silicon nitride quasi-molecule (Si_3N), where the Si-N bonds have less ionic character than the Si-O bond. This observation is confirmed by the Si KLL spectrum of the nitride which has a well defined peak at 1618 eV, apparently identical to the "free" silicon Si-(Si_4) coordination, indicating a negligible charge transfer from Si to N in silicon nitride. We are not aware of X-ray photoemission spectra of Si_3N_4 or valence band structure calculations so an analysis beyond this mere descriptive one is not pursued here.

We have shown above that the Si_3N_4 LVV spectrum is strongly influenced by oxygen adsorbed on the surface. Oxygen adsorption completely removed the 92 eV "free" silicon peak. This phenomena suggests that amorphous silicon nitride is a microscopic mixture of Si and Si_3N_4.

ELECTRON STIMULATED DESORPTION EFFECTS

We have already mentioned in the previous section that the stoichiometry of silicon oxides may be changed by electron exposure. The effect is to reduce the oxygen content in the sample. This phenomenon is commonly known as electron stimulated desorption (ESD), and is thoroughly reviewed in the literature [13]. We have investigated electron beam exposure effects on Auger spectra of SiO_X ($1.2 < X \leq 2$) and Si_3N_4 films on Si (100) single crystals. Si_3N_4 appears to be stable to electron exposure at energies less than 2 keV. Apart from desorption of surface contaminants (carbon and oxygen) the LVV and KLL spectra appear unchanged upon prolonged exposure. Silicon oxides on the other hand are more volatile, and we will restrict our discussion to these compounds.

SiO_2 is known to decompose under electron irradiation. It has been shown that oxygen desorption from SiO_2 is accompanied by the formation of "free" silicon [14]. Our findings are similar for SiO. However, where the stoichiometry of silicon oxide films is SiO_x with $0 < X < 2$, this effect is much more pronounced. In Figure 6a and b, we show the growth of the 92 eV Si LVV peak as a function of exposure time for $SiO_{1.4}$ (a) and SiO_2 (b), the parameter is the electron flux density, and the primary electron energy is 2 keV. There appears to be a linear increase at small exposure times followed by a saturation region. The linear slope and the saturation level both increase with increasing flux density. The former being related to decomposition of SiOx followed by desorption of oxygen. The saturation level is most probably determined by oxygen depletion in the surface layer and out diffusion of oxygen from deeper lying layers. Note that the saturation level in $SiO_{1.4}$ is more than three times that of SiO_2.

Decomposition and desorption of oxygen is shown in Figure 7, where the O KLL peak-to-peak height is plotted against exposure time for the same samples discussed in Figure 6. We find that in order to minimize electron irradiation distortion of silicon oxides, the dose should be kept at 10^{19} electrons/cm^2 or below, at 2 keV primary energy. This corresponds to 2.5 min. exposure at 10^{-2} A/cm^2.

CHEMICAL DEPTH PROFILES AND ION BEAM EFFECTS

Chemical depth profiles are obtained by recording AES spectra as a function of time during simultaneous ion sputtering. The technique is well known, and we shall restrict the discussion to some of the factors that limit the depth resolution.

In Figure 8, we show a typical depth profile through a 1080 Å thick layer of SiO_X ($X \simeq 1.4$) vacuum deposited on Si(100). Only the initial and the final part of this particular profile are shown. The initial part of the curve shows how adsorbed carbon is removed, and how a balance between bound oxygen and "free" silicon is reached by oxygen removal. The saturation level gives a measure of the stoichiometry of the sample. The final part of the profile shows the interface between film and substrate, and the finite transition region between the two. In this case, the width is 29 Å (defined as distance between 80% and 20% of the oxygen peak-to-peak height). The question is now what factors control and determine the observed width or depth resolution. A recent paper by Ishitani et.al. [15] deals with these problems in model calculations of knock-on atomic mixing. They find a depth resolution decreasing with increasing ion energy, and increasing with incidence angle of the ion beam between 0° and 60°. An experimental investigation of Ta_2O_5 on Ta [16] has shown a minimum transition width of ∿ 60-70 Å for ion energies between 6 and 7 deV. We have employed A^+ ions at 3 keV of varying current density. In Figure 9, we show the transition with ΔY as a function of ion power density for silicon oxides and silicon nitride on Si(100). The general trend is that ΔY decreases with increasing power density for both compounds, towards a broad minimum or saturation level of the order of 30 to 40 Å. This value is roughly 50% of that reported for Ta_2O_5 on Ta [16]. Figure 9 also shows that the nitride interface is sharper than the oxide interface at low power densities. We find that the sputtering yield for silicon nitride is 0.5 molecule/ion, and for silicon oxide ∿ 1.5 molecule/ion, and an ion energy of 3 keV. We find our experimental results in qualitative agreement with the knock-on mixing model [15], when we take into account the lower ion energy and the angle of incidence we have used. The lower limit of 30 - 40 Å interface width may be reduced even further by reducing the ion energy. However, other factors such as surface roughness, preferential sputtering, and inhomogeneities may set an upper limit to the depth resolution. The ultimate limit is set by the escape depth of the Auger electrons, which will be discussed in the next paper.

CONCLUSION

The results presented in the preceeding sections may be summarized in the following conclusions. The electronic structure of silicon compounds is largely determined by the molecular bonds and the local atomic arrangement. Thus, in silicon oxides it is the Si-O bond and in silicon nitride it is the Si-N bond that gives the major contribution to the electronic structure. The Si-O bond energy is larger than Si-Si bond*. The charge transfer associated with the Si-O bond gives rise to a chemical shift in the binding energy of the Si $L_{2,3}$ level of 3.9 eV [18]. This gives rise to a shift in the Si KLL transition energy of 7 eV from Si-(Si_4) coordination to Si-(O_4) coordination [18]. We have observed varying amounts of these two states in electron irradiated SiO_X films, $X \leq 2$. Similar chemical shifts have not been observed in silicon nitride. We believe that this is due to a much smaller charge transfer associated with the Si-N bond.

Electron distortion of silicon oxides by dissociation and desorption of oxygen can be reduced to a negligible level by keeping the total electron dose below a limit of 10^{19} el/cm^2 at 2 keV electron energy. Silicon nitride is stable to electron irradiation within the experimental conditions of this investigation. Why this is so is not fully understood. It may be associated with the higher ionization potential of nitrogen compared with oxygen.

We have observed knock-on mixing of elements caused by energetic ions during depth profiling of silicon oxides and silicon nitride. The mixing effect results in reduced depth resolution. By varying the ion flux we were able to reduce the width of the interface between silicon oxide or silicon nitride and silicon, to 30 to 40 Å at an argon ion energy of 3 keV. This result is encouraging in that it indicates the possibility of studying the interface region of MOS and MNOS devices where charge is accumulated.

ACKNOWLEDGEMENT

We would like to thank Forrest Futtere for preparing the SiO_X samples, and Krishna Saraswat for supplying us with thermally grown SiO_2 and reactor grown Si_3N_4 samples.

REFERENCES

1. Hirose, H., and Wada, Y., *Japan. J. Appl. Phys.* 3, 179 (1964).
2. DiStefano, T. H., and Eastman, D. E., *Phys. Rev. Lett.* 27, 1560 (1971).
3. Hollinger, G., Tousset, J., and Tran Minh Duc, Tetrahedrally Bonded Amporphous Semiconductors, M. H. Brodsky, S. Kirkpatrick and D. Weaire, Eds., p. 102 (Am. Inst. Phys., New York, 1974).
4. Danyluk, S., and McGuire, G. E., *J. Appl. Phys.* 45, 5141 (1974).
5. Stupian, G. W., *J. Appl. Phys.* 45, 5278 (1974).
6. Pauling, L., *The Nature of the Chemical Bond,* 3rd ed., (Cornell Univ. Press, Ithaca, New York, 1960).
7. Siegbahn, K., Nordling, C., Fahlman, A., et. al., *Electron Spectroscopy for Chemical Analysis,* Technical Report AFML-TR-68-189, Inst. Phys., Uppsala, Sweden (1968).
8. Grant, J. T., and Haas, T. W., *Surf. Sci.* 23, 347 (1970).
9. Kane, E. O., *Phys. Rev.* 146, 558 (1966).
10. Maguire, H. G., and Augustus, P. A., *J. Phys. C.* 4, L174 (1971).
11. Ibach, H., and Rowe, J. E., *Phys. Rev.* B10, 710 (1974).

12. Johannessen, J. S., Spicer, W. E., and Strausser, Y. E., Use of Auger Electron Spectroscopy To Determine The Structure of Silicon Oxide Films, ARPA/NBS Workshop IV, *Surface Analysis for Silicon Devices,* A. G. Lieberman, Ed., NBS Spec. Publ. 400-23 (March 1976).

13. Madey, T. E.,and Yates, Jr., J. T., *J. Vac. Sci. Technol.* 8, 525 (1971).

14. Thomas, S., *J. Appl. Phys.* 45, 161 (1974).

15. Ishitani, T.,and Shimizu, R., *Appl. Phys.* 6, 241 (1975).

16. Ishitani, T., Shimizu, R.,and Tamura, H., *Appl. Phys.* 6, 271 (1975).

17. Roberts, J. D., Stewart, R. , and Caseuio, M. G., *Organic Chemistry* (W. A. Benjamin, Inc., Menlo Park, California 1971).

18. Wagner, C. D., to be published.

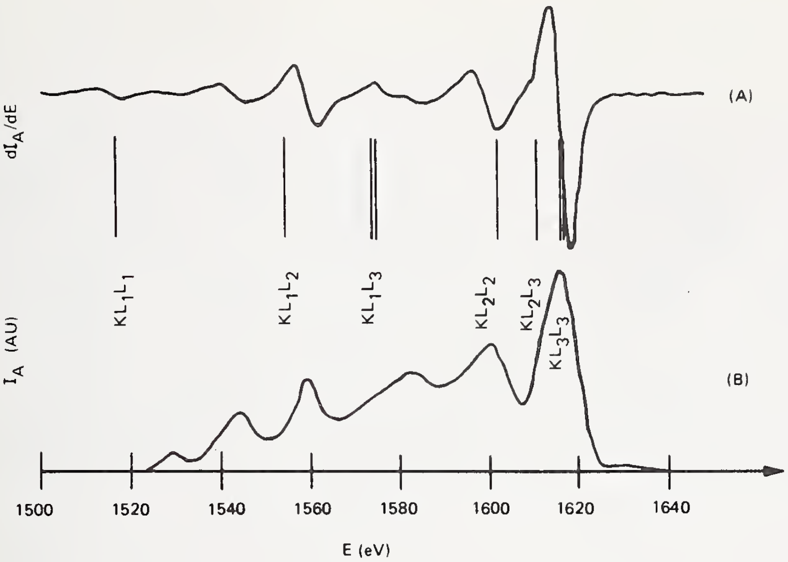

Figure 1. The Si KLL spectrum (B) and the differentiated Si KLL spectrum (A). Also, shown as vertical lines are theoretical Auger transitions [10].

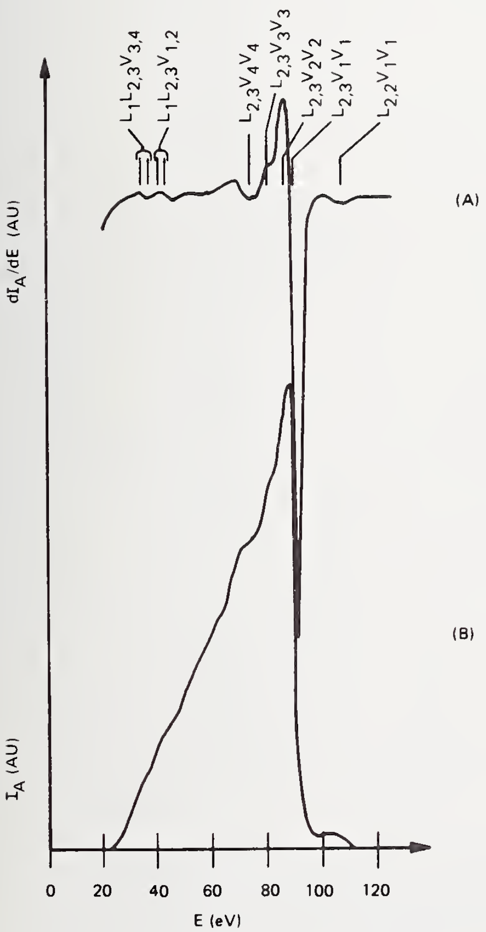

Figure 2. The Si LVV spectrum (B) and the differentiated Si LVV spectrum (A). The vertical lines indicate the most probable LVV transition based on the density of states in the valence band of silicon.

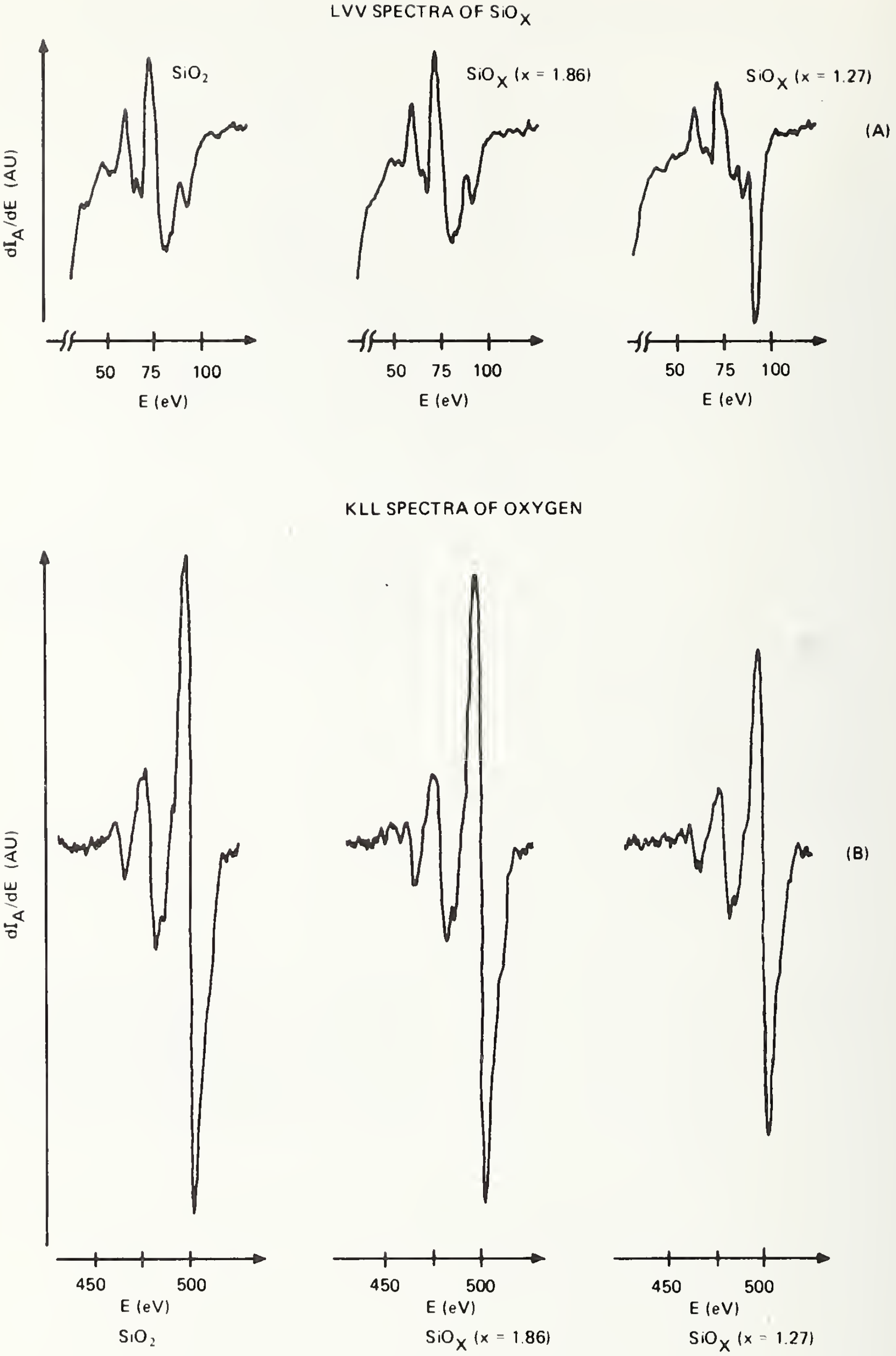

Figure 3. LVV spectra of SiO_x films (A) and KLL spectra of oxygen in SiO_x films (B). The oxygen peak-to-peak height is used to calculate the stoichiometry of the samples. 500 Å has been removed by argon ion sputtering.

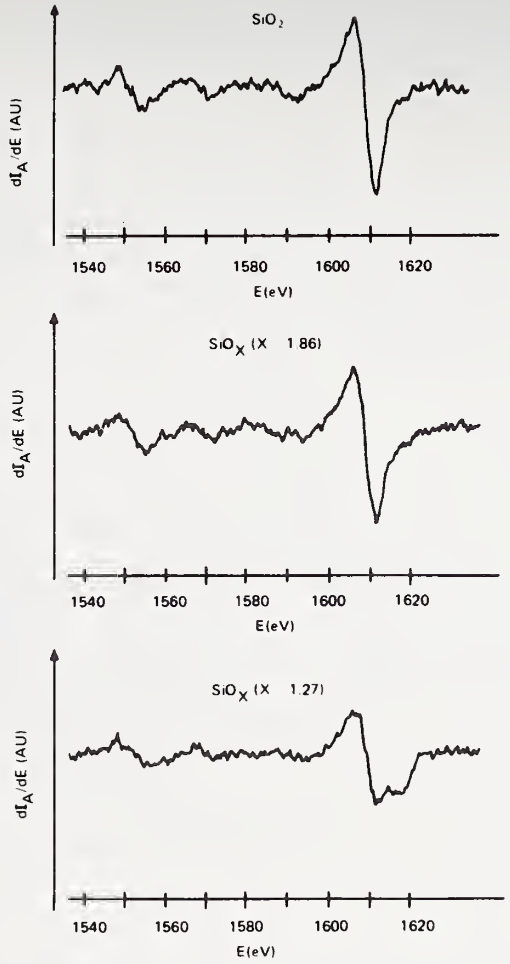

Figure 4. Si KLL spectra of SiO_x films of different stoichiometry (x).

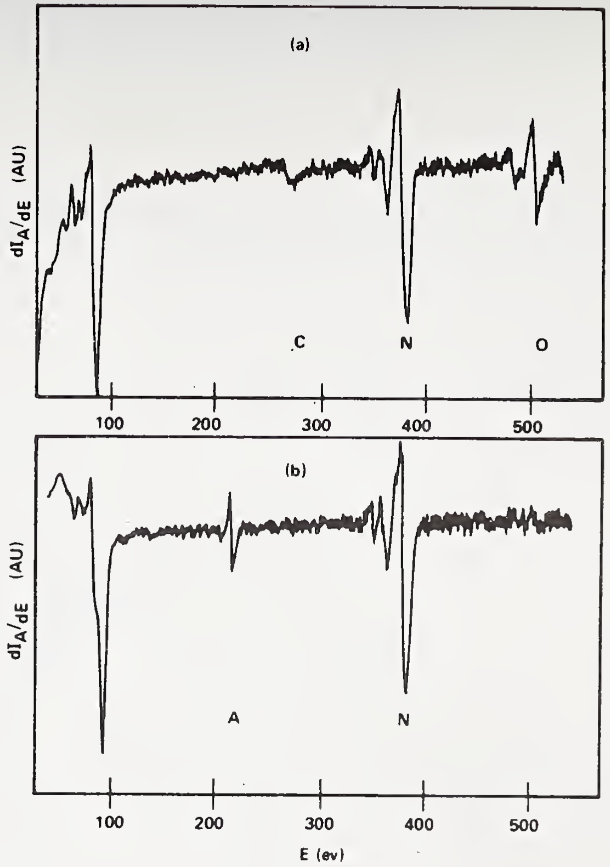

Figure 5. Auger spectra of Si_3N_4 films exposed at atmosphere (a) and after the surface layer has been removed by argon ion sputtering.

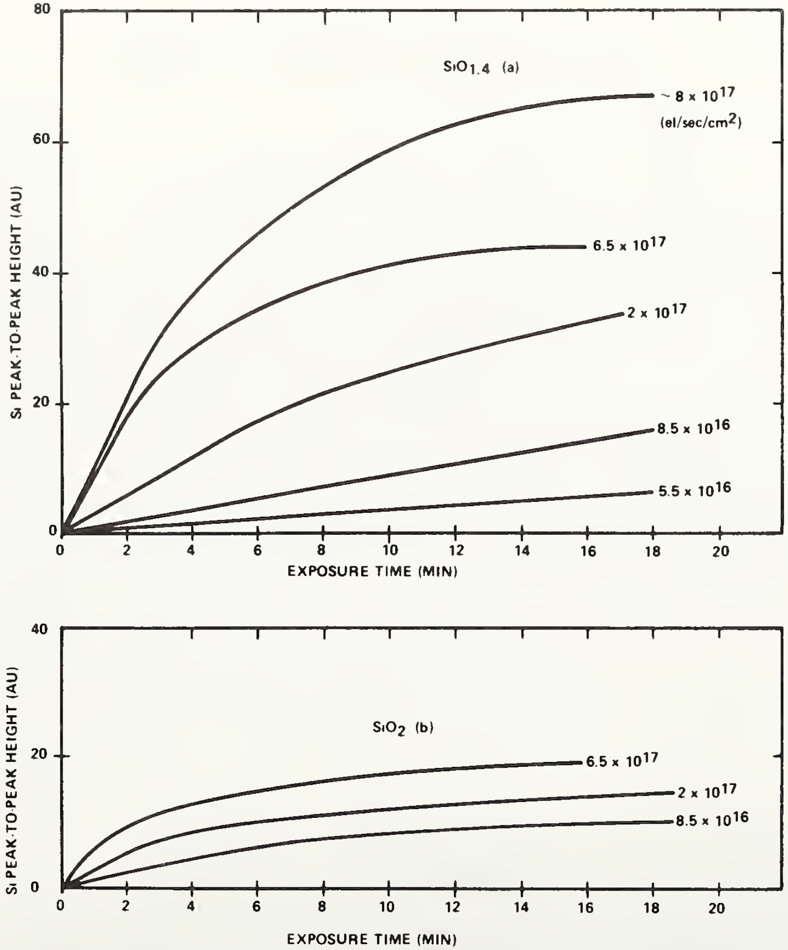

Figure 6. The outgrowth of the "free" silicon peak in the LVV spectrum of $SiO_{1.4}$ (a) and SiO_2 (b) films under electron irradiation. The parameter is the electron flux density Φe.

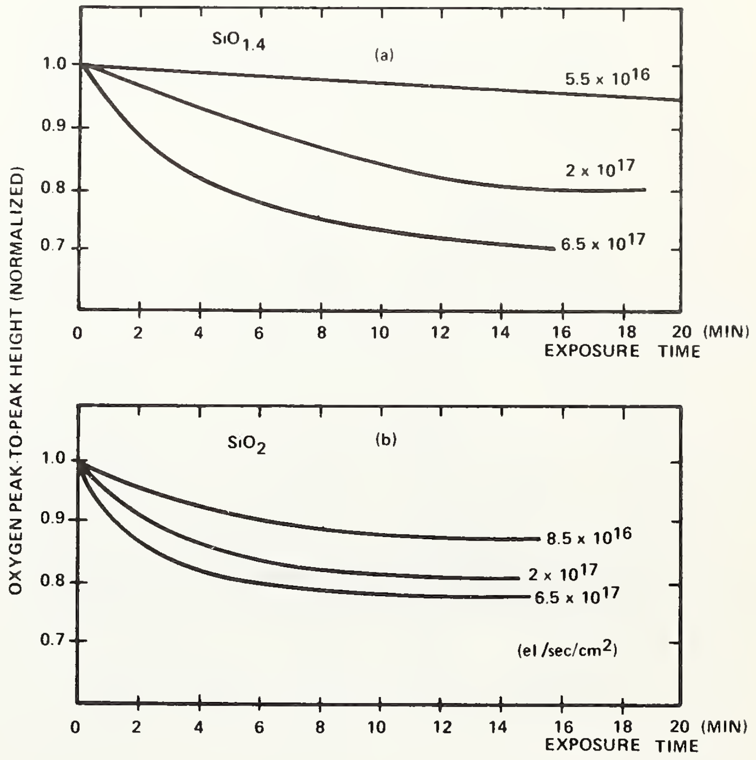

Figure 7. Electron stimulated desorption (ESD) of oxygen from $SiO_{1.4}$ (a) and SiO_2 films (b). The parameter is the electron flux density Φe.

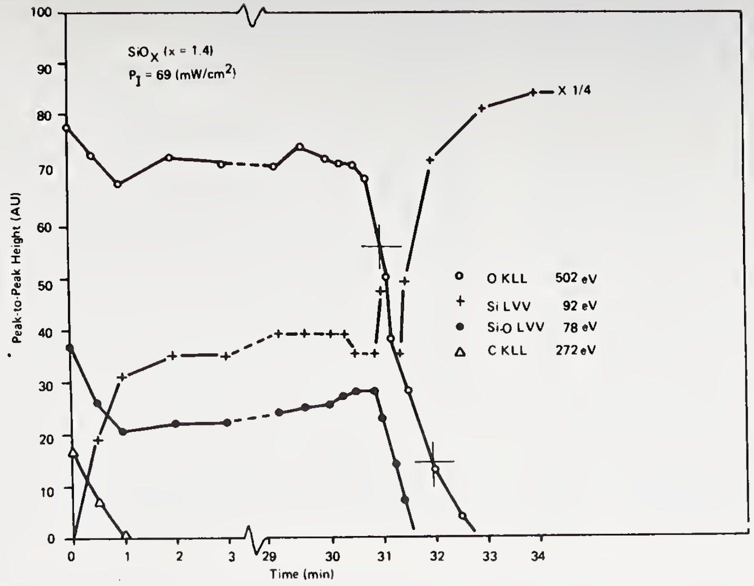

Figure 8. Depth profile of a 1080 Å thick $SiO_{1.4}$ film on Si (100) substrate. The ion energy is 3 keV. The ion power-density is given in the figure. The large crosses indicate the definition of the transition width ΔY.

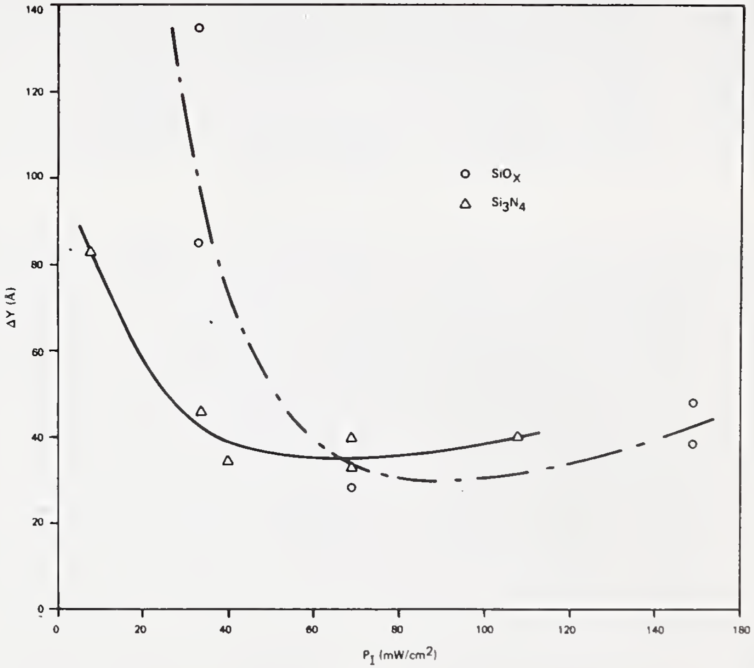

Figure 9. The interface transition width ΔY, in SiO_x (o) and Si_3N_4 (Δ) films on Si (100) substrates, as a function of ion power density.

DISCUSSION OF THE PAPERS BY STRAUSSER AND JOHANNESSEN

Thomas: Without resurrecting the argument about the assignment of the Auger peaks of elemental silicon, I have to say that two of the peaks on the low energy side of your major KLL peak are not really Auger peaks but rather plasma loss peaks; the same is true of the 107 eV silicon peak you have labeled as an Auger peak, but there is some controversy over that too. That is the point that I had to make, but could you also tell me how you determined the stoichiometric factor x in your SiO_x?

Strausser: As to your comment first of all, I certainly agree that those are plasma loss peaks in the silicon KLL spectrum. We simply didn't label them. For the 107 eV peak, we are inclined to accept the interpretation by Grant and Haas, namely, that it is a doubly ionized silicon Auger transition. Now as to your question, we have done some quantitative work using normalization factors, which is basically like Joe Morabito's second technique. He normalizes all the peaks, applying an empirical correction factor to the major peaks, normalizing them all to one particular peak and dividing each of them with a total signal, thus calculating percentages. Instead of experimentally deriving the normalization factors, we have calculated them. We use calculated ionization cross sections, a linear correction for the energy dependence of the CMA transmission, measured and extrapolated fluorescent yields and escape depths. We combine all of these into a normalization factor. We can then calculate the stoichiometry, and we have verified the stoichiometry of thermally grown silicon dioxide, for instance, that it is SiO_2. However, on that particular figure we simply used the oxygen peak heights to determine the stoichiometry of the subdioxide films using a known SiO_2 film as a reference for the suboxides.

Thomas: During the past two or three years, I have been looking, day in and day out, at "SiO_2" whatever that may be. We have prepared SiO_2 by various techniques. If I were to measure just the ratio of the oxygen peak to a silicon peak, you would notice that the ratio would change, depending upon which technique were used to prepare the oxide. In other words, you would have a different value for quartz, dry oxides, or oxides grown in steam, or spin-on oxides, or whatever it is; the peak ratio can change significantly. So I do not know whether you take the value two because you always say, SiO_2, and particularly how do you get that value, x = 1.2. Do you measure the value of, for example, the oxygen peak of SiO_2 and then measure the ratio of oxygen to some suboxide? I did not quite follow that.

Strausser: We convinced ourselves that a particular dioxide film really was SiO_2. Then we measured the oxygen peak height in that film and we measured the oxygen peak heights in the suboxide films and used those peak heights to determine exactly what the stoichiometry of those films were. For the calculations of stoichiometry of SiO_2 films, I have used the KLL peak rather than the LVV peak, we find that it is more reliable.

Thomas: Just one more comment. I have never seen anything like a 7 eV chemical shift in the KLL Auger peak. For one thing, the ESCA 2p shift for silicon is only about 4 eV, maybe 5 eV, depending on the author you read. Can you explain why you see 7 eV?

Johannessen: Well, we do see a 7 eV shift in the main Si_{KLL} peak, between elemental silicon and silicon dioxide, and we see both peaks as a doublet in the suboxide. I can refer you to a recent paper by C. D. Wagner. A simple explanation is that the Auger shift is approximately twice that of the shift in the $L_{2,3}$ level, which is around 2.5 eV.

Thomas: No, why should it be? All the levels are changing equally. You are talking about $KL_{2,3}L_{2,3}$, why should it be double?

Johannessen: Our value of a 7 eV Auger shift in an unsaturated silicon oxide agrees well with similar results obtained by Wagner in oxidized silicon. In response to your question, I implied that a part of the shift was due to different chemical shifts of the K and L levels, although the problem is more complex than that.

Thomas: I have to disagree with you because I have never seen anything like that doublet structure. Also, it is an unfair method of looking at the stoichiometry because when you sputter and come to the interface you may not be removing material uniformly at all. What you may be seeing is really an SiO_2 chunk sitting here on the silicon so you may be getting a silicon signal and a surface charged SiO_2 chunk more than anything else. I have never seen a doublet like that of equal intensity. You can get the 7 eV shifts if you have a very large surface charge.

Johannessen: You will see a similar thing if you look at the natural oxide on silicon.

Strausser: I think the important thing is that this analyzer has enough resolution to resolve that peak and you have to consider what instrument you are using.

Erickson: In doing ESCA spectroscopy we quite frequently find that Auger shifts are approximately double the corresponding shifts one finds in the ESCA spectrum. In fact, for the case of copper oxide, there is no energy difference between metallic copper and a copper in cuprous oxide, but there are tremendous differences, 3 or 4 eV, in the Auger binding energies for the two states of copper. So it is not unexpected to find larger shifts in the Auger spectra than in the ESCA spectra. The reason is partly that in the ESCA spectra you start out with, say a neutral atom and the final state is a unipositive ion, whereas in the Auger case, you start out with a unipositive ion and you end up with a doubly positive ion. You have to consider the energy difference between the initial state and the final state. There is a concept known as extra-atomic or atomic relaxation which can account for these differences in binding energy, or kinetic energy in the case or Auger electron.

Thomas: The Auger shifts do not have to be double the ESCA shifts.

Erickson: It does not have to be double. In fact, in the cuprous oxide case there is no shift at all in the ESCA binding energy but there is a 3 or 4 eV shift in the Auger energy. So there are some mysterious things which are not completely understood theoretically, but they are certainly experimentally real. I would agree that the observed shifts in the KLL peaks for silicon and silicon dioxide are entirely reasonable. I have seen shifts with that order of magnitude myself.

A question addressed to either one of the speakers: In ESCA spectroscopy, one normally determines a direct N(E) curve and I am always a little suspicious of derivative type curves for the following reason. If you look at the ESCA spectrum of silicon 2p for a thermally annealed clean silicon surface and compare that with an argon bombarded silicon surface, one finds out that the areas of two peaks are approximately the same. However, the silicon 2p line for the argon implanted specimen is broadened by a factor of about 2 or 3. On the other hand, the silicon 2p line for the dioxide is, to start with, considerably broader than it is for pure silicon so the effect of the residual argon in the lattice after bombardment does not have as great an effect on the peak height or on its width. I am wondering whether or not you see effects in the Auger spectrum due to residual argon in the lattice, and if you find any differences in the peak heights depending on whether or not you annealed the sample after argon bombardment.

Johannessen: We have not done any annealing of our samples after ion sputtering, and we have not seen any significant effects on either the oxygen or silicon spectra due to argon ion implantation. The only observable change due to ion sputtering is the removal of surface contaminants, such as water vapor and carbon. These contaminants tend to affect the appearance of, for instance, the LVV spectra of silicon nitride. We do not see any effect on the Si_{KLL} spectra. This may be due to the larger escape depth, and hence, the larger sample volume being probed. I have here a viewgraph (Fig. 6) showing some recent data on the escape depths of electrons from silicon and silicon oxide. The low energy data are taken from a paper by Lindau and Spicer, and the data on the high energy side are taken from a recent paper by Flitsch and Raider. If you look at the 1 KeV region, you will see that the escape depth for the Si_{KLL} electrons is on the order of 30 Å. The oxygen KLL electrons at roughly 500 eV escape from a depth on the order of 10 to 15 Å. There is a factor of at least 2 in the escape depth between the oxygen and silicon KLL transitions.

In the depth profile of the SiO_2-Si interface we "saw" the effect of the interface on the Si_{KLL} transition roughly 30 Å before any changes appeared in the oxygen peak. Therefore, the effect of different escape depths is born out in our experimental data, and this also shows that the ion beam does not disturb the sample deeper than some 10 - 15 Å.

Morabito: I would also like to comment that 7 eV is not an unreasonable Auger shift. Secondly, if the shift is due to a surface charge, then you should also see a shift in the oxygen peak and this was not seen.

Strausser: If the shift was due to a surface charge, all the peaks should shift the same amount and we really did not see that at all, and we did not see a double peak at the oxygen position. We always see the oxygen peak at the same energy in the oxide film.

Harrington: For an escape depth, let us say, of 20 to 30 Å, is not this just the width over which you are talking about seeing this transition, and would that not equally well explain the transition rather than non-stoichiometry?

Strausser: That is the escape depth of the silicon KLL peak. We are talking about the fall off of the oxygen KLL peak, and the O_{KLL} escape depth is much smaller. Johannessen was showing the change in the shape of the Si_{KLL} transitions through the interface region, which indicates not only a change in stoichiometry but also a change in chemical state of the Si atoms.

Johannessen: We define the metallurgical interface as the fall off in the oxygen KLL signal. What we have seen is that the oxygen atoms apparently always exist in only one state in silicon oxide; they are always bonded to two silicon atoms as an Si_2O quasi-molecule.

Harrington: But the changes in the silicon peak were what you are showing for the silicon KLL and that is just the region you are talking about here in thickness, and so you are interpreting the effect of the penetration or escape depth as stoichiometry changes.

Johannessen: It is true that we average over a depth of the order of the electron escape depth. In the case of the Si_{KLL} Auger transition, it sees a much wider interface than that defined by the fall off of the oxygen peak. It is difficult to exactly determine the stoichiometry in the interface region because we deal with a differential spectrum.

Harrington: Take the situation, where, ideally, there is just an abrupt interface, and because you have a penetration depth (escape depth) you are going to see the silicon and oxygen peaks of the oxide gradually shift, even though you have an abrupt interface.

Johannessen: That is correct and it would be on the order of 10 Å, referred to the oxygen KLL peak.

Harrington: That would be on the order of 20 to 30 Å according to your figures.

Johannessen: Yes, using the silicon KLL peak, but we are referring to the oxygen KLL electrons which have an escape depth around 10 Å. As a matter of fact, we have seen narrower interface regions in vacuum deposited SiO_x, where one would expect an abrupt interface due to the condensation process on the cold substrate. So we are able to see differences for different deposition processes.

Morabito: Consider the particular example of a thin anodic tantalum oxide film on top of tantalum, and I have done this. If you now monitor all the tantalum transitions, the higher energy tantalum transition come first, you see it coming into the interface before the lower energy transition. In addition to that, if you have a change in the Auger yield you are going to have a corresponding change in intensity and that could be in either direction, up or down.

Johannessen: I agree we see a broader interface in the silicon KLL than in the oxygen KLL.

DiStefano: After unfolding the effects of the escape depth, allowing you to see the silicon before you get there because some electrons are escaping through the thin layer of SiO_2, and after unfolding the spatial variations in the sputter rate, how much of that 35 Å estimated interface width is left? How much of that graded junction is real?

Strausser: I think that the last effect is very, very small. We have looked at these craters under SEM's and have seen very, very smooth craters. Secondly, our electron probe beam is only 5 microns wide, and so it is not sampling a big enough area to have large variations in sputter yield across it.

DiStefano: Let me paraphrase, after sputtering 1000 Å of SiO_2, how much variation in thickness would you have? If you have 1% sputtering variation across that area, you would have 10 Å difference in the interface position. So it looks like you are very sensitive to variation in the sputter yield across the area.

Johannessen: We have been worried about things like that, and we have seen surface roughening effects due to the ion beam at very low sputtering rates, less than 10 Å/min. The present data are obtained at approximately 80 Å/min using a rastered low energy ion beam. No surface irregularities were visible even if we used the TEM and replica technique. We believe that the provisions I just mentioned are essential for this type of work.

Now taking all of these effects, escape depths, ion beam distortion, etc., into account, our estimate of the interface width is on the order of 20-30 Å.

NBS Special Publication 400-23, ARPA/NBS Workshop IV, Surface Analysis for Silicon Devices, held at NBS, Gaithersburg, Maryland, April 23-24, 1975 (Issued March 1976)

SURFACE COMPOSITIONAL CHANGES WITH ELECTRON BOMBARDMENT OBSERVED BY AES

Simon Thomas

Semiconductor Analytical Laboratory
Motorola Semiconductor Products Division
Phoenix, Arizona 85008

ABSTRACT

Auger Electron Spectroscopy (AES) is generally considered to be a 'non-destructive' surface analytical technique. However, there are many instances where the incident electron beam can alter the surface composition of the solid being analyzed. The commonly observed effects of the electron bombardment are the surface decomposition, desorption, outdiffusion, surface migration and co-adsorption. Some typical examples of these effects, often encountered in the AES analyses of semiconductor devices are given.

Auger Electron Spectroscopy (AES) has emerged as a very powerful and popular surface analytical technique for semiconductor device fabrication and failure analyses. The elemental specificity, sensitivity, depth of analysis and the spatial resolution have contributed to its popularity as an analytical technique for the characterization of a 'practical surface'. In addition to the elemental specificity, the chemical effects often observed in the Auger spectra provide further insight into the surface composition. Noble gas ion sputtering is generally coupled with AES as a means of removing the adsorbed species from a typical processed surface or for obtaining the depth composition profiles. Generally, AES is considered to be a non-destructive surface technique. It is assumed that no significant surface compositional changes are induced by the incident electron beam which is typically of energy 1-5 keV and beam currents of 1-50 μA. However, there are many exceptions to the non-destructive nature of this technique. The intent of this brief report is to draw the attention of the numerous Auger spectroscopists, particularly in the semiconductor industry, to the typical surface compositional changes which may occur as a result of prolonged electron bombardment. The beam effects do not necessarily undermine the immense capabilities of AES as a surface analytical technique. Nevertheless one has to be aware of these effects and try to minimize them, if present. If any deleterious effects are present they should be reckoned with in any quantitative analysis. The most commonly observed effects of the electron beam bombardment on the surface composition, are the surface decomposition, desorption, outdiffusion, surface migration and co-adsorption. Some examples of these are given below.

SURFACE DECOMPOSITION

In the surface analysis of silicon devices, the most commonly observed adverse effect is the decomposition of silicon dioxide. With the prolonged electron bombardment of SiO_2, one observes the appearance of the $Si\text{-}L_{2,3}VV$ Auger peak at ~92 eV which is characteristic of elemental silicon. Simultaneously, there is a reduction in the 75 eV Auger peak characteristic of silicon in SiO_2 and also a reduction in the oxygen Auger peak height. The various parameters affecting the decomposition of SiO_2 have been reported in the literature(1) and will not be discussed here. There are many other examples of the decomposition of oxides by electron bombardment. An example is given in Figure 1a where phosphorus pentoxide present on an aluminum substrate is reduced to mostly elemental phosphorus in a matter of minutes (E_p = 3 keV; I_p = 12 μA). It is interesting to note the large chemical effects present in the Auger features of P in P_2O_5. A large chemical shift of ~12 eV and a pronounced change in the peak shape are observed from P in P_2O_5. These features resemble the chemical effects from Si and SiO_2. The decomposition of P_2O_5 with electron bombardment appears to be matrix dependent as evident from Figure 1.b. In this case P_2O_5 is present as an impurity on an oxidized GaAs substrate. No changes in the Auger features of P_2O_5 are observed with prolonged bombardment. Oxides in which decompositional effects have been observed in our laboratory include B_2O_3, GeO_2, hydrous oxides of Al, TiO_2 and some cases of bulk Al_2O_3. This list is by no means exhaustive.

DESORPTION

Another consequence of the electron bombardment is the desorption of selected surface species. Electron stimulated desorption (ESD) has been studied extensively by many authors and comprehensively reviewed by Madey and Yates(2). Typical cross sections for the desorption of adsorbed species are in the range 10^{-16} - 10^{-22} cm^2. The most conspicuous desorption effect is observed in the Auger analysis of adsorbed halogens with desorption cross sections of $\sim 10^{-16}$ cm^2. In Figure 2 is shown the variation of the Auger signal from fluorine adsorbed on an aluminum substrate, as a function of electron bombardment time (E_p = 3 keV, I_p = 5 μA). The beam current of 5 μA used in this study is usually considered a moderately low value for typical AES analysis. However, one can observe the rapid decrease in the Auger signal, which makes the absolute peak height measurement somewhat difficult. Assuming the surface concentration to be uniform one may translate the area of analysis and obtain a fairly accurate estimate of the peak height. In addition to the halogens, the alkali metals show similar desorption effects with a strong dependence on the matrix. The total desorption cross sections for the alkali metals appear to be much smaller than those for the halogens.

OUTDIFFUSION

Semiconductor devices are commonly passivated with silicon dioxide doped with phosphorus. In the surface compositional analysis of such phosphosilicate glass (PSG) using AES, one of the commonly observed phenomenon is the increase in the phosphorus Auger signal with electron bombardment time. This is due to the outdiffusion of phosphorus from the bulk to the surface. In all the PSG surfaces typically used in the device fabrication, the outdiffusion of P has been observed. The rate of P outdiffusion appears to be dependent on the PSG deposition temperature and the stoichiometry, besides the incident electron beam parameters. Although the mechanism of P outdiffusion is not well understood it is thought that the electric field established at the surface of the PSG with electron bombardment is the driving force. The phenomenon of the P outdiffusion has to be borne in mind while attempting to obtain Auger calibration curves for P in PSG. In addition to the P outdiffusion, the surface decomposition also is observed in the Auger analysis of P in PSG. Phosphorus appears to be present at the surface of the PSG as P_2O_5, although this could not be conclusively proved for the bulk using the Auger peak features. P_2O_5 present at the surface of the PSG is converted to elemental phosphorus with electron bombardment.

Chou et.al.(3) have observed similar outdiffusion of chlorine from SiO_2 grown in chlorine or HCl and the subsequent desorption from the surface.

SURFACE MIGRATION

Mobile ions, particularly alkali ions, can migrate along the surface under the influence of the electron beam. However, this is not a serious impediment in most typical Auger analyses. Desorption of the alkali ions is a more serious problem than the surface migration.

CO-ADSORPTION

It is generally observed that the electron beam assists in the adsorption of oxygen and carbon from the residual vacuum in the chamber. Although its presence is duly recognized, co-adsorption is the least problematic effect as far as the Auger analysis of 'practical surfaces' encountered in silicon device technology is concerned. Under typical vacuum of $<10^{-7}$ Pa, routinely obtained in an AES chamber, no significant co-adsorption occurs in the time required to plot an Auger spectrum. The problem, of course, can be aggravated by the high residual pressures of reactive gases such as H_2O, CO, CO_2 or CH_4 present in the chamber.

In many cases one may observe one or more of the above beam effects. If such effects are present, proper care must be taken in minimizing them and in interpreting the Auger data. The need for caution is acute in the simultaneous ion sputtering and Auger analysis when the ion beam and the electron beam are bombarding the surface continuously. Notwithstanding the likely surface compositional changes which may occur in selected cases, AES is one of the most valuable surface analysis techniques for semiconductor processing and device failure analyses.

REFERENCES

1. S. Thomas, J. Appl. Phys., 45, 161 (1974).

2. T. E. Madey, and J. T. Yates, J. Vac. Sci and Technol. 8, 525 (1971).

3. N. J. Chou, C. M. Osburn, Y. T. van der Meulen, and R. Hammer, Appl. Phys. Lett. 22, 380 (1973).

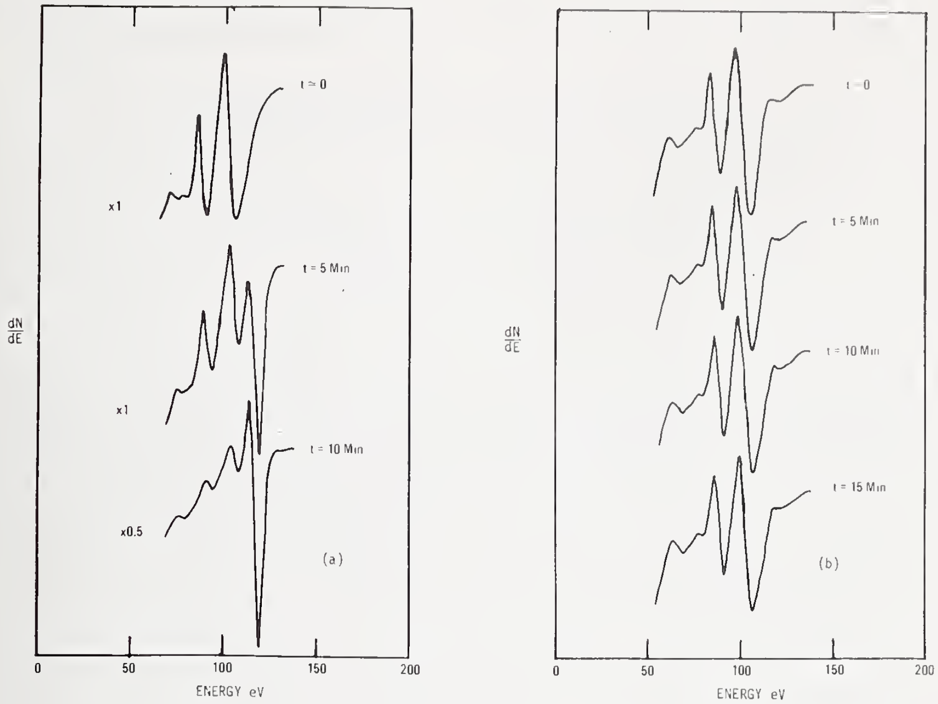

Figure 1. Effect of electron bombardment on the Auger spectrum from P_2O_5. $E_p = 3$ keV, $I_p = 12$ μA. (a) P_2O_5 present on an Al substrate is decomposed to mostly elemental form. (b) P_2O_5 present on oxidized Ga As. No decompositional effect observed.

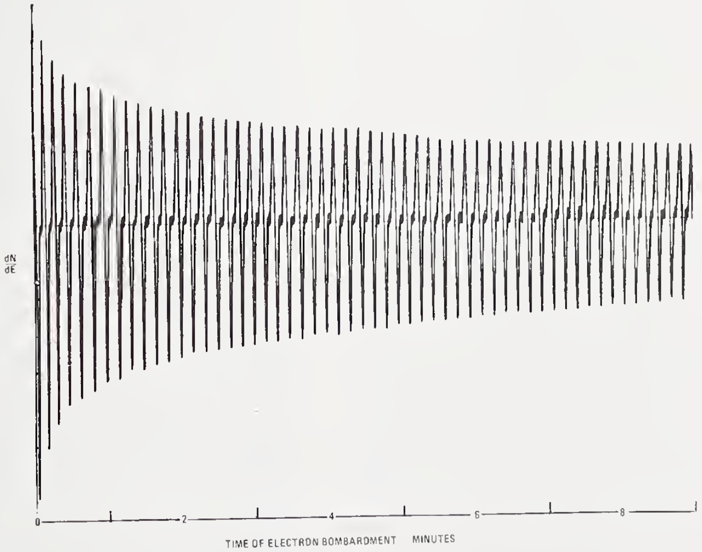

Figure 2. Progressive decay of the Auger signal from fluorine adsorbed on an Al substrate, as a function of electron bombardment time. $E_p = 3$ keV, $I_p = 5$ μA.

NBS Special Publication 400-23, ARPA/NBS Workshop IV, Surface Analysis for Silicon Devices, held at NBS, Gaithersburg, Maryland, April 23-24, 1975 (Issued March 1976)

COMBINED SCANNING ELECTRON MICROSCOPY-AUGER SPECTROSCOPY FOR MICRO-SPOT SURFACE AND IN-DEPTH ANALYSIS OF SILICON AND TRANSISTOR METALLIZATIONS

A. Christou, W. Weisenberger and H. M. Day
Naval Research Laboratory
Washington, D. C. 20375

ABSTRACT

Auger Spectroscopy with a focused electron beam in the scanning electron microscope (SEM) has provided an extremely powerful diagnostic technique for silicon surfaces and transistor metallization systems. The focused electron beam in a SEM allows one to determine the surface topography of the specimen which can be correlated with the Auger spectra of selected areas. In addition, a scanning Auger image may be obtained by using the amplitudes of a selected Auger peak for intensity modulation of the CRT. The normal modes for micro-spot AES investigation in the SEM include spot analysis, line scan and Auger electron imaging. Secondary electron image resolutions of less than 2000 Å have been correlated with Auger spectra of submicron regions. Surface features associated with gold and aluminum metallizations of microwave power transistors have been analyzed in detail using the AES-SEM technique. In addition the submicron Auger spatial resolution capability has been applied to the identification of contaminants on silicon surfaces.

INTRODUCTION

The analysis of failed regions on fine geometry devices has previously been extremely difficult. Energy dispersive x-ray analysis includes a reaction area about one micron (at 15 kV) below the surface. Auger analysis only examines about a 10 Å depth, however most systems use an analysis area which has a 50 μm diameter. Even the scanning Auger microprobe (SAM) uses a 5 μm beam and has no corresponding high spatial resolution SEM topography information. Microwave power transistors are characterized by cells on the order of 50 to 100 μm with line spacing on the order of 1 μm.

The utilization of electrostatic lens and the geometric configuration[1,2] of present day Auger detectors has made the attainment of submicron size electron beam a formidable problem. In the present investigation, the focused electron beam in the scanning electron microscope (SEM) is used as the primary beam for Auger spectroscopy [3,4,5] thereby improving the AES spatial resolution to .2 μm. The microspot technique therefore allows the determination of Auger spectra of selected areas in addition to the surface topography (SEM mode) of a failed region. Scanning Auger images may also be obtained by using the amplitude of the Auger peaks for intensity modulation of the cathode ray tube. The spatial resolution of .2 μm to 2 μm for Auger spectroscopy obtained by this technique is ideally suited for the analysis of (1) localized interdiffusion regions in metallizations, (2) adhesion problems and (3) process associated contamination. The instrument requirements for high resolution Auger spectroscopy of solid state devices in a commercial scanning electron microscope will be reviewed in order to understand the usefulness and limitations of the micro-spot SEM-AES technique.

General Requirements for AES-SEM Instruments

The requirements for AES in a scanning electron microscope are the vacuum chamber, the energy analyzer and the electron optical column. The vacuum system used to achieve a clean ultra-high vacuum in our SEM is an electro-ion pump with a mechanical carbon vane pump and cryo-sorption pumping for an oil free 2 stage roughing system[5]. The electro-ion pump is a four-cell triode type electrostatic getter-ion pump with a speed of 1600 l/sec for dry nitrogen. The pump is closely connected to the specimen chamber of the SEM by a 6 inch ultra high vacuum gate valve. Figure 1 shows a schematic of the entire system. The SEM is an ETEC autoscan specially made for this application[6]. The entire system is of stainless steel construction. The only non-stainless steel part exposed to vacuum is the viton seal at the gate valve. The ports contain the Auger detector, ion etching capability, secondary electron detector, leak valve and one sight port with an optical microscope. Pressures of 3 × 10^{-9} torr in the specimen chamber have been obtained after a mild bakeout at135°C. Under normal operational conditions, the system is operated at pressures between 5 × 10^{-9} torr and 1 × 10^{-8} torr. A residual gas analysis of the system was attempted in order to determine the presence of contaminants. A quadrupole mass spectrometer was installed in the approximate vicinity of the specimen stage. The constituents due to water had partial pressures of the order of 1 × 10^{-8} torr, while nitrogen partial pressure was below 3 × 10^{-9} torr.

The Electron Optics and Auger Detector

The electron optical column is the ETEC multi-lens system housed in a modular prealigned column. The energy source was a triode electron gun with a high emission tungsten filament. The spherical aberration coefficient of the final lens was 3 cm for a working distance of 8 mm. Figure 2 shows the relationship between probe current and probe diameter for a fixed working distance of 19 mm. The curved lines are for the 400 and 500 μm aperture. The straight line is for the optimum aperture obtained by varying aperture diameter. Since most of the AES investigations were accomplished with a probe current of 10^{-7} A to 10^{-8} A the optimum spatial resolution possible is between 2000 Å and 1 μm at 20 kV. However, one must also take into account such parameters as escape depth, atomic number, surface area and beam energy when determining spatial resolution. A second factor other than beam current which must be considered in obtaining the required resolution is recording time. The signal to noise (S/N) ratio can be increased by utilizing longer recording times. The recording time of an Auger spectrum can be increased to reduce the beam current while maintaining the same S/N ratio.

The Auger detector used is the cylindrical mirror type[5] designed to minimize the working distance of the scanning electron microscope to 19 mm. The analyzer energy resolution was measured to be .5% at 3 kV beam voltage with 10% transmission. Using a sputter ion gun and a multiplexing unit for monitoring peak to peak amplitudes, up to six Auger peaks can be monitored while the specimen surface is etched.

AES-SEM Modes and Analyses

a. Spot Analysis. The normal analytical modes include spot analysis, line scan and scanning Auger imaging. Each of these analyses can be combined with sputter etching in order to obtain an in-depth analysis. The Auger image can be recorded for a specified array of points or for a specified number of line scans. The amplitudes of the Auger peaks are then recorded or displayed as intensity or amplitude modulation of the recording cathode ray tube.

The spot analysis will now be applied to the failure analysis of a microwave power transistor in order to illustrate the unique application of this instrument as a diagnostic tool. Figure 4 illustrates a region typical of a failed microwave power transistor from pulsed RF accelerated life tests, showing the presence of a film material between the metallizations. Micro-spot AES-SEM analysis was applied to the reacted regions between the metallizations in order to identify the reaction products (oxide overcoat and aluminum reaction).

Application of the energy dispersive x-ray analysis technique (EDXA) on the area of interest was attempted before the initial AES analysis. A large 1740 eV Si peak was observed (figure 3) along with the 1490 eV aluminum line. The silicon detected could have been present in the reaction region or it may be from the substrate silicon. In addition, the EDXA technique cannot differentiate between aluminum in Al_2O_3 and free aluminum or between free silicon and silicon in SiO_2. The AES spectrum with the SEM electron beam situated on the reacted region is shown in figure 4. The position of the aluminum KLL Auger transition is indicated at 1407 eV. Also shown is an aluminum oxide peak at 57 eV. Therefore, the surface of the reacted zone consists essentially of Al_2O_3, oxygen and carbon (from handling and testing). Free silicon, up to the sensitivity limitations of the instrument which is 1.0 percent per monolayer was not detected. The lack of detection of silicon is shown by the absence of the 92 eV LMM and 1619 eV transitions. Auger analysis of the unreacted emitter metallization shows the position of the Al (KLL) transition at 1396 eV as expected for pure aluminum[7]. In addition, the position of the Al LMM transition was located at 69 eV instead of the 57 eV peak found for the aluminum reacted zone. The peak shift and change in shape of the KLL peak for aluminum clearly indicated that the film region of figure 4 was the result of the formation of Al_2O_3.

b. Auger Imaging. A problem related to semiconductor device reliability is the thermal dissolution of silicon into aluminum enhanced by microcracks or flaws in the aluminum thin film. At 450°C the diffusion process is extremely rapid and the solubility requirements are satisfied within a few minutes. However, microcracks in the film accelerate the diffusion process and often result in the migration of silicon to the top surface. Figure 5 shows the example of silicon diffusing through aluminum after a one hour anneal at 450°C. The surface of the interdiffused aluminum film was scanned with the analyzer set on the 92 keV KLL peak maximum and with a frame time of approximately .35 h. The signal was amplitude modulated in order to obtain the Auger image shown in figure 5. Figure 5 indicates resolution of submicron details in the scanning Auger mode at a working distance of 23 mm. A feature of interest on the silicon stripe can now be analyzed by moving the specimen to the center of the display stopping the primary beam scan and measuring the Auger spectrum in the usual manner.

c. Auger Line Scan Analysis. Analyses given thus far have reviewed the spot and imaging techniques. A third Auger technique which can be accomplished successfully in an SEM is Auger line scan analysis, for example, of an extruded silicon particle on the surface of a microwave transistor. The image of figure 6 was obtained with the analyzer set on the 92 eV Si Auger peak and shows the results of a single scan of the electron beam across the particle. The position of the particle correlates with the maximum of the Si line scan indicating that the particle is essentially silicon. Also shown in figure 6 is the spot Auger analysis of the particle identifying the 92 eV silicon peak, the 270 eV carbon peak and the 1619 KLL silicon peak.

d. Micro-spot Sputter Profiles. The AES-SEM technique when combined with electronic multiplexing[2,5] has been applied to obtain micro-spot Auger sputter profiles of reacted thin film structures. Figure 7 shows localized gold-silicon recrystallized regions of reacted gold-tungsten films on a silicon substrate. Analysis of the globular regions formed at 450°C were found to have a 3:2 surface composition of Au-Si as shown in figure 7a. The interdiffused region of Au-Si was approximately 1500 Å thick (assuming a sputtering rate of 60 Å/min. The migration of tungsten into the Au-Si structures was observed during the initial 25 minutes of sputtering. After sputtering for 100 minutes, the gold was completely removed, with silicon remaining probably as a WSi_2 structure[8]. The areas adjacent to the globular regions were found to be gold with trace amounts of silicon out-diffused from the silicon substrate (figure 7b). The silicon distribution was found to be uniform throughout the gold and tungsten films with the surface composition varying between 2 and 10 percent.

In summary, the general approaches for high spatial resolution Auger spectroscopy in an SEM have been reviewed. A system consisting of a commercial SEM with an ultra-high vacuum capability, integrated with an Auger electron spectrometer and sputter capability has been demonstrated. A secondary electron image resolution of approximately 2000 Å and Auger spectra of features less than 1 µ has been attained. Data taken on aluminum contacts of semiconductor devices has been reviewed in order to examine the capabilities of the instrument.

REFERENCES

1. Chang, C. C., *Surface Science* 25, 53 (1971).

2. Weber, R. L., *Research Development* 23 (10), 22 (1972).

3. MacDonald, N. C., Auger Electron Spectroscopy for Scanning Electron Microscopy, *Scanning Electron Microscopy* 1971, O. Johari and I. Corvin, Eds., pp. 89-96, (IIT Research Institute, Chicago, Illinois, 1971).

4. Brandis, E. K., and Hoover, R. A., *Proc. 7th Natl. Conf. on Electron Probe Analysis*, 1972, Paper 84.

5. Christou, A., Auger Spectroscopy of Solid Surfaces in a Dry Pumped High Resolution SEM, *Scanning Electron Microscopy* 1975, O. Johari and I. Corvin, Eds., pp. 149-156 (IIT Research Institute, Chicago, Illinois, 1975).

6. ETEC Autoscan SEM, ETEC Corporation, Hayward, California 94545.

7. Palmberg, P. W., *Handbook of Auger Spectra* (Physical Electronics Industries. Eden Prairie, Minnesota, 1972).

8. Sinha, A. K., *Thin Solid Films* 20, 115 (1974).

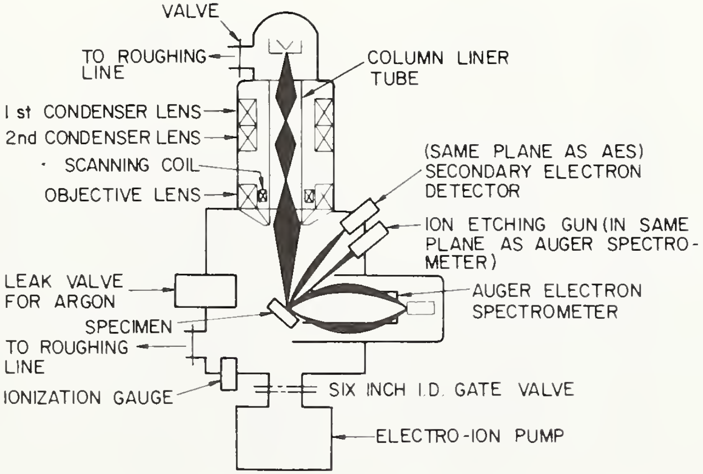

Figure 1a. Schematic diagram of AES-SEM instrument used for high spatial resolution Auger spectroscopy.

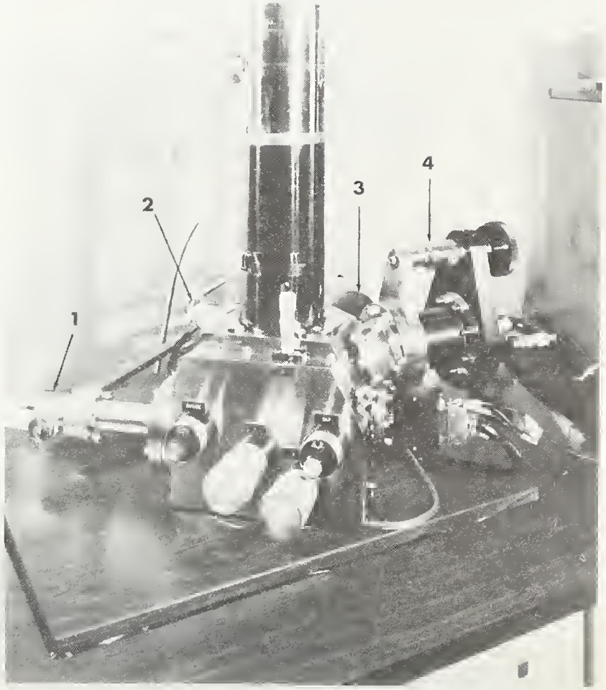

Figure 1b. AES-SEM system showing (1) apron leak valve, (2) sputter ion gun, (3) SEM detector, and (4) Auger electron detector.

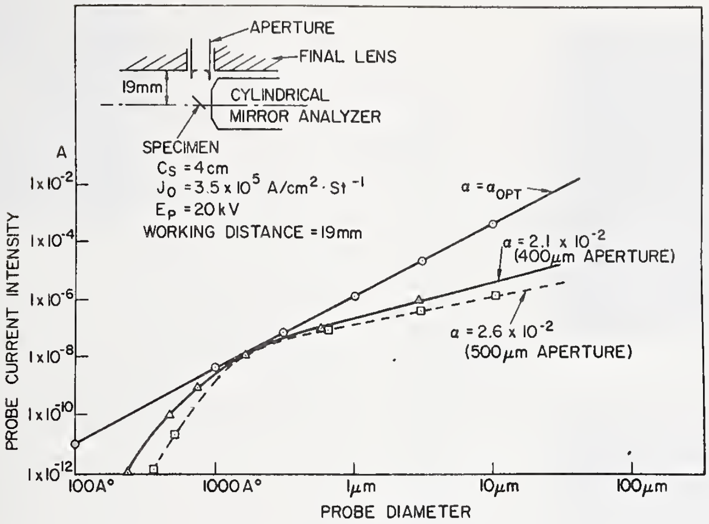

Figure 2. The relationship between probe current and probe diameter for AES-SEM system.

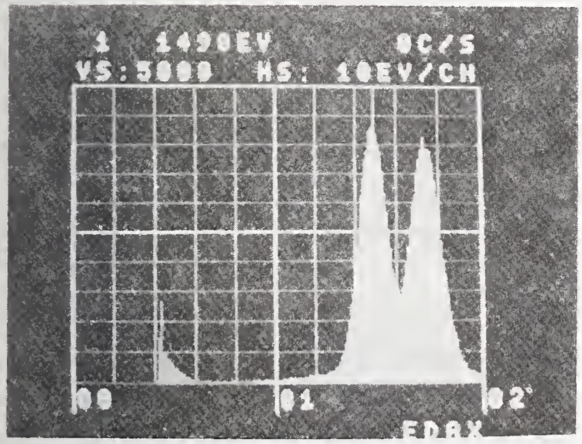

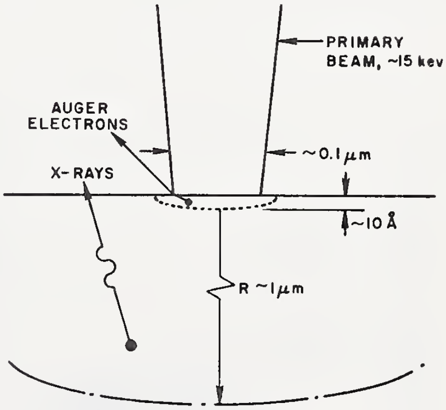

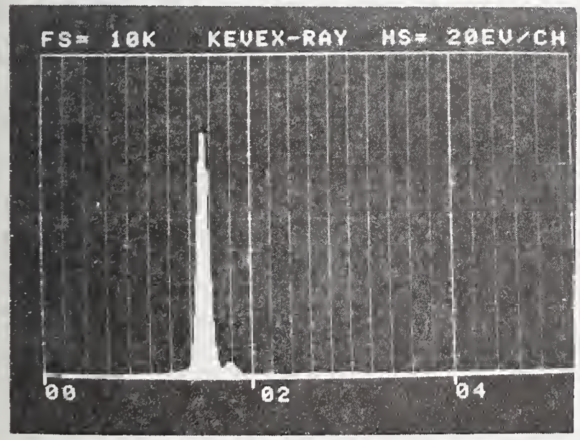

Figure 3. EDXA analysis of a failed microwave power transistor showing the detection of both a large 1740 eV Si peak along with the 1490 eV aluminum peak. Also shown is a schematic comparing the X-ray and Auger electron analysis regions.

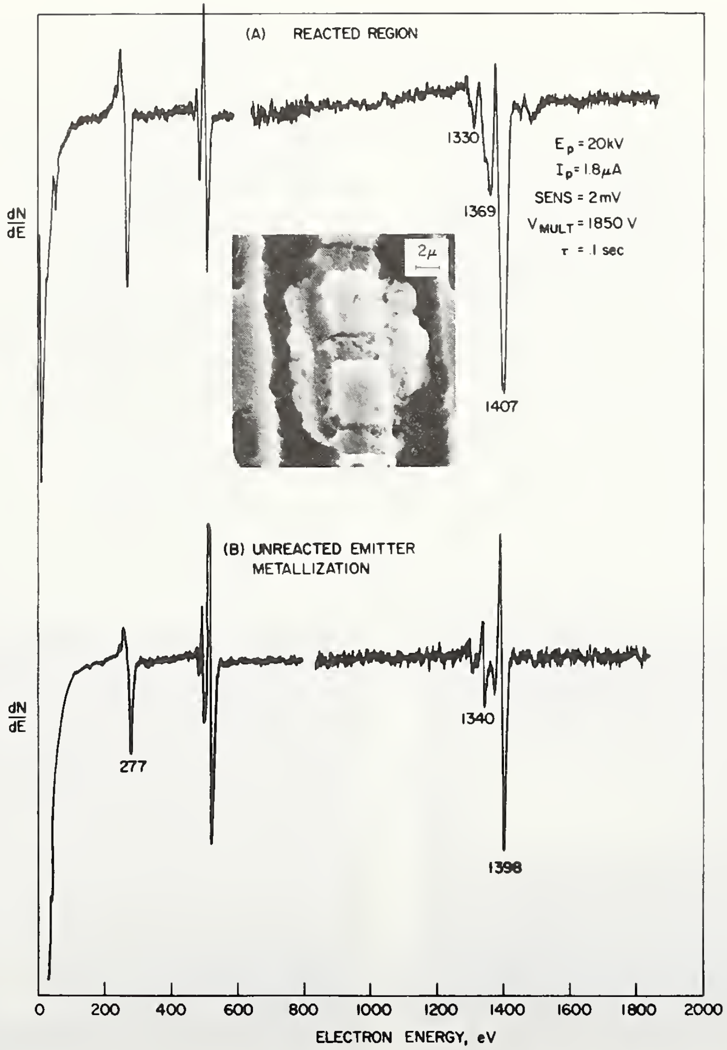

Figure 4. Auger analysis of a failed microwave power transistor showing the presence of a film material between the metallizations.

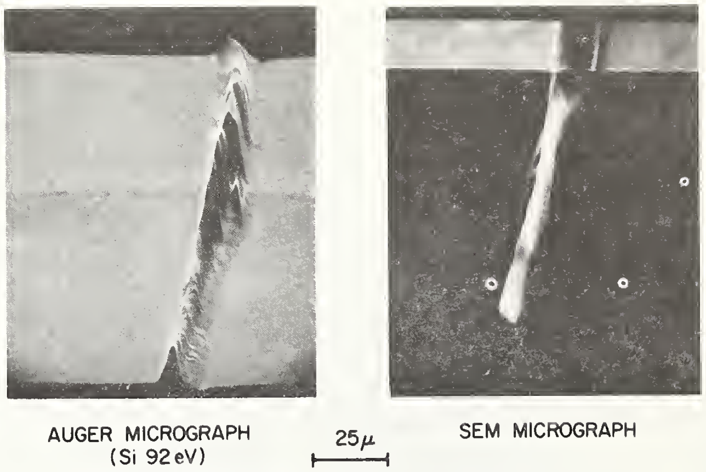

Al THIN FILM CONTACT SHOWING Si DIFFUSING THROUGH Al
WORKING DISTANCE = 23 mm

Figure 5. Auger imaging of silicon interacting with aluminum surface.

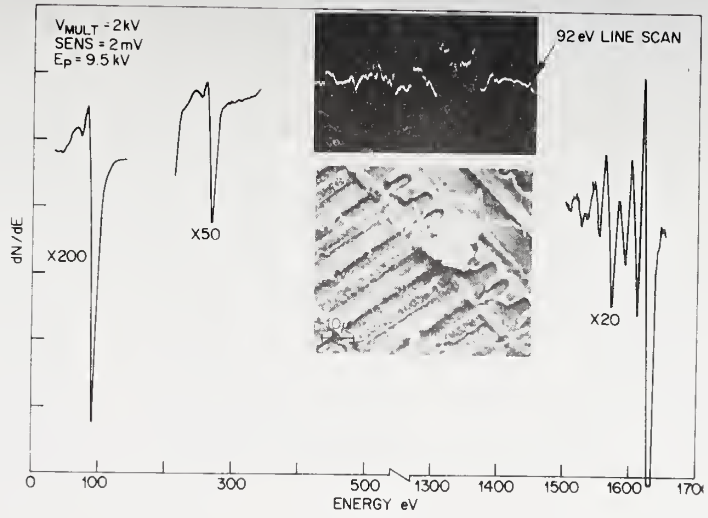

Figure 6. Line scan analysis of a silicon particle on the surface of a microwave power transistor.

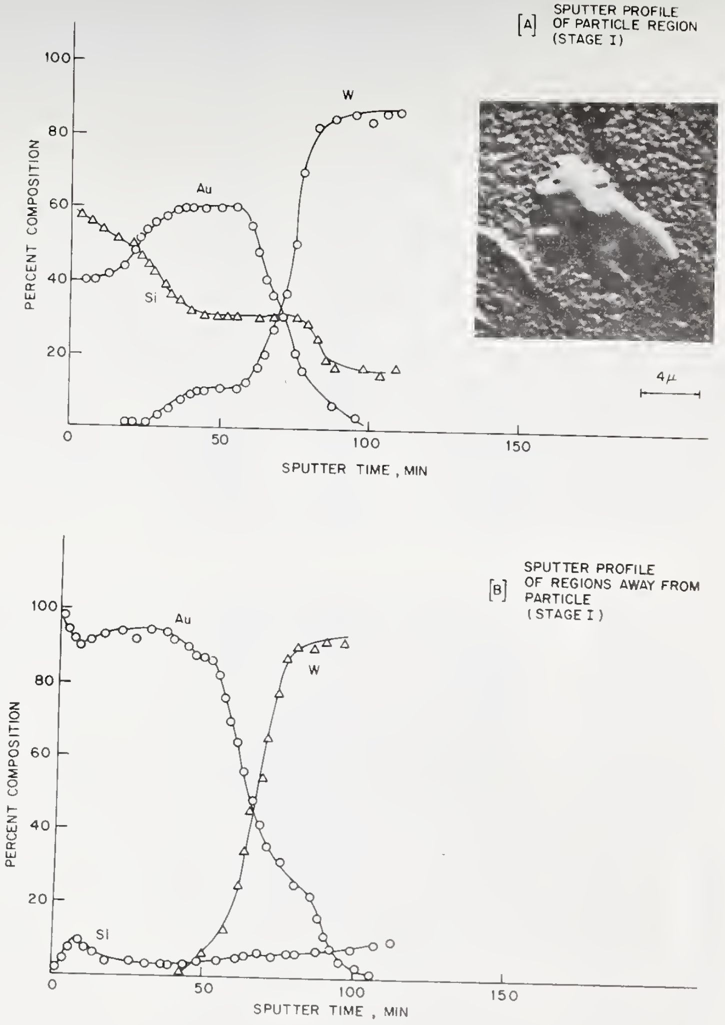

Figure 7. Micro-spot Auger sputter profile of interdiffusion in gold-tungsten thin films.

DISCUSSION OF THE PAPER

Harrington: Although you gain in spatial resolution what you do feel you loose in sensitivity with the Auger technique at the small beam diameters?

Christou: I do not have a quantitative answer for that, but you certainly degrade the signal to noise ratio significantly. The best way would be to computer interface your system so that you could observe peaks hidden in the noise.

Madey: I would just like to issue a word of caution about beam induced damage and problems of the sort that you have described here. I think it is particularly acute when you have such a small beam and a high current. For the situation you described with 10^{-9} amps and a 0.1 micron beam diameter you have a current density that is of the order of 10 amps per square centimeter. Now for electron stimulated desorption and decomposition, typical cross sections are of the order of 10^{-20} to 10^{-22} square centimeters for decomposition of surface oxides, desorption of oxygen and other species from surfaces. Under these conditions the average lifetime of the oxygen on the surface could be of the order of 1 to 100 seconds which is of the same order of magnitude as you need to get a workable signal to noise ratio. So it is quite possible then you can get appreciable beam decomposition and damage, particularly in compounds, insulators and semiconductors.

Christou: Yes, I agree and it is for that reason that we have been mainly applying this technique to interdiffusion phenomena and thin films.

NBS Special Publication 400-23, ARPA/NBS Workshop IV, Surface Analysis for Silicon Devices,
held at NBS, Gaithersburg, Maryland, April 23-24, 1975 (Issued March 1976)

APPLICATIONS OF X-RAY PHOTOELECTRON SPECTROSCOPY (ESCA) TO MIS DEVICES*

Frank J. Grunthaner

Jet Propulsion Laboratory
California Institute of Technology
Pasadena, California 91103

Summary

X-ray photoelectron spectroscopy (XPS, or ESCA) is described as both an analytical and experimental tool for the characterization of metal-insulator-semiconductor (MIS devices. A brief description is given of general problems which lend themselves to the application of this technique. Key experimental methods in XPS are discussed. Several illustrative applications are considered including characterization of the Si/SiO_2 interface, surface corrosion in hermetically sealed packages, mobile ion instabilities, organic surface contamination, etchant residues and heavy-metal impurities. New developments in XPS are discussed and some limitations of the technique are assessed.

Introduction

In the last three to four years, major advances have been made in the technologies of surface spectroscopy. These spectroscopies perturb the surface of a sample with photons, ions or electrons, and monitor the relaxation processes which results. This yields a variety of data concerning the physical parameters of the surface. Several of these methods give estimates of the elemental composition of samples. One of these techniques, XPS, also gives significant chemical information about the surface.

The production of an MIS device is basically an exercise in chemical processing technology. The fabrication of high reliability devices is dependent on achieving an understanding of the interaction of processing chemistry with device physics. In CMOS technology, for example, several dominant failure modes can be identified including: oxide breakdown, threshold voltage shifts, resistive and open connections, excess leakage and shorts, and changes in channel resistance. In each of these modes, several failure mechanisms can be detailed which are dependent on the chemistry of the oxide, that of the defects in the oxide, and that of residual species determined by the process. The study and characterization of the process requires chemical and physical information resulting from the probing of well-defined regions of the device. The study of the surfaces of devices can yield such information.

X-Ray Photoelectron Spectroscopy

XPS has seen considerable development since the first monograph on the phenomenon appeared in 1967.[1] Work in this field has also been catalogued under the more general description of electron spectroscopy for chemical analysis (ESCA). A number of recent reviews have appeared[2-5] and can be consulted for experimental detail.

Figure 1 describes the physical process. A soft x-ray source is used to irradiate the surface of a sample with photons of a characteristic energy (e.g., Aℓ $K\alpha_{1,2}$). The absorption of the photon can lead to two excitation cases: 1) x-ray absorption where an electron is excited from a core-level to the Fermi level, and 2) electron emission in which the electron is excited from the bound core state into the vacuum continuum. Either of these processes result in the excitation of the absorbing atom. The system can undergo relaxation through electron or photon emission or through more complicated radiationless processes. The photon emission process gives rise to an x-ray quantum (x-ray fluorescence). The electron emission event is termed auto-ionization and gives rise to an Auger electron. Auger electron spectroscopy (AES) typically uses high-energy electrons to create the core-level holes required to stimulate this electron emission.

In the case of photon absorption followed by direct electron emission, the energy of the ejected electron is given by:

$$h\nu = E_{kin} + E^{F}(k) + qV_s + W_{spec} \qquad (1)$$

where $h\nu$ is the photon energy, E_{kin} the

---

*This paper presents the results of one phase of research performed at the Jet Propulsion Laboratory, sponsored by the National Aeronautics and Space Administration under Contract NAS 7-100.

kinetic energy of the photoelectron, V_s the sample surface potential, W_{spec} the work function of the spectrometer, and $E^F(k)$ is the total final energy of the absorber after the ejection of an electron from the k^{th} orbital as a photoelectron, referenced to the Fermi level.

Since W_{spec} has a constant value for a particular spectrometer, V_s has a constant value under controlled conditions, and hν is well known, the kinetic energy of the photoelectron is directly related to the total energy with which it was bound in the adsorber. This relationship is generally written as

$$E_{BE} = h\nu - E_{kin} \tag{2}$$

where E_{BE} is the binding energy of the photoelectron.

$E^F(k)$ is a function of the orbital as well as the element, and consequently a number of photoelectron lines can be resolved for each element. This is illustrated in figure 2, where the ordinate is given in units of atomic number and the abscissa is given in binding energy (eV) of the appropriate photoelectron. Each of the elements has an XPS line well separated from the others, and peak positions can be readily determined with precisions of better than 0.1 eV. The corresponding plot of Auger electron (AES) lines plotted in units of apparent binding energy (eV) is given in figure 3. At high kinetic energies (low binding energies), these lines are also quite distinct. In practice, both AES and XPS lines are used to characterize the presence of an element.

The intensity of a photoelectron peak is determined by the photon flux, the effective sample area, the spectrometer acceptance angle, the photoelectric cross section, the mean-free-path of the photoelectron in the sample, and the number density of emitting atoms.[6] Individual photoelectron lines have been empirically scaled to a common element (fluorine) and the result plotted in figure 4. Here, relative intensity is plotted vs atomic number for several photoelectron lines.

XPS spectra are formulated through determination of the kinetic energy distribution of the photoelectrons emitted from the surface of the sample. The experiment is surface-sensitive because the measured photoelectron line represents those electrons escaping the solid without undergoing inelastic scattering. This escape depth determines the probing region of the experiment and is a strongly varying function of the electron kinetic energy and the density of delocalized valence electrons in the material. Metals have much shorter photoelectron escape depths than do insulators. The kinetic energy dependence of the escape depth of the photoelectrons is diagrammed in figure 5. The position of the curve along the length axis is determined by the material characteristics as discussed above.

The surface or bulk sensitivity of XPS and AES is largely determined by the kinetic energy of the escaping electron and not by the method of excitation.

The analytical aspects of the XPS spectrum are illustrated in figure 6 which shows a 0 - 1000 eV binding energy scan of the kinetic energy distribution. These spectra correspond to a 63 Å film of SiO_2, thermally grown on Si. The ordinate in this spectrum is the number of electrons expressed in arbitrary units. On the abscissa is plotted the binding energy (eV) increasing from right to left. The lines at 100 and 150 eV are the silicon 2p and 2s lines, respectively. The line at 285 eV corresponds to the carbon 1s level, which the peak at 530 eV is O1s level. The peak to the far left at 985 eV arises from the KLL oxygen Auger transition. The photoelectron lines show widths of 0.58 - 1.45 eV, while Auger electron lines range from 2 to 27 eV wide.

In addition to the analytical aspects of XPS spectra, the line positions are shifted by the chemical state of the element. This chemical shift parameter is the most important information available in the experiment. The position of XPS lines was found to have an "error" of ± 5 eV in early experiments.[1] Upon closer examination, line positions were found to be quite reproducible for a particular compound, but varied for different compounds of the same element. This chemical shift has a magnitude of ± 5 eV over the range of chemical states observed for a given element. Recent advances in instrumentation have reduced line widths to 0.55 eV from 1.0 eV, resulting in a major increase in chemical definition. This chemical shift is illustrated in the insets of figure 6. The right inset is a 10 eV expansion of the silicon 2p region. In the Si 2p spectra, two distinct lines are observed. The peak at 102.5 eV corresponds to the silicon of the silicon dioxide while that at 99 eV is due to the silicon substrate beneath the SiO_2 films.

In summary, the XPS experiment gives analytic information in terms of quantitative and qualitative analysis. Quantitative information requires calibration, and precisions in the ± 1% range are easily achieved. In qualitative terms, sensitivities of about 1 ppm have recently been demonstrated.[7] The chemical shift is the most important aspect of the experiment and permits assignment of the chemical state of various surface species. The observation depth is typical of surface spectroscopies and ranges from 3 - 4 Å to about 125 Å.

Experimental Considerations

The execution of the XPS experiment is diagrammed in figure 7. An x-ray source is required to irradiate (excite) the sample surface. The kinetic energy distribution of the emitted electrons is determined by means of an electron monochromator. This sequence requires that source, sample and analyzer be contained in a high vacuum system.

In practice, however, this basic experiment imposes several serious constraints on the equipment. The most important of these are listed in table I. An ultra-high-vacuum system is mandated by the surface nature of the experiment. Unless sample limited pressures of 10^{-9} torr and less are achieved, the surface can become recoated during analysis. The residual gases present in the spectrometer must be as non-reactive as possible, e.g., He, A, N_2, etc., with low sticking coefficients.

Since photoelectron spectra consist of sharp lines rising out of a significant scattered electron background, the highest possible signal-to-background ratio must be achieved. The background level is determined by the S/B ratio of the x-ray source, the surface features of the sample, the presence of secondary electrons in the sample chamber, and the electron background of the analyzer/detector. High S/B ratios in the x-ray source require the use of soft x-ray monochromators. The use of monochromated sources gives rise to collimated x-ray beams, which reduce the secondary electron flux in the sample chamber.

The analyzer, x-ray source and detector must be treated as a system and optimized for the maximum throughput; that is, for each photon impinging on the sample surface, the largest possible fraction of electrons must reach the detector.

A sample-mounting system is required which will permit variation in the electron acceptance angle of the analyzer in relation to the sample surface. This variation permits depth analysis in the range 2 - 120 Å without destruction of the sample.[9] Control of secondary electrons in the sample chamber enables a series of electrical experiments which will be described later. Variable temperature capability permits capture of reaction intermediates as well as study of "in situ" reactions, thermal degradation, etc.

The actual XPS experimental setup is illustrated for the JPL electron spectrometer in figures 8-10. Figure 8 gives a simplified diagram of the basic ESCA spectrometer. The soft x-ray source consists of an aluminum target bombarded with 15 keV electrons. These photons are focused by the spherically bent quartz-crystal monochromator on the sample surface in a separate chamber. The x-ray beam is collimated to a spot size of 1 × 5 mm. Electrons enter the energy analyzer through the 4-element electron lens, which retards and focuses the electrons. The analyzer is a spherical capacitor operated at a fixed energy transmission. The electrons are then directed against the multielement detector and the data then read into the multichannel analyzer.

A physical representation of the sample chamber of the spectrometer is given in figure 9. The x-ray source and analyzer are indicated in perspective. The sample is mounted on a sample rod which permits variation of the electron take-off angle seen by the analyzer. This permits the emphasis of either surface or bulk features in the ESCA spectrum. A low-energy electron-irradiating device (flood gun) is mounted in order to control charging effects and thus the surface potential. It provides a diffuse beam of electrons whose average energy can be varied from 0 - 10 eV above the vacuum level of the gun. Emission current can be varied over three orders of magnitude. An electron probe is being installed for direct measurement of the surface potential. The probe is provided with high-resolution optics at low kinetic energies and with capability for x-y scanning along the surface. The sample support is insulated from ground and therefore can be connected through a sensitive ammeter to the ground in order to detect currents from the electron probe.

The general surface analytical installation is diagrammed in figure 10. The key component is the high-resolution electron spectrometer (HP-5950A). The electron probe discussed above is also planned to operate as a scanning electron gun to stimulate Auger electron spectra. A sample reaction area is provided which is separate from the analyzer chamber and which contains equipment for secondary ion mass spectroscopy, electron-stimulated desorption, ion milling, metal deposition, and gas-solid reactions. A sample-preparation area is attached to the inlet chamber of the spectrometer consisting of a dry box with introduction lock. The dry box is under 5 psi pressure of nitrogen, which is dried over LN_2. A high-temperature furnace is provided for controlled growth of oxides on silicon. The furnace has an introduction lock permitting direct transfer of samples to spectrometer without aqueous or carbonaceous contamination. A plasma-cleaning facility is interlocked to the dry box to permit removal of trace organic contamination.

Sample Preparation

For reproducible results in XPS, considerable attention must be given to sample-mounting procedures. In this specific case, where the SiO_2/Si interface is the object of study, reproducible electrical contacts must be fabricated to the silicon substrate. The problems of ohmic contact and that of physical mounting were solved by using low-melting-point solders, such as InSn and GeAu. The sample and the mounting configuration are indicated in figure 11. A gold (Au) platen is prepared by washing with TCE, acetone, then several rinses with high resistivity (20 megohm) water. The platen is bonded to the rough underside of the oxidized silicon wafer by heating on a hot stage in the nitrogen atmosphere of the dry box. A gold window is placed over the top surface of the sample. The area illuminated by x-rays is indicated in the center of the window zone and is somewhat less than 1 × 5 mm (0.3 × 4 mm). Since the detector of the HP-5950A spectrometer is positionally sensitive, the long dimension can be reduced to approximately 1 mm, giving 0.3 mm^2 as the minimum analytical area.

During the experiments described in the following sections, the spectrometer was operated at a pressure of 6×10^{-10} torr. The ambient gas consisted primarily of H_2, He with lower levels of N_2 and N. H_2O and A were minor components, but some CO was present.

Applications

Silicon-Silicon Dioxide Interface

In CMOS technology, the fundamental device characteristics are determined by the oxide-semiconductor interface. Our initial experiments indicated that the escape depth of photoelectrons in SiO_2 was consistent with $\lambda_e = 40$ Å. This suggested that one could study the elemental silicon surface when covered by thin layers of SiO_2 up to 100 Å thick. Other experiments[9] have indicated that reproducible pinhole-free thermal oxides can be grown on silicon with thicknesses in the range of 15 - 200 Å. These oxides, grown in our laboratory, show extremely uniform thicknesses, and give excellent device characteristics.

Figure 12 reproduces the silicon 2p photoelectron spectrum of a freshly etched *p*-type silicon crystal. The spectrum comprises 10 eV, and the 2p spin-orbit doublet of silicon is clearly resolved. The spin-orbit splitting of silicon has a magnitude of about 0.6 eV. An instrumental system resolution of 0.55 eV is indicated by this spectrum.

In order to demonstrate the chemical shift between silicon in the elemental state and silicon in the +4 oxidation state (SiO_2), the spectra of figure 13 show both cases. The upper spectrum arises from the 2p doublet of elemental silicon. This sample is identical to that of the lower spectrum except that, in this case, the SiO_2 has been stripped with H_2O/HF and a monolayer of fluoride is present on the sample surface. The lower spectrum is due to a wet 40 Å oxide grown on silicon 100. In this spectrum, the Si 2p line due to the substrate occurs at nearly the same energy as in the elemental case. The peak at higher binding energy (104.3 eV) is due to the oxidized silicon of SiO_2. This shift of about 4.0 eV is characteristic of the 2p binding energy differences between Si^o and Si^{4+}.

There is reason to believe that the line width, line shape, and spin-orbit splitting of Si^{4+} is similar if not identical to that of Si^o. The broader structure of the oxide peak is indicative of a distribution of chemically inequivalent states. Although this distribution can be mathematically determined from the data,[10] it cannot be directly observed through higher instrumental resolution. It is possible, however, to experimentally modify this distribution of states by applying electrical stress to the oxide film.

In the XPS experiment, the metal-oxide interface of an MIS device can be modelled by the vacuum/oxide boundary. Electrical contact to the oxide can be accomplished by means of the vacuum level. The XPS experiment tends to produce a positive surface charge in the case of an insulator. An x-ray photon interacts with the surface of the sample creating an electron hole pair. If the electron is emitted into the vacuum, a hole is left behind. Therefore, a positive charge can build up in the thin surface layer interrogated in the XPS experiment (∿ 100 Å). The steady-state surface charge reflects the balance of the depletion current (photoemission) against the replenishment currents (vacuum secondaries, tunneling currents, etc.). Since the vacuum secondaries are minimized through x-ray collimation, and low x-ray flux densities, a significant positive surface charge can be developed in SiO_2. In very thin oxides this potential is ultimately limited by electrons tunneling from the Si interface.[11]

A corresponding negative potential can be induced by increasing the current density of low-energy electrons to the sample surface from the flood gun. Therefore, a bias of either polarity can be applied dynamically in the course of the XPS experiment.

Figure 14 illustrates the effect of bias on Si 2p spectra of a 44 Å SiO_2 layer on silicon (100). The positive bias spectrum is given as the lower curve. The negative bias spectrum (upper curve of figure 15) was recorded while bombarding the sample surface with electrons of an average energy of 8.6 eV above the vacuum level. A change in line shape of the elemental line is observed, as is a change in the relative position of the oxide peak.

Previous work of just two to three years ago identified the escape depth of photoelectrons in SiO_2 at 10 - 15 Å (λ_e).[2] Figures 15-a and 15-b give the Si 2p spectra of a 113 Å film of SiO_2 over Si. In figure 15a, the large difference in relative intensities of the oxide and substrate peak are evident, while figure 15b shows the line shape of the substrate silicon line at higher gain (20 X). Its binding energy of 99.06 eV is in good agreement with that of the Si^o peaks of figures 12 and 13.

The Si^{4+} state (SiO_2) is clearly resolved from that of Si^o. The determination of silicon to oxygen ratio can be directly calculated by comparing the oxidized silicon peak intensity with the intensity of the oxygen 1s peak. The magnitude of excess silicon, and reduced silicon oxides can now be directly measured, within the sensitivity of the experiment. For these thin oxides, no ion milling is required to see the interface and hence no ion-stimulated redistributions need be considered in interpreting the data.

Migratory-Gold-Resistive-Short

The technology of metallization in integrated-circuit devices is based on either aluminum or gold. The presence of moisture within the device package has long been known to leak to electrolyte corrosion of aluminum. This corrosion results in a well-documented failure mode. The chemistry of gold suggested that metallization schemes using this noble metal would be free from susceptibility to such electrochemical attack.

Recently, electrolytic corrosion has been observed and described phenomenologically as the migratory-gold-resistive-short (MGRS) mode.[12] The failure is seen as the abrupt decrease of resistance between two or more adjacent metal stripes. The shorting current are on the order of milliamperes. SEM micrographs of failed parts reveal that fern-like or dendritic gold deposits have formed a bridge between metal stripes.

The dendritic deposits appear to progress from the negatively-biased stripe (cathode) toward the positive one. The general form or morphology of the growth is quite specific and similar to that of deposits found in electrochemical silver migration.[13] This well-known phenomenon results from the surface transport of silver which is driven by large electric fields. This surface transport is strongly dependent on the presence of moisture and on the nature of the substrate surface.

The MGRS failure is observed on the surface of integrated circuits using Ti/W/Au metallization which has been covered with a layer of e-beam-evaporated quartz. Failure analysis of affected parts showed significant levels of water in the purportedly hermetically sealed package.

The presence of water made possible a corrosion cell. This implied that the rate of attrition of parts is determined by the amount of time adequate potential is applied across adjacent metal stripes. The major difficulty, however, was that dendritic growth requires as few as 10^{10} atoms of gold to bridge a stripe.

Since gold cannot be simply dissolved in aqueous solutions, we studied the surface of failed and reference parts to determine the nature of the impurities residing atop the passivating glass layer. The presence of significant levels of halogens was observed by means of XPS.

This is an example of surface corrosion chemistry, and three points are relevant to this discussion: 1) positionally sensitive detection, 2) limiting sensitivity, and 3) decomposition of sample system. The first of these points is illustrated in figures 16 and 17. Figures 16 shows a 0 - 1000 eV binding energy scan of the top of the chip, together with the bonding pads, wire leads, and some parts of the package base. This is determined by the relative intensities of the gold 4f photoelectron line at about 85 eV and of the oxygen 1s line at 530 eV. The gold line is approximately 25% more intense than the oxygen 1s line. In figure 17, the detector is adjusted to scan the top of the chip, and the oxygen/gold intensity ratio has changed by a factor of 22.

The analysis of the surface of the glassivated substrate by XPS indicates that significant quantities of the halogens (Cl^-, Br^-, I^-) are present together with hydro- and fluorocarbons and several trace metals, such as Na^+, K^+ and Hg. Of the halogens, Br was most abundant while Cl and I had relatively equal concentrations. The bromine 3d region of the photoelectron spectrum is given in figure 18. The structure arises from at least 2 different chemical states of the element. The iodine 3d region of the spectrum is plotted in figure 19. The spin orbit doublet is clearly defined in this spectrum.

Over the range of failed and unfailed parts which have been examined by XPS, the concentration of I^- has varied over four orders of magnitude. Levels of iodine as low as 1 ppm can be readily detected. This represents a sensitivity limit about three orders of magnitude lower than was previously observed.[2] This is related to the relatively high photoelectric cross-section of the iodine 3d electrons for 1.5 keV x rays, and to the magnitude of the spin-orbit splitting. This separation of two lines with an appropriate intensity relationship facilitates the use of sophisticated noise-removal techniques for data manipulation.[14]

Interestingly, many of these impurity atoms were not observed in electron-stimulated Auger and x-ray spectra. This suggests that for many problems, electron-stimulated desorption is a serious experimental difficulty. Monochromatized x-ray excitation offers a minimal source of secondary electrons for such desorptions.

Mobile Ion Instability

The role of mobile ions in causing instabilities in MOS devices is well known and several reviews have appeared.[15-19] The previous work has demonstrated that sodium is the most common source of such instabilities. Sodium contamination in thermally grown SiO_2 is often introduced by the sodium in the oxidizing or annealing ambient.[20] Most of the sodium present in the ambient can be introduced through the walls of the furnace tube since this tube is usually fabricated of silica, which permits extremely high diffusion rates of sodium at the required operating temperatures. Additional furnace tube liners are often used to reduce this source of contamination. The processing steps following high-temperature oxidation are also potential sources of sodium contamination, since most solvents—organic and aqueous—show significant sodium levels if not controlled. The effective concentration of sodium in the bulk arising from surface contamination of the oxide is directly determined by the maximum temperature to which the structure is exposed. Finally, sodium contamination can be introduced during metallization unless extreme precautions are taken.

It has been established that the rate of removal of sodium from the SiO_2/Si interface is much faster than that from the SiO_2/metal or SiO_2/vacuum interface. The mobility of Na^+ ions in the "bulk" of the SiO_2 is quite high (at least 4×10^{-13} cm^2/V sec at room temperature). The rate-limiting step during forward drift appears to be the "emission" of ions from "traps" at the SiO_2/metal interface. The trapping at the SiO_2/Si interface is much weaker and is strongly dependent on the conditions of oxidation and annealing.

The existence of two forms of traps for Na^+ at the SiO_2/Si interface has been suggested where one of these becomes saturated at high ionic contamination levels. This patch model has been developed to explain variations at the metal/oxide interface as well.[21]

Recently, methods have been developed to getter sodium ions in SiO_2 or to neutralize Na^+ at the Si/SiO_2 interface. Phosphosilicate glass (PSG) is widely used to trap or getter Na^+ moving from the metal/SiO_2 boundary to the SiO_2 interface. Recent experiments[22] have indicated that the addition of HCl in the high-temperature oxdiation step modifies the silicon interface and permits charge neutralization of

Na^+ as it approaches the Si boundary. These methods basically involve a modification of the chemistry of trapping defect sites within the oxide.

Unfortunately, these traps created through process variation are highly susceptible to high-energy gamma- and electron-radiation. In radiation fields, the sodium is again released, leading to device failure. We chose to initiate a study of mobile ions in thin SiO_2 by means of XPS in order to understand the chemistry of the defect-site mobile-ion interaction.

Conversations with device physicists indicated that there existed two fundamentally different forms of sodium in silicon oxides. One of these is termed positive, has a +1 charge, and moves when subjected to appropriate fields. The second form is termed neutral sodium because it is positionally trapped and cannot translate in response to dc fields.

These observations, together with the "patch" model of specific traps suggested a coordination chemistry of sodium which might lead to well-resolved states in the XPS spectrum.

In a previous section, it was observed that a positive or negative bias could be applied to the surface of an insulating sample in the course of the XPS experiment. The combination of applied bias and elevated temperatures was employed to pull the Na^+ in the oxide out to the oxide/vacuum interface, or alternately push the Na^+ into the oxide silicon interface. The effects on the silicon, oxygen and sodium spectra have been catalogued and interpreted.[23] Figure 20 gives the Na 1s spectrum of an as-processed device. Electronic measurements of this sample indicated a mobile-ion concentration of about 10^{11} atoms/cm^2. This spectrum is the result of 51 hours of accumulation time. In figure 21, the Na 1s spectrum of a different area of the silicon wafer is given. In this case, however, the SiO_2 film has been etched in H_2O/HF. The accumulation time for this spectrum is identical to that of figure 20. A composite of the peak positions observed in this experiment is reproduced as figure 22.

Five species of sodium are discernible and the corresponding peaks are numbered in the figure. With positive bias at 525°K, peaks 3 and 4 diminish in intensity, while peaks 1 and 2 increase. Application of negative bias results in an increase in the intensity of 3 and 4 with a decrease in 1 and 2. No change is seen in peak 5 as a function of bias. In a particular sample its intensity appears to scale as the flood gun current; however, this effect has not been firmly established. Alternating positive and negative bias fails to transfer more than 30% of the intensity of peaks 3 and 4 to peaks 1 and 2.

Finally, as a function of increased intensity of peaks 3 and 4 at negative bias, a splitting is observed in the apparent vacuum level of the SiO_2 under the x-ray beam. The splitting is of the order of 0.7 to 1.0 V and is quite reproducible.

A number of additional states were observed in some samples but were not adequately reproducible to warrant including them in this composite. The possibility exists, however, that future work may resolve as many as 4 additional states of Na in SiO_2.

Significant changes in the spectra of the oxygen 1s and silicon 2p regions were also observed and correlated with ion movement.[23]

Organic Surface Contamination

The fabrication of an MIS device can be reduced to a sequence of chemical processes which are implemented under clean conditions at atmospheric pressure or at high vacuum. Throughout these process steps, the wafer is exposed to a number of organic compounds present in the gas phase. As a consequence, all wafers have a surface coating of carbonaceous material which is generally several atomic layers thick.

Rinsing with organic solvents leaves this overlayer unaffected. Oxidizing and reducing cleaning treatments modify the chemistry of the layer but do not remove it. There is mounting evidence[24] that this overlayer persists after oxidation at 1000°C in dry O_2.

The presence of these overlayers can lead to bond failure and anomalous contact resistance in metallization systems. Tentative overlayers of appropriate chemical characteristics can modify etchant performance. Residual carbon doping at the Si/SiO_2 interface during gate-oxide growth may effect device performance.

Unfortunately, thin overlayers of carbon are difficult to analyze. Electron- and ion-stimulated surface analyses cause rapid desorption of the layer in vacuum, and can induce chemical changes in its structure. Since XPS involves the lowest magnitude of electron flux to the sample surface, we have begun a study of organic contamination in MIS device processing.

Figure 23 illustrates the presence of such films. This 0 - 1000 eV binding energy scan is that of a kovar package interior. Gold, copper, chromium, iron, cobalt, oxygen, chlorine, fluorine and a number of other elements are readily observed. The carbon line at about 285 eV represents a major component of this surface.

Simple element detection is not an adequate use of XPS. The importance of this experiment is the ability to identify chemical parameters. This is illustrated in figures 24 and 25. These represent scans of the surface of a GaAs sample on which a thin oxide has been grown. Experiments in a solar-cell research program at JPL have indicated that oxides grown in different conditions of carbon contamination had markedly superior operating parameters. The sample giving rise to figure 24 was significantly superior to that of figure 25. In both spectra, a number of aliphatic carbon states can be assigned. Similarly, carbonyl or carbon-oxygen chemistry is found in both samples. In the superior device an amide carbon signal is observed. The presence of amines in an epoxy used to attach the wafer to a metal substrate had resulted in the incorporation of some of these compounds on the surface of the GaAs. This observation permits the design of a process to inject this species at the surface. If this had not been observed directly, the process would have to be developed through random optimization of conditions.

Figure 25 gives a final illustration of the tenaciousness of surface adsorbed carbon. This silicon sample had been etched in hot H_2O, HF under dry N_2 and directly introduced to the spectrometer. This 0 - 1000 eV spectrum is now dominated by the silicon 2s and 2p lines. The fluorine 1s line is clearly observed as is the fluorine KLL Auger structure. Note, however, the intensity of the C 1s is still quite significant. In these experiments, silicones, freons, and simple halocarbons can be readily detected. Proteins and lipids resulting from human handling can also be observed. In our work, only cleaning in an O_2 plasma resulted in removal of the carbon overlayer.

Etchant Residues

Yet another of the fundamental chemical steps in device processing involves the etching of metals and oxides in conjunction with photoresist masking. Although the chemistry of metal and oxide dissolution is well understood for bulk materials, little work has been done to characterize the effect of these solution techniques on the device surface.

One of the basic difficulties with liquid/solid reactions concerns the possibility of etchant residues deposited on the wafer surface. Often the presence of the surface alters the solubility of the end products of the etch and consequently such films are exceedingly difficult to remove. Proper removal requires the ability to directly monitor their presence. In figure 26, several peaks are observed at high binding energy which can be attributed to the presence of two or more forms of cerium oxide.

This sample was prepared from a wafer which had a chromium/gold metallization over the gate oxide. The metal contact was etched with KI_3 solution to remove the gold, followed by ceric ammonium sulfate solution to dissolve the chromium. This sample was then treated with hot H_2O/HF to remove the SiO_2 film. After these processing steps, little tri-iodide is observed on the surface, but the cerium remains.

Such residues, if undetected, can then be driven into the device by subsequent processing.

Figure 27 shows a narrow energy scan of the cerium region showing the splitting of states in the individual components of the cerium 3d doublet. Exposure of the wafer to chemical solutions of appropriate pH can virtually eliminate this oxide residue.

Heavy Metal Impurities

In the region of 920 and 950 eV in the spectrum of figure 28, components of the copper 2p doublet can be detected. Most of the samples studied in our laboratory are fabricated on single-crystal silicon substrates which have been polished by the copper-ion polishing method. This polishing system involves exposure of the wafer to cupric ion solutions. After polishing, these wafers are pre-oxidized to a depth of several thousand Angstroms. This oxide is then stripped to remove any heavy metal contamination as well as crystallographic damage introduced by the polishing mechanism.

Our studies indicate that copper persists at the Si/SiO_2 interface in spite of these precautions. Figure 28 illustrates this situation with the copper 2p region of a freshly etched wafer. The copper 2p doublet is clearly resolved. A scan of this sample before removal of the 50 Å SiO_2 film indicated that the copper was barely detectible through the oxide. The intensity ratios of the Cu 2p line before and after oxide removal indicate that the copper is located at the Si/SiO_2 interface, and is probably imbedded in the elemental silicon. Repeated preoxidations slowly reduce the amount of copper present.

Three types of copper can be discerned over the range of wafers studied, and there are indications that the different species have unique effects on the electrical characteristics of the device.

New Developments

One of the basic problems facing the application of electron-emission spectroscopies to the study of semiconductor and insulator samples is that of referencing the observed data. As was developed previously, the binding energy observable is a function of the work function and surface potential. In insulator samples the work function and surface potential are not fixed, but, rather, are a function of the x-ray flux density, the emission currents, and the secondary electron currents.

A new method has been devised which enables measurement of hard reproducible values for the work function and surface potential of the sample during the XPS experiment. In order to illustrate this approach, figure 29 shows the relation of the energy levels of the flood gun/vacuum/SiO_2/Si system. All XPS measurements are referenced to the Fermi level E_F of the spectrometer which is fixed to E_F of the silicon substrate (a known bias may be applied to the substrate). The surface potential V_s of the sample determines the fields in the sample near the surface, affecting the energy shifts in the XPS lines. The magnitude of V_s is given by the sum

$$V_s = F_{ox} w + V_{ss}$$

where F_{ox} is the oxide field, w is the oxide thickness, and V_{ss} is the surface potential at the silicon interface.

In this experiment, the flood gun cathode is biased to ground by a known voltage V_{fg}. When the vacuum levels are such that $E_{fg} > E_{ox}$, some of the electrons emitted from the flood gun reach the sample surface, charging the surface more negatively and causing a current through the sample. When $E_{fg} < E_{ox}$, these electrons are totally reflected from the surface. When $E_{fg} = E_{ox}$, a threshold condition exists. Let the value of V_{fg} for threshold be V_o; then, by scanning V_{fg} from some bias setting such that V_{fg} scans from $V_{fg} < V_o$ to $V_{fg} > V_o$, the current through the sample must abruptly rise at $V_{fg} = V_o$ to a saturation value. This scanning is accomplished in a time shorter than the relaxation time of the surface charge generated during the fixed bias. The first derivative of the current with respect to V_{fg} gives a maximum determining V_o. In figure 29, the cathode work function W_c, the electron affinity of the oxide χ_{ox}, the SiO_2/Si barrier energy, ϕ_B, and the silicon bulk potential V_B are all constant. Therefore, changes in V_o equal changes in V_s and provide a hard energy reference for XPS of insulators.

The current from the flood gun through the sample is monitored with the experimental arrangement shown in figure 30. The sample is connected to ground through an ammeter with a lock-in amplifier. A reference oscillation is applied to the cathode of the flood gun and phase-sensitively detected at the lock-in amplifier. The first harmonic of the ac signal gives the first derivative of the current.

Since the flood gun gives a broad diverging source of electrons, maxima appear in the scan corresponding to both the x-ray irradiated and unirradiated region of the oxide as well as the gold mask region at the periphery of the sample window. The maximum due to the gold mask is constant and equal to the difference in work functions of the gold and flood gun cathode. The irradiated region of the oxide is shifted to more positive potentials by the positive charging effect of the x-rays.

Figure 31 gives a representative indication of the variation in surface potential (of the SiO_2 under the x-ray beam) as a function of different flood-gun parameters. A range of approximately 4 eV was observed in the case of a 30 Å dry oxide thermally grown in Si. An analogous shift was observed in the relative positions of the Si 2p peaks for SiO_2 and for Si, as a function of different flood-gun parameters. Additional experimental detail concerning these experiments and those planned with the electron probe have been reported elsewhere.

Since this experiment can be accomplished in a time scale of 10^{-8} to 10^{-9} seconds, the ability to determine hard reference energies permits energy lock-in and should lead to much narrower line widths. Also, the routine intercomparison of data between laboratories would be greatly facilitated.

Recent advances in sample preparation make possible the fabrication of clean active surface adsorbers. Placing these adsorbers in contact with solutions and gaseous atmospheres should facilitate the sampling of impurities at sub-part per billion levels.

Conclusions

XPS is a powerful tool for the study of the surface and interface chemistry of MIS device processing. It offers reasonable sensitivity together with minimum interferences for analytical capabilities. The chemical shift observed in this spectroscopy is its most important feature. The physics of the experiment can be manipulated to give considerable electronic/chemical information about the insulator/semiconductor interface. Since the observational depth of the method is sharply defined, this chemical information is often lost in the application of conventional techniques. Consequently, this data is often of critical utility in the solution of processing problems.

Although technical advances on the part of instrument manufacturers have made possible promising new applications of XPS, several difficulties remain. The most fundamental difficulties are those of sample area and time. Current state-of-the-art limitations on sample size are about 0.1 × 0.3 mm. This restriction is imposed by the physical difficulty of making high fluence x-ray sources and focussing soft x ray. Electron-stimulated methods, though more destructive than XPS, offer a considerably narrower field of view. This limitation is directly related to the second fundamental difficulty: time. Low sodium levels reported here required observation times on the order of 50 hours. The corresponding SIMS experiment would require less than one hour's accumulation time.

References

1. Siegbahn, K., Nordling, C., Fahlman, A., Nordberg, R., Hamrin, K., Hedman, J., Johansson, G., Bergmark, T., Karlsson, S., Lindgren, I., Lindberg, B., *Electron Spectroscopy for Chemical Analysis - Atomic, Molecular, and Solid-State Studies by Means of Electron Spectroscopy* (Almqvist & Wiksells Boktryekeri AB, Stockholm, Sweden, 1967).
2. Brundle, C. R., *J. Vac. Sci. Technol.* 11, 212 (1974).
3. Bremser, W., X-Ray Photoelectron Spectroscopy, *Topics in Current Chemistry*, p. 36, (Springer-Verlag, Berlin, 1973).
4. Fadley, C. S., Theoretical Aspects of Electron Spectroscopy, NATO Conf. on Electron Emission, Ghent, Belgium, 1973.
5. Hollander, J. M., and Shirley, D. A., *Ann. Rev. Nucl. Sci.* 20, 435 (1970).
6. Henke, B. L., *X-Ray Optics and X-Ray Microanalysis*, pp. 157-172, (Academic Press, New York, 1963).
7. Grunthaner, F. J., Griswold, T. W., and Clendening, P. J., Migratory Gold Resistive Shorts: Chemical Aspects of a Failure Mechanism, *Proc. 13th Annual Reliability Physics Conf.*, Las Vegas, Nevada, April 1-3, 1975, pp. 99-106.
8. Fadley, C. S., *J. of Electron Spectroscopy* 5, 725 (1974).
9. Kriegler, R. J., Cheng, Y. C., and Colton, D. R., *J. Electrochem. Soc.* 119, 388-392 (1972).
10. Grunthaner, F. J., Klein, J., Barton, J., (to be published).
11. Williams, R., and Woods, M. H., *J. Appl. Phys.* 44, 1026 (1973).
12. Shumka, A. and Piety, *Proc. 13th Annual Reliability Physics Conf.*, Las Vegas, Nevada, April 1-3, 1975.
13. Butts, A., and Coxe, C. D., Silver, Chapt. 34, (Van Nostrand Company, 1967).
14. Grunthaner, F. J., (to be published).
15. Kriegler, R. J., *Proc. 12th Annual Reliability Physics Conf.*, Las Vegas, Nevada, April 2-4, 1974, pp. 250-258.
16. Kerr, D. R., *Proc. 9th Annual Reliability Physics Conf.*, Las Vegas, Nevada, 1971, pp. 1-8.
17. Szedon, J. R., and Handy, R. M., *J. Vac. Sci. Tech.* 6, 1-12 (1969).

18. Snow, E. H., and Deal, B. E., *Trans. Metal. Soc. AIME* 242, 512-523 (1968).

19. Hofstein, S. R., *Solid-State Electron.* 10, 657-570 (1967).

20. Kriegler, R. J., *Proc. 2nd International Symposium on Silicon, Materials and Technology,* Electrochem. Soc. Meeting, Chicago, Illinois, 1973, pp. 363-375.

21. DiStefano, T. H., *J. Appl. Phys.* 44, 527 (1973).

22. Kriegler, R. J., Cheng, Y. C., and Colton, D. R., *J. Electrochem. Soc.* 119, 388-392 (1972); or see Grunthaner, F. J. and Maserjian, J., *Proc. 13th Annual Reliability Physics Conf.*, Las Vegas, Nevada, 1975, p. 15-26.

23. Grunthaner, F. J., Lewis, B. F., Griswold, T. W., and Maserjain, J., Differential Charging in X-Ray Photoelectron Spectroscopy, ACS Meeting, Honolulu, Hawaii, June 12, 1975.

24. Clendening, P. J., Maserjain, J., and Grunthaner, F. J., Chemical Structures of Carbon Contamination at Si/SiO_2 Interfaces, submitted to *J. Electrochem. Soc.*

TABLE I

EXPERIMENTAL CONSIDERATIONS

- Ultra High Vacuum
- "Clean" Residual Gas Background
- High Signal/Background Ratio
- Highest Possible Throughput

  X-Ray • Analyzer • Detector
- Rotatable Samples
- Collimated X-Ray Source
- Electron Control
- Variable Temperature Capability

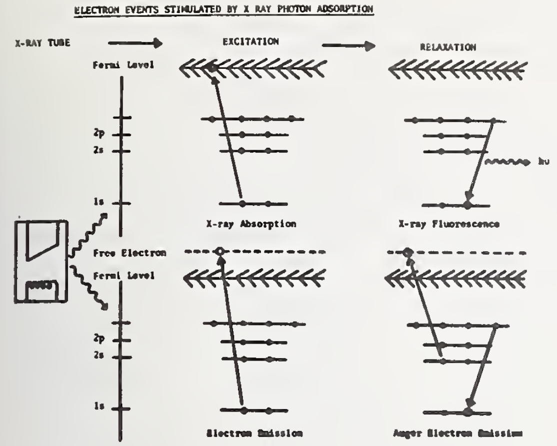

Figure 1. Electron events stimulated by x-ray photon absorption.

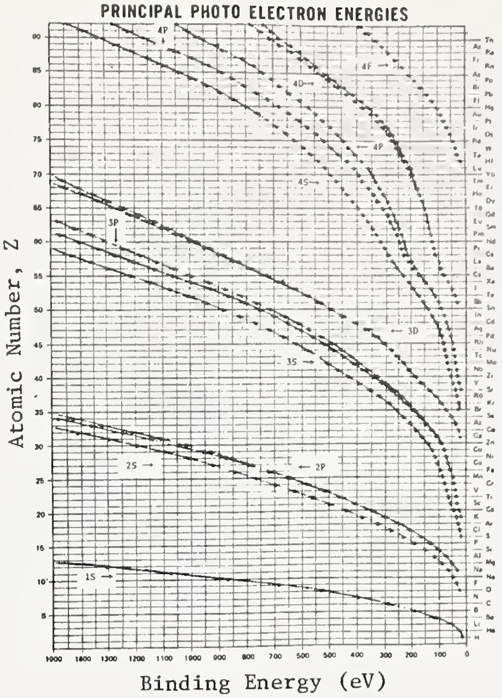

Figure 2. Principal photoelectron energies plotted by atomic number versus binding energy for Al $K\alpha_{1,2}$ (1483.6 eV) excitation.

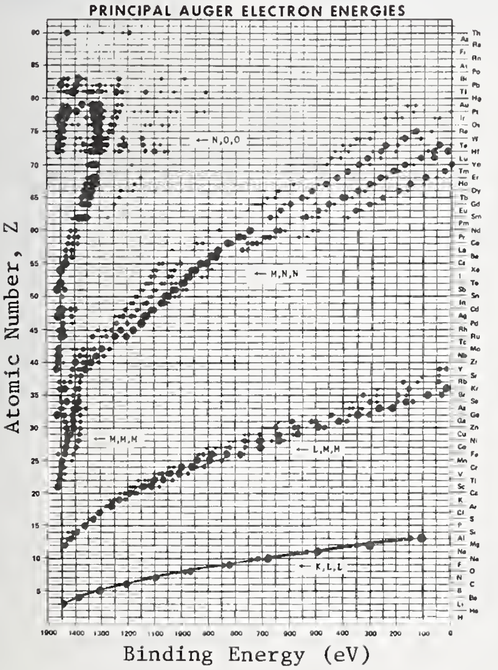

Figure 3. Principal Auger electron energies plotted by atomic number. Abscissa is given at apparent binding energy (i,e., electron kinetic energy minus 1483.6 eV).

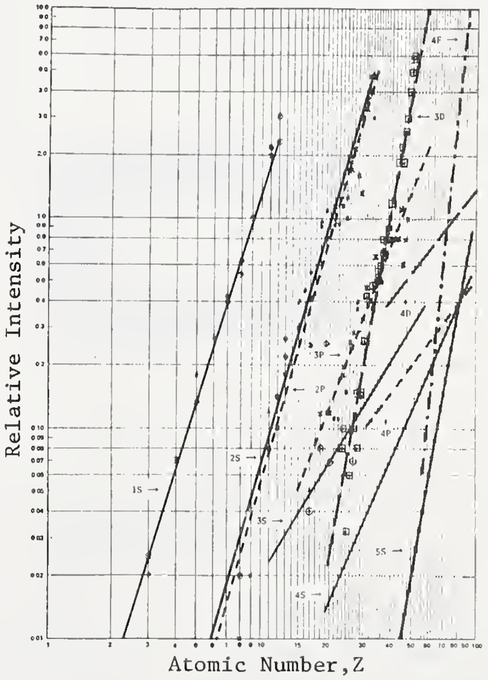

Figure 4. Relative intensities of the photoelectron lines normalized to sodium line intensity = 1.0 .

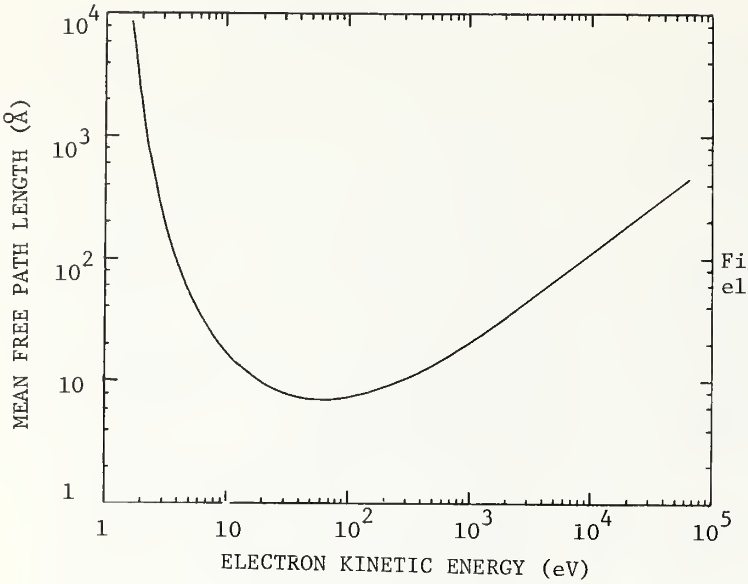

Figure 5. Mean free path for inelastic electron scattering.

Figure 6. XPS spectra of 63 Å SiO_2 film on silicon substrate.

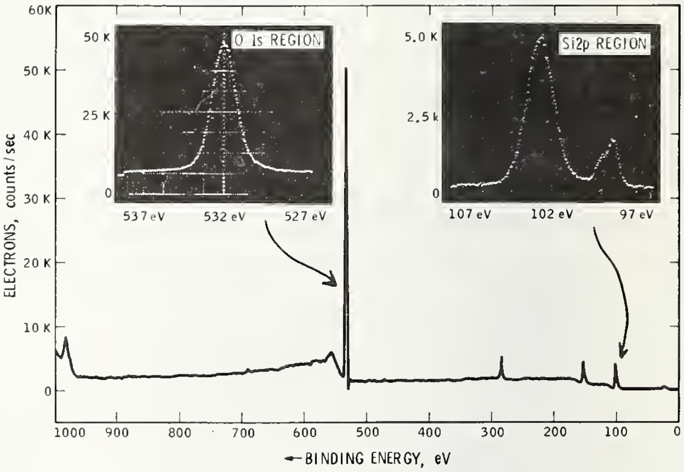

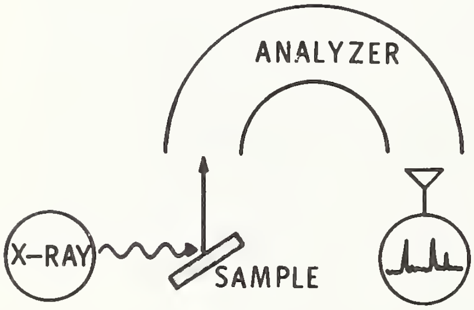

Figure 7. Simplified diagram of photoelectron experiment.

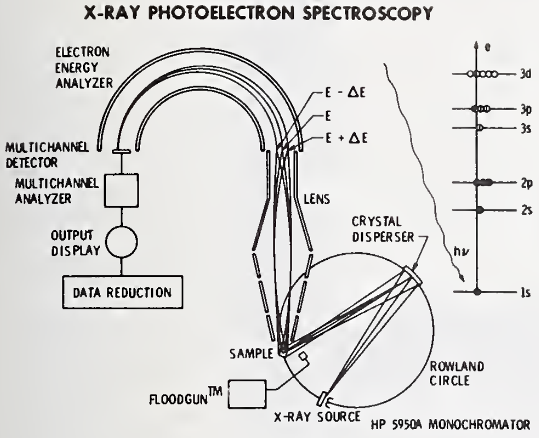

Figure 8. Simplified diagram of optics of x-ray photoelectron spectrometer.

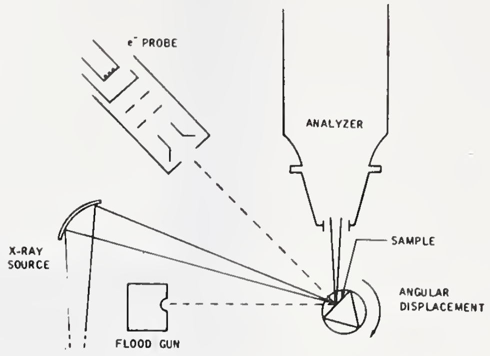

Figure 9. Representation of excitation sources and sample arrangement in sample chamber.

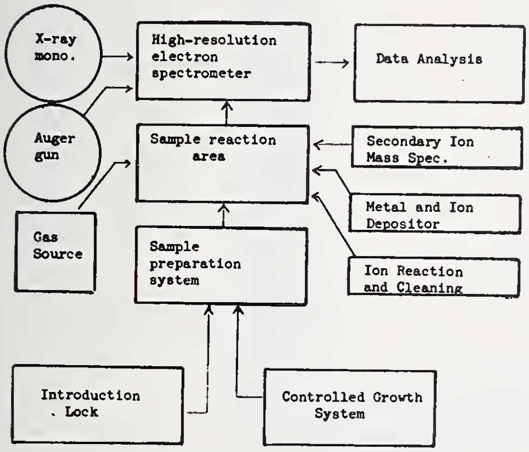

Figure 10. Block diagram of JPL XPS facility.

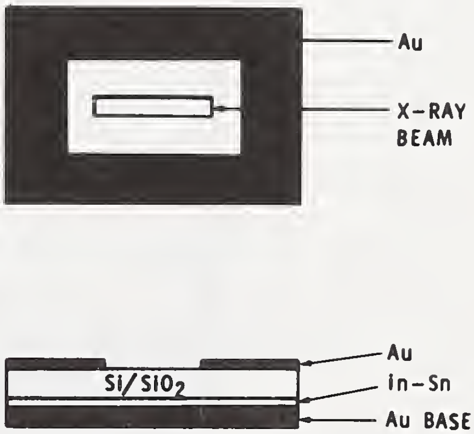

Figure 11. Sample preparation diagram giving x-ray illumination area.

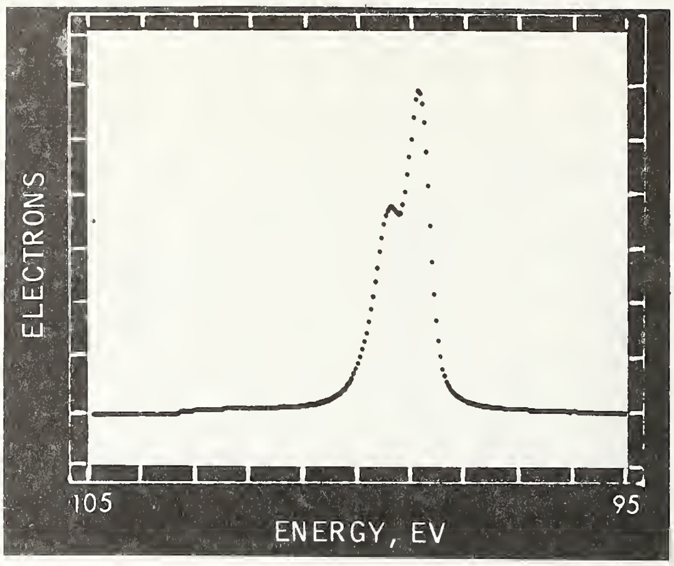

Figure 12. Silicon 2p spectra of etched silicon substrate.

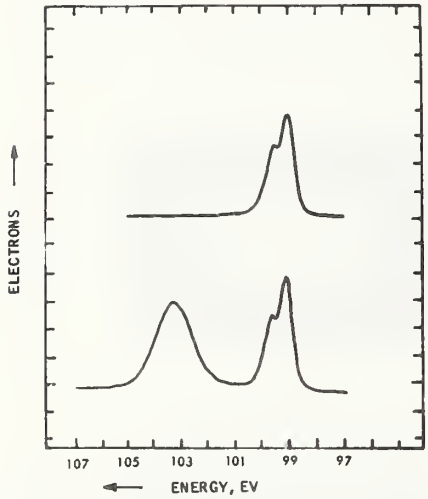

Figure 13. Silicon 2p spectra of freshly etched silicon and a 42 Å film of SiO_2 on Si.

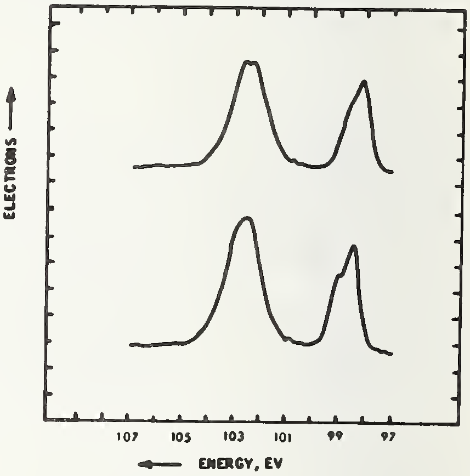

Figure 14. Silicon 2p spectra of 44 Å SiO_2 on Si under positive and negative (upper curve) bias.

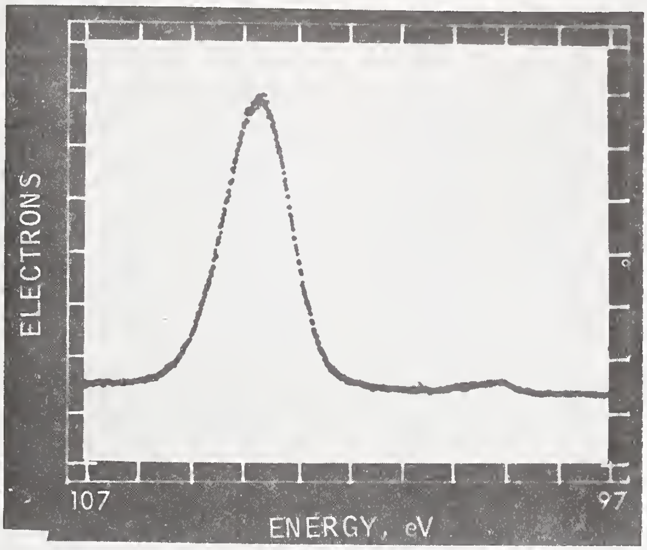

Figure 15a. Silicon 2p spectra of a 113 Å film of SiO_2 on Si.

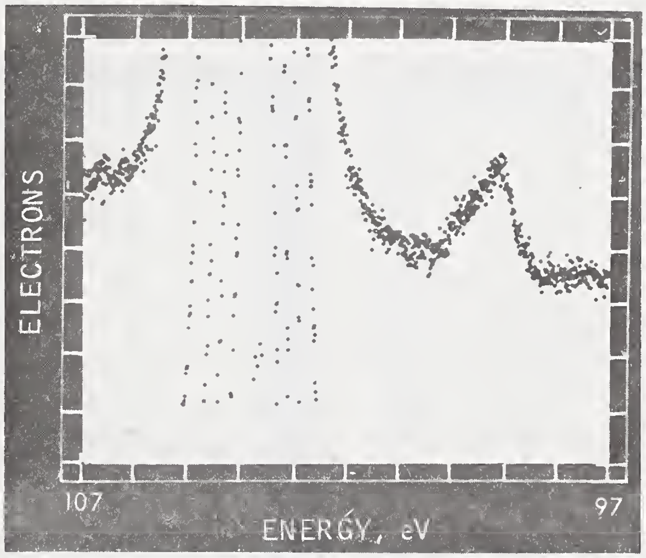

Figure 15b. Spectrum of figure 15a but with 20 X gain.

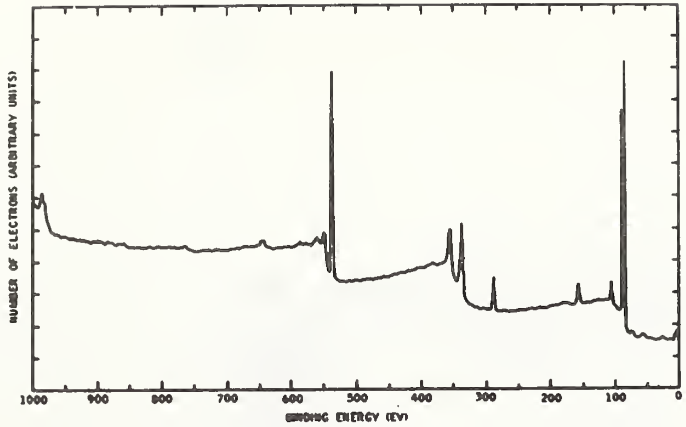

Figure 16. Wide scan of surface of MGRS part with wide horizontal detector.

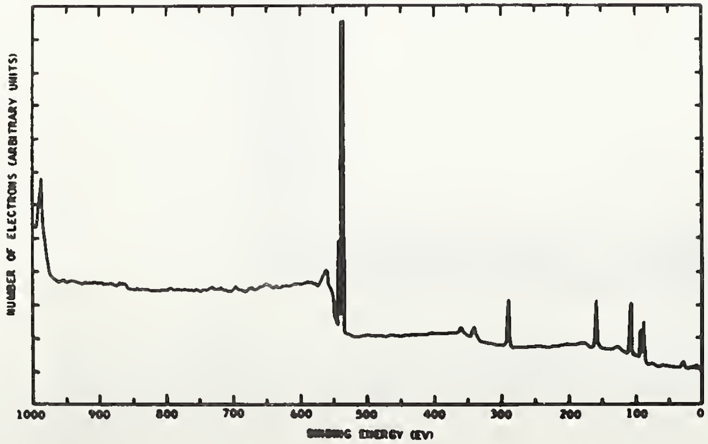

Figure 17. Wide scan of top of IC chip of MGRS part with narrow horizontal detection.

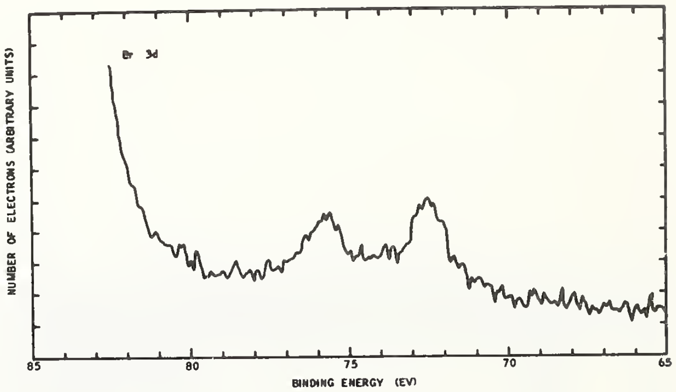

Figure 18. XPS scan of chip surface, bromine 3d region.

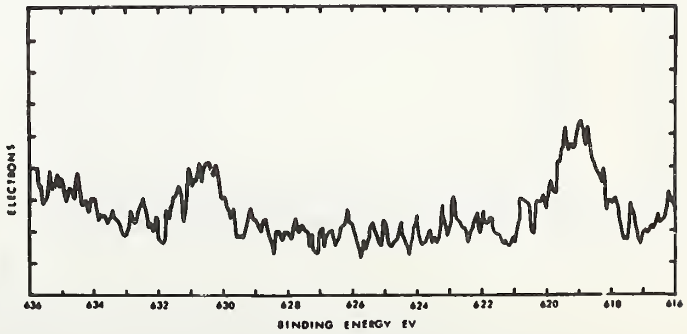

Figure 19. XPS scan of chip surface, iodine 3d region.

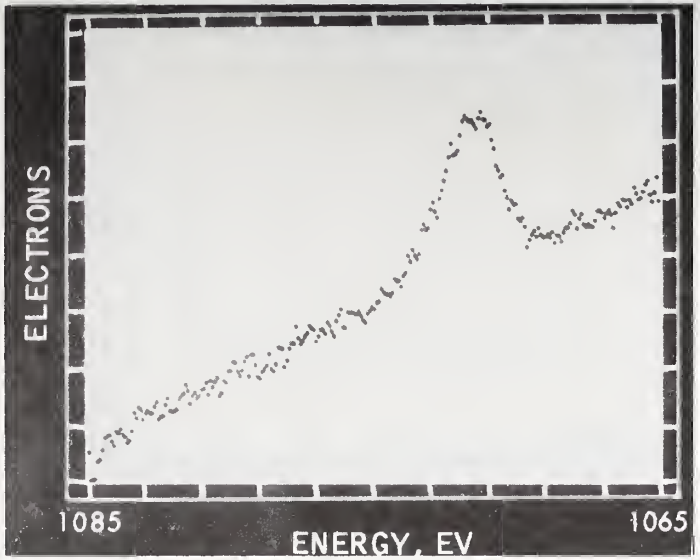

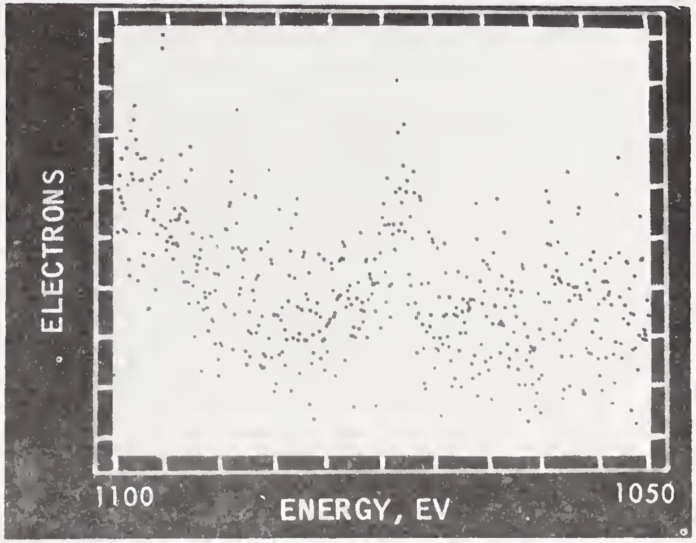

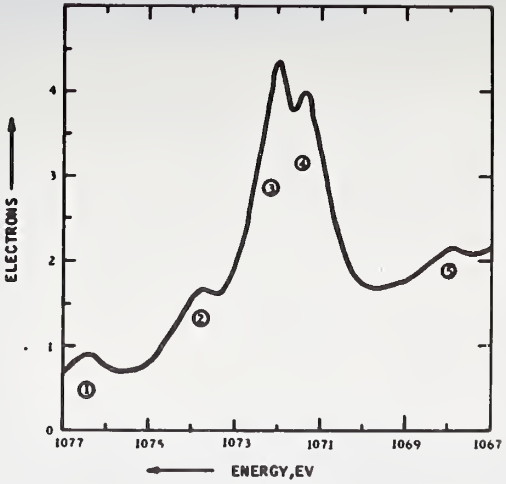

Figure 20 (upper left). Na 1s spectrum of Na^+ in sample of 44 A SiO_2 film on silicon. This is a natural level of Na^+ sample.

Figure 21 (lower left). Na 1s spectrum of residual Na^+ on surface of etched Si sample.

Figure 22 (above). Composite of Na^+ spectra seen in this experiment under conditions described in text.

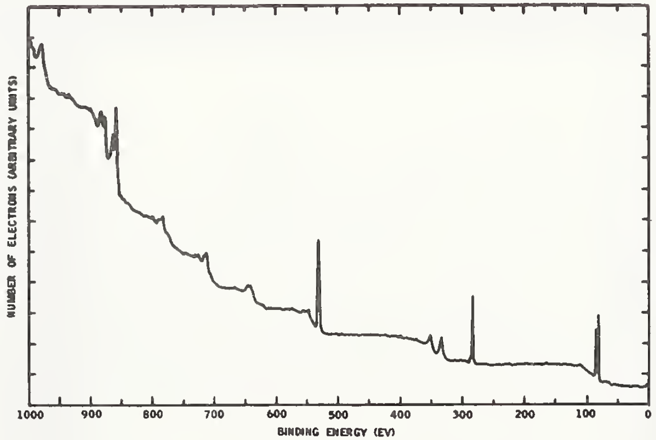

Figure 23 (above). XPS wide scan of kovar package surface.

Figure 24 (upper right). XPS scan of oxidized GaAs surface, carbon 1s region. This sample exposed to amines and epoxy.

Figure 25 (lower right). XPS scan of baseline GaAs cell, carbon 1s region.

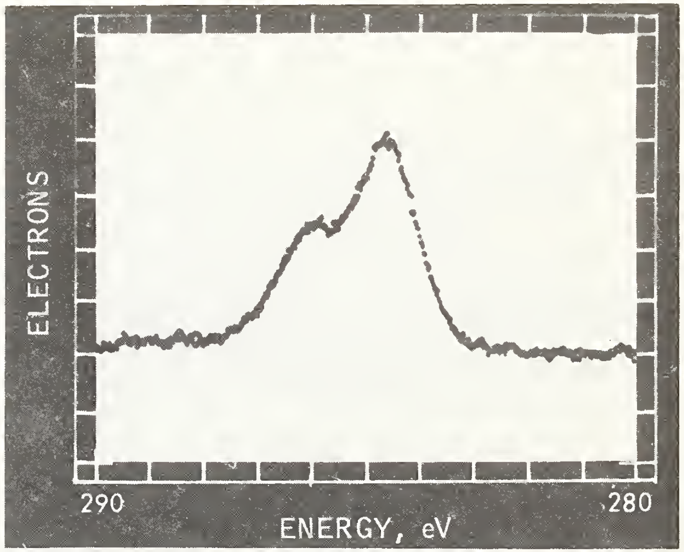

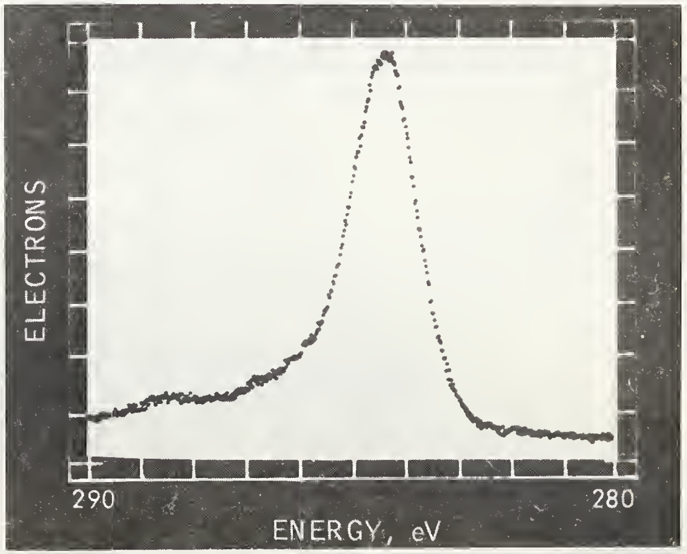

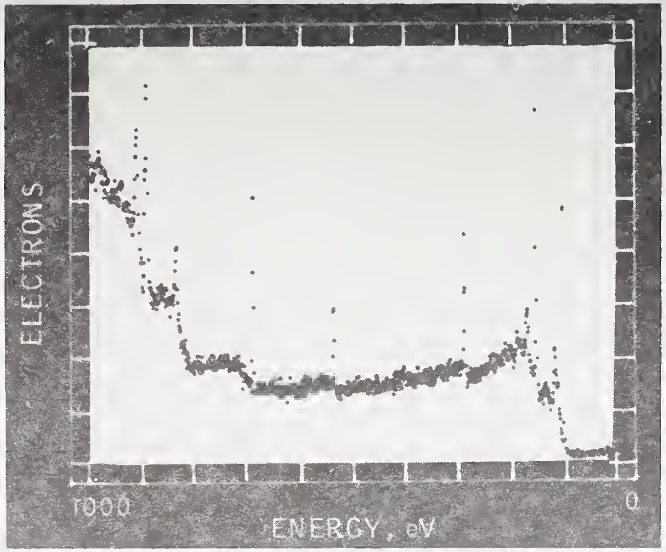

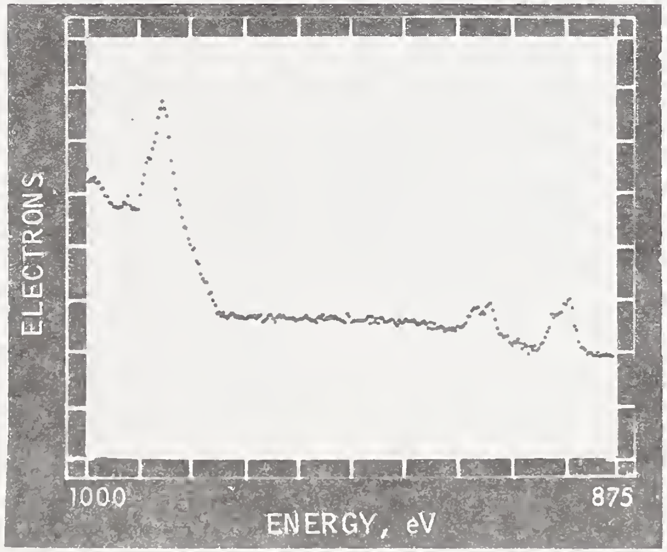

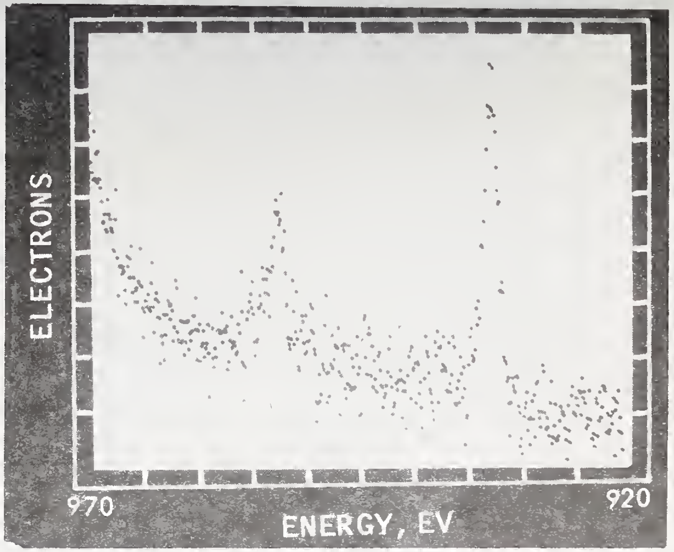

Figure 26 (upper left). XPS wide scan of freshly etched silicon surface.

Figure 27 (lower left). XPS scan of etched silicon chip, cerium 3d region.

Figure 28 (above). Copper 2p spectra of etched silicon substrate.

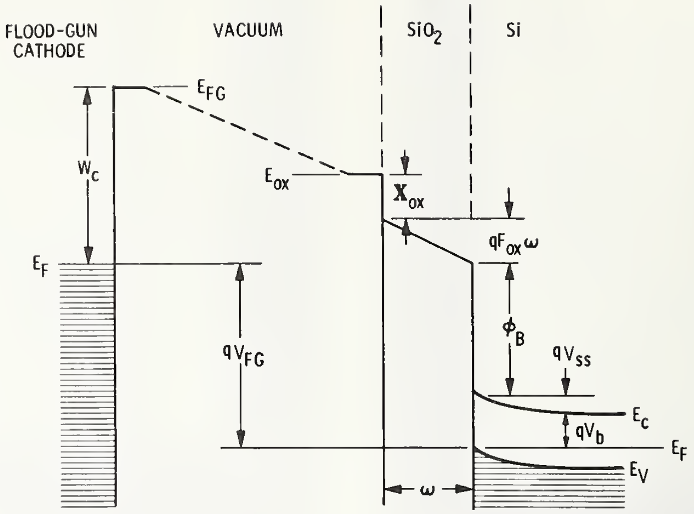

Figure 29. Band diagram showing electronic levels of Si/SiO_2/vacuum system with electron probe.

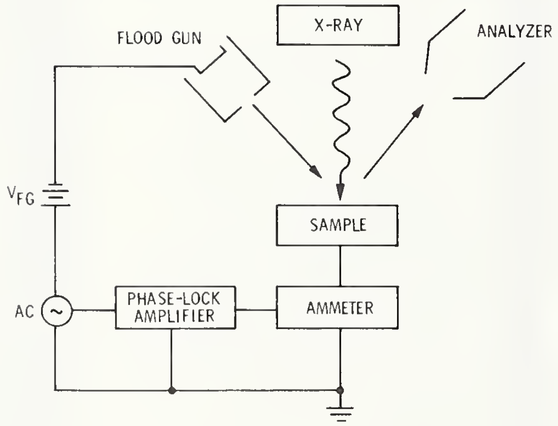

Figure 30. Diagram of bias experiment and appropriate electronics.

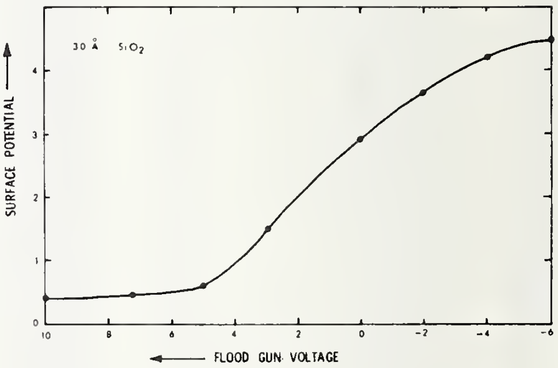

Figure 31. Surface potential variation as a function of flood gun voltage setting for a 30 Å SiO_2 film on silicon.

DISCUSSION OF THE PAPER

Morabito: You skipped over the gold migration problem somewhat. Could you go into more detail?

Grunthaner: The gold migration problem can be treated from two points of view. The physical cause is the failure of the part's hermeticity. This resulted in the injection of water into the package during a thermal shock test. The chemical cause of the problem is the simultaneous presence of the halide ion for gold ion complexation and a thin film of water on the surface of the part. The existence of water and applied potential would have resulted in slow corrosion of the metal stripes. This would have been of little long-term concern. The presence of the halogens permitted gold transport. The glassivated coating has a multitude of open cracks and incomplete coverages in the region of the gold. The combination of strong complexation of the gold ion and high current densities resulted in dendritic growth. The morphology of the dendrite is related to the strength of the gold complex, since this, together with the actual concentration of gold ions, determines the effective concentration of gold at the depositing electrode.

Initially, we had felt that an extremely clean electrode surface was required for dendritic growth. Subsequent experiments indicated that high-current density and low source ion concentrations were the limiting requirements. The presence of iodine was due to residual etchant which was strongly adsorbed to the surface of the remaining gold. Bromine and chlorine were also found, although the sources of these ions have not been clearly established. The chlorine may have been present from human handling or may have had a significant concentration in the water entering the package.

Morabito: Was chlorine more of a problem than iodine?

Grunthaner: The gold-chloro-complex is much more stable than the iodo-complex. In large gold ion concentrations, the chloro-complex would be most effective in generation of dendritic growth. In these lesser concentrations the iodo-complex provides transport, and reasonable concentrations. The polarized iodine on the gold surface also assisted in the dissolution of the gold stripe. The chlorine will be active but the iodine is probably the more important immediate problem. Bromine and bromate were also observed. The bromine case would be intermediate between chloride and iodide.

The primary question to our program was the possibility that there existed a long-term failure mechanism, i.e., parts failing after one or more years of operation. This failure mechanism was observed over periods of hundreds of hours with multilayer coverage of H_2O over the surface. Was failure at extended times possible at one- or two-layer coverage? The situation is resolved into ionic and hydrogenic currents and current study is addressing this problem.

The data available at this point are adequate to suggest several possible corrective actions to minimize MGRS failures: 1) Reduce the water content of the package to several hundred ppm (by volume) or less. 2) Reduce the impurity levels at the electrode and substrate surfaces, so as to eliminate transport. 3) Getter reactive impurities by chemical reaction, thereby modifying their chemistry, or by use of clathrates to immobilize them. 4) Treat the surface of the device to produce a hydrophobic surface, such as by use of methyl silane or other silicone derivatives.

NBS Special Publication 400-23, ARPA/NBS Workshop IV, Surface Analysis for Silicon Devices,
held at NBS, Gaithersburg, Maryland, April 23-24, 1975 (Issued March 1976)

CHOOSING BETWEEN ESCA AND AUGER FOR SURFACE ANALYSIS

Gary E. McGuire

Materials Characterization Laboratory
Texas Instruments Incorporated
Dallas, Texas 75222

ABSTRACT

Although photoelectron and Auger spectroscopy were developed over similar time frames and required similar hardware development, until recently the two techniques have remained as separate tools for surface analysis. Auger spectroscopy was readily accepted by the semiconductor industry for materials characterization. Interest in photoelectron spectroscopy did not develop as quickly nor did it become as widespread as Auger spectroscopy.

The two techniques being quite complementary can be used very well within the same laboratory if not within the same vacuum system. A number of examples will be discussed for which one would choose by preference ESCA over Auger. Although the choice may not be apparent beforehand, ESCA can be the more valuable characterization technique in certain aspects of polymer surfaces, electroplating and thin film metallization systems for semiconductor devices.

INTRODUCTION

If one takes into consideration all the commercial and non-commercial designs of electron spectrometers there are two basic differences that continue to distinguish the Auger electron (AES) spectrometer from the X-ray photoelectron (ESCA) spectrometer, resolution and excitation source. Auger spectrometers emphasize high transmission and use an electron beam for excitation while ESCA spectrometers emphasize high resolution and use soft X-rays for excitation. The soft X-ray source irradiates a much larger sample area with less intensity than an electron beam. Soft X-rays cause less damage to the sample, allowing longer times for data acquisition without altering the surface. The high resolution capabilities of the typical ESCA spectrometer and simplicity of the photoelectron spectra permits the identification of chemical shifts.

The two factors, resolution and excitation, ultimately govern the choice of which technique to use for a particular problem. The next few examples will be used to demonstrate occasions where these factors favor the use of ESCA. Because of the speed of data acquisition and excellent spatial resolution of Auger spectroscopy, it has been readily adapted for analysis of semiconductor surfaces. The examples presented here are not intended to downgrade the capabilities of Auger spectroscopy but are an effort to show how one would choose between the two techniques intelligently. These examples are slanted toward ESCA because we feel it has not been exploited as much in problem solving for semiconductor materials.

Chemical Identification

A feature that has always been one of the major strengths of ESCA has been the ability to observe chemical shifts in the spectra corresponding to the chemical states of the system being studied. For example in Figure 1 the separation between the peak positions for Si and SiO_2 is approximately 4.5 eV. The line widths are sufficiently small that the peaks are well resolved and easily distinguishable. The corresponding Auger chemical shift for Si and SiO_2 is much larger at 13 eV. The two chemical states may be easily identified in the Auger derivative spectrum but the transitions cannot be completely separated. Frequently it is possible to enhance certain features using integration techniques; however the integrated Si-SiO_2 Auger transitions overlap extensively (Figure 2).

In general photoelectron line widths, expressed as full width at half maximum (FWHM), are usually narrower and less complicated than the corresponding Auger line widths. Most Auger series consist of a family of curves with one or two dominant features. Even in examples where the AES shift is much larger, the chemical shift in the ESCA spectrum continues to be more easily distinguished. This may be enhanced by the higher resolution capability of the typical ESCA spectrometer (0.02%) over that of the typical AES spectrometer (0.5%).

With the numerous cited examples of chemical shifts in the literature, one may get the impression that every chemical combination produces a unique combination of photoelectron binding energies that are readily distinguishable. Although the combinations may be unique, the magnitude of the shifts may be so similar the peaks overlap extensively. These then may not be reduced to meaningful data except by comparing elemental ratios which could also be accomplished from the corresponding AES spectra.

Frequently the simplest method of studying a process that malfunctions is to compare "good" and "bad" samples in order to identify the presence of anything that may be detrimental or unusual. Numerous useful examples of this type may be found throughout the literature. Typical AES spectra of gold-plated surfaces which displayed "good" and "bad" plating characteristics are presented in Figure 3. The AES spectra reveal the presence of large deposits of K, C, N and Sn associated with "poor" plating characteristics. The same information concerning the elemental composition can just as easily be obtained by ESCA. In addition, ESCA gives some insight into the failure mechanism. From the AES data, it is not apparent whether the presence of K, C and N on the gold plated surface is due to adsorption of the gold salt $KAu(CN)_2$ on the surface or due to coprecipitation of the end product, K^+ and CN^-. By comparing the binding energies of gold 4f lines (Figure 4) from evaporated Au, $KAu(CN)_2$, a commercial gold salt, and the gold plated surface, we get an indication of the failure mechanism. The binding energies of the gold plated surface agree with those of evaporated gold while those of the commercial gold salt and $KAu(CN)_2$ agree. From this figure one could make the observation that the gold plated surface displayed the same chemical behavior as evaporated gold. The potassium, carbon and nitrogen present on the surface are end products of the plating process that are trapped in the gold. The similarity in the binding energies of the commercial gold salt and $KAu(CN)_2$ suggests a common chemical form for the two. Correlations such as this may be used to obtain substitute chemicals for expensive commercial formulations.

Excitation Source Influences

It is generally accepted that the influence of an X-ray source is less severe than that of an electron beam. Electron induced desorption and decomposition can alter the sample sufficiently to make data from some samples meaningless. (Bremsstrahlung from the X-ray source may produce the same results but to a smaller extent.) It is very difficult to obtain AES data from rough insulating surfaces such as printed circuit board because of charging induced by the primary beam. Examination of the same types of materials by ESCA are straightforward and simple. In Figure 5 is a representative ESCA spectrum of printed circuit board which we were unable to analyze by Auger. The analysis picked up the presence of Pb and Na on the surface even in areas away from the Pb-Sn plate.

If electron induced desorption or migration occurs then the Auger spectrum may not distinguish differences in samples with widely varying surface properties. In the following example, we were unable to detect any differences in surface composition by AES while the ESCA data displayed some significant variations (Figure 6). The samples examined were clean tin oxide, tin oxide treated in a N_2 atmosphere and tin oxide treated in an O_2 atmosphere. The untreated surface exhibits a clean tin oxide spectrum as observed by the $Sn3d_{3/2}$-$3d_{5/2}$ doublet. Treatment in a nitrogen atmosphere results in a small amount of Na appearing on the surface. The tin oxide surface is masked by a thin layer of Na when an O_2 atmosphere is used. The presence or absence of Na was verified by the Na KLL Auger transition that occurs in the same energy region of the ESCA spectrum as the Sn3d doublet. The important point we are trying to make is that examination of the same samples by AES does not reveal the presence of Na at all while ESCA indicates significant differences that correlate with the known physical properties of these films. We also observe a reversal in the physical properties of these films to the original state upon examination by AES (electron beam exposure) which has been correlated with the absence of Na.

Metal Contact Systems

ESCA may prove to be one of the most useful techniques available for examination of metallurgical contacts and thin film metallization systems, particularly heavy metals.

Most of the heavy metals, Au, Pt, Ta, W, used in semiconductor schemes have very intense 4f transitions with very narrow FWHM. The AES spectra for these same metals have complex structures with a number of observable transitions, none of which are particularly intense. The high energy Auger transitions which are the most distinctive of these metals have broad FWHM and require a 5 to 10 keV primary beam in order to optimize cross sections.

Using ESCA one could examine both implanted and alloyed contacts. In the case of implanted heavy metal contacts, the region of maximum concentration is approximately 200 Å below the surface. An example of this type is shown in Figure 7 of an Au-implant in silicon. In this example the surface has been chemically etched to the region of maximum concentration. Since the sample was exposed to air after etching, a transition due to SiO_2 from residual oxide formation appears in the spectrum accompanying transitions due to Si and Au. Although the implanted dose is rather large (6.8×10^{14} ions/cm^2), it would be possible to detect doses of several orders of magnitude smaller. The same results may be obtained by ion sputtering as opposed to chemical etching. Since the signal comes from a large area it is necessary to use a mask in order to analyze a uniformly sputtered region. This results in a reduction of signal by a factor of three. Since the dose required to implant metal contacts is within the detection limits of ESCA and since the implant is to such shallow depths, ESCA is useful in the study of doping profiles and compound formation.

The alloyed Pt contact to Si is presented as an example of the usefulness of ESCA in the study of compound formation. This system is commonly used for integrated circuits and silicon Schottky barrier diodes. When a thin film of platinum is deposited on a silicon substrate and the couple sintered, platinum silicide is formed. The stoichiometry has been identified as PtSi.[1] After the system is sintered, any unreacted Pt is removed by chemical etching with aqua regia. Contact resistance measurements as well as the etching characteristics indicate the presence of an additional high resistivity layer at the Pt-PtSi interface.

Rand and Roberts[2] examined this system by Auger spectroscopy and identified the resistive layer as SiO_2. When we examined the same system by ESCA,[3] we came up with a different interpretation. In Figure 8 are the ESCA spectra for the three different regions of the Pt-PtSi system, the surface, interface and PtSi region. From these spectra can be identified three different valence states of silicon (99.8, 102.3, 103.3 eV) and three distinct valence states of platinum (71.0, 71.4, 72.4 eV). The lowest binding energy Si2p peak was identified as being due to elemental silicon. The presence of free silicon is observed in each of the three spectra and acts as a reference point. The presence of elemental silicon on each of these surfaces may be due to a combination of rapid silicon diffusion and reduction of silicon compounds due to Bremsstrahlung radiation from the X-ray source. Neither of the remaining two Si2p transitions can be identified as due to SiO_2 since the Si2p binding energy in SiO_2 is 104.3 eV. The Si2p transition at 103.3 eV appears to be associated with the $Pt4f_{7/2}$ 72.4 eV transition while the 102.3 eV Si2p transition appears to be associated with the 71.4 eV $Pt4f_{7/2}$ transition.

The $Pt4f_{7/2}$ binding energy of 71.0 eV was identified as platinum metal. This assignment agrees with other literature values.[4] The line shape of this $Pt4f_{7/2}$ transition is slightly broadened due to the presence of a second chemical state of Pt with a binding energy slightly higher than Pt metal. When the surface is chemically etched to the Pt-PtSi interface, the 72.4 eV Pt and 103.3 eV Si peaks dominate the spectrum. Since SiO_2 has a Si2p binding energy of 104.3 eV its presence at the interface is ruled out. From our experimental results, we have observed that the binding energies of Pt and Si at the interface region displayed associated shifts. This fact has been taken as an indication of compound formation involving Pt, Si and O. Comparing the intensities of these transitions with those from pure Pt and Si targets indicates a stoichiometry of $PtSiO_4$.

Examination of the platinum silicide region is easily achieved by ion etching beyond the interface region. The binding energies displayed by Pt and Si in this region are 71.4 and 102.3 eV respectively.

By the use of ESCA it was possible to identify the layers of the metallization system as well as the compounds being formed. Careful examination of the intensities of the transitions may also be useful in determining the stoichiometry of the system. Other analytical techniques are available for structural identification when sufficient material is available but these metal systems may only be several hundred angstroms thick.

SUMMARY

ESCA has proven useful for many applied semiconductor research problems. Except for spatial resolution and speed, it offers the same advantages as AES as a surface characterization technique. In addition it may be used when sample charging, decomposition and electron induced migration are potential problems. It also offers the advantage of high resolution with resultant chemical shift information. The simplicity of the photoelectron transitions are easily reduced to quantitative information.

In the future one can expect to see ESCA used to obtain "chemical in-depth profiles"[5] as opposed to the more common elemental profiles. ESCA will also prove to be useful in the study of diffusion mechanisms[6] with the added dimension of elucidating compound formation.

REFERENCES

1. Muta, H. and Shinoda, D., *J. Appl. Phys.* 43, 2913 (1972); Poate, J. M. and Tisone, T. C., *Appl. Phys. Lett.* 24, 391 (1974).

2. Rand, M. J. and Roberts, J. F., *Appl. Phys. Lett.* 24, 49 (1974).

3. Danyluk, S. and McGuire, G. E., *J. Appl. Phys.* 45, 5141 (1974).

4. Bearden, J. A. and Burr, A. F., *Rev. Mod. Phys.* 39, 125 (1967).

5. McGuire, G. E., unpublished results.

6. Danyluk, S., McGuire, G. E., Koliwad, K. M. and Yang, M. G., *Thin Solid Films* 25, 483 (1975).

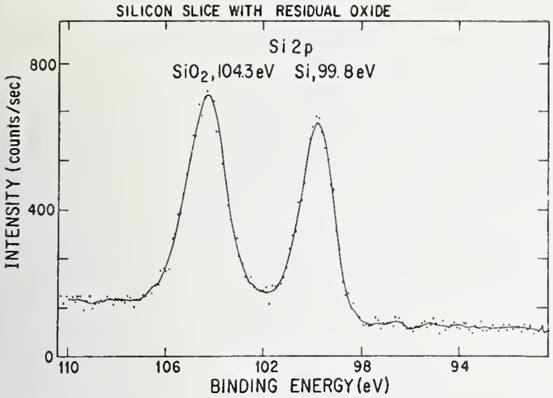

Figure 1. X-ray photoelectron spectrum of a silicon slice with a residual oxide coating. The Si(2p) transitions of Si and SiO_2 display a chemical shift of 4.5 eV.

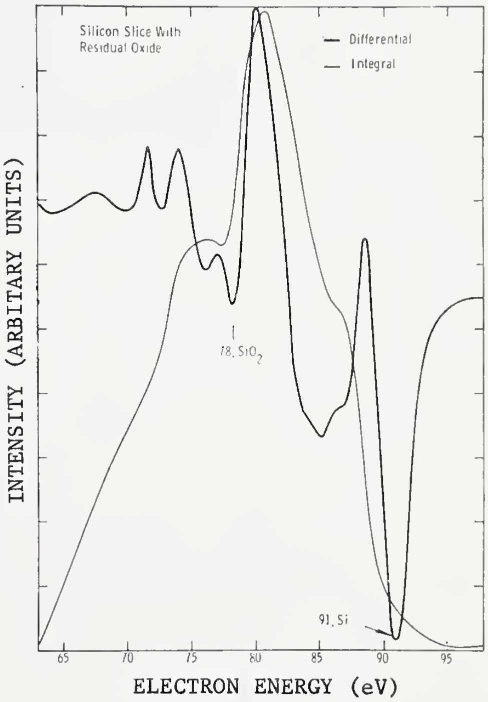

Figure 2. The characteristic minima at 78 and 91 eV for SiO_2 and Si respectively can be observed in the derivative Auger spectrum. The integrated curve is superimposed over the derivative curve.

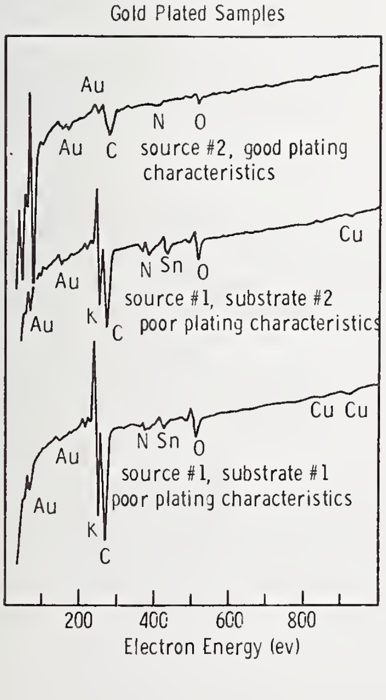

Figure 3. Auger spectra of gold-plated surfaces. The presence of potassium, carbon and nitrogen was identified with Au-plated surfaces with poor bonding characteristics.

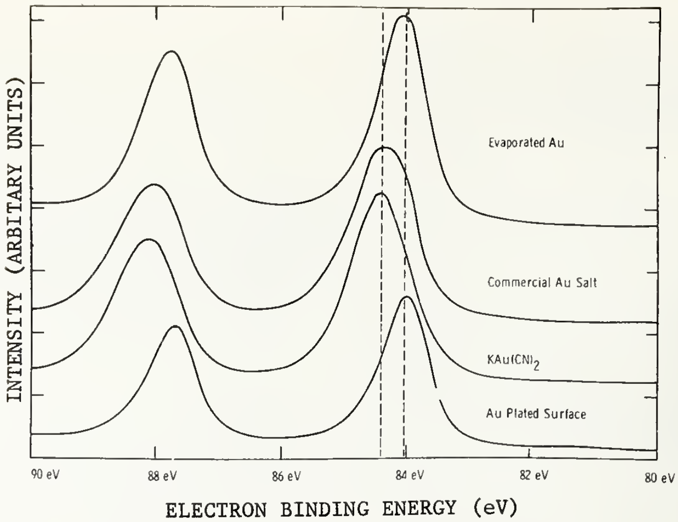

Figure 4. X-ray photoelectron spectra of Au, $KAu(CN)_2$, commercial gold salt and gold plate. The binding energies of the Au4f transitions may be used as an indication of the valence state of the gold.

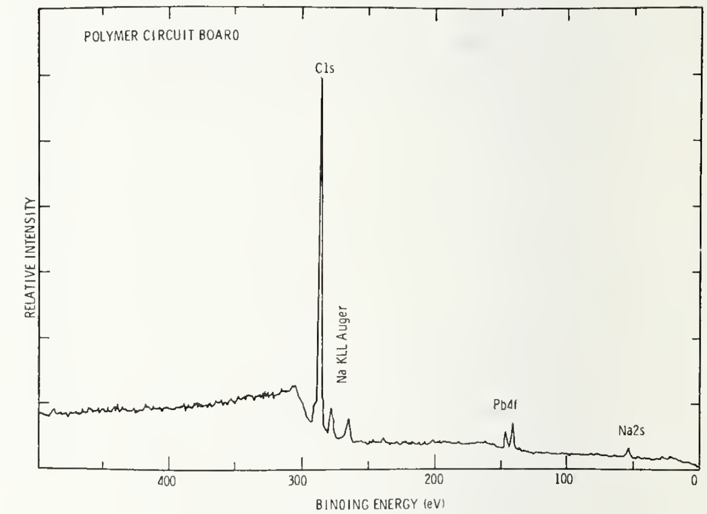

Figure 5. X-ray photoelectron spectrum of printed circuit board. Lead and sodium were found on the surface and associated with leakage currents causing the printed circuit to fail.

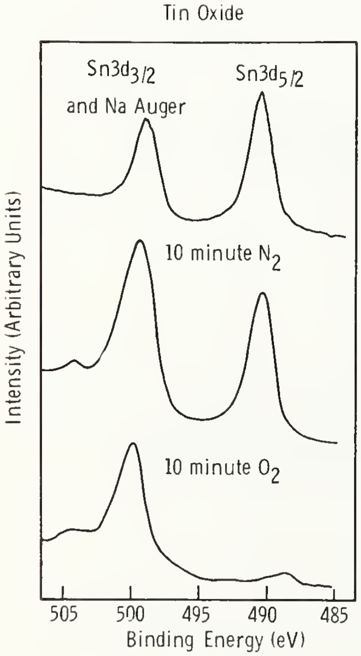

Figure 6. X-ray photoelectron spectrum of tin oxide surfaces. Treatment of the tin oxide surface in an O_2 or N_2 atmosphere leaves a thin coating of Na. The sodium is induced to migrate away from areas exposed to an electron beam as in Auger analysis.

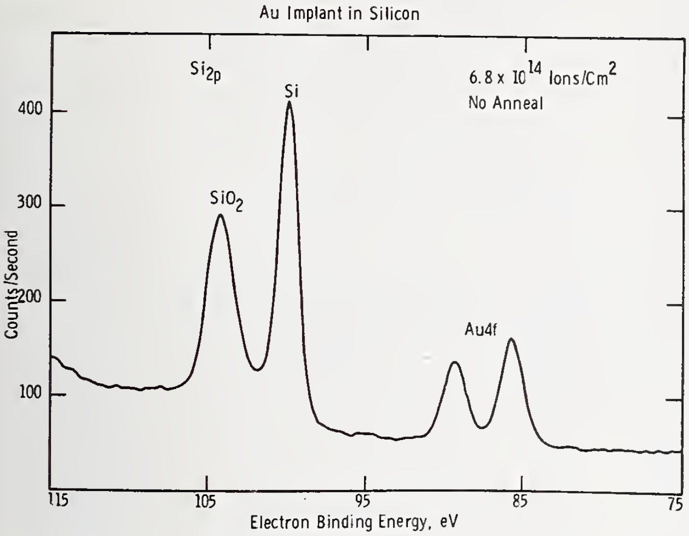

Figure 7. X-ray photoelectron spectrum of Au implant in silicon. The surface has been chemically etched to the region of maximum concentration.

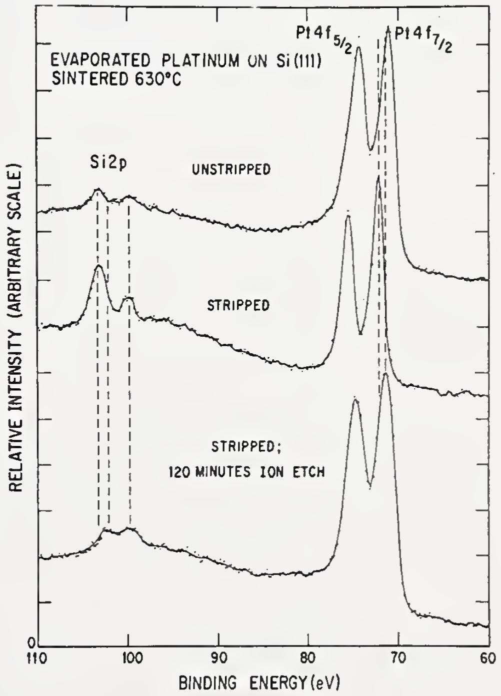

Figure 8. X-ray photoelectron spectrum of Pt contact to silicon. Three spectra are shown: (a) platinum surface, (b) sample that has been chemical etched of excess platinum, and (c) sample that has been chemically etched then ion etched to the PtSi region.

DISCUSSION OF THE PAPER

Grunthaner: I would like to comment about your statement concerning the line widths of the gold as opposed to silicon. The silicon lines in the spectra are probably the narrowest lines that one observes at all, although the presence of the silicon 2p doublet, when broadened by the instrument and that sort of thing does give rise to a somewhat broader line. The silicon lines that we have seen in the spectrometer are of the order of about 520 millivolts wide. The narrowest gold lines we have observed are of the order of about 680 millivolts wider.

McGuire: Most people get the impression looking at the commercial brochures that the gold and the silver give the narrowest lines, but sometimes these elements are merely the most convenient, they are good conductors and the separation between the doublet is quite large.

Morabito: Because of the difference in the escape depth between the ESCA photoelectron as compared to the Auger electron, it is possible that, for the last example you showed, the layer within 5 or 10 Å of surface could be SiO_2. You are sampling a much deeper region with ESCA, so below you may have platinum silicide but above that it is possible you have SiO_2.

McGuire: I would like to make a comment concerning the escape depth. I have seen both Auger and ESCA papers that have come up with different escape depths but I have a hard time believing that an electron, whether it is due to an Auger process or a photoelectron process, will behave differently as far as its coming out of a given material. I do not think they should differ.

Morabito: That depends on the kinetic energy of the electron.

McGuire: Yes, so I would say electrons from either process with the same kinetic energy should have identical escape depths.

Participant: I would like to point out that in stripping off the platinum and looking again whether you have not really done anything to the surface, which presumably would have the oxide or silicate on it, you could be changing the Fermi level of the sample with respect to the vacuum, which may give you a shift in the lines.

McGuire: Well, in the spectrum I showed we were using the elemental silicon as a reference point. That is the reason we used the data we got from the McPherson instrument, i.e., it was very convenient. We had a lot more difficulty with the Hewlett-Packard instrument because we did not always see the presence of the elemental silicon.

NBS Special Publication 400-23, ARPA/NBS Workshop IV, Surface Analysis for Silicon Devices, held at NBS, Gaithersburg, Maryland, April 23-24, 1975 (Issued March 1976)

SILICON DEVICE APPLICATIONS USING A COMBINED ESCA/AUGER ANALYSIS SYSTEM

L. E. Davis and G. E. Riach

Physical Electronics Industries, Inc.
Eden Prairie, Minnesota 55343

ABSTRACT

Silicon device applications are described which emphasize the advantages of measuring both X-ray induced photoelectrons and electron beam stimulated Auger electrons as a function of depth in the same analysis system. The measurements include depth-composition profiles and chemical binding information for nichrome thin films and boron predeposits on silicon.

INTRODUCTION

ESCA and Auger electron spectroscopy have much to offer in the study of semiconductor devices.[1] In conventional Auger systems, electron beam excitation allows localized surface analysis and rapid signal readout. ESCA, on the other hand, offers a means of characterizing chemical bonds at the surface. When used in conjunction with sputter-etching, both techniques can be used to obtain data as a function of depth. The applications to follow illustrate how a combined ESCA/Auger electron spectrometer can be used to give a more complete characterization of thin films than either technique alone.

EXPERIMENTAL APPARATUS AND METHOD

The schematic diagram of a commercial electron energy analyzer optimized in design for high transmission and energy resolution is shown in Figure 1. In the ESCA analysis mode (via pulse counting) the essential advantages of the analyzer are: 1) selective area analysis within an area 2mm in diameter and 2) adjustable energy resolution. In the conventional Auger analysis mode (via the lock-in amplifier) the high transmission (approximately 7%) of the analyzer allows real-time measurement of the Auger electron peak-to-peak heights as a function of sputter-etching time. A complete description of the electron spectrometer functions and specifications have been reported by Palmberg.[2]

The analysis was performed in an ultrahigh vacuum system capable of reaching pressures less than 10^{-10} Torr. The electron spectrometer, X-ray source and sputter ion gun are pre-aligned so that when the specimen is positioned for optimum (photoelectron or Auger electron) signal, the ESCA/Auger analysis area and ion beam coincide. In this manner, X-ray photoelectron and electron beam excited Auger electron measurements could be made after ion beam sputtering without moving the specimen. The typical analysis procedure was to record the Auger electron peak-to-peak [$dN(E)/dE$] amplitudes simultaneously with argon ion beam sputtering and, thus, obtain a depth-composition profile.[3] High energy resolution ESCA analysis was performed at selected depths by turning off the ion gun at the desired depth, making the ESCA measurement, and then resuming the Auger depth profile measurement. The two types of data are then easily correlated.

APPLICATIONS

Oxidation of a Nichrome Film

As indicated in the Auger electron depth-composition profile of Figure 2, the nichrome film after heating in air for 30 seconds at 450°C is composed of a metallic oxide layer at the surface. A chromium rich layer dominates near the surface while nickel has formed a distinct layer at the metal/silicon interface. To gain a better understanding of the effect this heating process had on the chemical bonding, high energy resolution ESCA measurements of chromium and nickel were made at the surface and at depths A, B, C and D indicated on the depth profile. This data is shown in Figure 3.

The chromium and nickel $2p_{3/2}$ photoelectron lines are shifted to higher binding energies (approximately 2.5eV for chromium and 3.0eV for nickel) at the surface. These shifts are consistent with Cr_2O_3[4] and NiO[5] oxidation states. Slightly below the surface, at depth A, the Ni $2p_{3/2}$ line has shifted to a binding energy consistent with elemental nickel. The chromium, however, remains in oxide form until depth B where both oxide and metallic states are apparent. At depths C and D, both chromium and nickel are predominantly metallic.

In conclusion, it can be seen that heating this nichrome film in air produced a surface oxide layer about 100Å thick consisting mainly of Cr_2O_3. Within 15Å of the surface a small amount of NiO was formed. Deeper than this within the structure, however, the nickel remained entirely in the metallic state.

Boron Predeposit on Silicon

In the doping of silicon with boron, the first processing step is the deposition of a shallow layer of boron on a silicon wafer. The predeposit is produced by allowing a boron gas (e.g., a borane) to react with the silicon surface at elevated temperatures. As Figure 4 indicates, a glass surface layer is formed during the predeposit process. The next step in doping is to chemically remove the boron glass, leaving only a boron rich silicon surface. The remaining boron then is diffused at high temperatures into the bulk silicon to the desired depth and concentration level. In some cases the predeposition is carried out at a high enough temperature that the diffusion occurs simultaneously with the predeposit.

In order to achieve reproducible dopant levels, it is of considerable aid to the process engineer to know the properties of the predeposit before glass removal. The main properties of interest are (1) the thickness of the glass layer, (2) the boron concentration as a function of depth and (3) the chemical state of boron and other elements as a function of depth.

The depth-composition profile of Figure 4 illustrates that by monitoring the Auger signals of Si, B and oxygen during sputter-etching, the predeposit glass layer and boron density can be rapidly characterized as a function of depth. In the example, the boron is entirely within the glass overlayer. The glass removal and diffusion steps have not been carried out on this specimen at this point. At the depths A, B, C and D indicated on the plot, the profile was interrupted so that high energy resolution ESCA measurements could be made to determine the chemical state of the important components of the predeposit layer.

ESCA spectra of the Si 2p and B 1s photoelectron lines at the depths indicated in Figure 4 are shown in Figure 5. The Si 2p binding energies (103eV) at depths A and B are consistent with SiO_2. At depths C and D the elemental silicon lines (at 97.8eV) are also present. The boron photoelectrons at 193eV do not change in binding energy as a function of depth. B 1s electrons at this binding energy belong to the oxide state of boron.

The depth-composition profile in Figure 6 shows the results of a combined boron predeposit and diffusion carried out at 1050°C on polycrystalline silicon. Note that here the boron is concentrated at the glass/silicon interface. The ESCA spectrum in Figure 7 obtained at depth A shows that two B 1s photoelectron lines exist at the glass/silicon interface. The photoelectrons at 193eV correspond to the boron oxide state, the same binding energy as the B 1s electrons shown in Figure 5. The lower binding energy electrons at 186.2eV belong to elemental boron.

These examples point out the usefulness of joint ESCA and Auger analysis for complete characterization of thin films on silicon surfaces. Both composition and chemical binding information as a function of depth are obtainable without changing specimen orientation. In addition, the examples show that the information obtained is in a form that can be applied directly for definitive process control and evaluation of silicon devices.

Acknowledgements

The authors gratefully acknowledge Drs. N. C. MacDonald and P. W. Palmberg for suggesting the application topics and supplying background information about specimen processing.

REFERENCES

1. McGuire, G. E., Choosing between ESCA and Auger for Surface Analysis, ARPA/NBS Workshop IV, *Surface Analysis for Silicon Devices*, A. G. Lieberman, Ed., NBS Spec. Publ. 400-23 (January 1976).

2. Palmberg, P. W., *Vac. Sci. Technol.* 12, 379 (1975).

3. Weber, R. F., *Research/Development* 23, 22 (1972).

4. Kim, K. S., Purdue University, private communication.

5. Fiermans, L, Hoogewijs, R., and Vennik, J., *Surf. Sci.* 47, 1 (1975).

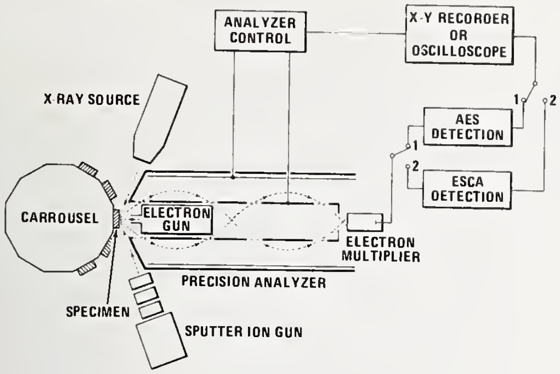

Figure 1. Schematic diagram of the ESCA/ Auger Electron Spectrometer (Physical Electronics Industries, Inc., Model 548).

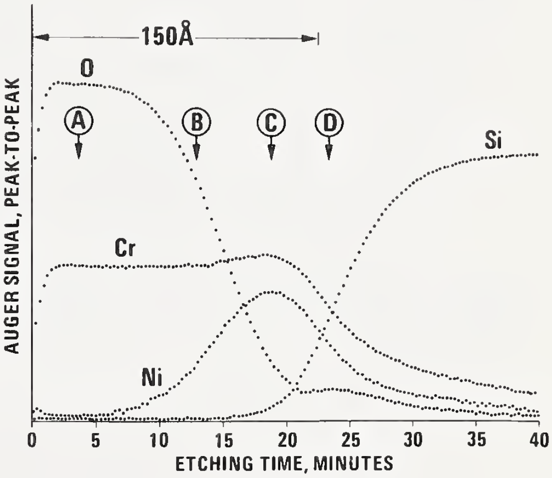

Figure 2. Auger electron depth-composition profile of a thin nichrome film heated (450°C for 30 seconds) in air.

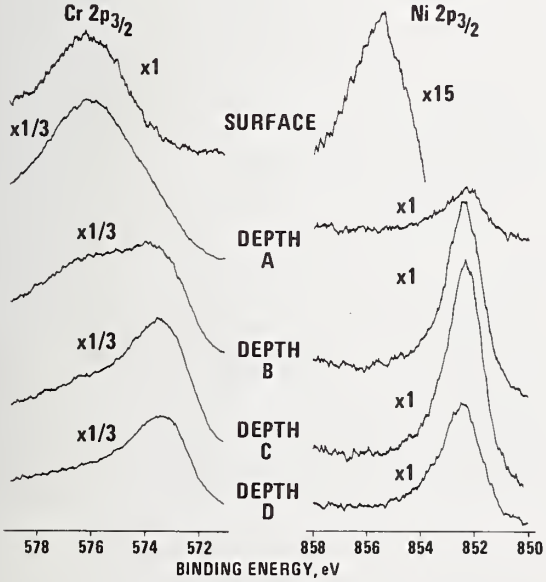

Figure 3. High resolution ESCA spectra of Cr $2p_{3/2}$ and Ni $2p_{3/2}$ photoelectron lines as a function of depth.

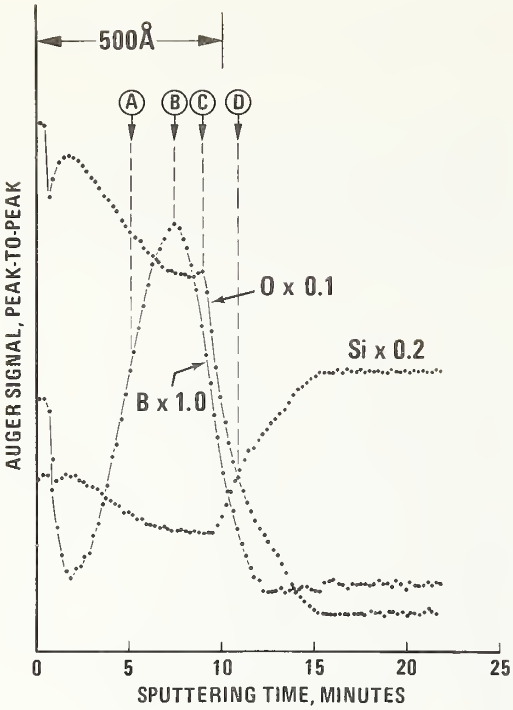

Figure 4. Auger electron depth-composition profile of a boron predeposit on single crystal silicon.

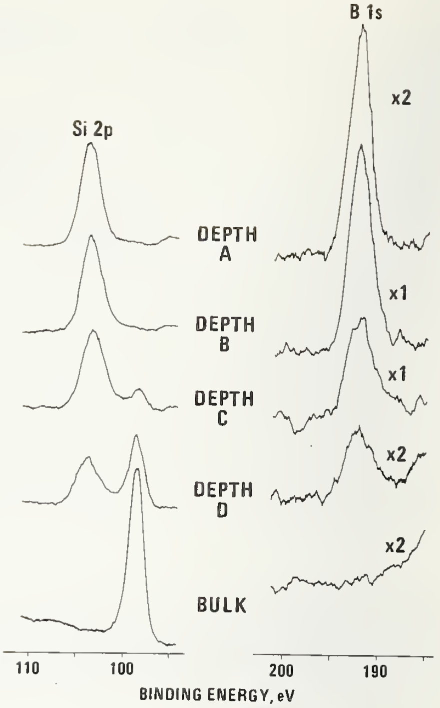

Figure 5. Silicon 2p and boron 1s photoelectron spectra as a function of depth.

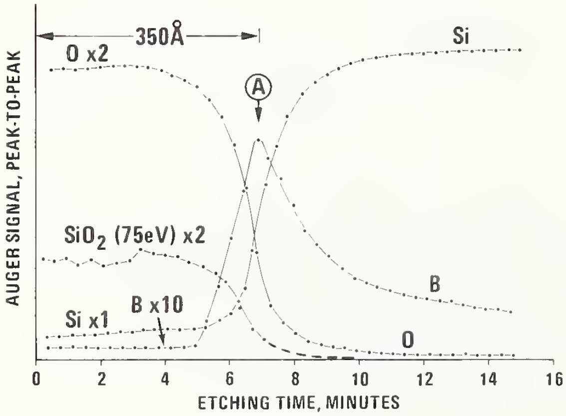

Figure 6. Auger electron depth-composition profile of boron diffused into polycrystalline silicon.

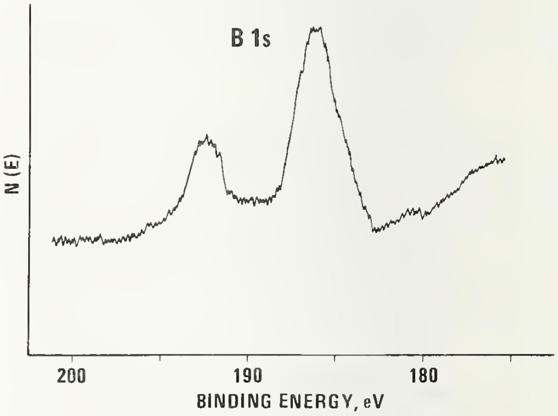

Figure 7. Boron 1s photoelectron lines at the glass/silicon interface.

DISCUSSION OF THE PAPER

Thomas: Did you say that the boron had been oxidized by the glass structure?

Davis: No, I did not mean to imply that. My interpretation is that the boron in the first predeposit example exists as boron oxide, probably as a borosilicate. The Auger electron peak shape of boron in the glass layer (not shown) was quite different from the elemental boron peak shape. This, of course, is additional evidence that the boron in Figure 5 is in oxide form.

NBS Special Publication 400-23, ARPA/NBS Workshop IV, Surface Analysis for Silicon Devices,
held at NBS, Gaithersburg, Maryland, April 23-24, 1975 (Issued March 1976)

PHOTODEPOPULATION TECHNIQUE FOR THE STUDY OF ELECTRONIC TRAPS IN INSULATORS*

T. H. DiStefano

IBM Watson Research Center
Yorktown Heights, New York 10598

and

J. M. Franz

IBM System Products Division
Essex Junction, Vermont 05452

ABSTRACT

A new type of photodepopulation spectroscopy has been used to obtain the energy distribution of electrons trapped in an insulator. The change in the trapped charge produced by monochromatic light is detected by a silicon surface effect device, which serves as one of the electrodes. The result is the spectral photoyield for trap ionization, free of any complication of extraneous currents. This photodepopulation technique was applied to the SiO_2-Si_3N_4 system to determine the trap distribution responsible for charge storage in the MNOS transistor. The results, although somewhat complicated by photoinjection from the electrodes, show an ionization energy of 3.0 eV. Generally, the technique is applicable to the very sensitive spectroscopic measurement of deep traps in wide bandgap insulators.

INTRODUCTION

A new photodepopulation technique[1] has been developed and used to examine spectroscopically the impurities and trapped electrons in insulating thin films. Essentially, the technique involves a measurement of the relaxation of the charge stored in an insulator that is exposed to monochromatic light. From the discharge of the traps produced by illumination from a scanned monochromator source, the spectral yield for photoemission from the traps is obtained directly. The charge in the insulator is detected by means of one of the electrodes, which is a field effect device that serves as an electrometer. Either of two modes of detection, small signal capacitance or surface conductance, is satisfactory for measuring the field at the electrode from which the net charge is determined. The photodepopulation technique has an advantage in that it samples only the density of occupied trap levels, and it is unaffected by extraneous sources of current. It also has an advantage over a photocapacitance technique[2] used by Harari and Royce to study traps at the SiO_2-Al_2O_3 interface; our photodepopulation technique is not influenced by a redistribution of the electrons among the various trap levels in the system caused by light[3] or by thermal excitation. However, as with any photoionization technique for thin film insulators, our technique is limited to a window equal to the electrode barrier energy; for photon energies greater than this barrier, the photodepopulation results are complicated by injection from the electrodes.

We have used the photocapacitance technique to determine the distribution of the specific traps, near the SiO_2-Si_3N_4 interface, which are filled and emptied by electron tunneling during the normal operation of an MNOS device. Electron traps in the Si_3N_4 itself have been well characterized by several techniques including thermally stimulated currents[4,5] and I-V measurements[6,7]. Both techniques are able to determine the binding energy of traps which are characteristic of the bulk of Si_3N_4. Binding energies are found to lie in a range from about 0.5 eV to 0.9 eV, as measured by thermally stimulated currents and from about 0.5 eV to 1.5 eV determined from the I-V dependence. However, neither of these techniques is capable of being used to characterize the deep trapping levels associated with charge storage near the SiO_2-Si_3N_4 interface, since they are obscured by the shallow traps in the conductivity measurements. It is the

---

* Work supported in part by the Defense Advanced Research Projects Agency and monitored by AFCRL under contract number F19628-74-C-0077.

deep traps which are of specific interest since these states near the interface of SiO_2 and Si_3N_4 are responsible for the charge storage in MNOS memory transistors. Models for switching[8] and charge retention[9] in the MNOS transistor would benefit by a determination of the deep trapping states. The spectral photoyield was obtained for traps filled to various charge levels by tunneling. From the photoemission spectra and thresholds, information is derived about the energy distribution of the deep traps in the SiO_2-Si_3N_4 structure.

EXPERIMENT

The capacitive mode of charge detection was used for the photodepopulation study of trapped electrons near the SiO_2-Si_3N_4 interface. To some extent this particular technique is a variation of photocapacitance spectroscopy, which has been used to study traps in the depletion region of a semiconductor junction. During the measurements, a bias voltage is applied to the MNOS sandwich to maintain a null electric field at the silicon surface, as is shown in Fig. 1. The zero surface field condition was sensed by a capacitance measurement at 100 kHz and maintained by a feedback loop in which the capacitance measurement is used to control the sample bias. The capacitance is measured by a phase sensitive detector in order to reject leakage currents and the photocurrent. In this "flat-band" condition, the bias voltage is directly related to the net charge density stored near the SiO_2-Si_3N_4 interface,

$$\rho = \frac{\varepsilon_0 \varepsilon_1 V_{fb}}{d} , \qquad (1)$$

where ρ is the net charge density, ε_1 is the dc dielectric constant of the Si_3N_4, V_{fb} is the bias voltage necessary to maintain the "flat-band" condition, and d is the thickness of the Si_3N_4 layer. It was assumed that the stored charge lies near the SiO_2-Si_3N_4 interface; the assumption is reasonable in this case, where the charge was introduced either by tunneling from the silicon or by photoemission from the silicon.

The photoresponse of the system was obtained by shining monochromatic light through the semitransparent aluminum electrode and onto the traps near the interface. The light source was a Bausch and Lomb 0.5 meter monochromator with a Hg-Xe high pressure arc source. The emergent light was de-focused to cover uniformly the area of the sample electrode. The light intensity was measured with an RCA 1P42 photodiode covered by a layer of sodium salycilate phosphor; the photodiode was calibrated against an Eppley thermopile. Measurements were obtained for photon energies from 2 eV to 6 eV, which is the upper practical limit of the light source. A filter was used at energies below 3.5 eV to eliminate second order light in a range over which the sample was extremely sensitive. All of the spectra were obtained at room temperature. The measurements were performed on samples which are characteristic of an MNOS transistor. The sandwich structure comprised a silicon substrate, 25 Å of SiO_2 formed on the silicon by oxidation, 535 Å of Si_3N_4 formed by chemical vapor deposition at 875°C, and finally 125 Å of aluminum to form a semitransparent electrode. Samples were formed on (100) 2Ω-cm silicon substrates of both n and p type. The semitransparent electrodes, 0.060" in diameter, were deposited by evaporation in a vacuum of about 2×10^{-6} torr. The samples exhibited typical hysteresis effects, with a maximum total stored charge of about 8×10^{12} electrons/cm^2.

Light of sufficient energy $\hbar\omega$ excited electrons from the deep traps into the conduction band of the Si_3N_4. For the condition shown in Fig. 1, excited electrons are collected by the aluminum electrode; re-trapping of the electrons in the Si_3N_4 was not found to be a significant factor at room temperature and at fields above 10^6 V/cm. Because the photoexcitation of electrons from traps results in a discharge of the insulator, the flat-band voltage shifts with exposure to light. The photoyield $Y(\hbar\omega)$ is then obtained as

$$Y(\hbar\omega) = \frac{\varepsilon_0 \varepsilon_1}{d e I(\hbar\omega)} \left. \frac{\Delta V_{fb}}{\Delta t} \right|_{\hbar\omega} , \qquad (2)$$

where $I(\hbar\omega)$ is the photon flux at energy $\hbar\omega$ and e is the electronic charge. The measurements were made in steps of finite interval Δt, between 10 and 60 seconds. The interval Δt was chosen to be sufficiently brief so that the total spectrum was not appreciably distorted by a depletion of the trapped charge near the end of the measurements sequence. The discharge measurements were performed in order, from low to high photon energy.

Photodepopulation spectra were obtained from the decay of V_{fb}, shown in Fig. 2, produced by a sequence of exposures to light of increasing photon energy. In this case, the sample was exposed for 15 sec. at each photon energy, and the charge measurement was made between the intervals of exposure. Measurements were taken in the dark because any incident light would cause a shift in V_{fb} due to a small induced surface photovoltage. Some portion of the initial trapped charge is depleted during the course of the measurement, leading to a distortion of the spectra from this data.[3] Throughout the set of measurements reported in Fig. 2, the electric field in the Si_3N_4 was always greater than 10^6 V/cm, which is sufficient to ionize shallow traps in the bulk of the Si_3N_4 and to assure the collection of electrons injected into the conduction band of the Si_3N_4.

RESULTS

Photoyield spectra obtained from V_{fb} discharge curves are shown in Fig. 3 for an initial charge density of 7.8×10^{12} e^-/cm^2. Similar spectra were obtained for initial conditions of 6.6 and 5.1×10^{12} e^-/cm^2. The spectra display a parabolic rise above a threshold of about 3.0 eV. The yield reaches a saturation level at a photon energy of about 4.0 eV and then falls off. For photon energies within the 4.25 eV window, the spectra are relatively simple, characteristic of emission from a single trap level with an ionization energy of about 3 eV. At photon energies above the 4.25 eV window, the yield drops rapidly to a negative value because of a filling of the traps by photoinjection from the silicon substrate. Because of this photoinjection, the photoyield spectrum is valid only for photon energies in the window below 4.25 eV. The curves above 4.25 eV are shown as a dashed line in the figure. Below 4.25 eV, the yield spectrum shows no structure other than the parabolic edge near threshold for all values of net negative charge; the shape of the yield curve is not significantly influenced by the total charge density. At photon energies near threshold, a plot of the half power of yield vs photon energy fits the data quite well, as in Fig. 4, to determine a threshold for ionization of about 3.0 eV. It is interesting that the threshold increases from 3.00 eV to only 3.05 eV when the net negative charge is changed from 5.1×10^{12} e^-/cm^2 to 7.8×10^{12} e^-/cm^2. This suggests that the distribution of traps is not filled in sequence from low to high energy, but rather the traps are filled uniformly at all energies of the distribution.

Some information on the photodepopulation process can be obtained from the decay of V_{fb} or stored charge in response to light of different photon energies. Fig. 5 shows time dependent discharge curves for 3.5 eV, 4.0 eV, and 4.5 eV. Both the 3.5 eV and 4.0 eV discharge curves decay to the same saturation value, corresponding to a drop in net stored charge from 7.8×10^{12} e^-/cm^2 to about 3.0×10^{12} e^-/cm^2. Presumably, saturation corresponds to the point at which all electrons accessible to ionization by a photon of energy $\hbar\omega$ have been removed. Since the saturation level is the same for 3.5 and 4.0 eV photon energy, one might conclude either that no significant trap levels lie between 3.5 and 4.0 eV or that any traps lying between 3.5 and 4.0 eV are ionized by a multiple excitation. The evidence from the photodepopulation spectra indicates that the former possibility is reasonable; the photoyield saturates at an energy of about 3.8 eV, indicating that few traps appear between 3.8 eV and the 4.25 eV window. The discharge curve is quite different for light of 4.5 eV, which lies above window of photon energy. Here, the V_{fb} decays rapidly to a saturation level which is higher than that at 3.5 eV or 4.0 eV. This larger net charge at saturation results from the operation of two competing processes, the filling of traps by photoinjection and the emptying of them by photoionization.

There is some question about the effect of charge carrier injection at the Al-Si_3N_4 interface upon the "window" available for photodepopulation spectroscopy. The photoinjection of holes into the Si_3N_4 would compete with photodepopulation in the discharge of trapped electrons. However, the process of photoinjection of holes or electrons from a metal electrode into Si_3N_4 is very inefficient, and is not thought to be a significant factor in the spectra presented for SiO_2-Si_3N_4. To test this hypothesis, we measured the accumulated positive charge photoinjected into the insulator from the Al electrode, after all of the accessible electron traps had been emptied. During the interval of exposure to light, the gate electrode was maintained at +10 V, and the silicon surface field was not nulled. No evidence was found for any significant photoinjection of holes from the aluminum, so that the Al-Si_3N_4 contact does not seem to limit the available "window". Injection from the aluminum may, however, contribute an insignificant component to the photodepopulation spectra.

The information derived from the photoionization study adds to our knowledge of the SiO_2-Si_3N_4 interface, which is shown schematically in Fig. 6. The electronic levels are shown for the specific MNOS structure comprising Si-SiO_2-Si_3N_4-Al. As found in the photoionization study, the electron traps lie in a band beginning 3.0 eV below the Si_3N_4 conduction band. The total width of this trap band is probably less than 0.5 eV. However, other trap bands may exist below the 4.25 eV limit of the photoionization technique. Another technique would be necessary to probe the deep traps, with a binding energy greater than 4.25 eV. No evidence is found in the photoionization measurements for electrons in the shallow traps, seen in TSC and I-V measurements of 0.5 eV to 1.5 eV binding energy, which are characteristic of bulk Si_3N_4. Presumably, the shallow traps throughout the Si_3N_4 are ionized by the high electric field present during the measurement. As a result, the traps responsible for charge storage in MNOS structures are not the shallow bulk traps, but rather, they lie at 3.0 eV or more binding energy. With the generally accepted 1.1 eV discontinuity in conduction bands between the SiO_2 and the Si_3N_4, the top of the trap distribution is 0.15 eV above the silicon valence band. This trap energy is somewhat lower than might be expected. However, the trap is only approximate because of the uncertainty in the 1.1 eV step at the SiO_2-Si_3N_4 interface. A downward adjustment of the 1.1 eV step would raise the trap distribution with respect to the silicon.

DISCUSSION OF THE TECHNIQUE

Photopopulation spectroscopy is a simple and powerful technique for examining deep traps in insulating thin films. The spectra can be used to determine the photoionization thresholds of traps within an energy "window", which is equal to the electrode contact barrier. A principal advantage of the technique, a high sensitivity for examining very small numbers of traps, results from a measurement of a change in total charge rather than a current. Extraneous sources of current do not obscure the photodepopulation spectra for photon energies within the "window". The technique should be particularly useful in examining traps introduced into MOS structures by ion implantation, impurities, or radiation damage.

REFERENCES

1. DiStefano, T. H., and Franz, J. M., to be published.

2. Harari, E., and Royce, B. S. H., *J. Appl. Phys.* 22, 106 (1973).

3. DiMaria, D. J., and Feigl, F. J., *Phys. Rev.* B9, 1874 (1974).

4. Kendall, E. J. M., *Phys. Stat. Sol.* 32, 763 (1969).

5. Franz, J. M., Fitzgerald, D., and DiStefano, T. H., Charge Trapping in NMOS Capacitors, *Extended Abstracts* of the Meeting of the Electrochemical Society, 145th Meeting, San Francisco, May 1974.

6. Kendall, E. J. M., *Canadian J. of Phys.* 46, 2509 (1968).

7. Swaroop, B., and Shaffer, P. S., *J. Phys.* D3, 803 (1970).

8. Lundström, K., and Svensson, M., *IEEE Trans. Electron Devices* ED-19, 826 (1972).

9. Lundkvist, L., Lundström, I., and Svensson, C., *Solid State Electronics* 16, 811 (1973).

10. Deal, B. E., Fleming, J. J., and Castron, P. L., *J. Electrochem. Soc.* 115, 300 (1968).

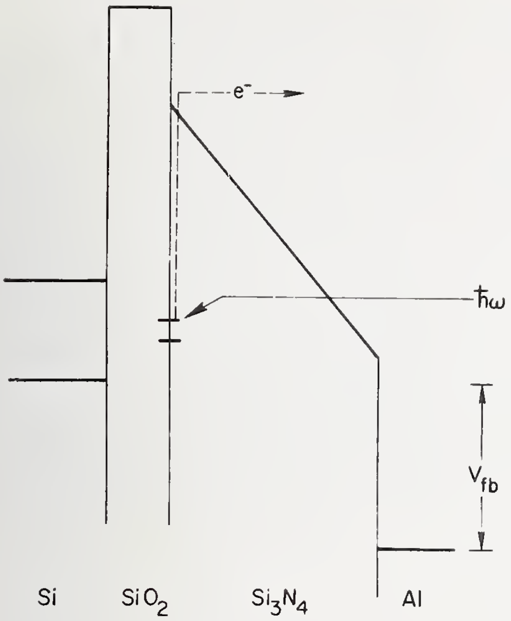

Figure 1. Schematic representation of the photocapacitance technique which was used to determine the energy distribution of electrons trapped in a SiO_2-Si_3N_4 system. A semitransparent aluminum electrode is maintained at a potential V_{fb}, for which the electric field at the silicon surface is zero. The zero field condition is sensed by a high frequency capacitance measurement and maintained by a feedback loop. Photons of energy $\hbar\omega$ excite electrons from traps in the system to cause a change in the V_{fb} which can be related to the photoemission yield for the process.

Figure 2. Spectral dependence of the photon induced discharge of the trapped electrons for three different levels of initial charge. The discharge curves show the decay of the flat-band voltage caused by 15 second exposures to light of increasing photon energy.

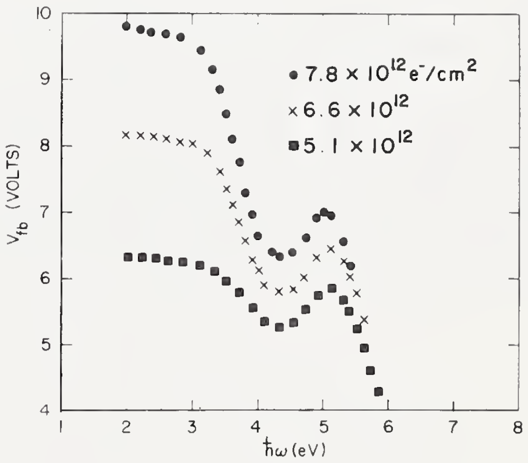

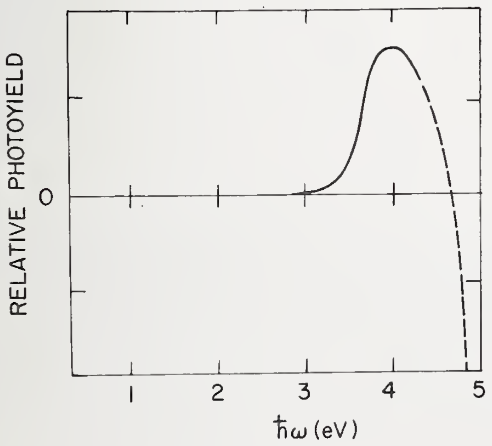

Figure 3. The spectral dependence of the yield for photoemission from traps near the SiO_2-Si_3N_4 interface. The photoyield at photon energies above $h\omega$ = 4.25 eV contains a component due to the filling of traps by photoinjection from the silicon electrode. This injection current causes a net increase in the number of trapped electrons for photon energies above 4.7 eV.

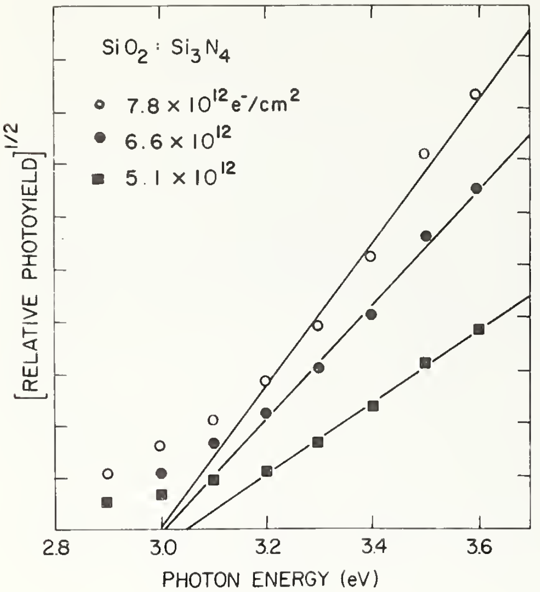

Figure 4. The spectral dependence of photoyield. Near the threshold for photoexcitation, the yield is nearly parabolic with photon energy above extrapolated thresholds of 3.00, 3.01, and 3.05 eV for initial charge densities of 5.1, 6.6 and 7.8 × 10^{12} e^-/cm^2.

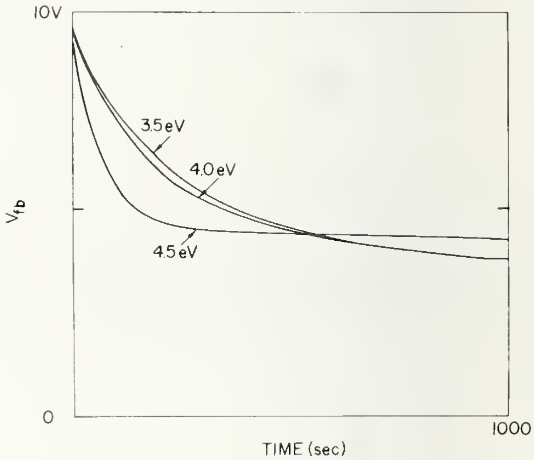

Figure 5. The decay in V_{fb} produced by exposure to photons of three different energies. The flat-band voltage relaxes to a saturation value of 3.9 V for a photon energy of 4.25 eV and below. For a photon energy above the 4.25 eV "window", the saturation charge level is somewhat higher and the behavior more complex because of the operation of two competing processes: photoionization of traps and trap refilling by photoinjection from the silicon.

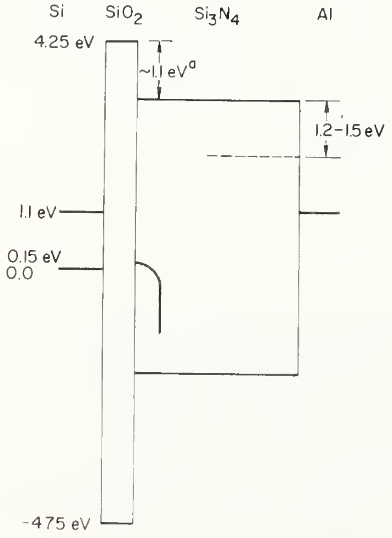

Figure 6. The energy level diagram for the SiO_2-Si_3N_4 system showing the energy of the electron traps near the interface. This assignment assumes a 1.1 eV discontinuity in the conduction bands of SiO_2-Si_3N_4.
a. (Ref. [12]: B. E. Deal, P. J. Fleming, and P. L. Castro, *J. Electrochem. Soc.* 115 300 (1968)).

DISCUSSION OF THE PAPER

Participant: How will you determine the trap density?

DiStefano: The density of occupied traps is determined by working back to get the photoyield as a function of photon energy. From an assumed ionization cross section you can get an approximate value for the trap density. The point is that you can determine the photoemission yield from a measurement of the photodepopulation without actually measuring that current directly. I might also point out that often you cannot measure the photocurrent from the traps directly because the currents involved are small and obscured by other currents in the system. The only way you can detect the trap depopulation current is to measure the charge and then differentiate that.

Participant: This is specifically for a nitride film?

DiStefano: No, this is for the MNOS systems we have examined. You can, I guess, measure the current directly in the case of a large amount of charge trapped in the insulator. You can look at photocurrent and get a photoconductivity by a beaching of those traps. But, for the case of a very small number of traps in insulators like SiO_2, the discharge time is so long and the total charge density is so small it is very hard to detect the photocurrent directly. Also, with the photocapacitance technique, we measure only the current from the deep traps of interest, without the complication of extraneous currents.

NBS Special Publication 400-23, ARPA/NBS Workshop IV, Surface Analysis for Silicon Devices, held at NBS, Gaithersburg, Maryland, April 23-24, 1975 (Issued March 1976)

PHOTOEMISSION AND PHOTOVOLTAIC IMAGING OF SEMICONDUCTOR SURFACES*

T. H. Di Stefano

IBM Watson Research Center
Yorktown Heights, New York 10598

ABSTRACT

The new electro-optical techniques of scanned internal photoemission and scanned surface photovoltage can be used to obtain images of non-uniformities and defects at semiconductor surfaces or interfaces. The spatial resolution of either method is primarily determined by the wavelength of the laser used as a collimated light source. The images obtained by the photoemission technique are replicas of the local contact barrier at the interface between two materials. Typically, photoemission images show details due to variations of stoichiometry or local concentration of impurities. The photovoltage technique, on the other hand, displays recombination centers such as precipitates, dislocation, stacking faults, cracks, and gross damage near a semiconductor surface. Each of these electro-optical imaging techniques provides information about interfaces that was previously inaccessible to observation.

INTRODUCTION

Focused beams of various types of ionizing radiation have been used in the past [1-20] to probe semiconductor surfaces and devices, generally in the region near a p-n junction. The signal induced in a junction by a scanned optical beam has been found to provide information [3-10] on resistivity fluctuations in the material, on gross defects in the device, and on surface irregularities or inversion layers near the junction. Generally, in this type of measurement, a beam of electrons or photons is scanned across an area of a semiconductor to produce hole-electron pairs in the material. An irregularity in the material will produce a fluctuation in a sample current of some sort measured when the beam scans across the defect. In the standard configuration, a p-n junction collects current produced within a diffusion length of the junction. Any change in either the generation or recombination rate near the junction is detected as a fluctuation of the collected current. The beam induced current is displayed on a rastered CRT to produce an image of the defects and inhomogeneities. Imaging techniques of the electron beam induced current [11-20] (EBIC) or photon induced current type [4-10] are useful in identifying defects in individual semiconductor devices, but they cannot easily be applied to the study of semiconductor surfaces or interfaces on which no p-n junction exists. The necessity of a p-n junction to collect the beam induced current makes non-destructive evaluation of material surfaces at various stages of processing virtually impossible.

Recently, several scanned beam techniques, including scanned internal photoemission [21-24] (SIP), scanned surface photovoltage [25, 26] (SSP), and the corresponding electron beam analogs [27, 28] have been developed to probe free semiconductor surfaces. These new techniques provide images of defects near surfaces or interfaces without the necessity of a p-n junction to detect the signal current. As a result, they can be used to examine non-destructively the defects which occur on semiconductors at various stages of material processing. Each of the techniques has characteristic advantages and capabilities. The e-beam techniques provide the best resolution, better than about 1000 Å, [27] but they are complicated by beam induced charging of any insulating film on the surface.[28] On the other hand, the optical techniques have a resolution capability of on the order of one micron, but they do not charge the surface insulating or passivating film. Hence, the optical techniques can also be used to examine charge non-uniformity in the insulating film on the surface without disturbing the system. Additionally, the optical scanning apparatus can be made to be cleaner than existing e-beam systems because it does not require a complex vacuum system.

---

* Work supported in part by the Defense Advanced Research Projects Agency and monitored by AFCRL under contract number F 19628-74-C-0077.

Of the optical techniques, SIP determines small inhomogeneities in the contact barrier Φ between two materials, one of which is typically an insulator such as SiO_2. The SIP technique is useful in imaging changes in Φ which are due to contamination, interface chemical reaction, impurity segregation at the interface, or surface crystallographic defects. In contrast, the SSP technique is sensitive to local recombination centers that are within about one micron of the surface and to charge inhomogeneities in the insulating overlayer. Typical recombination centers seen in SSP images include crystallographic defects, precipitates, and gross surface damage; these defects are usually introduced during growth, cutting, polishing, and high temperature processing of the semiconductor material. The SSP technique has a unique advantage in that no direct contact to the sample is required if the photovoltage measurement is made by capacitive coupling. Since physical contact is unnecessary, the SSP technique is clean and completely non-destructive.

OPTICAL SCANNING SYSTEM

The instrumentation for the two scanned optical techniques is quite similar in that a small spot is rastered on the sample surface while a signal, either photoemission or photovoltage, is detected and displayed on a CRT. A cw laser was used for the light source in order to obtain a measurable signal from a small, nearly diffraction limited light spot. Reasonable signals were obtained with 1.0 mW of light incident on the sample, without any noticeable thermal damage to the sample at the 10^5 W/cm^2 power density at the focused spot. The spot was swept by the sawtooth motion of a galvanometer driven mirror, which was scanned at a 20 Hz rate. In the other direction, the beam was swept slowly in order to complete a 600 line single frame in 30 sec. The frame rate, which is limited by the rate of the fast scan mirror, could easily be increased an order of magnitude by increasing the fast scan rate to 200 Hz. A further increase, at the expense of a reduced spacial resolution, could be obtained with an accoustic deflection system for the fast scan direction. The total resolution capability of the optical scanning technique is limited by three equally important factors: the divergence of the light output from the laser, the diffraction limit of the objective lens, and the bandwidth of the detector. At best, the spacial resolution (of the SIP measurement) is estimated to be about 0.43 microns, with the dominant factors being lens diffraction at λ = 3250 Å and laser divergence.

The simple optical system shown in figure 1 was used to scan a light spot over a square area of the sample surface. Radiation from a laser source was focused onto a 50 micron pinhole in order to eliminate the light that diverged by more than 0.5 mrad. The laser source was chosen to be either an RCA He-Cd laser operating with 3mW at 3250 Å or a Spectra Physics He-Ne laser with 5 mW at 6328 Å. Light emergent from the pinhole was projected a distance of one meter onto a series of two front surface mirrors, which rotate through angles θ and ϕ. Light from the two scanned mirrors completely filled the aperture of the objective lens for the full range of the scanned angles. Then, the focused spot of light from the objective lens scanned an area of the sample as the two orthogonal mirrors were rotated. The size of the scanned area, and to some extent, the resolution of the system, were determined by the objective lens. The focal length of the lenses used in the measurements range from 0.54 cm to 20 cm. Reflecting objective lenses were used for the high resolution measurements so that correction of the optics for the wavelength of each laser was unnecessary.

The fast scan mirror was driven at about 20 Hz by a rotary galvanometer, G-306, available from General Scanning, Inc. Care was taken to balance the mirror and rotor in order to minimize parasitic oscillation of the mirror assembly. This parasitic oscillation or vibration causes deflection of the light perpendicular to the direction being scanned by that particular mirror. Although faster galvanometer scanners are available, the relatively conservative rate of 20 Hz was chosen to minimize the problems caused by vibration and to optimize resolution.

The problem of positioning and focusing the sample, something which is particularly difficult in the case of UV light, was solved by detecting light reflected back into the system from the sample. Initially, light from the pinhole goes through the scan system which focuses it onto the sample. When the system is in focus, the light reflected from the sample is focused by the system back onto the pinhole, independent of the mirror positions θ and ϕ. However, if the system is out of focus, the reflected light falls outside the pinhole where it strikes a fluorescent screen. The system is brought into focus by adjusting the sample position along the optical axis until all of the reflected light is refocused back onto the pinhole.

In order to locate the sample in the beam and to examine the surface conditions during the measurements, a reflectivity image of the sample can be obtained and displayed in the coordinate frame of the CRT. A portion of the light reflected from the sample is directed onto a photocell by a beamsplitter. The light falling on the photocell comes to focus at a point which is independent of the scan angles θ and ϕ. Current from the photocell, when displayed as Z-axis modulation of a rastered CRT, forms an image of the sample at the wavelength of the laser source and in the same coordinate frame as the SSP or the SIP image of the same area.

Both the photoemission and the photovoltaic signals are detected and displayed on a CRT screen by the circuitry shown schematically in Fig. 2. The signal current is detected by a Kiethley 18000 picoammeter which has been modified for a fast response; the modification involves a reduction of the feedback capacitance in each of the two amplifier sections, while maintaining the stability of the overall system. The signal in the SIP measurement is the photocurrent, while the signal in the SSP measurement is the capacitive current induced in the probe electrode by the surface photovoltage. The amplitude and dc level of the signal are adjusted and applied to the Z-axis of the CRT, along with a retrace blanking pulse derived from the fast scanner. The X and Y axes of the CRT are driven by voltages proportional to those directly across the drive motor armatures. Images of the Z-axis modulated display of the SSP or the SIP signal are recorded photographically.

The measurement apparatus, shown in figure 3, includes the scan mirrors, the galvanometer motors, the reflecting microscope objective, the sample positioning stage, and the picoammeter. Light, incident on the mirrors from the right, is deflected onto the two orthogonally mounted scanning mirrors by a stationary positioning mirror. From the fast scanned mirror, the beam enters the reflecting objective lens (Beck 36/.5) which focuses the light onto the sample. Because of the curvature of the focal plane of this objective, the overall resolution is noticeably degraded for beam deflections greater than ±0.5°. In order to extend the useable field of view, it is necessary to use a refractive plano-objective which is corrected for flatness of field at the laser wavelength.

The sample is held in position and focused by an X-Y-Z adjustable hot stage. Signals from the sample are detected by the picoammeter located behind the hot stage in figure 3. The entire assembly is secured to a two meter optical bench.

SCANNED INTERNAL PHOTOEMISSION

Scanned internal photoemission (SIP) is a relatively recent technique [21-24] for probing interfaces with a beam of light to produce electronically an image or replica of the interface contact barrier. Typical images display a modulation of the internal photocurrent induced by the scanned beam which is due to a lateral inhomogeniety of the contact barrier. The technique is somewhat analogous to scanning electron microscopy (SEM), except that in this case a light beam is used to excite electron emission into a dielectric instead of into vacuum. As in the SEM technique, the emitted current is displayed on the Z-axis of a CRT.

The mechanism of SIP is internal photoemission on a local scale, as shown in figure 4. A scanned light beam of energy $\hbar\omega$ penetrates a transparent [29] or semi-transparent [30] electrode and is absorbed in the opposite electrode where it excites electrons into the conduction band. Some of the electrons have sufficient momentum normal to the interface so that they are able to surmount the barrier Φ and reach the opposite electrode. Near threshold, the quantum yield for photoemission is

$$\Psi = \gamma \, (\hbar\omega - \Phi)^{\alpha} \; ,$$

where γ is a constant and α is an empirically determined power, typically in the range 2 to 3. A small percentage reduction in Φ leads to a relatively larger increase in yield,

$$d[\ln \Psi] = \frac{\alpha\Phi}{(\hbar\omega - \Phi)} \, d[\ln \Phi] \; .$$

The sensitivity of the SIP technique depends upon the rapid increase of photocurrent produced by a small decrease of Φ below the photon energy $\hbar\omega$. For a reasonable image contrast, the laser and any Schottky barrier reduction are chosen so that $\hbar\omega$ is several tenths of an eV above Φ.

The Si-SiO$_2$ interface is an interesting candidate for examination by SIP imaging, as can be seen in figure 5 and 6. Here, the Si-SiO$_2$ interfaces have been uniformly coated with about 4 x 10^{12} Na/cm^2 by electrodeposition in order to reduce the interface barrier[31] from 4.25 eV down to a level that is accessible to the He-Cd laser operating at 3.81 eV. Actually, the sodium acts as a "staining agent," increasing the local photocurrent in those places where ions accumulate on the interface. Since the sodium coverage is influenced by defects, it was found to enhance the SIP contrast around defects. Fig. 5 shows an interesting pattern of dark spots seen in the emission from an Si-SiO$_2$ interface grown on $\sim 10^{20}$ P/cm^3 doped (100) Si. These spots, which are about 10 microns in diameter, have been identified as phosphorous that has segregated onto the Si-SiO$_2$ interface during high temperature growth [32, 33] of the 1000 Å thick SiO$_2$. Apparently, sodium that does reach the Si-SiO$_2$ interface is rendered ineffective by chemical combination with the phosphorous lying within a few atomic layers of the interface [33]. These phosphorus islands, observed for the first time by the SIP imaging technique, were found to be correlated with the phosphorous doping density in the silicon substrate. Another type of defect on the Si-SiO$_2$ interface is seen in figure 6 as a line, about 30 microns long, with bright spots at either end. The defect, which lies along the <110> crystallographic direction, is thought to be a stacking fault that has been decorated by sodium ions. The contrast of the stacking fault is enhanced by the sodium decoration.

The SIP technique was also used to study metal-insulator interfaces such as Nb$_2$O$_5$-Bi, which is of interest because of the fast switching found in this structure. The SIP image in figure 7 represents photocurrent emitted from a 200 Å Bi electrode into Nb$_2$O$_5$. The light source was a He-Ne laser at 1.96 eV, which is close to threshold where the technique is most sensitive. In this system, the contrast mechanism is not simple because of the large number of traps in the Nb$_2$O$_5$.

SCANNED SURFACE PHOTOVOLTAGE

Photovoltage images show defects that cause minority carrier recombination on a semiconductor surface. The SSP images have also been found to show any non-uniform charge in the passivating layer on a semiconductor. An SSP image is formed by displaying the first or second derivative of the photovoltage induced by a scanned beam of light on a semiconducting surface. The travelling light spot produces a comet shaped cloud of minority carriers which are captured on the slightly depleted surface, as represented in figure 8. Carriers from the moving cloud cover the surface to produce a photovoltage. When the beam passes over a defect, some of the charge cloud is lost to recombination, leading to a dip in the photovoltage. This dip is detected by a capacitively coupled electrode near the surface, and displayed on a CRT. Since the charge cloud is quite large, on the order of the diffusion length, the resolution of images produced directly from the photovoltage is rather poor. The high resolution [25] of the SSP technique is due to the use of the first or second derivative of the photovoltage to form the image. The differentiation accentuates the signal in the region around the light spot, where the charge cloud density has a logarithmic singularity. In practice, the first derivative is obtained directly by measuring the capacitive current induced by fluctuations of the surface photovoltage.

By using conduction of minority carriers along the slightly depleted surface, it is possible to obtain SSP images at some distance from the electrode. The local photovoltage is coupled to the entire surface by the slightly conducting surface. In some cases, it is necessary to enhance the surface conductivity by generating extra minority carriers by a dc blanket illumination. The resolution of remotely detected images was found to be reduced if the surface conductivity is too low. Also, in order to develop a photovoltage signal, the surface must be depleted, either by a blanket electrode (the electrode can be an aquous solution, as was shown by Lile and Davis [26]), or by a surface treatment such as that produced by dry oxidation of p-type silicon.

The signal S' is proportional to a convolution of the excess local recombination rate R with an experimental sampling function, which is approximately equal to the x-derivative of the charge cloud density n. Mathematically,

$$S'(x_o,y_o) \sim \left(\frac{Gv\varepsilon_b\delta}{\varepsilon_a\tau_o t}\right)\iint dx\,d\Psi \,\frac{dn(x-x_o,y-y_o)}{dx}\,R(x,y),$$

where G is the total generation rate, S is the effective depletion width, E_a is the permittivity of the semiconductor, E_b is that of the dielectric, and τ_o is the surface minority carrier lifetime. Ideally, dn/dx would be a singly differentiated Dirac delta function and the signal S' would then be proportional to dR/dx. Because of the finite size of the light spot, however, the resolution is reduced. In a coordinate system centered on the moving spot, a modified diffusion equation [25] is solved to obtain the charge density n in the region around the scanned spot. The charge density

$$n = A \exp\left(-\frac{vx}{2D}\right)K_o(\kappa r) \;,$$

where

$$\kappa = \frac{1}{\sqrt{D\tau_o}}\left(1 + \frac{v^2\tau_o}{4D}\right)^{1/2} ,$$

and where K_o is a modified Bessel function of the second kind, and D is the surface diffusion coefficient. The sampling function dn/dx is plotted in figure 9 for several scan velocities, with the reasonable parameters

$D = 15\ cm^2/sec$ and $\tau_o = 0.01$ sec. The form of dn/dx deviates little from 1/r near the light center at r = 0. Based on this simple theory, the resolution at 1/e is approximately 2.7 times the light spot diameter for singly differentiated SSP and nearly 1.0 for the doubly differentiated technique.

Several examples of SSP images, obtained from (100) silicon surfaces, display the resolution, sensitivity, and comparative advantages of this relatively simple technique. An SSP image of several clusters of emergent dislocations which penetrate the (100) surface of a sample are shown in Fig. 10. The dislocations were produced by mechanically damaging the reverse side of a silicon wafer, and then annealing it in dry He at 800°C for 30 min. It is known[34] that such damage will cause dislocations to propagate through to the front surface during high temperature processing. Surface defects were also found in SSP images of nominally defect free silicon, an example of which is shown in figure 11. Here, a semitransparent blanket electrode was used in order to maximize resolution. The image shows scratches, some as long as 1000 microns, which are not parallel to a low order crystallographic direction. Presumably, these scratches were introduced during the polishing process. Another type of defect, commonly seen in device grade silicon, occurs throughout the area of figure 12. These small spots are thought to be crystallographic defects associated with precipitates of oxide or other foreign material. The density of these defects was found to be correlated with oxygen concentration, suggesting that the defect may be associated with an oxide precipitate. The density was found to be as high as $10^5\ /cm^2$ (within several microns of the surface). A rather uncommon surface defect, displayed in figure 13, was found on a device-grade silicon wafer. It appears to be similar to the surface defects, identified as microsplits by Schwuttke [35], which are small cracks along the <110> direction in the silicon surface, with stacking faults at either end. Schwuttke has found that microsplits like that in figure 13 are introduced during the saw cutting of the silicon.

It is interesting to compare the SSP technique with the useful but destructive technique of selective etching. A sample was prepared [36] for this purpose by polishing a piece of saw cut silicon at a 2° bevel off normal to the (100) surface. The sample geometry is represented in figure 14. A Sirtl etch was applied to half of the surface to reveal the saw damage. The sample was then oxidized and the series of SSP images in figures 14 A' - D' were measured. For comparison, figures 14 A - D are micrographs of the etched surface at points of polish depth equal to that of the equivalent SSP image. Both the etch pattern and the non-destructive SSP technique appear to provide the same type of information. However, it is thought that the SSP measurement is sensitive to sub-surface structure such as precipitates which may not appear in an etch pattern.

CONCLUSION

Each of the scanned optical techniques, scanned internal photoemission and scanned surface photovoltage, has unique capabilities for examining semiconductor surfaces and interfaces. Photoemission imaging is useful in determining interface reaction or contamination. However, it is not amenable to wide use in process control or material evaluation because of the difficulty of the measurement and the requirement of a contacting counter-electrode. On the other hand, photovoltage imaging is a simple, fast, non-contacting, non-destructive technique that offers reasonalbe resolution, about half a micron for a double differentiated measurement at a wavelength of 3250 Å. Since scan speed does not degrade resolution, there is no inherent physical limit on the frame repetition rate. The photovoltage technique has been used routinely to detect stacking faults, dislocations, precipitates, gross surface damage, and local insulator charging.

The photovoltage imaging technique SSP has great potential for use in semiconductor material evaluation and in process control in the production of semiconductor devices. By observing the defects introduced during the various stages of production, it is possible to identify and control the factors that introduce defects. In the particular case of silicon integrated circuits, both the production and the reliability of the devices is critically dependent upon crystalline perfection of the material which can be monitored by SSP imaging. The use of Photovoltage imaging is somewhat less useful as a research tool than the electron beam analog, as developed by Bottoms [28], because the special resolution is considerably lower.

REFERENCES

1. Adam, G., *Physica* 20, 1037 (1954).

2. Avery, D. G., and Gunn, J. B., *Proc. Phys. Soc.* B 68, 918 (1955).

3. Oroshnik, J., and Many, A., *J. Electrochem. Soc.* 106, 360 (1959).

4. Tihanyi, J., and Pasztor, G., *Solid State Electronics* 10, 235 (1967).

5. Potter, C. N., and Sawyer, D. W., Optical Scanning techniques for semiconductor device screening and identification of surface and junction phenomena, *Physics of Failure in Electronics*, Shilliday, T. S. and Vaccaro, J., Eds., Rome Air Development Center Series in Reliability, 1967, vol. 5, p. 37.

6. Summers, R. A., *Solid State Technology*, p. 12, (March, 1967).

7. Haberer, J. R., Photoresponse Mapping of Semiconductors, in *Physics of Failure in Electronics*, Shilliday, T. S. and Vaccaro, J., Eds., Rome Air Development Center Series in Reliability, 1967, vol. 5, p. 51.

8. Phelan, Jr., R. J., and DeMeo, Jr., N. L., *Appl. Optics* 10, 858 (1971).

9. Kozhevin, V. E., *Sov. Phys.-Solid State* 8, 1979 (1967).

10. Kasprzak, L. A., *Rev. Sci. Inst.* 46, 17 (1975).

11. Lander, J. J., Schreiber, H., and Buch, T. M., *Appl. Phys. Lett.* 3, 206 (1963).

12. Everhart, T. E., Wells, O. C., and Matta, R. K., *J. Electrochem. Soc.* 111, 929 (1964).

13. MacDonald, N. C., and Everhart, T. S., *Appl. Phys. Lett.* 7, 267 (1965).

14. Czaja, W., and Patel, J. R., *J. Appl. Phys.* 36, 1476 (1975).

15. Everhart, T. E., *Proc. IEEE* 54, 1480 (1966).

16. Foss, N. A., *J. Appl. Phys.* 41, 823 (1970).

17. Ravi, K. V., Varker, C. J., and Volk, C. S., *J. Electrochem. Soc.* 120, 533 (1973).

18. Varker, C. J., and Ravi, K. V., *J. Appl. Phys.* 45, 272 (1974).

19. Gonzales, J. A., *Scanning Electron Microscopy 1974*, Johari, O., Ed. p. 94 (ITT Research Institute, Chicago, Illinois, 1974).

20. Kato, T., Matsukawa, T., Koyama, H., and Fujikawa, K., *J. Appl. Phys.* 46, 2288 (1975).

21. DiStefano, T. H., *Appl. Phys. Lett.* 19, 280 (1971).

22. DiStefano, T. H., *J. Appl. Phys.* 44, 527 (1973).

23. Williams, R., and Woods, M. H., *J. Appl. Phys.* 43, 4142 (1972).

24. DiStefano, T. H., and Viggiano, J. M., *IBM J. Res. Dev.* 18, 94 (1974).

25. Philbrick, J. W., and DiStefano, T. H., Scanning Surface Photovoltage Study of Defects in Silicon, *Proc. 13th Annual Reliability Physics Conf.* Las Vegas, Nevada, April 1, 1975 p. 159.

26. Lile, D. L., and Davis, N. M., to be published in *Solid State Electronics*.

27. Bottoms, W. R., and Guterman, D., *J. Vac. Sci. Technol.* 11, 965 (1974).

28. Bottoms, W. R., Guterman, D. and Roitman, P., *J. Vac. Sci. Tech.* 12, 134 (1975).

29. Goodman, A. M., *Phys. Rev.* 152, 780 (1966).

30. Williams, R., Injection by Internal Photoemission, *Semiconductors and Semimetals*, Vol. 6, Willardson, R. K., Ed., (Academic Press, Inc., New York, 1970).

31. DiStefano, T. H., and Lewis, J. E., *J. Vac. Sci. Technol.* 11, 1020 (1974).

32. Chou, N. J., van der Meulen, Y. J., Hammer, R., and Cahill, J. G., *Appl. Phys. Lett.* 24, 200 (1974).

33. van der Meulen, Y. J., *J. Vac. Sci. Technol.* 11, 985 (1974).

34. Dumin, D. J., and Henry, W. N., *Metallurgical Trans.* 2, 677 (1971).

35. Schwuttke, G. H., Tech. Rep't. 1 ,2, ARPA Contract No. DAHC 15-72-C-0274.

36. The bevel polished sample was prepared by J. W. Philbrick, IBM Hopewell Junction, New York.

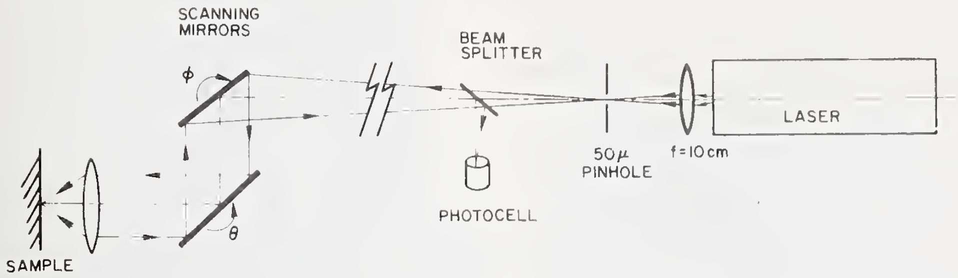

Figure 1. Optical system and measurement apparatus for the scanned optical measurements. Laser radiation is focused through a 50 µm pinhole and then deflected by two scanning mirrors rotating about perpendicular axes. The deflected light fills the aperture of a microscope objective lens for all deflection angles θ and ϕ. The system is brought to focus by adjusting the position of the sample along the optical axis to minimize the size of the light spot reflected onto the fluorescent screen on the back of the 50-µm pinhole. A portion of the reflected beam is diverted and brought to a stationary focus on a photocell in order to detect a reflectivity image of the scanned area.

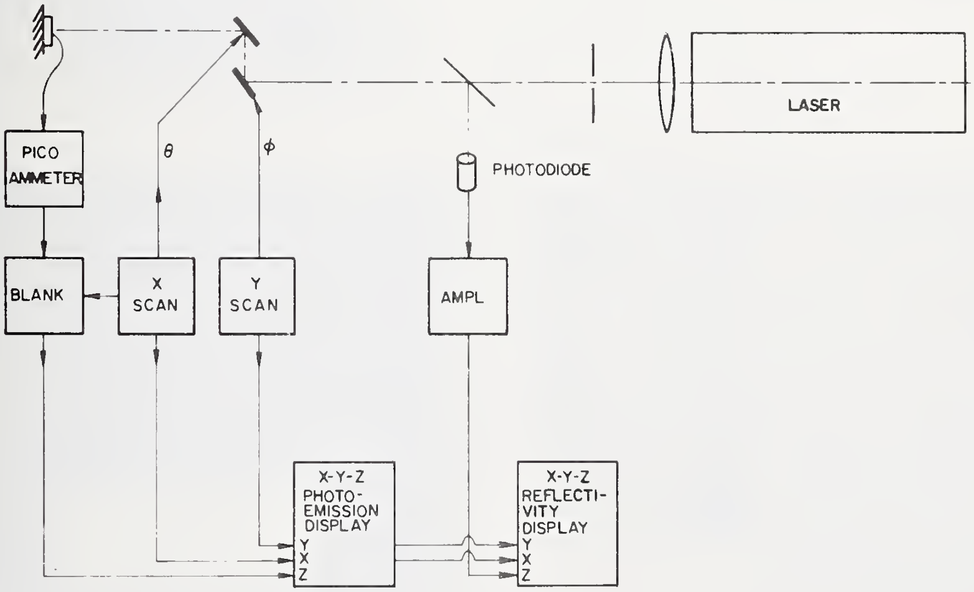

Figure 2. A schematic representation of the scanned optical system showing the instrumentation required to obtain SIP or SSP images. The x and y inputs to the CRT are driven by the voltage applied to the mirror galvanometer motors.

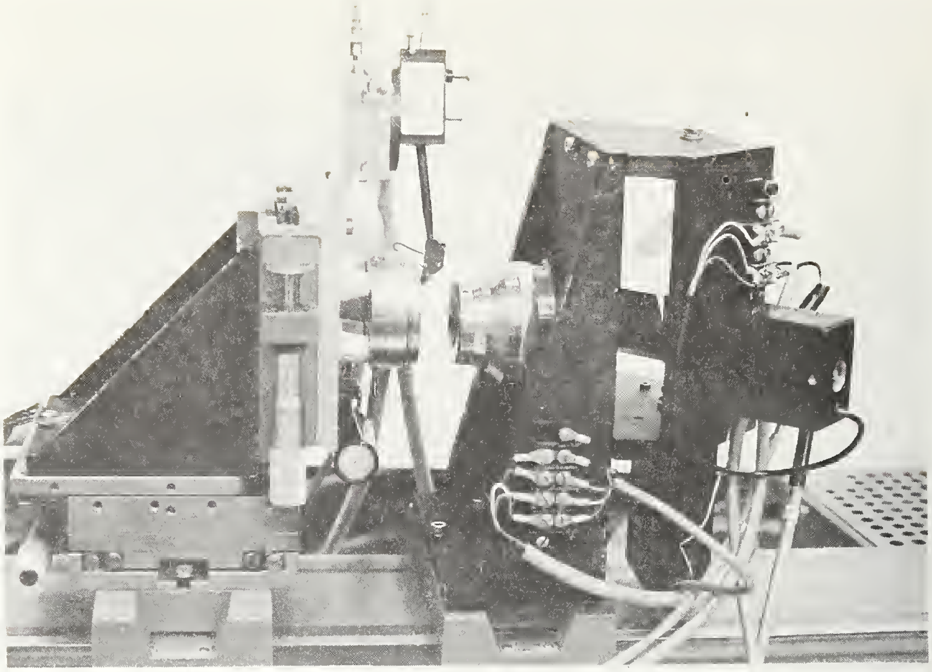

Figure 3. The optical scanning apparatus showing the scan mirrors, galvanometer drivers, microscope reflecting objective, sample positioning stage, and the preamplifier head.

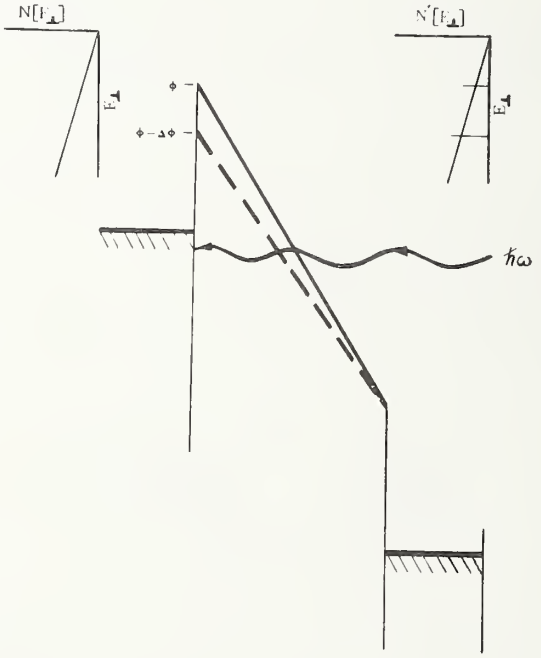

Figure 4. A representation of the processes involved in scanned internal photoemission. A small reduction in the effective interface barrier allows an enhanced photocurrent to flow.

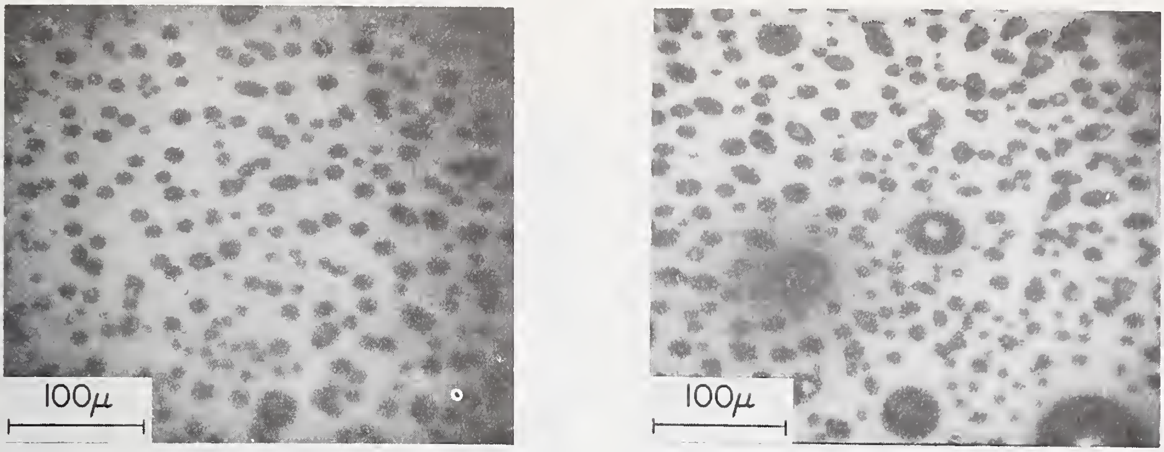

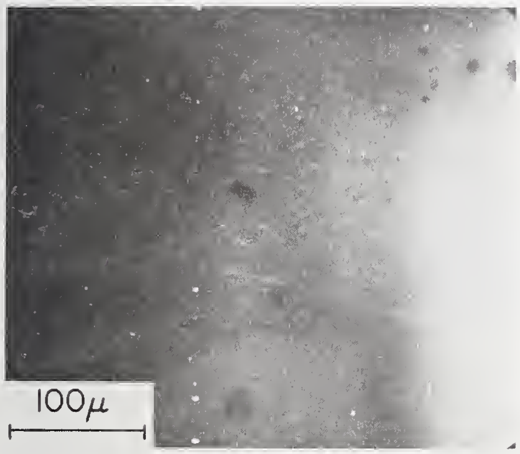

Figure 5. Scanning internal photoemission images of three samples of Si-SiO$_2$ interfaces covered with 4 × 10^{12} sodium atoms per square centimeter, and measured at a photon energy of 3250 Å. The light areas indicate a high photoyield produced by the presence of sodium on the interface. The dark areas are thought to be due to regions of phosphorus rich layers near the Si-SiO$_2$ interface. Phosphorus segregates at that interface during the formation of the SiO$_2$ layers, produced by the oxidation of 10^{20} P/cm^3 doped silicon.

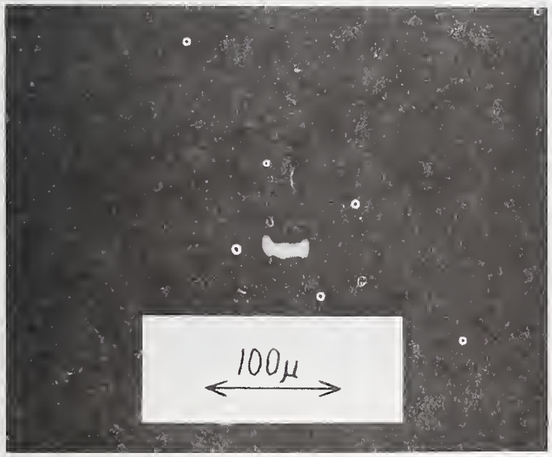

Figure 6. Scanned internal photoemission measurements of an Si-SiO$_2$ interface which has been uniformly coated with 4 × 10^{12} Na/cm^2. The Na is found to decorate a 30 μm, long defect which lies in the <100> direction on the silicon surface.

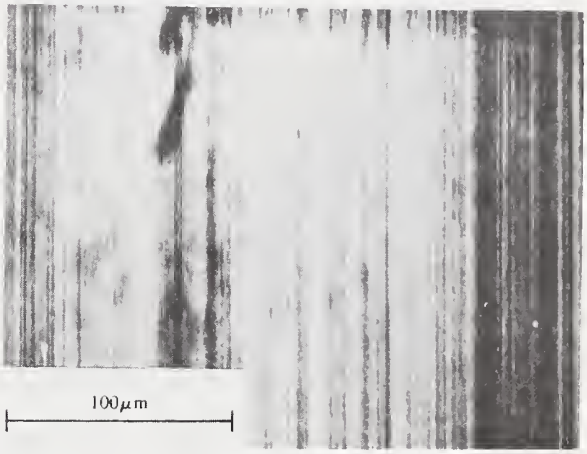

Figure 7. Scanned internal photoemission image of a Bi-Nb$_2$O$_5$ interface, measured at λ = 6328 Å. The vertical striae are due to a dc level shift of leakage currents.

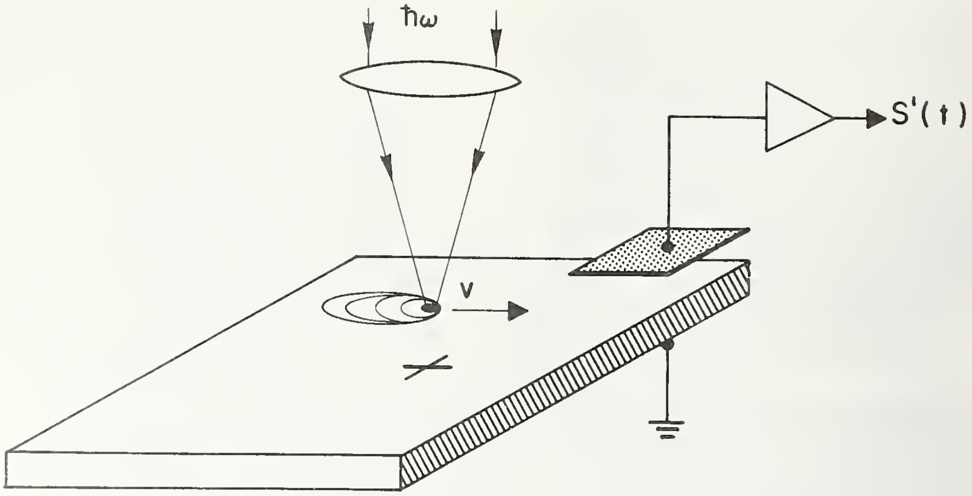

Figure 8. The rudiments of the scanned surface photovoltage measurement. A spot of light is swept across a semiconductor surface, generating a comet shaped cloud of minority carriers in a surface depletion region. The surface potential, capacitively detected by a remote electrode, fluctuates when the spot traverses a surface recombination center.

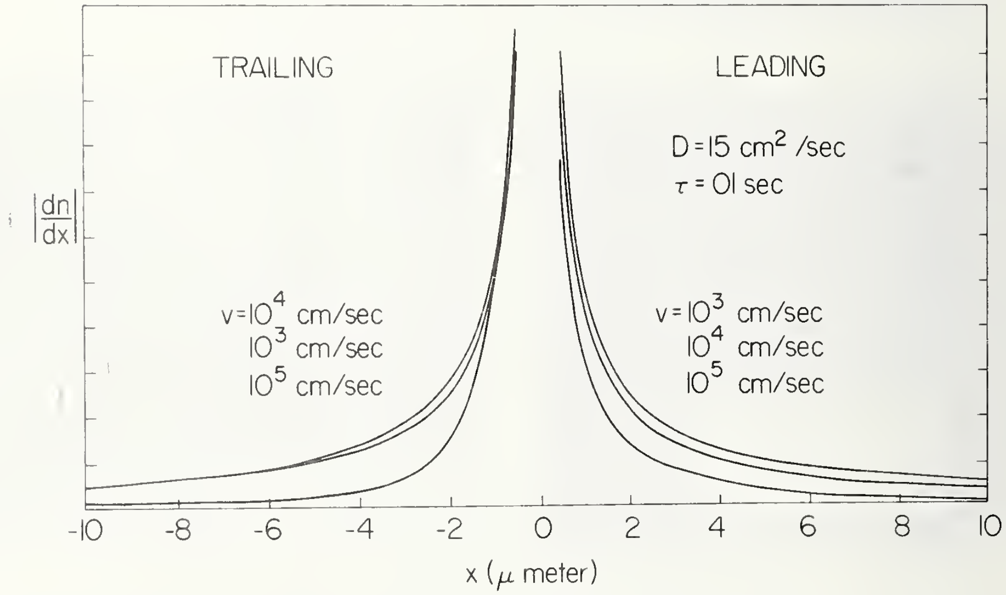

Figure 9. The spacial derivative of the surface minority carrier density, along a line in the direction of travel of a 1 μm spot of light. The derivative is relatively insensitive to the scan velocity v for the values shown in the figure. The quantity |dn/dx| is the sampling function in the singly differentiated scanned surface photovoltage measurement.

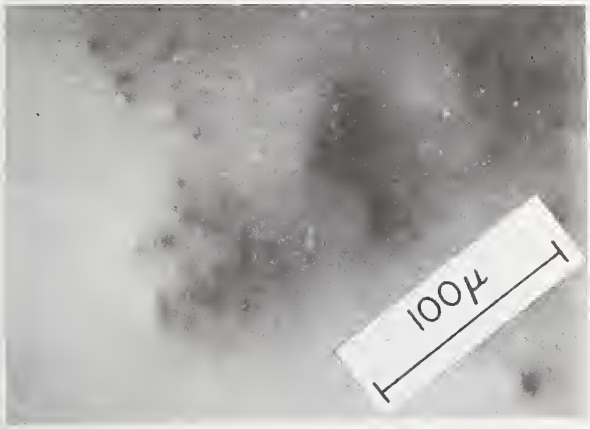

Figure 10. Scanned surface photovoltage image of several clusters of emergent dislocations through the (100) surface of a silicon wafer. The dislocations were generated by sandblasting a spot on the reverse side. During subsequent annealing and oxidation steps, the dislocation loops generated at the damage sites grow through the wafer, eventually penetrating the front surface.

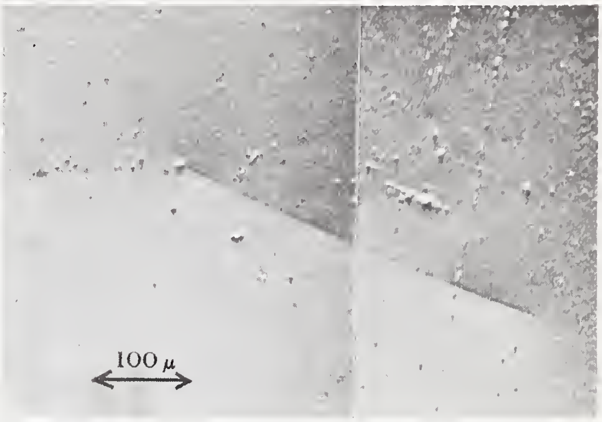

Figure 11. Scanned surface photovoltage image of surface damage produced during the cutting and polishing of a silicon wafer. The damage lines do not follow the <110> direction on the (100) surface.

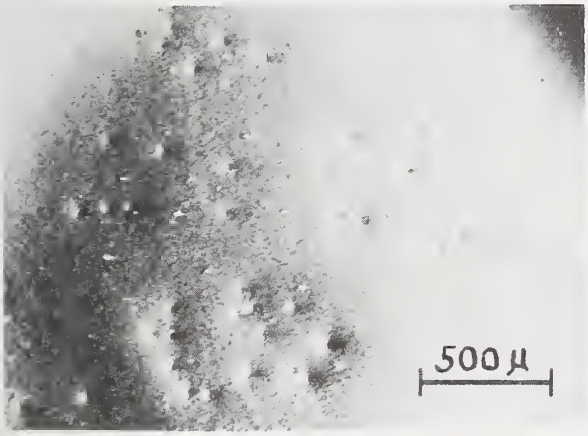

Figure 12. Scanned surface photovoltage image of a (100) silicon surface showing small, randomly distributed defects.

Figure 13. Scanned surface photovoltage image of a defect, apparently a microsplit, which was introduced during saw cutting of the (100) surface. The microsplit is thought to be flanked by stacking fault arrays in the <110> direction on the surface.

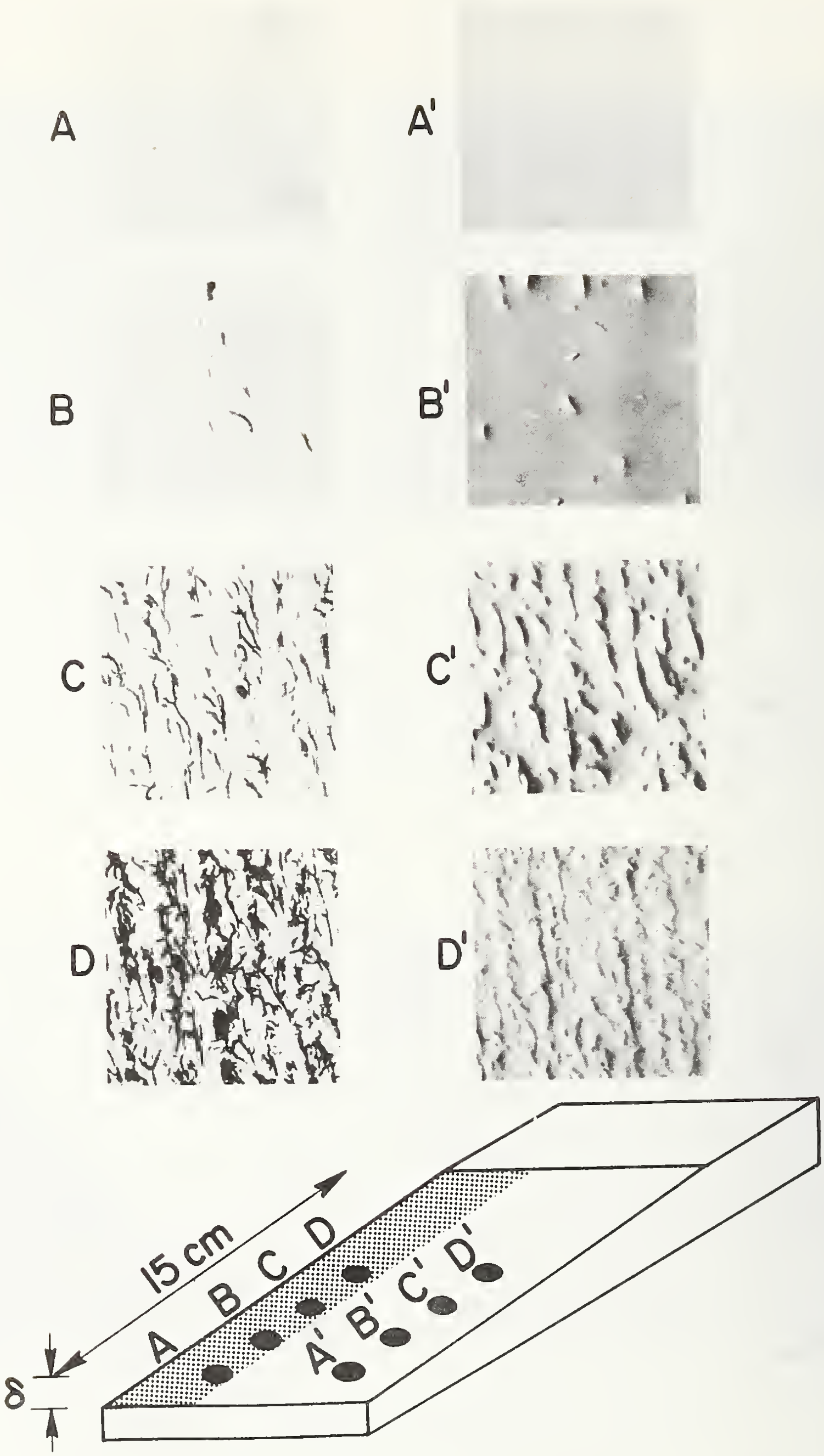

Figure 14. Scanned surface photovoltage images (A', B', C', D') of saw damage in a silicon wafer which has been polished at a 2° angle. For comparison, micrographs (A, B, C, D,) of an adjacent area of the surface were made after etching. Both sets of images, taken on a highly polished area of the beveled surface, show the transition from the damaged region to the undamaged region occuring at about the same depth, as is observed on an etched portion of the bevel.

DISCUSSION OF THE PAPER

Feigel: Photovoltaic imaging is a non-contacting technique, right?

DiStefano: That is correct. The only contact that is made to the sample is the capacitive contact. The sample is simply a sandwich between capacitive electrodes.

Feigel: Then is it relatively easy to engineer?

DiStefano: Nothing is hidden, everything was shown on the figure.

Feigel: I meant there are no super critical dimensions or dimensional stability problems you have to worry about?

DiStefano: Focussing is a problem but, as I mentioned, we use the back reflected light to focus the sample. Focussing is a problem in the ultraviolet because you cannot see the spot. Other than that, there is nothing intrinsically difficult about the technique.

Thomas: Can you actually identify the collecting species? You said it is actually copper.

DiStefano: In some of the cases we intentionally put copper into the system. It is an inference that the precipitate is copper, since there is copper in this sample.

Thomas: We also have found copper, but there are other metals that can actually decorate the defects. Would you say there is some similarity between this technique and the EBIC technique?

DiStefano: There are some similarities. With the electron beam induced current technique you need a junction, and you look at junction current. There is no problem with resolution, but it is necessary to have a surface junction on the sample. One of the beauties of the photovoltage technique is that it is nondestructive, so you can look at an area, process that area, and then go back and examine what defects were caused by the processing. We are studying various things such as nitride passivation and the defects introduced by the mechanical stress. We are looking at deep etching and oxide isolation in silicon. So this technique is ideal for following a piece of silicon through a stage of processing steps.

Participant: Can you use the amplitude of the surface photovoltage to obtain a three-dimensional representation of your data similar to the Y amplitude images?

DiStefano: We can do that, but we do not, because that tends to make it harder to identify the position of the defect. We do use a series of photographs in different colors to look at the depth of the trap. There is one thing that I have not mentioned, namely you can also bend the bands of the silicon surface and submerge a trap or a surface defect below the energy level so you no longer see it. You can take a series of images as a function of the Fermi level at the surface as defect disappears to obtain an X, Y, and energy representation of the defect.

NBS Special Publication 400-23, ARPA/NBS Workshop IV, Surface Analysis for Silicon Devices,
held at NBS, Gaithersburg, Maryland, April 23-24, 1975 (Issued March 1976)

ELECTRON BEAM INDUCED IMAGING OF SILICON SURFACES*

W. R. Bottoms

Department of Electrical Engineering
Princeton University
Princeton, New Jersey 08540

Modern electron optics can provide a focused beam of less than 100 angstrom units in diameter which may be swept across a sample in order to address any portion within the "field of view." This allows one to input energy to a well defined region and, by collecting the signals associated with the various energy relaxation processes which occur, an analysis of the structure of the sample with high spatial resolution can be undertaken. Figure 1 illustrates the primary signal channels which are activated by the electron beam with the principle type of analysis associated with each beam. The energy dissipated within the sample in terms of electron-hole pair production can be detected in an external circuit and images, associated with any process which alters the current measured in the external circuit, can be formed. The contrast mechanisms which are responsible for the images formed are listed in Table 1[1]. It is often difficult to determine which mechanism or which combination of mechanisms are responsible for the formation of a given image and, in an effort to deconvolute the various contributions to contrast, data is gathered from as many different sources as possible. Both C-V and G-V measurements are conducted to determine as fully as possible the effect of the incident beam and the various sample processing steps on the distribution of internal charge.

Electron beam induced imaging is carried out as a function of the incident beam voltage which can be related to the depth within the sample by the calculated range of the incident electron beam[2], Figure 2. Potential barriers of known depth within the sample also provide depth resolution since they contribute to the signal current by separating excess carriers generated by the incident beam. In addition, images are formed as a function of bias across the sample and processing history (principally the bias thermal stressing used to determine the number of mobile ions present and move them from one region of the sample to another).

The electron beam induced images of "bare" silicon surfaces and internal interfaces in MOS samples are analogous to the corresponding images which can be obtained using electromagnetic radiation as the exciting probe with two very important differences. The optical probe can be chosen so that the incoming beam does not see portions of the sample which are of little interest in a particular image[3] (i.e., the silicon-silicon dioxide interface can be probed with an optical beam of energy such that a signal is stimulated by internal photoemission at the interface but the oxide is transparent to the probing beam). In the case of electron beam excitation, it is possible to obtain images of interface structure associated with the excitation of secondary electrons across the potential barrier between the silicon and the oxide, as in internal photoemission, but this signal includes currents associated with all other interactions of the beam with the sample[4]. The various current components are convoluted and indeed, under most conditions, another imaging mechanism will dominate resulting in the reverse of the contrast obtained from the internal photoemission mechanism[5]. The result of this propensity of the electron to undergo energy exchange interactions which appear continuous rather than discrete (insofar as the scale of energy interactions of the experiment is concerned) limits the technique. Although the electron beam interacts much more strongly with the system under investigation and therefore is able to "see" events which could not be seen with optical or X-ray probes, this very density of information makes it difficult to deconvolute the contributions from various processes. The second important difference between the optical probe and the electron beam probe is that it is possible to generate an incident electron beam with a diameter more than an order of magnitude smaller than that of the optical probe and therefore, under many imaging conditions, provide a much higher spatial resolution with a similar improvement in the depth of field.

An example of the first of the contrast mechanisms listed in Table 1 is shown in Figure 3. This is the normal image which is derived from the scanning electron microscope (SEM) and it is a map of the topography of the

---

*Work supported by ARPA Contract No. F19678-72-C-0298.

sample as well as the variations in the plane of the secondary emission and reflection coefficients. An appropriate adjustment of incident beam parameters can give the situation where electrons of low energy are excited across the barrier between the gate metallization and the insulator in a MOS sample thus providing an image of the variations in the barrier height between the metal and the insulator. An example of such an image is shown in Figure 4. The structure has been attributed to local variations in barrier height due to mobile ion aggregation at the gate which was generated by bias thermal stressing of the sample. Figure 5 is an example of an image of the Si-SiO_2 interface. Variations in barrier height due to aggregation of Na ions at the interface are responsible for the structures in this image.

Figure 6 gives an example of image structure due to lateral nonuniformities in the charge stored in the insulator. In this case charge was stored selectively in some parts of the sample by the electron beam and the regions of bright and dark intensity with respect to the background showed that both positive and negative charge can be stored in the sample with the incident beam. This stored charge is an ever present artifact of the electron beam imaging technique and must be kept in mind when interpreting images formed in this manner.

When defect structures in a silicon sample cause local variations in recombination rates we can detect a signal due only to the change in the capacitance of the sample induced by the spatial variation of the charge.[1] This gives rise to the electron induced analog of the surface photovoltage mechanism[6]. Figure 7 shows stacking fault defects in a Si (111) crystal where the image formation has been attributed to this analog of the surface photovoltage technique. This image is of the Si-SiO_2 interface in an MOS capacitor. Figure 8 is an image of a "bare" silicon wafer which was mounted in the microscope with spring tension holding it between two flat metal plates. The natural oxide covering the silicon and the metal plates is of sufficient thickness to prevent large dc current flow across the sample and the ac signal is coupled out through the capacitor between the silicon and the top metal electrode. In this configuration the image is again attributed to the analog of the surface photovoltage mechanism.

CONCLUSIONS

The use of electrom beam induced images has been shown to be a powerful tool for the observation of subsurface and surface variations of electronic structure in silicon. Spatial resolution of the order of 1000 Å has been obtained for structure at an interface located several thousand angstroms below the surface. Structure located closer to the entrance can be imaged with even higher resolution since there is less spread of the incident beam. The electron beam can produce the analog of scanning internal photoemission and surface photovoltage images with better spatial resolution than is obtained for similar images induced by electromagnetic radiation. The major disadvantages of electron beam techniques are of cost and of the difficulty in deconvoluting the information obtained. We are, in most cases, only able to present models for the structural images which are consistent with our experiments. We are not able, at present, to make a unique determination of the mechanism responsible for a given image and therefore we cannot uniquely identify the structure. The ability to obtain images of defects on "bare" silicon has been demonstrated. This has important implications for developing technologies which place more rigid specifications on the starting semiconductor material such as high voltage power devices and large area CCD devices.

References

1. Bottoms, W. R., and Roitman, P., *Critical Reviews in Solid State Sciences* (in press).

2. Everhart, T. E., and Hoff, P. H., *J. Appl. Phys.* 42, 5837 (1971).

3. DiStefano, T. H., *Appl. Phys. Lett.* 19, 280 (1971).

4. Bottoms, W. R., and Guterman, D., *J. Vac. Sci. Tech.* 11, 965 (1974).

5. Bottoms, W. R., Guterman, D., and Roitman, P., *J. Vac. Sci. Tech.* 12, 134 (1975).

6. DiStefano, T. H., Photoemission and Photovoltaic Imaging of Semiconductor Surfaces, ARPA/NBS Workshop IV, *Surface Analysis for Silicon Devices,* A. G. Lieberman, Ed., NBS Spec. Publ. 400-23 (March 1976).

TABLE 1

SOURCES OF CONTRAST FOR ELECTRON BEAM INDUCED CURRENT IMAGES OF INTERNAL INTERFACES IN MIS STRUCTURES

* Variations in secondary emission and reflection coefficients at the sample/vacuum interface.

* Variations in the barrier height at the metal/insulator and insulator/semiconductor interfaces.

* Variation of the electric field within the insulating region resulting from interface barrier height changes.

* Local variations in the recombination/generation rates.

* Lateral nonuniformities in the charge stored within the sample.

* Local field variations resulting from topographic structure at the interface.

* Interface topography resulting in variation of the total energy dissipation within a given region.

SCANNING ELECTRON MICROSCOPE

MODES OF OPERATION

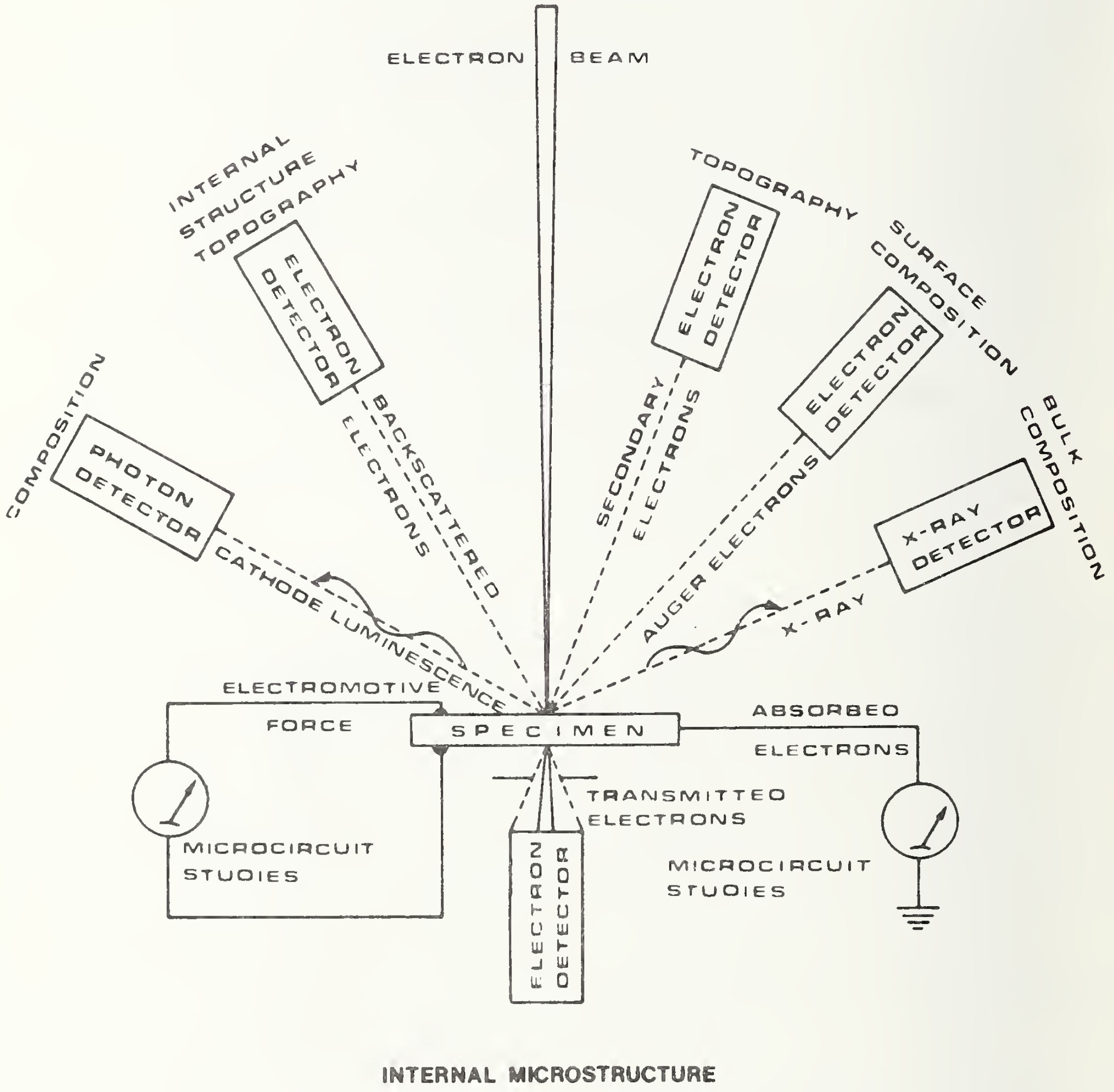

Figure 1. A schematic diagram illustrating the primary signal channels activated by an electron beam. The principle information contained in each signal is noted.

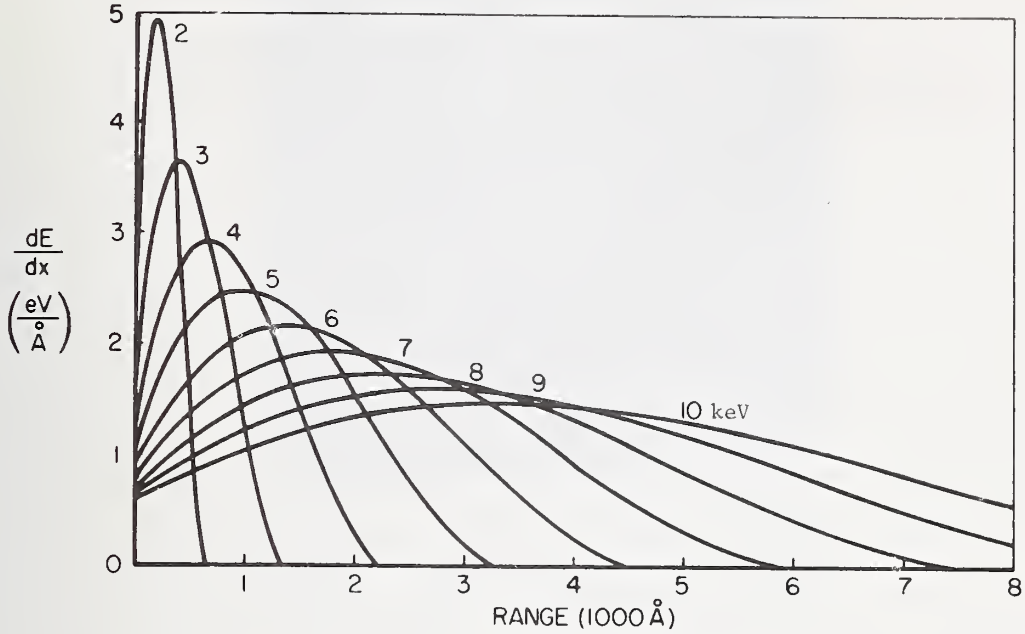

Figure 2. The rate of energy loss for electron beam penetration of Al-SiO_2-Si systems calculated using the Everhart-Hoff function.

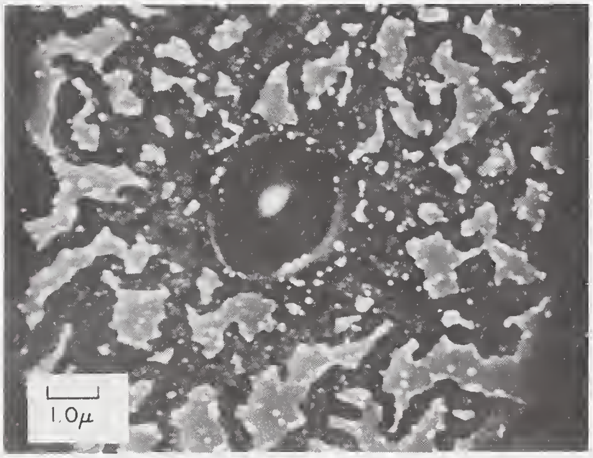

Figure 3. A conventional secondary electron image of a region on a MOS capacitor where a "self-healing" dielectric breakdown has occurred. The bright areas correspond to gate metallization not evaporated during breakdown.

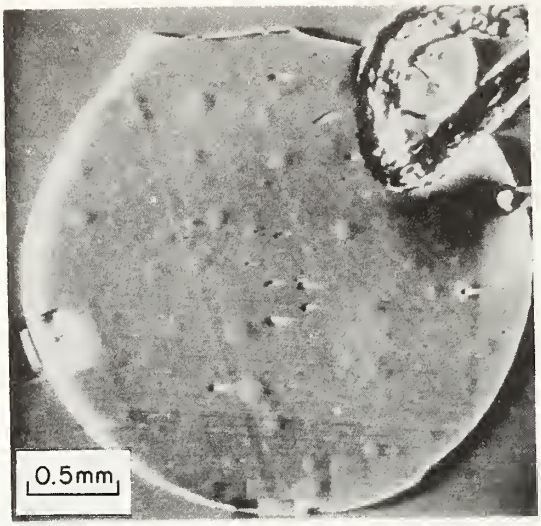

Figure 4. Interface image of the metal/insulator interface taken with a 2 Kev primary beam after BTS processing to drive mobile ions to the gate.

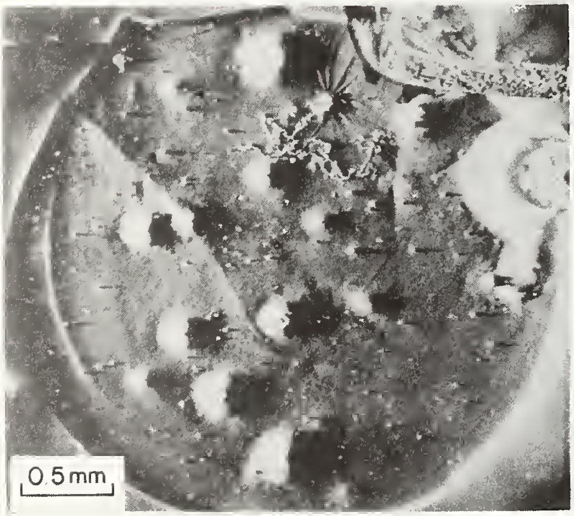

Figure 5. Interface image of the insulator/semiconductor interface taken on the same capacitor as in Figure 4 after additional BTS processing to drive the mobile ions to the insulator/semiconductor interface. This image was formed with a primary beam energy of 6 Kev.

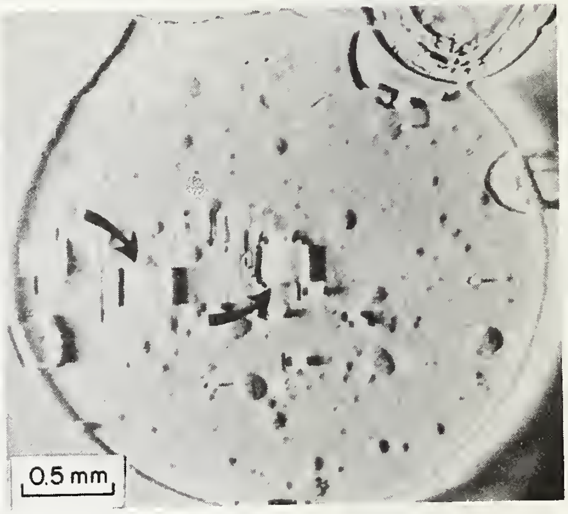

Figure 6. Interface image of the metal/insulator interface taken on the same capacitor with the same imaging conditions as in Figure 4 after it had been subjected to nonuniform electron beam irradiation. Image detail due to the resulting nonuniformity in stored charge is indicated.

Figure 7. An image of the insulator/semiconductor interface of an MOS capacitor taken with a 30 Kev primary beam. The defects visible with definite crystallographic orientation are attributed to stacking faults.

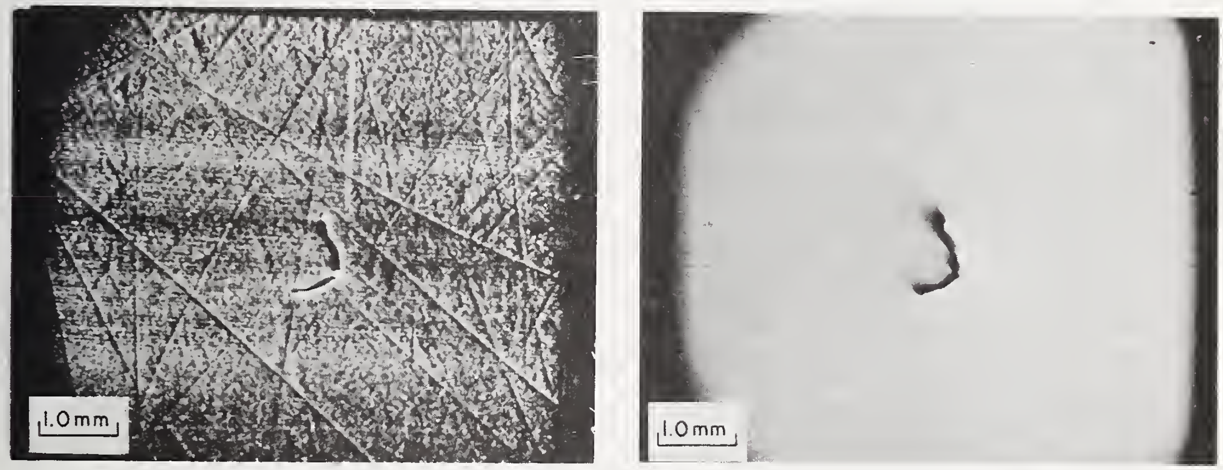

Figure 8. Electron beam induced images of a "bare" (111) oriented, 150 Ω-cm, p-type silicon wafer which has been mechanically polished. a) analog of the surface photovoltage image showing residual polishing damage on the wafer. b) conventional secondary electron image of the same area of the sample showing the topography of the surface.

DISCUSSION OF THE PAPER

Participant: Do you see exactly the same sort of phenomena in SiO_2 that Tom DiStefano had mentioned earlier regarding the use of photoemission and photovoltaic imaging?

Bottoms: Yes, we do see exactly the same things. For instance, there seems to be a correlation between those stacking fault defects that occur after processing and oxygen content as well as some metal content in the material. There is no disagreement in our data. Tom has more data that is tied to a production line than I do. I do not have a production line.

Participant: Do you share his inferences?

Bottoms: I am not sure of that. They are consistent with everything we know. We have samples not from IBM processes, but where the chemical processes were altered and the alteration in the images related to the chemical process alterations in the way consistent with everything Tom was talking about. We only have consistency but not specificity.

NBS Special Publication 400-23, ARPA/NBS Workshop IV, Surface Analysis for Silicon Devices,
held at NBS, Gaithersburg, Maryland, April 23-24, 1975 (Issued March 1976)

A COMPARISON OF THE TECHNIQUES FOR SILICON SURFACE ANALYSIS*

Charles A. Evans, Jr.

Materials Research Laboratory
University of Illinois
Urbana, Illinois 61801

This paper will summarize the five chemical analytical techniques that are most widely used to characterize surfaces and thin films in the silicon technology area. These are Auger Electron Spectroscopy (AES), Electron Spectroscopy for Chemical Analysis (ESCA), Ion Scattering Spectrometry (ISS), MeV on Backscattering Spectrometry (BS), and Secondary Ion Mass Spectrometry (SIMS) commonly referred to as the ion probe.

Because of space limitations, concepts rather than specifics will be discussed. As such, there will be exceptions to these generalizations. Sensitivities may be worse or may be better by a factor of two or three in certain circumstances. The most important conclusion to make is that every technique has its advantages and its limitations in a specific analytical feature. More importantly, the solution to a particular analytical problem may require the application of more than one of these techniques. So it is important to see how these techniques interdepend, interrelate, and compliment each other.

The first question that is generally asked about a technique is "What is its elemental sensitivity?" In Table 1 the five techniques are characterized in four features of elemental sensitivity:

1. Coverage - All of the techniques can detect from lithium to uranium (i.e., almost full periodic coverage). In addition the SIMS technique can detect hydrogen. This is a definite advantage. In terms of silicon technology, it could be very important to determine the role of hydrogen which may be coming from CVD processes, what is happening to it and how does it enhance or reduce diffusion, reactions, etc., in a thin film.

2. Specificity - This is the ability of the technique to resolve different elements, either as it is limited by the intrinsic nature of the technique or in terms of spectral interferences which can be encountered and reduce the ability to see a given element. Auger electron spectrometry has a reasonable specificity; intrinsically it can detect every element but hydrogen and helium. However, specific interference situations are encountered. Backscattering spectrometry specificity is definitely dependent upon the mass of the element. At low mass this technique provides good resolution, however, resolution decreases as one goes to higher mass. It becomes difficult to tell tungsten from gold in certain circumstances. ESCA has good specificity much as the AES technique. Ion scattering spectrometry exhibits much the same situation as MeV backscattering. As long as the probing particle mass is of the order of the target particle, good resolution is obtained. However, as the target atom mass greatly exceeds that of the probing ion, spectral resolution decreases. The SIMS technique has very good specificity. In particular, it gives isotopic detection capability which might be useful in self-diffusion studies.

3. Sensitivity - Sensitivity variations are very important in considering a technique since this affects the ability to relate the analytical signal to the concentration of that element. The two electron techniques, AES and ESCA, have only a factor of 10 variation from the least sensitive to the most sensitive element with perhaps a little bit more variation in ESCA. In BS there is a pronounced, but predictable, variation in sensitivity with atomic number. From bismuth to oxygen, a factor of about a hundred in sensitivity is lost. Over this same range, ISS suffers a sensitivity variation of about a factor of five. The SIMS technique has the largest variation in elemental sensitivity. Four to five orders of magnitude in variation of sensitivity is encountered between the least sensitive and the most sensitive element.

4. Detection limits - Auger electron spectrometry sensitivity is about 10^{-3} atomic fraction. Large variations in detection limits are encountered in backscattering spectrometry between lithium and uranium. The ESCA technique has average detection limits between 10^{-3}

---

*Supported in part by National Science Foundation Grants MPS-74-05745 and DMR-72-03026.

and 10^{-2} atomic fraction. Ion scattering spectrometry has an average detection limit of 10^{-2}. SIMS detection limits vary from 10^{-4} to 10^{-8} atomic fraction.

Figure 1 summarizes the detection limits in an interference free situation for the different techniques. This figure shows that there is a periodic dependence of detection limit on atomic number in the SIMS technique. It should be noted that these detection limits are for positive secondary ion spectrometry. Negative ion spectrometry with Cs^+ ion bombardment provides a reversal of these curves such that many of the less sensitive elements become the most sensitive. Backscattering spectrometry has a smooth curve which provides detection limits approximately 10^{-4} in the case of bismuth. Auger electron spectrometry is essentially atomic number independent. Thus AES detection limits are best related as a broad band across the periodic table with about 10^{-3} to 10^{-2} atomic fraction for detection limits. ESCA exhibits a periodicity whereas ion scattering has a smooth curve much the same shape as high energy backscattering but with somewhat poorer detection limits.

There are two important features to these data. Doping levels in semiconductors are at the 10^{-3} atom fraction ($\sim 10^{19}$ atoms/cm^3) and go to lower concentrations. Therefore, if the analyst is to look at doping levels there is really only one technique that is able to provide elemental identification and chemical concentration - the SIMS technique. Secondly, it is commonly assumed SIMS is quite subject to spectral interferences. However, the technique has tremendous sensitivity for many of the elements, and interferences do not become a problem above the 10^{-3} level. So the possibility for spectral interferences in SIMS does not generally occur until the concentration is below the detection limits of the other techniques. More recently, high mass resolution SIMS instruments have become available, and even in interference situations very good detection limits can be realized. As one goes to high mass resolution, these doping level detection limits can still be realized.

Another important aspect of any analytical technique is the matrix effects that are encountered, and these are summarized in Table 2. As has been discussed during the whole conference, AES is subject to matrix or chemical shifts. These generally occur only for a few elements, and they have become quite useful in characterizing certain types of compounds. Backscattering is a nuclear process and exhibits no matrix effects. In ESCA chemical shifts are the justification for the technique. So chemical effects and matrix effects are very important in ESCA and are the key to the technique. ISS does exhibit some matrix effects. This dependence on the matrix results from the matrix influence on ion neutralization. Differences in intensities are encountered for the same concentration when going from one matrix to another because of probing ion neutralization. In SIMS, matrix effects are quite often found. Researchers are trying to use them to understand compound presence or absence in materials, but at the present time they are generally considered a nuisance.

Since the amount of sample for analysis may be limited, the alteration or consumption of material during analysis can be important. As seen in Table 3, the only truly nondestructive technique for depth profiling is high energy backscattering. It is nonconsumptive in all modes. However, radiation damage of organic material can result. If channeling experiments are done to determine radiation damage during an implantation, interstitial versus lattice locations in silicon, etc., there can be alteration of the sample with respect to these aspects upon extended exposure of the sample to the probing beam. The remainder of the techniques break down into two areas. The first area includes those techniques which are nondestructive during the analytical process, i.e., the AES and ESCA techniques, but must use ion etching in order to perform depth profiles. Again, there must be concern about radiation damage; electron impact desorption can be quite important with AES. ESCA is less subject to radiation damage in the analytical mode when sensitive materials are examined. In the second area, ISS and SIMS consume sample material in all modes. Even though helium ions may be used for low sputtering rates during the analytical step, there will still be some material sputtered, and one must be aware of this at all times.

Now, combining all of the above factors, how does one make these techniques quantitative? As seen in Table 4, none of the techniques except backscattering are quantitative on an absolute basis. Only for the backscattering technique can a sample be analyzed using no standards. From the data, quantitation in both concentration and in the depth scale can be provided. There is no dependence on the sputtering rates. The use of standards in BS can improve quantitation from about 5% to about the 2% level. Standards are required by all the other techniques: AES, ESCA, ISS, and SIMS. Obviously, one would hope to remove the requirement for standards and start using some sort of mechanistic or fundamental approach in order to quantitate the other four techniques. Quantitation procedures are just beginning in Auger. The author is not familiar with any quantitation or mechanistic approach to quantitation in ESCA. In the ISS technique, known scattering cross sections for two different elements can be used to determine relative concentration by the application of these known scattering cross sections. In SIMS, some work is being done in terms of mechanistic approaches. The most successful process gives ± 200% (that is, a factor of 2) in almost every case and in many cases gives quantitation in the ± 20% range.

As was implied above, another important point of quantitation is the ability to quantitatively locate a particular subsurface feature within the sample. Only the backscattering technique can provide this on an absolute basis. As an example, Fig. 2 shows the energy loss observed versus the thickness as calibrated by a variety of other techniques for a tantalum oxide matrix [1]. The points shown are actual data points, but the curves are not best fits. These are theoretical curves - two with a depth correction and one assuming just a straight linear approximation. Two different densities were used since the density is required. As is seen, the theoretical calculation fits very well with the data points for a variety of tantalum oxide films as thick as 5,000 angstroms. This is a very, very important aspect of the backscattering technique. It does provide absolute calibration of the thickness of the layers in a multilayer film. The as-deposited thickness of a film may be known, but the annealed structure can only be characterized by one of these analytical techniques. Only backscattering spectrometry can provide this information without need for sputtering rate calibration.

It is very important in actual device characterization and in debugging a product line to be able to perform chemical analyses with high lateral resolution (< 10 μm). Those techniques that provide microanalysis are the AES technique with a microfocussed primary electron beam, the SIMS technique with a microfocussed ion beam, i.e., the ion microprobe, or SIMS with a stigmatic mass spectrometer, i.e., the ion microscope. "Milli-analysis" is now available with ISS using 0.1 mm diameter probing ion beams. Macroscopic area analysis is provided by the backscattering technique since a one millimeter probing beam is generally used. There is one instrument available with a one to ten micrometer beam for backscattering [2]. It is a highly specialized instrument and very time consuming in its operation. ESCA usually illuminates rather large areas. People do work with masks to reduce X-ray illumination areas in order to obtain local analysis, but it still remains a macroscopic technique. Table 5 summarizes the lateral analytical features of these five surface analytical techniques.

Examination of the two microanalytical techniques reveals that there is a very intimate interrelationship between the detection limit that can be realized and the probe, or analytical, area being used as illustrated in Fig. 3. The detection limits for Auger electron spectrometry decrease as a smaller probe is used. This results from a smaller exciting current available at the smaller diameters. In this instance, the fall-off begins at about 10 μm diameter. Unfortunately going to larger probes and hence larger currents does not provide detection limits better than about 0.1% atomic. Such an effect is observed since the sensitivity is detector limited in the AES technique. However, with the ion probe technique, since material is consumed and the technique is not detector limited, the volume consumed determines the number of ions that are available for analysis. Thus there is an interrelationship between the realizable detection limit and the probe area. Given the assumptions shown in the box of Fig. 3, the larger the analyzed area, the better are the detection limits for SIMS. The attainable limits will vary depending on the ion yield of the different elements. For the sensitive elements such as aluminum and iron, the ion probe technique (for all probe sizes) is much more sensitive than Auger. However, as elements with lower yields are analyzed, the ion probe may be more or less sensitive than Auger depending on the available analytical area. Before one can choose Auger or SIMS for a microanalysis, the relative sensitivity of the sought-for element and the analytical area must be considered.

As has been discussed, all of these techniques provide an in-depth analytical capability. Backscattering spectrometry samples all depths simultaneously and, therefore, gives an instant readout of all depths as well as chemical identification. The other techniques — — AES, ESCA, ISS and SIMS — — require ion sputtering with the analytical excitation in order to realize a depth profile. When using the sputtering techniques one must be concerned about a variety of artifacts which can distort the analytical information. One must be concerned about how the sputtering process distorts the chemical information provided by ESCA. Is the ion beam going to damage the sample so that it is no longer in the same chemical state it was before? Under reasonable conditions, the sputtering process can provide remarkable results. We have been able to detect with both AES and SIMS a 5 angstrom layer of antimony under 8,000 angstroms of amorphous silicon. Even after diffusion we were able to detect the antimony. Sputtering in either amorphous or in single crystal situations is not a particular problem. It is only when polycrystalline, compound or multi-phase systems are sputtered that one can run into problems. Depth resolution in the backscattering technique is controlled by detector resolution and energy straggling in the sample. Whereas in all the techniques employing sputtering, the controlling parameters are the flatness of the crater, differential sputtering, "knock-on" of atoms into deeper layers, and the need to calibrate the sputtering rate. This latter point is quite important because somehow time must be converted into distance. Table 6 summarizes the concepts and concerns to be considered in depth profiling.

If the analyst is required to depth profile a large volume of thin films, he must be concerned about analytical time and system turnabout. Table 7 compares the five techniques in the time required to depth profile a 5000Å film. Backscattering is very fast. All accessible depths are sampled simultaneously, and the vacuum requirements are minimal. It is not a monolayer surface analytical technique but really a technique for chemical and compositional analysis of multilayer thin films. The time for a 5,000 angstrom film is 10 or 15 minutes. Since the analytical time is independent of thickness, the same time would be required for a 1,000 or 10,000 angstrom film. Backscattering spectrometry is the fastest technique for depth profiling thick films (or thin films depending on your definition). The SIMS technique is also generally quite fast. The use of sample carousel systems or vacuum interlocks provides fast sample turnaround times. Approximately 10 to 15 minutes would be required for this 5,000 angstrom film since sputtering rates of 300 to 500 angstroms per minute are attainable. However, to realize this type of efficiency, a computer or multichannel analyzer data system must be employed. AES is generally slow in its turnaround time since vacuum compatibility with the analytical process is required and the spectrometer must be calibrated for every sample. The sputtering rates employed in AES can approach those of SIMS. However the analyst must be somewhat careful if he wishes to monitor subtle changes in concentration because it takes a finite amount of time to measure Auger peak height or SIMS ion intensity. Thus depth resolution can be reduced if sputtering rates are too large. The ESCA and ISS techniques are very slow in their turnaround time because of the low signal to noise encountered, which implies a very slow sputtering rate. They are not amenable to the depth profiling of very thick films. They are, of all of these techniques, the true surface analytical techniques. They are not intended for, or amenable to, thick film depth profiling.

Several general conclusions (Table 8) can be made about these techniques. Auger is a good technique with its sensitivity to low Z elements, minimum matrix effects, and microanalytical capability. Backscattering, most importantly, is fast as well as being quantitative in concentration and depth. This is extremely important in the characterization of thin films. Unfortunately, it has very poor sensitivity for low Z elements and has poor lateral resolution. The most outstanding feature of ESCA is its chemical information. The outer monolayer analysis capability of ISS is its distinguishing feature. SIMS has ppm detection limits for almost all the elements, provides isotopic resolution, is fast and is a microanalytical technique. As far as disadvantages are concerned, ESCA has poor detection limits, poor lateral resolution and very slow profiling time. ISS has low sensitivity, poor lateral resolution and slow profiling. The limitations of SIMS are the troubles with quantitation and the matrix effects encountered.

The most important conclusion from the above discussion is that complete characterization of a system may well require more than one of the above techniques. Joint research on reactions and transport in thin films with M-A. Nicolet and J. W. Mayer of Caltech has evolved a multi-technique approach to the characterization of thin film systems as illustrated in Fig. 4.

Every sample is subjected to a backscattering analysis. A large number of samples per unit time can be characterized in this manner. If we wish to do additional in-depth profiling, we then go to AES because of its low Z element capability. This is to supplement the BS analysis to provide the major and minor element overview and depth scale calibration. If we must go to low concentrations for impurities and dopants, we then go to SIMS. If they were available to either laboratory, we would use ISS for outer monolayer analysis and ESCA for chemical information. We do not have these two techniques but they are in the figure for prospective. If we require lateral analysis after the backscattering analysis, scanning Auger microscopy or the ion microprobe is used. We find more and more it has become necessary to begin to look at structural information because of transport, precipitation, etc., when we are studying reactions. So structural information is provided by using optical microscopy for morphology or an SEM (with X-ray detection for elemental characterization). If we wish to do microstructure phase identification or crystal quality, we go to transmission electron microscopy and use X-ray diffraction for macrophase identification.

For other perspectives of the relative features of these techniques and the instrumentation required the reader is referred to references [3-7].

LITERATURE CITED

1. Chu, W. K., Nicolet, M-A., Mayer, J. W., and Evans, Jr., C. A., *Analytical Chemistry* 46, 2136 (1974).
2. Cookson, J. A., and Pilling, F. D., *Thin Solid Films* 19, 381 (1973).
3. Coburn, J. W., and Kay, E., *CRC Critical Reviews in Solid State Sciences* 4, 561 (1974).
4. Honig, R. E., Surface,and Thin-Film Analysis of Semiconductor Materials, *Thin Solid Films,* 1975 (to be published).
5. Evans, Jr., C. A., *J. Vac. Sci. Technol.* 12, 144 (1975).
6. Evans, Jr., C. A., Surface and Thin Film Compositional Analysis - A Description and Comparison of Techniques, *Anal. Chem.* Feature article (August, 1975).
7. Evans, Jr., C. A., Instrumentation for Surface and Thin Film Analysis, *Anal. Chem.*, Instrumentation article, (August, 1975).

TABLE 1

ELEMENTAL SENSITIVITY

	Technique	Coverage	Specificity	Sensitivity Variation	Detection Limits (Atomic Fraction)
1.	Auger Electron Spectrometry (AES)	Li-U	Good	Less than a factor of 10	10^{-3}
2.	MeV Ion Backscattering Spectrometry (BS)	Li-U (2 MeV $^4He^+$)	Lo Z-Good Hi Z-Poor	Sensitivity increases with Z (BI/O $\gtrsim$ 100)	10^{-1} - 10^{-4}
3.	Electron Spectroscopy for Chemical Analysis (ESCA)	Li-U	Good	Less than a factor of 10	10^{-2} - 10^{-3}
4.	Ion Scattering Spectrometry (ISS)	Li-U	Small $\frac{M}{m}$ -Good Large $\frac{M}{m}$ - Poor	Sensitivity increases with Z (BI/O $\gtrsim$ 5)	$\sim 10^{-2}$
5.	Secondary Ion Mass Spectrometry (SIMS)	H-U	Good (also provides isotopic detection)	Depends on ionization efficiency 10^4 - 10^5	10^{-4} - 10^{-8}

TABLE 2

MATRIX OR CHEMICAL EFFECTS

	Observed	Extent	Comment
1. AES	Yes	Few Elements	Generally useable
2. BS	No	—	—
3. ESCA	Yes	All Elements	Basis & justification for technique
4. ISS	Yes	Depends on matrix	Influences extent of ion neutralization
5. SIMS	Yes	Often	Can be used but is generally a nuisance

TABLE 3

SAMPLE CONSUMPTION and/or ALTERATION

1. Non-destructive in all modes
   a. BS (can get radiation damage of organics and in channeling studies)

2. Non-destructive during analysis
   Destructive for depth profiles

$$\left.\begin{array}{l}\text{a. AES}\\ \text{b. ESCA}\end{array}\right\}\text{ may get radiation (}e^{-}\text{ or }h\nu\text{) damage}$$

3. Sample consumed for all modes
   a. ISS - sputtering rates may be slow with $^4He^+$
   b. SIMS - volume of material available controls elemental sensitivities

TABLE 4

QUANTITATION (CONCENTRATION & DEPTH SCALE)

	Absolute	Standards	Mechanistic Procedures
1. AES	No	Needed	Just beginning
2. BS	Yes (± 5%)	Help in some cases (± 2%)	Permits absolute quantitation
3. ESCA	No	Needed	———
4. ISS	No	Needed	Can use known scattering cross-section for relative concentration information
5. SIMS	No	Needed	Most successful gives ± 200% in almost all cases ± 5-20% in many cases

TABLE 5

LATERAL ANALYSIS

1. Microanalysis (≤ 10 μm resolution)
   a. AES via microfocused primary electron beam
   b. SIMS via microfocused primary ion beam (ion microprobe) or stigmatic secondary ion optics (ion microscope)
2. Millianalysis (∼ 0.1 mm resolution)
   a. ISS with millifocused primary ion beam
3. Macroscopic area (≥ 1 mm resolution)
   a. BS generally uses 1 mm probing beams
   b. ESCA illuminates large areas (> 1 mm^2) with x-rays

TABLE 6

IN-DEPTH PROFILING ANALYSES

1. Backscattering spectrometry samples all depths simultaneously

2. AES, ESCA, ISS & SIMS require ion sputtering for sequential layer removal

CONCERNS WITH SPUTTERING

a. Analytical signal must come from flat-bottomed part of crater

b. Must be aware of sputtering artifacts
    1. Preferential removal of one element over another
    2. Crystallinity effects
    3. Sample may be multi-phase

TABLE 7

TIME REQUIRED FOR DEPTH PROFILES

		Turnaround Time	Time for 5000 Å Film	Comment
1.	BS	Fast (due to minimal vacuum requirements)	10-15 min. (independent of film thickness)	Fastest technique for depth profiles
2.	SIMS	Generally fast	10-15 min. (300-500 Å/min.)	Need automation to realize best efficiency
3.	AES	Generally slow (due to vacuum requirements & need to calibrate spectrometer)	25-30 min. (150-200 Å/min.)	Need automation to realize best efficiency
4.	ESCA & ISS	Generally slow (due to vacuum requirements)	Not suited to profiling of thick layers due to low signal-to-noise which requires very slow sputtering rates. (1-10 Å/min.)	

TABLE 8

CONCLUSIONS

		Advantages	Disadvantages
1.	AES	a. Sensitivity to low Z	a. Difficult to quantitate
		b. Minimal matrix effects	b. 0.1% detection limits
		c. Microanalysis	
		d. Good all around technique	
2.	BS	a. Fast	a. Low sensitivity especially for low Z
		b. Quantitative in conc and depth	b. Poor lateral resolution
3.	ESCA	a. Chemical information	a. 0.1% detection limits
			b. Poor lateral resolution
			c. Slow profiling
4.	ISS	a. Outer monolayer analysis	a. Low sensitivity
			b. Poor lateral resolution
			c. Slow profiling
5.	SIMS	a. ppm detection limits for many elements	a. Quantitation and matrix effects
		b. Isotopic resolution	
		c. Fast	
		d. Microanalysis	

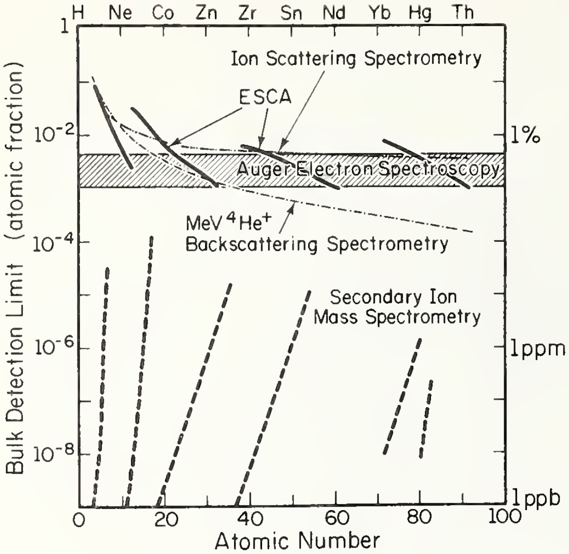

Figure 1. A comparison of bulk detection limits vs. atomic number for five surface sensitive analytical techniques.

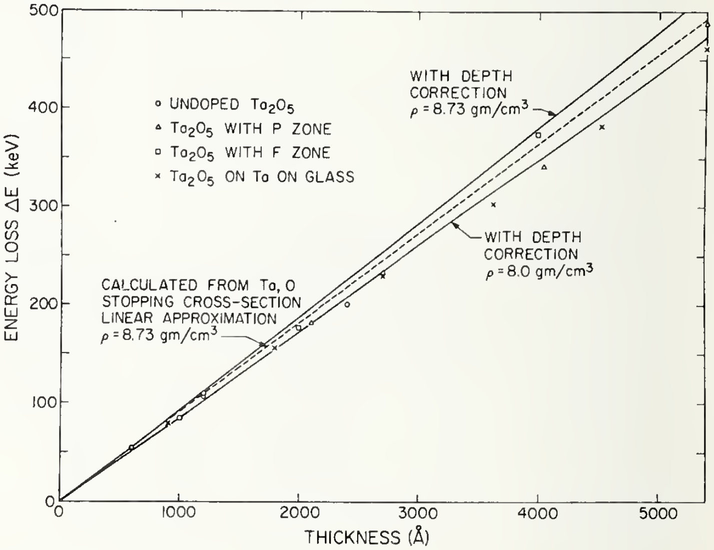

Figure 2. Energy loss by $^4He^+$ in Ta_2O_5 vs. known thickness. Curves represent various calculated relationships.

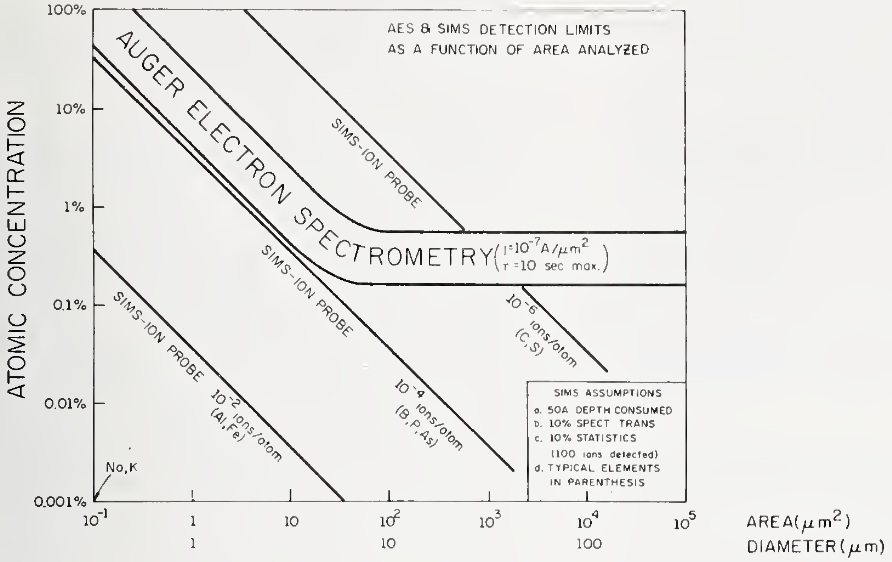

Figure 3. Calculated detection limits vs. analytical area for AES and SIMS.

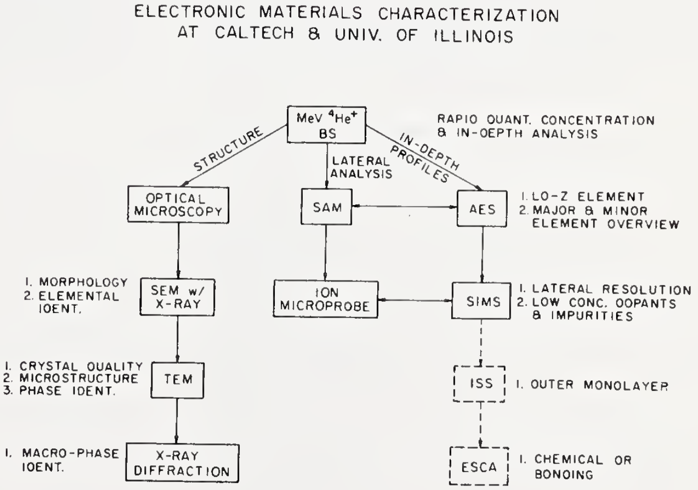

Figure 4. Flow chart for electronic materials characterization at the California Institute of Technology and the University of Illinois.

DISCUSSION OF THE PAPER

Participant: In one of the slides you show sensitivity vs beam diameter for Auger and SIMS, where does the hydrogen sit on that diagram?

Evans: If you remember in the beginning we excluded hydrogen as being unobservable by the Auger. As far as SIMS is concerned, we are not really sure. I am only familiar with the work in our own laboratory on hydrogen and we have not really been looking at low levels. We have been looking at the formation of niobium hydride in hydrogen charged niobium. I would guess the ionization yield for H probably sits between 10^{-4} and 10^{-6} ions/atom and as such H appears in the middle of the diagram.

Newbury: Is it worth mentioning that with the selection of the primary ion beam you might, in fact, get enhanced sensitivity from say, gold, carbon, or sulphur by possibly using a cesium beam? It is possible by selection of your beam to improve the situation.

Evans: Hughes and other laboratories are developing cesium ion sources for ion microprobes. If you do use cesium ion bombardment and negative ion spectroscopy instead of oxygen ion bombardment and positive ion spectroscopy, those elements such as gold, carbon, etc., which used to be very insensitive are now very sensitive. In fact, in positive ion spectroscopy sodium is the most sensitive element, in negative ion spectroscopy using cesium ion bombardment gold is probably the most sensitive element. So as instrument developments come along we may find improvements in the Auger curve but there will definitely be a dramatic improvement in the SIMS curves as soon as a good cesium ion source is developed.

Lucke: You mentioned one of the disadvantages of SIMS was quantitation. I wonder what you could say about the possibilities of eventually obtaining absolute concentration numbers.

Evans: There are laboratories working on the fundamentals of the secondary ionization process. The most successful of the resultant techniques are those used by Anderson, and Anderson and Hinthorn. Basically, they try to calculate what the conditions are in the ionization region. They assume that it is a plasma in local thermal equilibrium. Then the actual concentrations are calculated from the assumed ionization conditions and the measured secondary ion intensities.

Lieberman: The alternative approach toward quantitation is to develop working curves based on measurements of reference materials having elemental concentrations similar to those of the unknown sample. The Electronic Technology Division of NBS is endeavoring to develop and document techniques for the application of SIMS to silicon material and device analysis. This work includes the development of methods of sample preparation and data analysis for reliable quantitative SIMS analysis of impurities on silicon and silicon dioxide surfaces.

WORKSHOP PARTICIPANTS

John Albers
National Bureau of Standards
Washington, DC 20234

Gordon Anderson
Naval Research Laboratory
Washington, DC 20375

James Anthony
National Security Agency
Fort Meade, MD 20755

Donna Bakale
Varian Vacuum
Springfield, NJ 07081

W. D. Baker
Naval Research Laboratory
Washington, DC 20375

William R. Bandy
National Security Agency
Fort Meade, MD 20755

Robert Barr
Technics Inc.
Alexandria, VA 22310

Lt. Richard Bernard
Rome Air Development Center
Griffiss Air Force Base
Rome, NY 13440

J. B. Bindell
Bell Telephone Laboratories, Inc.
Allentown, PA 18103

W. R. Bottoms
Electrical Engineering Department
Princeton University
Princeton, NJ 08540

M. G. Buehler
National Bureau of Standards
Washington, DC 20234

James W. Butler
Naval Research Laboratory
Washington, DC 20020

Sidney R. Butler
Lehigh University
Department of Metallurgy and Materials
Science
Bethlehem, PA 18015

Robert C. Cargill
Physical Electronics Industries, Inc.
Eden Prairie, MN 55343

Forrest L. Carter
Naval Research Laboratory
Washington, DC 20034

Thomas R. Cass
Hewlett-Packard Laboratories
Palo Alto, CA 94304

Jar-Mo Chen
Martin Marietta Laboratory
Baltimore, MD 21227

A. Christou
Naval Research Laboratory
Washington, DC 20375

Thomas E. Cody
Applied Research Laboratories
Allentown, PA 18101

Donald K. Conley
Western Electric Company
Allentown, PA 18103

Dwight Cook
Bell Telephone Laboratories
Murray Hill, NJ 07974

Lawrence P. Cook
National Bureau of Standards
Washington, DC 20234

Becky P. Corbin
Commonwealth Scientific Corporation
Alexandria, VA 22314

Howard S. Danaceau
The Kearns Group
Rockville, MD 20850

David Darbo
NASA Goddard Space Flight Center
Greenbelt, MD 20771

John E. Davey
Naval Research Laboratory
Washington, DC 20375

L. E. Davis
Physical Electronics Industries, Inc.
Eden Prairie, MN 55343

Howard M. Day
Naval Research Laboratory
Washington, DC 20390

Bruce E. Deal
Fairchild Semiconductor
Palo Alto, CA 94304

T. H. DiStefano
IBM Research
Yorktown Heights, NY 10598

Robert D. Dobrott
Texas Instruments, Inc.
Dallas, TX 75222

L. G. Dowell
Union Carbide Corporation
Tarrytown, NY 10591

Kenneth L. Dunning
Naval Research Laboratory
Washington, DC 20375

John W. Dzimianski
Westinghouse Electric Corp., S.D.D.
Baltimore, MD 21203

James Ehrstein
National Bureau of Standards
Washington, DC 20234

Nils E. Erickson
National Bureau of Standards
Washington, DC 20234

Charles A. Evans, Jr.
Materials Research Laboratory
Urbana, IL 61801

R. J. Farrar
Harry Diamond Laboratories
Washington, DC 20438

Frank J. Feigl
Department of Physics
Lehigh University
Bethlehem, PA 18015

Charles Feldman
The Johns Hopkins University
Silver Spring, MD 20910

David File
Cameca, Inc.
Elmsford, NY 10523

Judson C. French
National Bureau of Standards
Washington, DC 20234

Bill Gadzuk
National Bureau of Standards
Washington, DC 20234

Kenneth Galloway
National Bureau of Standards
Washington, DC 20234

Anthony J. Garratt-Reed
Massachusetts Institute of Technology
Cambridge, MA 02139

Richard Gerber
Aerospace Corporation
Los Angeles, CA 90009

Louis F. Giles, III.
National Security Agency
Fort Meade, MD 20755

Michael N. Giuliano
Westinghouse/Advanced Technology Laboratory
Baltimore, MD 21203

Ralph Gorden, Jr.
National Bureau of Standards
Washington, DC 20234

Leonard P. Grady
Deltaray Corporation
Burlington, MA 01803

Edward T. Graney
Physical Electronics Industries, Inc.
Springfield, NJ 07090

Henry F. Gray
Naval Research Laboratory
Washington, DC 20375

Frank Grunthaner
Jet Propulsion Laboratory
Pasadena, CA 91103

George A. Haar
Naval Research Laboratory
Washington, DC 20375

Hiroshi Harada
University of West Lafayette
West Lafayette, Indiana 47907

W. L. Harrington
RCA Laboratories
David Sarnoff Research Center
Princeton, NJ 08540

James K. Hirvonen
Naval Research Laboratory
Washington, DC 20375

H. Ward Huang
IBM Corporation
Essex Junction, VT 05452

H. Hughes
Naval Research Laboratory
Washington, DC 20375

James M. Hurd
Tektronix Inc.
Beaverton, Oregon 97077

Harry M. Hyman
RCA Corporation
Somerville, NJ 08876

N. L. Jarvis
Naval Research Laboratory
Washington, DC 20375

Marilyn A. Jasper, FIR
Night Vision Laboratory
Ft. Belvoir, VA 22060

Murzban Jhabvala
NASA Goddard Space Flight Center
Greenbelt, MD 20771

Jan S. Johannessen
Stanford Electronics Laboratory
Stanford University
Stanford, CA 94305

Phil F. Kane
Texas Instruments Inc.
Dallas, TX 75222

W. J. Keery
National Bureau of Standards
Washington, DC 20234

G. J. King
Army Night Vision Laboratory
Alexandria, VA 22307

T. D. Kirkendall
Comsat Laboratories
Clarksburg, MD 20734

W. J. Kitchen, Jr.
Department of Defense
Ft. Meade, MD 20755

Bruce E. Knox
Penn State University
University Park, PA 16802

Robert J. Kopp
Fairchild Camera and Instrument Corporation
Mountain View, CA 94040

Ram Kossowsky
Westinghouse Research
Pittsburgh, PA 15235

R. Koyama
National Bureau of Standards
Washington, DC 20234

Francis Kub
Westinghouse ATL
Baltimore, MD 21203

Chris Kuyatt
National Bureau of Standards
Washington, DC 20234

Alan J. Kushnir
Semi-Films
West Hurley, NY 12491

Max G. Lagally
University of Wisconsin
Madison, WI 53706

G. M. Lamb
NASA Goddard Space Flight Center
Greenbelt, MD 20771

Donald E. Lander
AEI Scientific Apparatus, Inc.
Falls Church, VA 22043

Graydon B. Larrabee
Texas Instruments Inc.
Dallas, TX 75222

K. O. Leedy
National Bureau of Standards
Washington, DC 20234

T. F. Leedy
National Bureau of Standards
Washington, DC 20234

Douglas H. Leong
Hughes Aircraft Company
Newport Beach, CA 92663

Leonard L. Levenson
University of Missouri-Rolla
Rolla, MO 65401

Miguel E. Levy
Hughes Aircraft Company
Culver City, CA 90230

Robert K. Lewis
Cameca Instruments, Inc.
Elmsford, NY 10523

A. G. Lieberman
National Bureau of Standards
Washington, DC 20234

Wen N. Lin
Rockwell International Corporation
Anaheim, CA

Y. Liu
National Bureau of Standards
Washington, DC 20234

W. H. Lucke
Naval Research Laboratory
Washington, DC 20735

Fred Luehrs
Tousimis Research Corporation
Rockville, MD 20852

Ingemar Lundstrom
IBM Corporation
Yorktown Heights, NY 10589

Gary McGuire
Texas Instruments, Inc.
Dallas, TX 75222

R. M. McLouski
Westinghouse
Baltimore, MD 21203

Joseph F. Martino
Night Vision Laboratory
Ft. Belvoir, VA 22060

Santos Mayo
National Bureau of Standards
Washington, DC 20234

David M. Metz
Penn State University
University Park, PA 16802

Reid A. Mickelsen
Boeing
Bellevue, WA 98006

T. A. Midford
Hughes Research Center
Torrance, CA 90509

Gaines W. Monk
Commonwealth Scientific Corporation
Alexandria, VA 22314

J. M. Morabito
Bell Telephone Laboratories
Allentown, PA 18103

Bernard Mrstik
Naval Research Laboratory
Washington, DC 20375

J. Munarin
Naval Ammunition Depot
Crane, IN 47522

J. S. Murday
Naval Research Laboratory
Washington, DC 20375

Brian A. Murphy
Semi-Films Technology
West Hurley, NY 12491

Madan Nanda
IBM/SDD
Manassas, VA 22110

Dale E. Newbury
National Bureau of Standards
Washington, DC 20234

Paul Norton
Bell Telephone Laboratories, Inc.
Allentown, PA 18103

Mylous S. O'Dell
Night Vision Laboratory
Fort Belvoir, VA 22060

F. F. Oettinger
National Bureau of Standards
Washington, DC 20234

Victor J. Ohm
Rome Air Development Center
Griffiss Air Force Base, NY 13441

Masatoshi Ono
National Bureau of Standards
Washington, DC 20234

Philip F. Ordung
University of California
Santa Barbara, CA 93106

J. Oroshnik
U. S. Navy
Rockville, MD 20853

John M. Pankratz
Texas Instruments, Inc.
Dallas, TX 75222

Donald L. Parker
Texas A & M University
College Station, TX 77843

Martin C. Peckerar
Naval Research Laboratory
Washington, DC 20375

Brad Phillips
Naval Ammunition Depot
Crane, IN 47522

Howard Phillips
Rockwell International Corporation
Anaheim, CA 92806

Dan Pierce
National Bureau of Standards
Washington, DC 20234

Larry E. Plew
Naval Ammunition Depot
Crane, IN 47522

Juergen L. W. Pohlmann
Army Night Vision Laboratory
Fort Belvoir, VA 22060

Cedric Powell
National Bureau of Standards
Washington, DC 20234

R. A. Reynolds
Advanced Research Projects Agency
Arlington, VA 22209

A. G. Revesz
Comsat Laboratories
Clarksburg, MD 20734

Giorgio Riga
Fairchild Camera
Mountain View, CA 94042

Frank G. Satkiewicz
Johns Hopkins University
Applied Physics Laboratory
Silver Spring, MD 20910

D. E. Sawyer
National Bureau of Standards
Washington, DC 20234

Harry Schafft
National Bureau of Standards
Washington, DC 20234

George H. Sigel
Naval Research Laboratory
Washington, DC 20375

Ronald L. Smith
National Security Agency
Fort Meade, MD 20755

Sherman D. Smith
Burroughs Corporation
Downingtown, PA 19335

Richard Stein
National Bureau of Standards
Washington, DC 20234

Yale Strausser
Varian Vacuum Division
Palo Alto, CA 94303

Barbara E. Sumner
Army Night Vision Laboratory
Fort Belvoir, VA 22060

Yen T. Tan
Kodak Research Laboratories
Rochester, NY 14650

Simon Thomas
Motorola SPD
Phoenix, AZ 85008

A. J. Tousimis
Tousimis Research Corporation, Inc.
Rockville, MD 20852

O. D. Trapp
Technology Associates
Portola Valley, CA 94025

Richard E. Tressler
Pennsylvania State University
University Park, PA 16802

J. C. C. Tsai
Bell Telephone Laboratories, Inc.
Reading, PA 19603

Charles Vath
Intel
Santa Clara, CA 95051

Theodore Vorburger
National Bureau of Standards
Washington, DC 20234

Bernie Waclawski
National Bureau of Standards
Washington, DC 20234

M. S. Wang
Monsanto Company
St. Louis, MO 63166

John C. Webber
IBM Corporation
Hopewell Junction, NY 12533

Clark W. White
Bell Telephone Laboratories, Inc.
Murray Hill, NJ 07974

W. R. Whitford
ORTEC, Inc.
Pearl River, NY 10965

Robert G. Wilson
Hughes Research Laboratories
Malibu, CA 90265

W. A. Wolstenholme
AEI Scientific Apparatus
Elmsford, NY 10523

K. H. Yang
IBM Corporation
Hopewell Junction, NY 12590

Carl Zanoni
Zygo Corporation
Middlefield, CT 06455

AUTHOR INDEX

NBS-114A (REV. 7-73)

U.S. DEPT. OF COMM. **BIBLIOGRAPHIC DATA SHEET**	1. PUBLICATION OR REPORT NO. NBS SP 400-23	2. Gov't Accession No.	3. Recipient's Accession No.

4. TITLE AND SUBTITLE

Semiconductor Measurement Technology: ARPA/NBS Workshop IV, Surface Analysis for Silicon Devices

5. Publication Date

March 1976

6. Performing Organization Code

7. AUTHOR(S)

A. George Lieberman

8. Performing Organ. Report No.

9. PERFORMING ORGANIZATION NAME AND ADDRESS

NATIONAL BUREAU OF STANDARDS
DEPARTMENT OF COMMERCE
WASHINGTON, D.C. 20234

10. Project/Task/Work Unit No.

11. Contract/Grant No.

ARPA Order No. 2397
Program Code 5D10

12. Sponsoring Organization Name and Complete Address *(Street, City, State, ZIP)*

Defense Advanced Research Projects Agency - 1400 Wilson Blvd.
Arlington, Virginia 22209
National Bureau of Standards, Washington, D. C. 20234

13. Type of Report & Period Covered

Final
April 23-24, 1975

14. Sponsoring Agency Code

15. SUPPLEMENTARY NOTES

Library of Congress Catalog Card Number: 76-608043

16. ABSTRACT *(A 200-word or less factual summary of most significant information. If document includes a significant bibliography or literature survey, mention it here.)*

This report contains the proceedings of the ARPA/NBS Workshop IV, *Surface Analysis for Silicon Devices*, held at the National Bureau of Standards on April 23-24, 1975.

The Workshop, as part of an NBS program to develop measurement technology for the field of semiconductor devices, was held to discuss the present capabilities and future prospects of modern analytical beam techniques as applied to silicon, and associated insulator films and device structures. Of particular interest were the determination of impurity profiles, surface contamination, and interface characteristics. Techniques utilizing impinging electron, ion, neutral or photon beams were considered. The Workshop was directed at the analysts, the semiconductor manufacturers who use the analysts' results, and the instrument people who design and manufacture the analytical equipment. Transcripts of the discussions following each paper are also included within these proceedings.

17. KEY WORDS *(six to twelve entries; alphabetical order; capitalize only the first letter of the first key word unless a proper name; separated by semicolons)* Auger spectroscopy; depth profiles; electron beam induced imaging; ESCA; insulator films; interface characteristics; internal photoemission; ion scattering spectroscopy; nuclear resonance profiling; photodepopulation; photovoltaic imaging: Rutherford backscattering: SCANIIR; secondary ion mass spectroscopy; semiconductor devices; silicon; surface analysis; X-ray photoelectron spectroscopy.

18. AVAILABILITY ☒ Unlimited

☐ For Official Distribution. Do Not Release to NTIS

☐ Order From Sup. of Doc., U.S. Government Printing Office
Washington, D.C. 20402,

☐ Order From National Technical Information Service (NTIS)
Springfield, Virginia 22151

19. SECURITY CLASS (THIS REPORT)

UNCLASSIFIED

20. SECURITY CLASS (THIS PAGE)

UNCLASSIFIED

21. NO. OF PAGES

238

22. Price

☆U.S. GOVERNMENT PRINTING OFFICE: 1976 210-801/190 1-3

Announcement of New Publications on Semiconductor Measurement Technology

Superintendent of Documents,
Government Printing Office,
Washington, D.C. 20402

Dear Sir:

Please add my name to the announcement list of new publications to be issued in the series: National Bureau of Standards Special Publication 400–.

Name ____

Company ____

Address ____

City ________________ State ____________ Zip Code ________

(Notification Key N-413)

NBS TECHNICAL PUBLICATIONS

PERIODICALS

JOURNAL OF RESEARCH reports National Bureau of Standards research and development in physics, mathematics, and chemistry. It is published in two sections, available separately:

- **Physics and Chemistry (Section A)**

Papers of interest primarily to scientists working in these fields. This section covers a broad range of physical and chemical research, with major emphasis on standards of physical measurement, fundamental constants, and properties of matter. Issued six times a year. Annual subscription: Domestic, $17.00; Foreign, $21.25.

- **Mathematical Sciences (Section B)**

Studies and compilations designed mainly for the mathematician and theoretical physicist. Topics in mathematical statistics, theory of experiment design, numerical analysis, theoretical physics and chemistry, logical design and programming of computers and computer systems. Short numerical tables. Issued quarterly. Annual subscription: Domestic, $9.00; Foreign, $11.25.

DIMENSIONS/NBS (formerly Technical News Bulletin)—This monthly magazine is published to inform scientists, engineers, businessmen, industry, teachers, students, and consumers of the latest advances in science and technology, with primary emphasis on the work at NBS. The magazine highlights and reviews such issues as energy research, fire protection, building technology, metric conversion, pollution abatement, health and safety, and consumer product performance. In addition, it reports the results of Bureau programs in measurement standards and techniques, properties of matter and materials, engineering standards and services, instrumentation, and automatic data processing.

Annual subscription: Domestic, $9.45; Foreign, $11.85.

NONPERIODICALS

Monographs—Major contributions to the technical literature on various subjects related to the Bureau's scientific and technical activities.

Handbooks—Recommended codes of engineering and industrial practice (including safety codes) developed in cooperation with interested industries, professional organizations, and regulatory bodies.

Special Publications—Include proceedings of conferences sponsored by NBS, NBS annual reports, and other special publications appropriate to this grouping such as wall charts, pocket cards, and bibliographies.

Applied Mathematics Series—Mathematical tables, manuals, and studies of special interest to physicists, engineers, chemists, biologists, mathematicians, computer programmers, and others engaged in scientific and technical work.

National Standard Reference Data Series—Provides quantitative data on the physical and chemical properties of materials, compiled from the world's literature and critically evaluated. Developed under a world-wide program coordinated by NBS. Program under authority of National Standard Data Act (Public Law 90-396).

NOTE: At present the principal publication outlet for these data is the Journal of Physical and Chemical Reference Data (JPCRD) published quarterly for NBS by the American Chemical Society (ACS) and the American Institute of Physics (AIP). Subscriptions, reprints, and supplements available from ACS, 1155 Sixteenth St. N. W., Wash. D. C. 20056.

Building Science Series—Disseminates technical information developed at the Bureau on building materials, components, systems, and whole structures. The series presents research results, test methods, and performance criteria related to the structural and environmental functions and the durability and safety characteristics of building elements and systems.

Technical Notes—Studies or reports which are complete in themselves but restrictive in their treatment of a subject. Analogous to monographs but not so comprehensive in scope or definitive in treatment of the subject area. Often serve as a vehicle for final reports of work performed at NBS under the sponsorship of other government agencies.

Voluntary Product Standards—Developed under procedures published by the Department of Commerce in Part 10, Title 15, of the Code of Federal Regulations. The purpose of the standards is to establish nationally recognized requirements for products, and to provide all concerned interests with a basis for common understanding of the characteristics of the products. NBS administers this program as a supplement to the activities of the private sector standardizing organizations.

Federal Information Processing Standards Publications (FIPS PUBS)—Publications in this series collectively constitute the Federal Information Processing Standards Register. Register serves as the official source of information in the Federal Government regarding standards issued by NBS pursuant to the Federal Property and Administrative Services Act of 1949 as amended, Public Law 89-306 (79 Stat. 1127), and as implemented by Executive Order 11717 (38 FR 12315, dated May 11, 1973) and Part 6 of Title 15 CFR (Code of Federal Regulations).

Consumer Information Series—Practical information, based on NBS research and experience, covering areas of interest to the consumer. Easily understandable language and illustrations provide useful background knowledge for shopping in today's technological marketplace.

NBS Interagency Reports (NBSIR)—A special series of interim or final reports on work performed by NBS for outside sponsors (both government and non-government). In general, initial distribution is handled by the sponsor; public distribution is by the National Technical Information Service (Springfield, Va. 22161) in paper copy or microfiche form.

Order NBS publications (except NBSIR's and Bibliographic Subscription Services) from: Superintendent of Documents, Government Printing Office, Washington, D.C. 20402.

BIBLIOGRAPHIC SUBSCRIPTION SERVICES

The following current-awareness and literature-survey bibliographies are issued periodically by the Bureau:

Cryogenic Data Center Current Awareness Service

A literature survey issued biweekly. Annual subscription: Domestic, $20.00; foreign, $25.00.

Liquefied Natural Gas. A literature survey issued quarterly. Annual subscription: $20.00.

Superconducting Devices and Materials. A literature survey issued quarterly. Annual subscription: $20.00. Send subscription orders and remittances for the preceding bibliographic services to National Bureau of Standards, Cryogenic Data Center (275.02) Boulder, Colorado 80302.

Electromagnetic Metrology Current Awareness Service Issued monthly. Annual subscription: $24.00. Send subscription order and remittance to Electromagnetics Division, National Bureau of Standards, Boulder, Colo. 80302.

U.S. DEPARTMENT OF COMMERCE
National Bureau of Standards
Washington, D.C. 20234